Department of Mechanical Engineering

Crystal Plasticity Finite Element Modeling of Slip System Activity and Post-localization Behavior in Magnesium Alloys

Mohsen Shahi

McGill University, Montreal
May 2008

A thesis submitted to McGill University
in partial fulfillment of the requirements of the degree of
Doctor of Philosophy

Abstract

During recent years, application of light metals has greatly increased in various industries. Magnesium, the lightest of structural metals, and its alloys have gained special attention, and, therefore, the interest in modeling the behavior of these alloys has increased. In many studies, the goal has been finding ways to improve the low formability of Mg alloys.

In this thesis, the effect of slip system activity on Mg alloy behavior in both the pre- and post-localization zones is examined. An available crystal plasticity model, that takes into account the initial texture of the material and its evolution with deformation, is modified for the case of HCP materials, and, then, implemented into the commercial finite element software ABAQUS. Employing the crystal plasticity finite element (CPFE) method, the link between micro-deformation on the slip systems in Mg alloys and the macro-scale response of these metals is established.

The model is verified for the case of Mg single crystals which are highly anisotropic. The minimum required size of the representative volume element (RVE), i.e. the minimum number of grains and the degree of inhomogeneity in each grain required in the CPFE modeling of Mg alloys is determined. Next, the role of different slip systems present in Mg alloys is studied. The effects of strain-rate sensitivity on the micro- and macro-scale behavior of the material and the link between them are also discussed. Using the observed trends for the slip resistances and strain-rate sensitivity factor, new relations are proposed for the change in these values over the range of warm temperatures (75-250°C). The mechanical response of samples cut from hot-rolled plates is simulated and the results are compared to the experimental results available in the literature.

In the last part, localized necking and post-localization behavior of Mg alloys are closely studied. The interaction between slip system activity and localization phenomenon is investigated, and a link is established between the onset of localization and texture evolution in the localized area. The results are of great importance in improving the forming limit of the material and extending forming to the post-localization zone.

Résumé

Au cours des dernières années, l'application de métaux légers a augmenté dans diverses industries. Le magnésium, le plus léger des métaux structuraux, et ses alliages ont acquis une attention particulière et, par conséquent, l'intérêt pour la modélisation du comportement de ces métaux a augmenté. Dans des nombreuses études, l'objectif a été de trouver les moyens d'améliorer la formabilité des alliages de Mg. Dans cette thèse, l'effet de l'activité du système de glissage sur le comportement de l'alliage de Mg dans les zones de pré- et post-localisation est examiné. Un modèle de plasticité cristalline disponible, qui prend en compte la texture initiale du matériau et de son évolution avec la déformation, est modifié pour le cas des matériaux à structure hexagonale compacte, et, ensuite, mis en œuvre dans le programme de calculs d'éléments finis, ABAQUS. Employant la méthode des éléments finis à plasticité cristalline (EFPC), le lien entre la microdéformation sur les systèmes de glissages des alliages du Mg et la réponse à l'échelle macroscopique de ces métaux est établie. Le modèle est vérifié pour le cas des monocristaux de Mg qui sont fortement anisotropes. La taille minimale prescrite de l'élément volumique représentatif (EVR), c'est-à-dire le nombre minimal de grains et le degré d'hétérogénéité dans chaque grain requis dans la modélisation EFPC des alliages du Mg, est déterminée. Ensuite, le rôle des différents systèmes de glissage dans les alliages Mg est étudié. Les effets de la sensibilité à la vitesse de déformation sur le comportement du matériau aux échelles micro- et macroscopique et le lien entre ceux-ci sont également discutés. En utilisant les tendances observées pour la résistances au glissement le facteur de sensibilité à la vitesse de déformation, des nouvelles relations sont proposées pour la modification de ces valeurs dans la gamme de températures élevées (75-250°C). La réponse mécanique des échantillons découpés à partir de plaques laminées à chaud est simulée et les résultats sont comparés aux résultats expérimentaux disponibles dans la littérature. Dans la dernière partie, la striction localisée et comportement post-localisation des alliages de Mg sont étudiés de près. L'interaction entre l'activité du système de glissage et le phénomène de la localisation est étudiée, et un lien est établi entre l'apparition de la localisation et l'évolution de la texture dans la zone localisée. Les résultats sont d'une grande importance pour l'amélioration de la limite de formation du matériau et l'extension de la formation jusqu'à la zone de post-localisation.

Acknowledgments

It has been my honor to have worked under the supervision of Prof. James A. Nemes, whose brilliant vision has given me a valuable insight for my future. I have always been fascinated by his excellence in directing and motivating me during my Ph.D. studies. I sincerely appreciate his highly professional manner which made my graduate life an enjoyable and an unforgettable experience.

I would also like to thank Prof. Stephen Yue, my co-supervisor, for giving me valuable advice and feedback, particularly during our several meetings and through my quarterly reports (submitted to GM Canada).

I also would like to thank my colleagues in the Metallurgy Dept of McGill University, in particular, Dr. Faramarz Zarandi, Dr Hualong Li, and Miss Emilie Hsu for helping me better understand the metallurgy aspects of my work. In addition, I had the opportunity to meet frequently with experienced researchers from CANMET Laboratories (Ottawa) and GM Canada, whose discussions has aided me greatly. In particular, I appreciate the valuable feedback of Dr. R. Verma from GM Canada on my work. I also wish to thank Prof. L. Anand of MIT for providing the initial UMAT subroutine used in this work.

I would like to express my gratitude towards all my past and current colleagues in the Mech. Eng. Dept. and its academic and non-academic staff. I particularly salute my friends in rooms MD252 and FDA015 who were part of my family for the past four years, and constantly gave me energy to continue my work. I, especially, thank my friend Mr. Vahid Mirjalili for proofreading parts of an early draft of this dissertation, and Mr. Sam Mahmoody for many discussions that we had on crystal plasticity. I also thank Mr. Daniel Sziriti for his help with the French translation of the abstract.

If it can be said by words, I would like to thank my parents for supporting me all the way during my studies, and for bringing me up as independent a person as I am today.

Last but not least, I want to thank my wife, Parastoo, for her constant support, patience, faith and love during my graduate studies; without her sacrifices, I would not have been able to accomplish or even start this project.

The financial support of this work, provided by GM Canada and NSERC, is greatly acknowledged.

Table of Contents

Abstract ..... **i**

Résumé ..... **ii**

Acknowledgments ..... **iii**

Table of Contents ..... **iv**

List of Figures ..... **ix**

List of Tables ..... **xviii**

List of Tables ..... **xviii**

List of Symbols ..... **xx**

List of Symbols ..... **xx**

Chapter 1 Introduction **1**

1.1 Background and Motivatoin 1

1.2 Objectives 4

1.3 Outline of the Thesis 5

Chapter 2 Review of the Literature **7**

2.1 Introduction 7

2.2 A Review of Crystal Plasticity Modeling 8

2.2.1 Crystal Plasticity Models – Early Work 8

2.2.2 Crystal Plasticity Finite Element (CPFE) Modeling 10

2.2.2.1 Combining Crystal Plasticity with the Finite Element Method 11

2.2.2.2 A Brief History of Single Crystal Visco-Plasticity 12

2.2.2.3 Applications and Verification of the CPFE Model (Cubic Materials) 13

2.3 Crystal Plasticity Modeling of HCP Materials – Magnesium Alloys 17

2.3.1 A Review of Some Studies on Slip Systems in Mg Alloys 19

2.4 Localization Studies 20

2.5 Summary 23

Chapter 3 CPFE Modeling: Theoretical Considerations and Methodology 25

3.1 Introduction 25

3.2 Constitutive Equations 27

3.2.1 Slip Systems Evolution and the Flow Rule 28

3.2.2 Hardening 32

3.2.3 Slip Systems in Magnesium Alloys 35

3.3 Methodology 38

3.3.1 The Interaction between Finite Element (ABAQUS) and Crystal Plasticity (Subroutine) 38

3.3.2 Algorithm of the Subroutine 40

3.4 Modifications Made 43

3.5 CPFE Modeling of Mg (alloys) Single Crystal 45

3.5.1 Tension Tests on a Single Mg Crystal 45

Chapter 4 The RVE Size and Grain Inhomogeneity in the CPFE Modeling of Mg Alloys 52

4.1 Introduction 52

4.2 The RVE Size (Effect of Total Number of Grains) 53

4.3 The Grain Inhomogeneity Effect 60

4.4 Grain Shape Effect 64

4.5 Grain Boundaries 66

4.6 Summary 71

Chapter 5 Slip Systems and Strain-rate Sensitivity in Mg Alloys 73

5.1 Introduction 73

5.2 Role of Individual Slip System in Mg Alloys 75

5.2.1 Random Texture 75

5.2.2 Tension and Compression in the ND 80

5.2.3 Tension in the RD 92

5.3 Strain-rate Sensitivity in Mg Alloys 99

5.3.1 Strain-rate Sensitivity on the Macro-scale 99

5.3.2 Strain-rate Sensitivity on the Micro-scale 101

5.3.3 Strain Rate Sensitivity (SRS) and Reference Shearing Rate (RSR) 103

5.3.4 Strain-rate Sensitivity and Slip System Activity 106

5.3.5 SRS Values in Mg Alloys 107

5.4 Modeling the Change in Slip Resistance Values and Strain-rate Sensitivity 113

5.4.1 Modeling the Change in the Slip Resistance Values 113

5.4.2 Modeling the Change in the Strain-rate Sensitivity 117

5.4.3 Results 118

5.5 Conclusions 123

Chapter 6 Localization in Mg Alloys 126

6.1 Introduction 126

6.2 Local Texture and Localization 129

6.3 Stress in the Localized Area 137

6.4 Texture Evolution and Slip System Activity in the Localized Area 141

6.5 Active Slip Systems and Localization 156

6.6 Conclusions 170

Chapter 7 Conclusions 171

7.1 Introduction 171

7.2 The Work Done: Results and Conclusions 172

7.3 Original Contributions 176

7.4 Recommendations for Future Work 177

7.4.1 Experimental Investigation of Localization 178

7.4.2 Multiple Deformation Mechanisms 178

7.4.3 Temperature Gradient and Forming Processes 179

7.4.4 Experimental Investigation 179

7.4.5 Grain Size (Scale Effects) and Grain Shape 180

References 181

Appendix A Texture Gradient in Hot-Rolled Mg Alloy 199

A.1 Introduction 199

A.2 Sample Preparation and Texture Measurement 199

A.3 Results 200

A.4 Summary 203

Appendix B List of Publications 204

Appendix C Design of the Proposed Experiments 205

C.1 Design of the Experiment Tables 205

C.2 Proposed Experiments 207

List of Figures

Figure 2.1 Marciniak–Kuczynski approach for a sheet with an initial thickness imperfection 21

Figure 3.1 Volume-averaged incremental plastic gradient due to slip 29

Figure 3.2 Slip systems mainly active in Mg alloys 36

Figure 3.3 Orthonormal system used to describe slip systems 36

Figure 3.4 Interaction between finite element (ABAQUS) and crystal plasticity (UMAT) 39

Figure 3.5 The cube considered for the simulation of Mg single crystal 46

Figure 3.6 Stress-strain curves for a Mg single crystal loaded along the c-axis, while assuming different slip systems to be active 47

Figure 3.7 Stress-strain curves shown in Fig. 3.5 on a different scale 47

Figure 3.8 Stress-strain curves for a single Mg crystal loaded along the c-axis, with different slip resistance values for active systems; $s_{basal} = 5$ MPa 48

Figure 3.9 Tension tests on a Mg single crystal with only pyraml<c+a> slip system active and two different initial orientations (a) stress-strain curves (b) deformed crystal A (c) deformed crystal B 50

Figure 3.10 the stress strain curves for a tension test on a single crystal assuming different slip resistance values 51

Figure 3.11 Deformed shapes of a Mg single crystal under tension for the cases shown in 3.9 (a-f) corresponding to case 1 to 6, respectively 51

Figure 4.1 Magnesium specimen under compression 54

Figure 4.2 Simple compression of Mg cube using 125 grains for 4 different initial random textures 56

Figure 4.3 Simple compression of Mg cube using 216 grains for 4 different initial random textures 56

Figure 4.4 Simple compression of Mg cube using 343 grains for 5 different initial random textures 57

Figure 4.5 Simple compression of Mg cube using 512 grains for 4 different initial random textures 57

Figure 4.6 Simple compression of Mg cube using 1000 grains for 3 different initial random textures 58

Figure 4.7 Stress-strain curves in simple compression of Mg cube for different number of grains 58

Figure 4.8 Stress at $\varepsilon = 0.14$ vs. different number of elements 59

Figure 4.9 The change in stress vs. strain with the number of elements per grain (125 grains) 61

Figure 4.10 The change in level of stress at a strain of 0.14 vs. the number of elements per grain (125 grains) 61

Figure 4.11 The change in stress vs. strain with the number of elements per grain (343 grains) 63

Figure 4.12 The change in stress vs. strain with the number of elements per grain (1000 grains) 63

Figure 4.13 Comparison between specimens with cubic grains and irregular shaped grain 65

Figure 4.14 The effect of grain shape on material behavior 65

Figure 4.15 Different hardening behaviors defined for grain boundary 68

Figure 4.16 Deformed and undeformed shape of Mg cube; grains and grain boundaries 68

Figure 4.17 The stress distribution (in MPa) in (a) specimen and (b) grain-boundary region 68

Figure 4.18 Stress-strain curve for Mg cube, considering the effects of grain boundaries using the hardening behaviors defined in Fig. 4.15. 69

Figure 4.19 Cube divided into grains and grain boundaries with different grain shape in each layer; (a) the whole model (b) all the GBs (c) GB in layers 1, 3 and 5 (d) grains in layers1, 3 and 5 70

Figure 5.1 The effect of prismatic<a> slip resistance on the stress-strain curves for specimens under compression; pyramidal<a> and pyramidal<c+a>: not active; $s_{basal<a>} = 1$ MPa 77

Figure 5.2 The effect of prismatic<a> on the stress-strain curves for specimens under compression; pyramidal<a> and pyramidal<c+a>: not active; $s_{basal<a>} = 10$ MPa 78

Figure 5.3 The effect of pyramidal <a> slip resistance on the stress-strain curves for specimens under compression; prismatic <a> and pyramidal<c+a>: not active; $s_{basal<a>} = 1$ MPa 78

Figure 5.4 The effect of pyramidal<c+a> slip resistance on the stress-strain curves for specimens under compression; pyramidal<a> and prismatic<a>: not active; $s_{basal<a>} = 1$ MPa 79

Figure 5.5 The effect of pyramidal<c+a> slip resistance on the stress-strain curves for specimens under compression; pyramidal<a> and prismatic<a>: not active; $s_{basal<a>} = 10$ MPa 79

Figure 5.6 (a) The hot-rolled plate and the corresponding specimen (b) specimen (1000 grains) 81

Figure 5.7 Initial texture of the specimen (rolled plate) (a) $\{0002\}$ pole figure (b) $\{10\bar{1}1\}$ pole figure 81

Figure 5.8 Effect of basal<a> slip system in the tension and compression tests; 83

Figure 5.9 Effect of prismatic<a> slip system in the tension and compression tests; 83

Figure 5.10 Effect of pyramidal<c+a> slip systems in the tension and compression tests; pyramidal<a>: not active; $s_{basal<a>} = 0.55$ MPa , $s_{prism<a>} = 105$ MPa 84

Figure 5.11 Change in the deformed shapes at nominal strain of 0.5 with the change in the activity of the pyramidal<c+a> under tension (a-e) and compression (f-j); the activity of pyramidal<c+a> decreases from top to bottom; pyramidal<a>: not active; $s_{basal<a>} = 0.55$ MPa , $s_{prism<a>} = 105$ MPa 85

Figure 5.12 Stress-strain curves of sample TC01 in tension and compression 88

Figure 5.13 Stress-strain curves of sample TC02 and TC03 in tension and compression 88

Figure 5.14 Final $\{0001\}$ and $\{10\bar{1}1\}$ pole figures of sample TC01 in (a-b) tension and (c-d) compression 89

Figure 5.15 Accumulated shearing increment on different slip systems for sample TC01 in tension and compression 89

Figure 5.16 Final $\{0001\}$ and $\{10\bar{1}1\}$ pole figures of sample TC02 in (a-b) tension and (c-d) compression 90

Figure 5.17 Accumulated shearing increment on different slip systems for sample TC02 in tension and compression 90

Figure 5.18 Final $\{0001\}$ and $\{10\bar{1}1\}$ pole figures of sample TC03 in (a-b) tension and (c-d) compression 91

Figure 5.19 Accumulated shearing increment on different slip systems for sample TC03 in tension and compression 91

Figure 5.20 Initial texture of the specimens (hot-rolled plate) 93

Figure 5.21 The effect of change in basal<a> slip resistance on the tension stress-strain curve; $s_{prism<a>} = 100$ MPa , $s_{pyram<a>} = 100$ MPa , $s_{pyram<c+a>} = 100$ MPa 94

Figure 5.22 The effect of change in basal<a> slip resistance on r-values; $s_{prism<a>} = 100$ MPa , $s_{pyram<a>} = 100$ MPa , $s_{pyram<c+a>} = 100$ MPa 94

Figure 5.23 The effect of change in prismatic<a> slip resistance on tension stress-strain curve; $s_{basal<a>} = 2$ MPa , $s_{pyram<c+a>} = 15$ MPa 96

Figure 5.24 The effect of change in prismatic<a> slip resistance on r-values; 97

Figure 5.25 The effect of change in pyramidal<a> slip resistance on the tension stress-strain curve; $s_{basal<a>} = 2$ MPa , $s_{prismatic<a>} = 100$ MPa 97

Figure 5.26 The effect of change in pyramidal<a> slip resistance on r-values; $s_{basal<a>} = 2$ MPa , $s_{prism<a>} = 100$ MPa 98

Figure 5.27 The effect of change in pyramidal<c+a> slip resistance on the tension stress-strain curve; $s_{basal<a>} = 2$ MPa , $s_{prism<a>} = 50$ MPa , $s_{pyram<a>} = 100$ MPa 98

Figure 5.28 The effect of change in pyramidal<c+a>slip resistance on r-values; 99

Figure 5.29 Change in the stress-level with the change in strain-rate from 0.0001 s^{-1} to 0.01 s^{-1} 103

Figure 5.30 Change of mechanical behavior with change in SRS and strain-rate $\dot{\gamma}_0 = 0.001\ s^{-1}$ 105

Figure 5.31 Change of mechanical behavior with change in SRS and strain-rate $\dot{\gamma}_0 = 0.01\ s^{-1}$ 105

Figure 5.32 The effect of change in the reference shearing rate $\dot{\varepsilon}_{nominal} = 0.01\ s^{-1}$ 106

Figure 5.33 Measured change in SRS with strain-rate at different temperatures for as-cast magnesium; values computed from stress-strain curves taken from Prasad and Sasidhara (1997) 109

Figure 5.34 Change in SRS with temperature at different strain-rates for as-cast magnesium; values computed from stress-strain curves taken from Prasad and Sasidhara (1997) 109

Figure 5.35 Values of SRS (m) for different magnesium alloys vs. strain-rate (average of the values at different temperatures); values computed from stress-strain curves taken from Prasad and Sasidhara (1997) 110

Figure 5.36 Values of SRS (m) for different magnesium alloys vs. temperature (average of the values at different strain-rates); values computed from stress-strain curves taken from Prasad and Sasidhara (1997) 110

Figure 5.37 Values of SRS (m) for different magnesium and its alloys (Mg-Zn-Mn) vs. ln Z; stress-strain curves taken from Prasad and Sasidhara (1997) 111

Figure 5.38 Values of SRS (m) for different magnesium alloys (Mg-Li-Al) vs. ln Z; stress-strain curves taken from Prasad and Sasidhara (1997) 112

Figure 5.39 Approximating the strain-rate sensitivity as a linear function of lnZ for two Mg alloy AZ31 (Zarandi *et al.*, 2007) 112

Figure 5.40 Predicted and experimental (Agnew and Duygulu, 2005) stress-strain curves in the TD vs. temperature using Eq. 5.9 115

Figure 5.41 Change in the slip resistance values vs. ln Z 116

Figure 5.42 Strain-rate sensitivity vs. temperature at strain-rate of 0.001 s^{-1} 117

Figure 5.43 Strain-rate sensitivity vs. strain-rate at 160^{o}C 118

Figure 5.44 Predicted and experimental (Agnew and Duygulu, 2005) stress-strain curves in RD vs. temperature using 5.10 119

Figure 5.45 Predicted and experimental (Agnew and Duygulu, 2005) stress-strain curves in TD vs. temperature using 5.10 119

Figure 5.46 Predicted and experimental (Agnew and Duygulu, 2005) r-values in RD and TD vs. temperature using 5.10 120

Figure 5.47 Predicted and experimental (Agnew and Duygulu, 2005) r-values in RD and TD vs. temperature using Eq. 5.10 and Eq. 5.11 122

Figure 5.48 The simulated change in stress-strain curve with the change in strain-rate 123

Figure 6.1 Initial texture of the specimens (hot-rolled plate). 130

Figure 6.2 The location of the simulated region in the specimen (one-fourth of the specimen) 130

Figure 6.3 Comparison between the stress-strain curves for the hardening (LH) 132

Figure 6.4 Using different random distribution of orientations over finite elements; no hardening on the slip systems (a) difference in the true stress-true strain curves (b) the reference distribution (c) redistribution Reshuffled 01 (d) redistribution Reshuffled 02 (e) redistribution Reshuffled 03 133

Figure 6.5 Using different random distribution of orientations over finite elements; hardening is assumed (LH) on the slip systems (a) Difference in the true stress-true strain curves (b) the reference distribution (c) redistribution Reshuffled 01 (d) redistribution Reshuffled 02 (e) redistribution Reshuffled 03 135

Figure 6.6 Using different random distribution of orientations over finite elements; higher initial hardening rate assumed on the slip systems (a) Difference in the true stress-true strain curves (b) the reference distribution (c) redistribution Reshuffled 01 (d) redistribution Reshuffled 02 (e) redistribution Reshuffled 03 136

Figure 6.7 Difference in the true stress-true strain curves of the localized area and the whole specimen comparison of the curves (b) the whole specimen (c) localized area labeled by local 01 (d) localized area labeled by local 02 (e) localized area labeled by local 03 139

Figure 6.8 Difference in the true stress-true strain curves of the localized area and the whole specimen comparison of the curves (b) the whole specimen (c) localized area labeled by local 01 (d) localized area labeled by local 02 (e) localized area labeled by local 03 140

Figure 6.9 Comparing the change in the true stress (averaged over the elements) for the whole specimen and the localized area (LH 01) 142

Figure 6.10 Comparing the activity of different slip system families for the whole specimen and the localized area (LH 01) 142

Figure 6.11 Comparing the texture evolution in the whole specimen and the localized area (LH 01) 144

Figure 6.12 Comparing the change in the true stress (averaged over the elements) for the whole specimen and the localized area (LH 01Reshuff 01) 146

Figure 6.13 Comparing the activity of different slip system families for the whole specimen and the localized area (LH 01Reshuff 01) 146

Figure 6.14 Comparing the texture evolution in the whole specimen and the localized area (LH 01Reshuff 01) 147

Figure 6.15 Comparing the change in the true stress (averaged over the elements) for the whole specimen and the localized area (NH 01) 149

Figure 6.16 Comparing the activity of different slip system families for the whole specimen and the localized area (NH 01) 149

Figure 6.17 Comparing the texture evolution in the whole specimen and the localized area (NH 01) 150

Figure 6.18 Comparing the change in the true stress (averaged over the elements) of the whole specimen and the localized area (HH 01) 151

Figure 6.19 Comparing the activity of different slip system families for the whole specimen and the localized area (HH 01) 151

Figure 6.20 Comparing the texture evolution in the whole specimen and the localized area (HH01) 152

Figure 6.21 (a) Comparing the stress-strain curves for specimens (b) with a basal texture and (c) with a “homogenized” texture 153

Figure 6.22 Comparing the change in the true stress (averaged over the elements) of the whole specimen and the localized area (LH 01 homo 01) 154

Figure 6.23 Comparing the activity of different slip system families for the whole specimen and the localized area (LH 01 homo 01) 154

Figure 6.24 Comparing the texture evolution in the whole specimen and the localized area (LH 01 homo 01) 155

Figure 6.25 The change in the localization strain with the change in the relative activity of <c+a> to other slip systems (slip resistances defined in Table 6.2) 158

Figure 6.26 The change in the localization strain with the change in the relative activity of <c+a> to other slip systems (slip resistances defined in Table 6.3) 158

Figure 6.27 Comparing the texture evolution in the whole specimen and the localized area (LH 01) 161

Figure 6.28 (cont'd) Comparing the texture evolution in the whole specimen and the localized area (SSE 02) 163

Figure 6.29 (cont'd) Comparing the texture evolution in the whole specimen and the localized area (SSE 03) 165

Figure 6.30 (cont'd) Comparing the texture evolution in the whole specimen and the localized area (SSE 04) 167

Figure 6.31 (cont'd) Comparing the texture evolution in the whole specimen and the localized area (SSE 05) 169

7.1 Change in $\{0002\}$ pole figure for *hot-rolled* (MS1, a-d) and *hot-rolled and annealed* (MS4, e-h) samples from surface to mid-plane 201

7.2 Texture Comparison between *hot-rolled* (MS1, a-d) and h*ot-rolled and annealed* (MS4, e-h) specimens at mid-plane 202

List of Tables

Table 3.1 Bravais indices and direction cosines for all important slip systems in Mg alloys 37

Table 5.1 Slip resistance values reported for magnesium and its aluminum-zinc alloy (AZ31B) 76

Table 5.2 Slip resistance values assumed for different systems for samples TC01-TC03 86

Table 5.3 Comparison of the computed macroscopic SRS values vs. values assumed in simulations 102

Table 5.4 Change in accumulated shearing increments with the change in m; 107

Table 5.5 The effects of higher activity of each slip system on the overall behavior of the material 124

Table 6.1 Material parameters assumed for non-hardening , hardening with low initial hardening rate (LH), and hardening with high initial hardening rate cases 131

Table 6.2 Slip resistance values of different families; change in prismatic<a> and pyramidal <a> 157

Table 6.3 Slip resistance values of different slip families; change in pyramidal<c+a> . 157

Table C.1 Central Composite Design - Inscribed (CCI) 206

Table C.2 Combined Central Composite Designs - Inscribed (CCI) 206

Table C.3 Combination of strain-rate and temerature; experiments to be done (**Tension - RD**) 208

Table C.4 Combination of strain-rate and temperature at which the experiments need to be done (**Compression - RD**) 209

Table C.5 Combination of strain-rate and temperature at which the experiments need to be done (**Tension - TD**) 210

Table C.6 Combination of strain-rate and temperature at which the experiments need to be done (**Compression - ND**) 211

Table C.7 Total number of specimens needed 212

List of Symbols

Latin Symbols

a_k	The area of the k-th dislocation loop on a slip system
$< a >$	The a- directions in HCP crystals (in the basal plane)
b	The magnitude of the Burgers' vector
$< c >$	The c- directions in HCP crystals (normal to the basal plane)
$< c + a >$	Directions in HCP crystals which are neither in the basal plane nor normal to it
C	A constant in the power law relation linking stress and strain rate
$\mathbf{C}^e$	The elastic right Cauchy-Green tensor
C_{ij}	The independent elastic moduli
$\mathbb{C}$	The fourth-order anisotropic elasticity tensor
$\mathbf{D}^e$	The elastic stretching tensor
$\mathbf{D}^p$	The plastic stretching tensor
$\mathbf{e}_i^c$	The orthonormal coordinate system associated with a crystal lattice
$\mathbf{e}_i^g$	The orthonormal basis associated with a fixed global rectangular coordinate system

$\mathbf{E}^e$	Green elastic strain tensor
f_{im}	Imperfection parameter (M-K approach)
f	Slip system family (i.e. basal<a>, prismatic<a>, pyramidal<a> or pyramidal<c+a>)
$\mathbf{F}$	The deformation gradient tensor
$\mathbf{F}^e$	The elastic part of the deformation gradient tensor
$\mathbf{F}^p$	The plastic part of the deformation gradient tensor
$\mathbf{F}_t^p(\tau)$	The plastic part of the deformation gradient tensor from time t to τ
G	Interactive hardening term
h	Spacing between the slip planes
$h_{\alpha\beta}$	Hardening moduli
h_s	Hardening parameter
h_β	Self-hardening rate of slip system β
$h_{\beta 0}$	Initial hardening rate for slip system β
h_0	Initial hardening rate of a slip system
h_s	Asymptotic hardening rates
k	Boltzmann's constant

$\mathbf{L}$	The velocity gradient tensor
$\mathbf{L}^e$	The elastic distortion rate tensor
$\mathbf{L}^p$	The inelastic distortion rate tensor
m	Strain-rate sensitivity factor
$\mathbf{m}_0$	Slip direction in the reference configuration
$\mathbf{m}^\alpha$	Slip direction for system α in the current state
$\dot{\mathbf{m}}^\alpha$	Evolution rate of slip direction for system α
$\mathbf{m}_0^\alpha$	Slip direction for system α in the reference configuration
$n, n', n_{\tilde{s}}$	Slip hardening parameter
$\mathbf{n}_0$	Slip plane normal in the reference configuration
$\mathbf{n}^\alpha$	Slip plane normal for system in the current state
$\dot{\mathbf{n}}^\alpha$	Evolution rate of slip plane normal for system α
$\mathbf{n}_0^\alpha$	Slip plane normal for system α in the reference configuration
nf	The number of slip systems in the family f
$q_{\alpha\beta}$	The matrix describing the latent hardening of a crystal
Q	The effective activation energy for deformation

r	r-value
$s_{basal<a>}$	The slip resistance of the basal<a> slip system
$s_{prism<a>}$	The slip resistance of the prismatic<a> slip system
$s_{pyram<a>}$	The slip resistance of the pyramidal<a> slip system
$s_{pyram<c+a>}$	The slip resistance of the pyramidal<c+a> slip system
s^{α}	The slip resistance of system α
$\dot{s}^{\alpha}$	The time rate of change in the slip resistance of system α
$s^{\alpha}(0)$	The initial value of the slip resistance of system α
s_s^{β}	The saturation value of slip resistance on system β
$\tilde{s}^{\beta}$	Slip hardening parameter
$\mathbb{S}_0^{\alpha}$	the Schmid tensor for the slip system α
$t,\ t_1$	time
t_0^b	Initial sheet thickness inside the imperfection band (M-K approach)
t_0	Initial sheet thickness outside the imperfection band (M-K approach)
T	Absolute temperature

$\mathbf{T}^*$	Symmetric second Piola-Kirchoff stress tensor, relative to the relaxed configuration
v_k	Volume of the k^{th} disk-like slip volume elements
v_{sl}	The total volume of disk-like volume elements for a slip system
V	The smallest volume element that contains enough dislocation loops on a slip systems for continuum representation
$\mathbf{W}^e$	The elastic spin tensor
$\mathbf{W}^p$	The plastic spin tensor
Z	The Zener-Hollomon parameter

Greek Symbols

α, β	Integer numbers used to define a slip system
$\Delta\gamma_{sl}$	The incremental shear due to slip
γ_{tr}	The transformation shear strain associated with each volume element of a slip system
γ_a	Accumulated shear on all the slip systems
γ_0	Reference value for accumulated shear
$\dot{\gamma}_0$	Reference shear rate (RSR)
$\dot{\gamma}^\alpha$	Shearing rate on the slip system α

$\left(\gamma^{acc}\right)^{f}$	Accumulated shearing increment on all the slip systems in family f
$\dot{\varepsilon}$, $\dot{\varepsilon}_1$, $\dot{\varepsilon}_2$	Macroscopic nominal strain rates
ε_w	Strain in the width direction
ε_t	Through thickness strain
ε_{TD}	Strain in the transverse direction
ε_{RD}	Strain in the rolling direction
ε_{ND}	Strain in the normal direction
$\dot{\varepsilon}^p$	The plastic part of macroscopic nominal strain rate
θ	Absolute temperature
σ	Flow stress value (true stress)
$\boldsymbol{\sigma}$	Cauchy stress
σ_1 , σ_2	Corresponding values of stress at a certain strain for two different strain rates $\dot{\varepsilon}_1$ and $\dot{\varepsilon}_2$
τ	Time
τ_0	Initial slip resistance value
τ_s	Hardening parameter (saturation value of the shear stress)
τ^{α}	Resolved shear stress on the slip system α

Chapter 1
Introduction

1.1 BACKGROUND AND MOTIVATOIN

Being one-third less dense than aluminum, with a higher strength-to-weight ratio, magnesium is the lightest of structural metals (Avedesian and Baker, 1999). Among other industries, it is used in the automotive industry to reduce fuel consumption thereby satisfying governmental and environmental regulations. As reported by Cole and Quinn (2007), magnesium usage in the automotive industry has grown by 10-15 percent per annum over the past 15 years to an average of 10-12 lbs (3% of total weight) for an average vehicle. In a 2020 strategic plan, Cole and Quinn propose that 340 lbs of magnesium components can be substituted for 630 lbs of current ferrous and aluminum parts bringing the total magnesium usage to 350 lbs (12.2% of total weight). This not only reduces the weight itself but also leads to secondary weight reductions and powertrain resizing which ultimately reduces the total weight of an average car by 15 percent.

Currently, high-pressure die casting (HPDC) is used to produce more than 99% of existing automotive magnesium components (Cole and Quinn, 2007). One of the current goals of the industry is to expand potential magnesium applications into metalworking

processes, particularly rolling and sheet metal forming, which can significantly reduce the processing cost. However, there are still some major obstacles in the use of Mg alloys, among which is its low formability. The hexagonal close-packed (HCP) crystal structure of magnesium requires higher processing temperatures (~225°C) as compared to aluminum or steel, which can be stamped near room temperature. Therefore, before the widespread use of Mg alloys is adopted, some methods must be developed for improving the bulk forming of these metals.

For metals, in general, considerable effort has gone into developing techniques for the design and optimization of bulk working processes. The ultimate objective is to manufacture components with controlled microstructure and properties, without macro or micro structural defects, on a repeatable basis in a manufacturing environment. This is usually done using trial and error techniques which are expensive as well as time consuming and may not always lead to a successful solution for optimization (Prasad and Sasidhara, 1997). In recent years, however, with increasing applications of light metals, such as magnesium, the interest in modeling the behavior of these metals has increased, and the trial and error methods are replaced by modeling techniques. Moreover, with the rapid growth in computational capabilities and finite element simulations, more precise constitutive relations can be employed in order to capture the micromechanical as well as the macro-scale features of deformation. Simulating Mg alloys behavior has been one area where a number of different models have been used for predicting material response.

In many studies on modeling of Mg alloys, the ultimate goal is finding ways to achieve high levels of formability at lower temperatures. Many of the traditional methods used for improving the formability of materials have proven to be inefficient for the case of Mg alloys. Recently, some innovative methods for increasing formability are being proposed. One of these alternative options is increasing the formability of material by selectively changing the micro-structure of the material such as activating particular deformation mechanisms (e.g. slip systems) to postpone the threshold of localization. The prerequisite for using these methods is a thorough understanding of the link between the micro- and macro-level deformations of the material and the role of different deformation mechanisms. On the other hand, along with the goal of increasing formability, the degree

to which the material can be formed after localization becomes important. In fact, it has been shown that a thorough understanding of post-localization behavior is critical for predicting formability (Daly *et al.*, 2007). Thus, studying the localization and post-localization behavior of Mg alloys and conditions that lead to localization would be a necessary step for improving the forming processes of these metals.

The deformation mechanisms affecting hardening, softening, and more interestingly the localization and post-localization behavior of Mg alloys are not fully discussed in the literature. Often the onset of softening has been attributed to the higher activity of different deformation mechanisms, such as grain-boundary sliding (GBS) or dynamic re-crystallization (DRX). However, in the presence of different deformation mechanisms (such as twinning, GBS, and DRX), the extent to which slip systems are active and the degree to which they affect the overall behavior of Mg alloys and the localization phenomenon is not well known. In addition, there are many unanswered questions related to the active slip systems in the deformation of Mg alloys at warm temperatures (75°C to 250°C), as well as the evolution of their slip resistance with temperature, and the role of other deformation mechanisms. The role of twinning in the deformation of polycrystalline alloys has been studied and discussed by many researchers (e.g. Van Houtte, 1978; Tome *et al.*, 1991; Myagchilov and Dawson, 1999; Kalidindi, 2003; Staroselsky and Anand, 2003). The amount of strain that twinning can accommodate is directly proportional to the volume fraction of the crystal which has twinned. Thus, there is a finite amount of strain that may be accommodated by twinning, even under ideal circumstances. For the primary twinning mode observed to operate within magnesium, the twinning shear is only 0.13. Therefore, the maximum tensile strain that twinning may accommodate is only 0.065 (Yoo, 1980). In addition, with the increase in the activity of non-basal slip systems at higher temperatures, the amount of twinning decreases, which emphasizes the important role of slip systems in the deformation of magnesium alloys.

Finally, with the prospect of extensive usage of Mg sheets in the automotive industry and others, mechanical response, anisotropic deformation, and localization behavior of Mg sheets (or samples cut from rolled plates) should be studied in detail.

1.2 OBJECTIVES

The first objective of this study is to establish the link between micro-deformations on the slip systems in Mg alloys and the macro-scale response of these metals. This is an essential prerequisite for proposing methods to increase the ductility of these alloys. The role of different slip systems present in Mg alloys is studied, and slip resistance values are proposed for the range of warm temperatures (75°C to 250°C). This is an important step in predicting the behavior of Mg alloys at warm temperatures, which is of particular interest to the automotive industry (and many others). Studying slip systems requires models that take into account the initial texture of the material and its evolution with deformation. In this thesis, the crystal plasticity finite element (CPFE) method is used for an in-depth study of the slip systems in Mg alloys.

The second objective of this work is to gain a thorough understanding of the localization phenomenon in Mg alloys and to investigate the link between micro-scale deformation and the localization phenomenon. During sheet metal forming, a detailed understanding of the necking and post-necking behavior is highly relevant (Keeler, 1968). The necking point specifies the forming limit of the sheet metal, and the width of the necking zone specifies the ductility of the post-failure behavior (Mikkelsen, 1997). In this thesis, the effects of local texture and slip resistance values on localization and post-localization behavior of Mg alloys are studied. The causes initiating localization and the parameters affecting this phenomenon are discussed in detail.

To accomplish the objectives stated above, two necessary tasks are required to be performed in this thesis. First, the optimum size of a representative volume element (RVE) should be determined for the CPFE modeling of HCP materials. Second, the role of strain-rate sensitivity in the micro- and macro-scale behavior of Mg alloys must be investigated.

It should be noted that a comprehensive model that can accurately simulate Mg alloys behavior over a range of temperatures (and/or strain-rates) is still far from reach. Such a model must take into account not only slip systems, but also twinning, grain boundary sliding (GBS), dynamic recrystallization (DRX), and other deformation mechanisms. The

objective of this work is not to define a comprehensive model that accounts for all deformation mechanisms, but rather to gain a better understanding of the role of slip systems on the overall deformation of Mg alloys and the localization phenomenon in these metals.

1.3 OUTLINE OF THE THESIS

The outline of the thesis is as follows:

In Chapter 2, a history of crystal plasticity models is presented; in particular, the work done on the crystal plasticity finite element (CPFE) modeling is summarized. The review continues with the work done on the CPFE modeling of HCP materials and specifically Mg alloys and the role of slip systems in these metals. In the last part of this chapter, a review of the work done on the localization phenomenon in different materials is presented.

Chapter 3 explains the theory behind the CPFE modeling used in this thesis. Then, the method used for combining the crystal plasticity and finite element is explained. Next, the modifications done in the model are presented, and, finally, the modified model is verified for the case of Mg alloys single crystals.

Chapter 4 is devoted to some preliminary studies for the CPFE modeling of Mg alloys. In particular, the optimum RVE size for the CPFE modeling of HCP materials is obtained. Then the effect of grain inhomogeneity and grain shape on the overall behavior of material is discussed. Finally, the effects of grain boundaries on material response are investigated.

Chapter 5 focuses on the role of slip systems and strain-rate sensitivity in Mg alloys. This chapter is divided into three parts; in the first part, the role of individual slip systems on the mechanical response of Mg alloys is studied. Several series of simulations are performed to simulate the behavior of Mg polycrystals assuming various levels of activity for slip systems. In the second part, the role of strain-rate sensitivity in the micro- and macro-level behavior of Mg alloys is investigated. In the third part, considering the trends observed for the slip systems effects and the strain-rate sensitivity factor, a series of

relations are proposed for the change in these parameters versus temperature and strain-rate. Then, using the proposed relations, the mechanical behavior and anisotropy of samples cut from hot-rolled plates are simulated over a range of temperature (75°C to 250°C). The results are compared to ones available in the literature.

Chapter 6 is devoted to studying localization phenomenon in Mg alloys. A series of simulations are performed starting with the texture of a hot-rolled plate, examining the tension simulations in the rolling direction (RD). In these simulations, localization behavior is predicted for a typical Mg alloy under different circumstances. The effect of local texture on the overall behavior of Mg alloys is discussed. Local texture, stress state, and slip systems activity in the necked area are studied, and the effect of change in the slip resistance values on localization is investigated. Then, by tracking slip systems activity and texture evolution in the necked area, a hypothesis linking the localization phenomenon with the activity of different slip systems, the orientation of crystals in the necked area, and other determining parameters is proposed. The findings explain some phenomena including different post-localization softening behaviors observed for Mg alloys in terms of slip system activity. These phenomena are conventionally attributed to the activity of some other deformation mechanisms (such as DRX) or presence of cavities.

In simulations done in Chapters 5 and 6, experimentally measured textures are used. Details of texture measurements are presented in Appendix A. Also a study on the through-thickness texture gradient of hot-rolled Mg alloy (AZ31) sheets is presented in this appendix.

Chapter 7 concludes the work done in the thesis. A summary of the work done is presented and results are briefly reviewed. Contributions to the literature are re-stated, and some recommendations are made for future work.

Chapter 2
Review of the Literature

2.1 INTRODUCTION

In the past, the constitutive laws that were used to describe the finite-strain plastic response of metals were almost exclusively phenomenological and macroscopic. However, these models were incapable of linking mechanical properties to evolving microstructures. Later, as interest in problems involving either large strains or complex loading histories grew, models which more closely follow the behavior of materials were needed. Since 1990, as a result of improvements in computational capacity, more complicated models have been employed. A clear trend has been to introduce ever greater detail of the material structure into solid mechanics simulations, and to develop multi-scale models. Dawson (2000) reviewed and discussed some methodologies for describing material structure at multiple scales.

During large plastic deformation of crystalline materials, such as that which occurs during metal forming, crystallographic deformation mechanisms induce lattice rotations which result in non-random distributions of the crystal orientations (or preferred orientations). Textures are macroscopic averages of such non-random orientations and are closely related to the structure of the single crystal lattice. Metals of hexagonal close-packed (HCP) crystal structure, in particular, develop a pronounced deformation texture

and a marked mechanical anisotropy. Incorporating texture, the major cause of anisotropic plastic response, is essential to predict the large strain behavior of polycrystalline materials (e.g. Mathur and Dawson, 1989; Kalidindi and Anand, 1994; Staroselsky, 1998; Neale *et al*., 2003), since texture imparts directionality in the flow stress. The degree of plastic anisotropy in the yield behavior of metals can be critical for subsequent fabrication processes, and the presence of texture can have many undesirable consequences. For example, when circular cups are stamped from metal sheets having preferred orientation, the sides of the cups are not even, an effect called "earing" (Mathur and Dawson, 1989). Crystal plasticity models, which take into account the initial texture of the material and its evolution with deformation, made it possible to solve the complex problem of including texture in modeling the mechanical behavior of materials. The important trend has been to develop adequate constitutive models suitable for texture evolution and stress-strain response prediction of materials in different material processing operations (Marin *et al*., 1995; Pi *et al*., 2004).

Polycrystal plasticity models describe the development of crystallographic texture and the accompanying anisotropy in the macroscopic mechanical response of polycrystalline materials. They are typically based on (i) constitutive equations that describe the mechanical behavior of single crystals, and (ii) mean field hypotheses that relate the macroscopic stress-strain response to the microscopic mechanical response of individual crystals (Marin *et al*., 1995).

In the first part of this chapter, Section 2.2, a brief history of crystal plasticity models and in particular the one employed in this thesis is presented. The following section is devoted to a review of the work done on HCP materials, and Mg in particular. The last section presents a review of the previous localization studies, which is closely related to work done in this thesis (Chapter 6).

2.2 A REVIEW OF CRYSTAL PLASTICITY MODELING

2.2.1 CRYSTAL PLASTICITY MODELS – EARLY WORK

Several different approaches have been used for modeling the behavior of polycrystals. A review of different crystal plasticity models and a quantitative comparison of them can be

found in Van Houtte *et al.* (2005). In most of the early work on polycrystal constitutive theories of plasticity, the plastic properties of a polycrystalline aggregate were treated as averages over all crystals. Sachs (1928) developed one of the first polycrystal models, proposing that the single crystals experience the same state of stress as the aggregate. This condition satisfies equilibrium across the grain boundaries, but does not satisfy compatibility between the grains. Taylor (1938) proposed the fully-constrained (FC) model based on the assumption of uniform plastic strain in the aggregate. This model satisfies the compatibility requirements but does not satisfy the equilibrium across the grain boundaries. The theory of Taylor was expanded upon by Bishop and Hill (1951) to include multi-axial stress states, thus developing the Taylor-Bishop-Hill (TBH) model. Later, the Taylor model was extended to elastic-plastic deformations by Payne *et al.* (1958), to visco-plastic deformations by Hutchinson (1964), and to finite elastic-viscoplastic deformations by Asaro and Needleman (1985).

The next improvement in polycrystal models was the development of self-consistent models, introduced in the early 1960's. These models address the interaction of the grain with its surroundings by considering the grains as inclusions in the polycrystal matrix, and satisfy both equilibrium and compatibility in the average sense. In one of the first studies on self-consistent modeling, based on the use of Eshelby's solution (1958) for an ellipsoidal inclusion in a linear elastic matrix, Kroner (1961) and Budiansky and Wu (1962) proposed the KBW self-consistent model. A generalized incremental self-consistent formulation for small elastic-plastic deformations was proposed by Hill (1965). To formulate the self-consistent scheme for large elastic-plastic deformations of polycrystals, Iwakuma and Nemat-Nasser (1984) proposed an extension of Hill's incremental approach. Self-consistent models were later developed further by many researchers to include small and large elastic-plastic deformations.

Lebensohn and Tome (1993) presented a visco-plastic self-consistent (VPSC) anisotropic approach for modeling the plastic deformation of polycrystals. They used the model for predicting texture development during rolling and axisymmetric deformation of zirconium alloys, and to calculate the yield locus and the Lankford coefficient of rolled zirc-alloy sheet. Lebensohn *et al*. (1998) presented an extension of the VPSC model for

calculation of the intergranular Cauchy stress in an aggregate. In their approach, the complete stress state in the grains was obtained by computing the deviatoric and the hydrostatic local deviations with respect to the overall corresponding magnitudes applied to the polycrystal. Tome *et al*. (2001) and Kaschner *et al*. (2001) implemented a VPSC model in finite element software and simulated pure Zr deforming under quasi-static four-point bending at room and liquid-nitrogen temperatures.

2.2.2 CRYSTAL PLASTICITY FINITE ELEMENT (CPFE) MODELING

In crystal plasticity models, two levels are always considered: mesoscopic and macroscopic scales. At the mesoscopic scale, a small RVE (representative volume element) is considered, which is supposed to have uniform properties (including crystal orientation) as well as homogeneous stress and strain distributions. A transition must then be provided from the mesoscopic scale to the macroscopic scale, i.e., a relationship must be provided between the local stresses and strains (at the mesoscopic scale) and those macroscopically observed.

The next generation of polycrystal plasticity models were the crystal plasticity finite element (CPFE) models, which use the basic principles of mechanics to achieve the transition from the mesoscopic scale to the macroscopic scale; i.e., the stress equilibrium and geometrical compatibility at the individual grain boundaries, and this simultaneously for all grains of a multi-crystal (Van Houtte *et al*., 2005). In the CPFE, polycrystal plasticity theory provides a micro-mechanical model for plastic flow, while the finite element method provides a numerical means to solve the field equations of elasticity or plasticity. In these models both compatibility and equilibrium are satisfied and there is no need for the averaging schemes such as Sachs, Taylor or self-consistent methods, which have been classically used to obtain the response of a polycrystalline aggregate. The finite element method also permits subdividing the grains into small finite elements and thus simulating the heterogeneity of plastic deformation in individual grains. On the other hand, calculations in which each finite element represents a single grain allow verification and calibration of constitutive models for polycrystals. The results obtained at this structural level can be used for verification of the scheme at the next structural level, where each element integration point represents a group of grains, which provides

computationally inexpensive first order approximate solutions for polycrystalline behavior. However, it should be noted that finite element formulations that employ polycrystal plasticity model are computationally demanding. If a large scale application is pursued on a single processor computer architecture, the calculations related to the crystal equations can take up to 95% of the execution time (Dawson *et al*., 1994).

2.2.2.1 COMBINING CRYSTAL PLASTICITY WITH THE FINITE ELEMENT METHOD

A variety of approaches exist for merging finite element formulations and crystal plasticity models. One possibility is to embed polycrystal plasticity theory within a finite element formulation as a constitutive theory in much the same way as was done classically for continuum elasto-plasticity models. In this case, a crystal ensemble is usually referred to as an aggregate and an averaging assumption such as the Taylor model should be used. An aggregate underlines a continuum point and is interrogated at appropriate times in a simulation to evaluate flow properties. In turn, hardening of crystal slip systems and crystal rotations follow from the continuum fields of stress and deformation. Polycrystal plasticity can be viewed in this context as a state variable constitutive theory in which the orientation distribution of crystal lattices along with the crystal hardness, comprise the description of state (Dawson, 2000).

A second combination of finite element and polycrystal plasticity is associated with more detailed study of the crystal ensembles themselves. In this case, finite elements divide the crystals or alternatively each element is assumed to be one single crystal. For this case, a crystal ensemble is usually called a polycrystal. Within an element the single crystal relations hold, while the finite element solution provides insight into the distribution of deformation and details of load sharing in the polycrystal.

Dawson *et al.* (1994) called the two approaches large and small scale applications, respectively. Large-scale applications are those in which the body is very much larger than individual crystals, such as the rolling of plates, sheet forming, and forging. A variety of technical issues arise as the focus of these applications, such as unsymmetric deformations (earing), texture gradients within the work-piece (and consequential effects on mechanical properties), macroscopic shear banding, and residual stress. Small scale

applications are the ones in which the crystal dimensions are comparable to the entire body. Finite elements typically have volumes similar to that of a single crystal, and in many cases are one-to-one. In defining the mesh, one also is prescribing the topology of the polycrystal. Gradients of the deformation are permitted over an element, and thus over individual crystals as well. In contrast to large scale applications, the balance laws are applied directly to a polycrystal.

In the CPFE modeling, the behavior of a single crystal is governed by crystal plasticity theories. In this thesis, a visco-plastic model is used for defining single crystal behavior. A short review of the single crystal visco-plasticity theories is presented in the next section.

2.2.2.2 A BRIEF HISTORY OF SINGLE CRYSTAL VISCO-PLASTICITY

The foundations of the (now classical) single-crystal viscoplasticity theory may be traced to the papers by Taylor (1938), Mandel (1965 and 1972), Hill (1965), Teodosiu (1970), Rice (1971), Teodosiu and Sidoroff (1976), Lee (1969), Asaro (1983), and Asaro and Needleman (1985) (the basics of this theory are explained in Chapter 3). The work on single and polycrystal visco-plasticity theory has been further advanced by many research groups (e.g. Dawson *et al.*, 1994; Bassani, 1994; Wu *et al*., 1996; Anand *et al*., 1997; Neale *et al*., 2002; Van Houtte *et al*., 2005).

Asaro and Needleman (1985) established a rigorous constitutive framework for modeling the evolution of stress-strain response and the crystallographic texture during finite deformations by slip mechanisms. The general structure of the elasto-viscoplastic constitutive equations for single crystals is based on the kinematic decomposition of the deformation gradient into elastic and plastic components. A feature of this decomposition is that it introduces an intermediate configuration between the reference and current configurations which is obtained by elastically unloading the crystal to a stress-free state. The current configurations (Peirce *et al*., 1983), the relaxed configurations (Kalidindi *et al*., 1992), and alternative intermediate configurations (e.g. Marin and Dawson, 1998a and 1998b) have all been used to write the crystal constitutive equations. When elastic deformation is neglected, all these descriptions reduce naturally to a rigid-viscoplastic

constitutive model expressed in the current configuration. Time integration procedures for these models have been developed by Peirce *et al*. (1983), and later by Kalidindi *et al*. (1992).

Kalidindi *et al*. (1992) and Bronkhorst *et al*. (1992) proposed a crystal plasticity model, which is used in this thesis. This model accounts for: (i) the polycrystalline nature of metals; (ii) the dominant mechanism of inelastic deformation by crystallographic slip; and (iii) the evolution of crystallographic texture during large deformations. They implemented this model together with a new fully implicit time-integration scheme in the finite element analysis to simulate the evolution of crystallographic texture during bulk deformation processing of FCC metals deforming by crystallographic slip.

2.2.2.3 APPLICATIONS AND VERIFICATION OF THE CPFE MODEL (CUBIC MATERIALS)

Since 1990, several groups have been working in the area of crystal plasticity based modeling of material behavior. The capabilities of the CPFE modeling have been verified by many researchers. In what follows, some work done on the CPFE modeling of materials with cubic crystal structure is presented.

Part of the work on the CPFE models has been focused on further developing the CPFE modeling and/or customizing it for certain applications. Kalidindi and Anand (1994) used a CPFE model with a Taylor-type assumption to predict the deformation response of initially textured FCC copper. To employ a rate-independent theory, Anand and Kothari (1996) presented a scheme for determining a unique set of active slip systems and the corresponding shear increments. They presented a calculation scheme for determining a unique set of active slip systems and the corresponding shear increments. They compared the predictions from the new computational procedure for the rate-independent theory to corresponding predictions from a procedure for a similar but rate-dependent theory. They observed that the results from the two procedures are essentially indistinguishable for low values of the rate sensitivity parameter (less than 0.01).

Marin and Dawson (1998b) presented a velocity-pressure formulation of the finite element equations using the elasto-viscoplastic crystal model for small elastic strains

developed in Marin and Dawson (1998a). Their formulation allowed for compressibility effects through the volumetric elastic response of the single crystal. The examples were solved using a three-dimensional Lagrangian finite element code developed for parallel supercomputers. The polycrystal response was obtained using the extended Taylor hypothesis. A discussion of the parallel computing strategies used in the implementation was presented in Dawson *et al*. (1994).

In 1998, Staroselsky and Anand formulated a rate-independent constitutive model taking into account slip and twinning. They also developed a new scheme for determining the active systems and the shear increments on the active slip and twin systems. They simulated the texture evolution and stress-strain curves in plane strain compression and simple compression of α-brass. They also evaluated the applicability of a Taylor-type model for combined slip and twinning, and showed that for the high-symmetry FCC brass, the results of a Taylor-type model are reasonably good, but not for less symmetric crystal structures like HCP.

Myagchilov and Dawson (1999) also presented a methodology for computing the deformation texture of polycrystalline metals that exhibit both crystallographic slip and mechanical twinning. Texturing was calculated by integrating a conservation equation for the orientation distribution function cast over an angle-axis parameterization of orientations. They also introduced a new criterion for the termination of twinning, which was based on the probability of different twin lamellae coexisting in the same single crystal without intersecting. Texture evolution was examined for polycrystals comprised of either FCC or HCP crystals. For the former, the method works well, while for the latter, it does not, they reported.

Using the CPFE modeling, much work has been done on the deformation and forming of metals. Mathur and Dawson (1989) modeled the evolution of texture in a multi-pass aluminum rolling simulation. Zhou *et al.* (1991) employed a rigid-plastic rate-sensitive crystal plasticity model to study the behavior of FCC polycrystals during rolling and subsequent biaxial sheet stretching. In these investigations, they focused on the so-called "ideal orientations" of rolling textures. The full-constraint Taylor theory was adopted in

their analysis. Neale (1993) reviewed some of the work done on the implementation of crystal plasticity constitutive relations in the simulation of metal deformation processes.

Anand *et al*. (1997), also reported on applications of the computational capability to simulate (a) a classical quasi-static deformation processing operation of cup-drawing, and prediction of the important earing defects, which develop during cup drawing from an isotropic sheet of FCC aluminum alloy; (b) the ovalization of pre-textured BCC tantalum cylinders during dynamic Taylor cylinder impact tests. Their experiments and calculations show that for FCC materials, the Taylor-type model is in reasonable agreement with the experiments regarding the texture evolution and the overall stress-strain response.

Marin and Dawson (1998b) solved four examples using the CPFE modeling: (i) the relaxation and reverse loading test of a single element subjected to uniaxial loading; (ii) the deformation of a polycrystal subjected to plane strain compression; (iii) the prediction of residual stresses in a thick ring; and (iv) the determination of the r-value for a rolled specimen. In examples (i) and (iii), an aggregate of crystals was placed at the centroid of the element, while for examples (ii) and (iv), a single crystal orientation was used at each element. The lattice for each case was assumed to be FCC where plastic deformation was accommodated by crystallographic slip.

Inal *et al*. (2002b and 2002c) investigated localized deformations in polycrystalline solids under plane strain and plane stress tension, using a rate-dependent crystal plasticity model and the Taylor assumption considering slip only (localization studies are reviewed in Section 2.4).

Tugcu *et al*. (2004) investigated the hydrostatic bulge test by studying the finite–strain deformation of a membrane under hydrostatic pressure using a rate-dependent polycrystal plasticity formulation based on the Taylor assumption for FCC structure and slip mechanism only. Numerical results were generated for a circular specimen using parallel computing features.

Wu *et al*. (2005a) studied the effect of pre-straining on material anisotropy by performing uniaxial tension tests at different angles from the rolling direction for both as-received

and pre-strained sheets of aluminum alloy. They investigated the influence of friction and rolling gap geometry on texture development for the six main orientation components, present in their final rolling textures for polycrystalline copper.

Simple shear and torsion tests have been extensively used for the verification of proposed constitutive models. Several works have been performed on simulating torsion and shear deformations problems of FCC and BCC materials using crystal plasticity models. Neale *et al*. (1990) analyzed fixed-end torsion of solid bar using a polycrystal plasticity model. Kalidindi *et al*. (1992) employed the model for simulating the stress-strain behavior and the evolution texture under both homogeneous and non-homogeneous deformation conditions by comparing numerical simulations to experimental measurements in simple shear and a simple plane-strain forging experiment on copper.

A finite element analysis of the Swift effect, based on a rate-dependent crystal plasticity model, was carried out by van der Giessen *et al*. (1992), where a special-purpose finite element developed previously by Wu and Van der Giessen (1991) was implemented in numerical simulations. An analogous simulation was carried out for the "inverse Swift effect" by van der Giessen and Neale (1993). Later on, Wu *et al*. (1996) evaluated Taylor-type polycrystal plasticity models with various single slip hardening laws by studying the large-strain behavior of FCC polycrystals during reversed torsion. Wu *et al*. (2001) developed a 2-D finite element analysis based on crystal plasticity to simulate the large-strain planar simple shear of Al alloy. Inal *et al*. (2002a) investigated the large strain behavior of Al sheets subjected to in-plane simple shear.

More recently some attempts have been made for employing the CPFE modeling to simulate material behavior over ranges of temperatures and strain-rates. Kothari and Anand (1998) employed a constitutive function for the shearing rates on slip systems, based on the thermally activated theory of plastic flow together with the CPFE model to predict the stress–strain response and texture evolution of BCC tantalum to large strains over a range of strain rates and temperatures. Balasubramanian and Anand (2002a) did similar work for the case of materials with FCC structure.

Crystal plasticity has also been used for studying the grain interactions and inter-granular stresses. Wei and Anand (2004) reviewed some of these studies and modeled the effects of grain boundaries in polycrystalline materials. They coupled a crystal-plasticity model for the grain interiors with a new elastic–plastic grain-boundary interface model, and studied the deformation and fracture response of nano-crystalline nickel.

In this thesis, the CPFE model proposed by Kalidindi *et al.* (1991) and further developed and verified by others (e.g. Anand and Kalidindi, 1994; Anand *et al.*, 1997; Kothari and Anand, 1998; Staroselsky and Anand, 1999) is used. The theory behind this model, basic assumptions, constitutive equations, and detailed formulation of this model for the case of single crystals can be found in Anand (2004).

2.3 CRYSTAL PLASTICITY MODELING OF HCP MATERIALS – MAGNESIUM ALLOYS

There have been considerable advances in the understanding of anisotropy due to crystallographic texture. A reasonably successful physically-based elasto-viscoplasticity theory for the deformation of FCC and BCC single crystals and polycrystals, at low homologous temperatures (<0.3) and low strain rates (0.001 to 0.1 s^{-1}), is now well established. However, the CPFE modeling is in its infancy when applied to the analysis of deformation processing problems under elevated isothermal and quasi-static conditions (e.g. Balasubramanian and Anand, 1996). In addition, the theory of finite plastic deformation in materials with hexagonal close packed (HCP) structure, such as magnesium, is less developed.

The reason for the lack of progress for HCP materials is the complexity of the deformation modes present in these materials. Unlike the FCC materials, inelastic deformation of a HCP crystal is highly anisotropic and the deformation resistances of different slip systems are substantially different. Furthermore, at some strain-rates and temperature ranges, other deformation mechanisms, such as twinning, grain boundary sliding (GBS) and dynamic re-crystallization can play important roles in maintaining plastic flow (e.g. Hauser *et al*., 1955 and Raynor, 1959). Balasubramanian *et al*. (2002b)

state that not even a slip-based theory applicable to high temperature deformation of HCP materials has been fully developed.

In the past it was believed that only basal slip systems are active in Mg alloys, and, thus, Mg crystals were assumed essentially inextensible along the hexagonal (c-axis) direction (slip mechanism and active slip systems are explained in Chapter 3). A number of models have been used to describe the response of such inextensible HCP crystals. A hybrid formulation was developed by Parks and Azhi (1990) and further studied by Prantil *et al*. (1995). This model describes the crystal mechanical response using a typical visco-plastic constitutive framework (Mathur and Dawson, 1989), which includes explicitly the kinematic constraint along the crystal c-axis. This model has been extended to include elasticity by Schoenfeld, Ahzi and Asaro (1995). In contrast to a finite element implementation of the Taylor model, in Parks and Azhi's hybrid model, the aggregate deformation is determined not only by the imposed macroscopic deformation but also by the average projection tensor, both of which depend on aggregate size. Marin *et al.* (1995) studied this dependence numerically using both material point and finite element simulations. Applications of the hybrid model have been limited mainly to predicting stress-strain response and texture evolution of hexagonal polycrystalline specimens subjected to simple modes of straining. Nowadays it is well-known that non-basal slip systems are active in Mg alloys and the assumption of no extension along c-axis does not hold.

Balasubramanian and Anand (2002b), attempted to simulate the large deformation of polycrystalline materials with hexagonal crystal structure deforming by crystallographic slip only at high homologous temperatures. Nominally-homogeneous experiments were conducted on initially textured commercially pure titanium at 750°C. Calibrating the model using simple tension and compression experiments, the stress-strain response and texture evolution for plane-strain compression and thin-walled tubular torsion were predicted.

Staroselsky (1998) and Staroselsky and Anand (2003) presented a constitutive model for HCP metals at room temperature. They suggested a constitutive model based on crystal plasticity by slip and twinning in the bulk of a grain, and an "isotropic" plasticity

component to model a thin grain boundary region. The features of isotropic plasticity and crystal plasticity were averaged over the grain volume with different weights. They calibrated the model parameters for the magnesium alloy AZ31B. By comparisons between model predictions and macroscopically-measured stress-strain curves and texture evolution, they deduced information about the values of the single-crystal parameters associated with slip and twin system deformation resistances.

2.3.1 A REVIEW OF SOME STUDIES ON SLIP SYSTEMS IN Mg ALLOYS

It has been reported in the literature that depending on the model used or the experimental method employed, different approximations of the slip resistance values of different slip systems in Mg alloys can be obtained (see e.g. Staroselsky and Anand, 2003; Barnett *et al.*, 2005; Agnew and Duygulu, 2005; Brown *et al.*, 2005; Levesque *et al.*, 2006; Lou *et al.*, 2007). For example, Agnew and Duygulu (2005) mention that the slip resistance ratio of prismatic to basal slip systems within Mg polycrystals must be less than 5, which is already an order of magnitude smaller than estimates based upon single crystal measurements of Reed-Hill and Robertson (1957) or polycrystal simulations of Staroselsky and Anand (2003). Others reported that the critical resolved shear stress (CRSS) of basal slip in pure magnesium is approximately 0.5 MPa, and other slip systems, such as non-basal slip of <a> and <c+a> are observed to have critical resolved shear stresses that are two orders of magnitude higher than basal slip (Burke and Hibbard, 1952; Kelly and Hosford, 1968; Kleiner and Uggowitzer, 2004). A comparison of some of the proposed slip resistance values for different slip systems in Mg alloys by different researchers is presented in the work of Lou *et al.* (2007). For the deformation of Mg at higher temperatures, the available data for the slip resistance values is scarce.

However, despite the apparent contradictions, the trends that are obtained by employing different models and the general conclusions that each of them proposes are of special interest and are crucial to the correct modeling of magnesium alloy behavior at high temperatures. One of the main objectives of this study is to understand the effect of the different slip systems present in magnesium alloys, and to propose slip resistance values by employing the Crystal Plasticity Finite Element (CPFE) method in an inverse approach using experimental data for a polycrystalline Mg alloy. This understanding can

lead us to predict the behavior of Mg alloys at warm temperatures (75°C to 250°C), which is of particular interest.

2.4 LOCALIZATION STUDIES

Studying localization phenomenon has been the subject of extensive research. The pioneering work of Considère (1885) shows that the problem of strain localization has been of interest for a long time. Considère proposed a criterion based on the maximum load as a basis for the detection of diffuse necking. This criterion was later more fully developed by different researchers (e.g. Swift, 1952; Hill, 1958; Rice, 1977). It is reported that in the limit of rather long specimens, this conventional criterion for instability appears valid (Burke and Nix, 1979).

The early work on localization was done primarily using the tension test on cylindrical specimens. The tension test does provide knowledge of the intrinsic stress-strain relation up to a point. However, after necking occurs in a tension specimen, the distributions of stress and strain become very complicated, and the data is conventionally obtained in an average stress-average strain form (Chen, 1971). In fact, since 1944, when Bridgman first determined the distribution of stresses in the narrowest section of the necked cylindrical bar in tension, there have been many other investigations of the problem (e.g. Davidenkov and Spiridonova, 1946; Thomason, 1969; Chen, 1971; Needleman, 1972; Norris *et al*., 1978; Saje, 1979) all using different methods and all coming to more or less different results.

The concept of localization in sheet metals has also been extensively studied. It is generally expected that there are two different sources of inhomogeneity in a metal sheet: material inhomogeneity, which is due to inhomogeneous spatial orientation distributions and geometrical inhomogeneity, which is associated with the initial surface topography (Wu *et al.*, 2007). In most of the investigations on localized necking in sheet metals under stretching, the concept of the forming limit diagram (FLD) has been used to represent conditions for the onset of sheet necking (see e.g. Hecker, 1975). The experimental determination of FLDs is time consuming and tedious, so accurate and efficient numerical predictions would be of considerable use.

Most theoretical and numerical FLD analyses utilize the M–K approach. This approach, introduced by Marciniak and Kuczynski (1967) and extensively investigated by Hutchinson and Neale (1977), is based on a geometric defect. This theory assumes the presence of an initial geometric imperfection in the form of a groove or band in the sheet. In that sense, an imperfection parameter is defined as $f_{im} = t_0^b / t_0 < 1$, where t_0^b and t_0 represent the initial sheet thickness inside and outside the band, respectively (Fig. 2.1). Within the M–K framework, the influence of various constitutive features on FLDs has been explored using phenomenological plasticity models (see e.g. Neale and Chater, 1980; Wu *et al.*, 2003; Stoughton and Zhu, 2004; Matin and Smith, 2005; Stoughton and Yoon, 2006; Vegter and Van der Boogaard, 2006) and crystal plasticity models (see e.g. Zhou and Neale, 1995; Wu *et al.*, 1998; Savoie *et al*, 1998; Knockaert *et al.*, 2002; Inal *et al.*, 2002b, Wu *et al.*, 2005b).

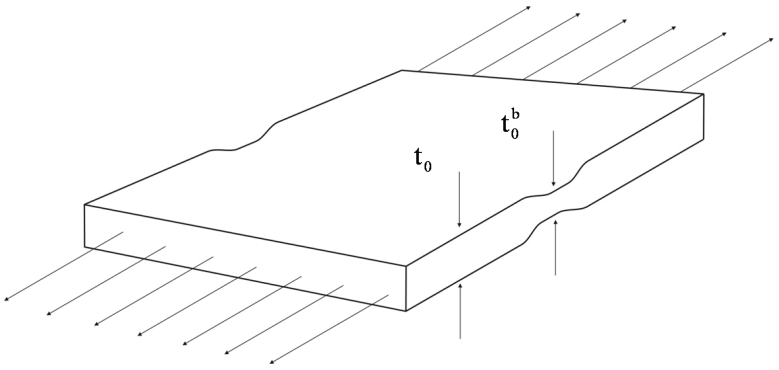

Figure 2.1 Marciniak–Kuczynski approach for a sheet with an initial thickness imperfection

Nevertheless, the M–K approach needs the value of an artificial initial imperfection parameter, f_{im}, which cannot be directly measured by physical experiments, and has to be estimated by fitting the FLD prediction to the corresponding experimental data. As pointed out by Tvergaard (1978), attempts to correlate predictions based on the M–K approach with experiments have shown that an unrealistically large initial imperfection must be assumed in order to get agreement between the limit strains. The localization of plastic flow is strongly influenced by deformation-induced textures and anisotropy (Asaro and Needleman, 1985). In turn, this localization can then affect, to some degree, the texture development in a polycrystal. This suggests that polycrystalline deformation

models, and in particular the CPFE models, are required to properly simulate plastic instability and localization phenomena.

The CPFE modeling has been used broadly in studying localization. Anand and Kalidindi (1994) studied the effects of crystallographic texture evolution on the process of shear band formation in plane-strain compression of initially isotropic FCC copper. A finite element model considering only the deformation in the flange area was developed by Inal *et al*. (2000) to simulate earing in textured aluminum sheets. Inal *et al*. (2002a and 2002b) investigated instabilities and localized deformations in polycrystalline solids under plane-strain and plane-stress tension tests. Simulations were carried out for an aluminum sheet alloy, and the effects of various parameters on the formation and prediction of necking and/or in-plane shear bands were examined.

Neale *et al*. (2003) studied instabilities and localized deformation phenomena of FCC polycrystals (Al alloys) subjected to some different deformation modes. Crystal plasticity theory was employed for specimens with the through-thickness texture gradients. Wu *et al*. (2004) studied the effects of ideal cubic texture on the initiation of localized necking numerically.

Recently, Wu *et al.* (2007) demonstrated that crystal plasticity finite element (CPFE) modeling omits the need for the artificial initial imperfection necessitated by the macroscopic M–K approach. They studied localized necking in a commercial Al alloy sheet using a 2D CPFE model under in-plane plane-strain tension. They assumed that localized necking is associated with surface instability, the onset of an unstable growth in surface roughening. They concluded that the initial surface imperfection has only a small effect on the strain to necking, and that the initial texture and its spatial orientation distribution are predominant factors for the development of localized necking.

In this thesis (Chapter 6), localization phenomenon in Mg alloys and the parameters affecting the pre- and post-localization behavior of Mg alloys are investigated using a 3D rate-dependent CPFE model. In numerical simulation, the classical elastic–plastic models reach their limits when plastic instability occurs, and the simulation becomes very sensitive to numerical parameters, which leads to poor prediction of post-localization

behavior. The 3D rate-dependent model removes the problems inherent in 2D and rate-independent models for studying localization; these problems are briefly addressed here.

Tvergaard (1993) stated that both the delay of the onset of localization and the post-necking behavior of an imperfect thin sheet are determined by three-dimensional (3-D) effects. Thus, two-dimensional (2-D) finite element analysis will give a physically unrealistic mesh sensitive solution, where the necking zone occupies the smallest possible area allowed for by the mesh (Mikkelsen, 1997). In a 2D analysis potential out-of-plane shears are restrained and spatial variations behind or in front of the model plane are neglected, which can affect the deformation field and texture evolution (Becker, 1998). Using a 3D model in this work eliminates these concerns.

Regarding the use of a rate-dependent model, there had been three long-standing problems. The first is to determine which slip systems are active; the second is to determine the increments of shear on the active slip systems and third, because of the multiplicity of slip systems in ductile crystals, the selection of slip systems required to produce an arbitrary deformation increment is not necessarily unique. In addition, numerical solutions to localization problems for rate-independent solids exhibit an inherent mesh dependence (e.g. Tvergaard and Needleman, 1981; Pietruszczak ad Mroz, 1981; Tvergaard, 1982; Belytschko and Bazant, 1986). For rate-dependent solids, the mesh sensitivity associated with numerical solutions is eliminated (Needleman, 1988). In addition, the rate-dependent models are well adapted to handle the post-localization behavior (Daly *et al.*, 2007) since the instability is delayed due to the introduced viscosity (Needleman, 1988) and the stabilizing effect of strain-rate sensitivity (Hutchinson and Neale, 1977).

2.5 SUMMARY

Crystal plasticity constitutive modeling has proven to be a robust approach. The CPFE modeling, in particular, has been extensively employed for (and verified in) predicting the mechanical behavior as well as texture evolution of FCC and BCC materials during different deformation modes and forming processes. Nevertheless, for non-cubic materials including HCP metals (and Mg alloys in particular), little work has been done.

Specifically regarding the mechanical behavior of Mg alloys, the following significant points have been noticed in the literature:

- Work done on crystal plasticity modeling of the mechanical behavior and texture evolution of Mg alloys is rare.
- In the available published work on modeling Mg alloys at room temperature and quasi-static conditions (Staroselsky and Anand, 2003), different sets of parameters have been used to simulate different deformation modes.
- The deformation behavior of Mg alloys over a range of temperatures and strain rates has not been studied thoroughly.
- No published work has comprehensively studied the role of slip systems in Mg alloys.
- No published theoretical work has been reported on the localization phenomenon of Mg alloys and the parameters affecting it.

This thesis employs the CPFE modeling to study the slip system activity and localization phenomenon in Mg alloys at warm temperatures.

Chapter 3

CPFE Modeling:
Theoretical Considerations and Methodology

3.1 INTRODUCTION

The physical picture of the deformation process in HCP metals is still far from clear. As mentioned in the previous chapter, the reason for the lack of progress in the modeling of HCP materials is the complexity of the deformation modes in these materials. Unlike the cubic materials, inelastic deformation of an HCP single-crystal is highly anisotropic and the deformation resistances of different slip systems are substantially different. In particular, for polycrystalline magnesium, deformation mechanisms are much more complex than those in single crystals. In addition to basal slip systems, there exists twinning and non-basal slip caused by inhomogeneous stressing and grain boundary constraints. Moreover, some non-crystallographic mechanisms can be active. The most important non-crystallographic mechanism of inelastic deformation is grain boundary sliding (GBS). Grain boundaries give rise to multiple slip and twinning in the adjacent grain boundary area, which results in additional plastic yielding and, consequently, in stress relief. At high temperatures, dynamic recrystallization (DRX) can also become an important deformation mechanism.

The main goal of this work is not the development of a new constitutive framework for analyzing the behavior of HCP materials or Mg, in particular, nor is it to provide a model which takes into account all the deformation mechanisms; but rather to modify the available framework of the CPFE modeling, and to utilize it in studying the role of slip systems and strain-rate sensitivity in Mg alloys, and localization phenomenon in these metals. In accordance with this goal, only crystallographic plastic deformation caused by slip systems will be considered and studied. This will be done by using a crystal plasticity finite element model (CPFE), which takes into account the plastic deformation caused by dislocation on slip systems. This model is explained in this chapter.

Vectors and second-order tensors are indicated with bold face lower and upper case letters, respectively, e.g. $\mathbf{m}$ and $\mathbf{T}$; calligraphic letters are used for fourth-order tensors, e.g. $\mathbb{C}$. The dyadic product of two vectors $\mathbf{m}$ and $\mathbf{n}$ is indicated as $\mathbf{m}\otimes\mathbf{n}$, where $\left(\mathbf{m}\otimes\mathbf{n}\right)_{ij}=m_i n_j$. Tensor operations between two second-order tensors $\mathbf{A}$ and $\mathbf{B}$ are shown as: $\mathbf{AB}$ for inner product which yields a second-order tensor with $\left(\mathbf{AB}\right)_{ij}=\mathbf{A}_{ik}\mathbf{B}_{kj}$; $\mathbf{A}\otimes\mathbf{B}$ for dyadic product resulting in a fourth-order tensor with $\left(\mathbf{A}\otimes\mathbf{B}\right)_{ijkl}=\mathbf{A}_{ij}\mathbf{B}_{kl}$ and $\mathbf{A}:\mathbf{B}$ for a scalar product giving a scalar value with $\mathbf{A}:\mathbf{B}=\mathbf{A}_{ij}\mathbf{B}_{ij}$. The contraction operation over two indices between a fourth-order tensor $\mathbb{C}$ and a second-order tensor $\mathbf{A}$ is written as $\mathbb{C}\left[\mathbf{A}\right]$. Also, the contraction operation over one indices between a second-order tensor $\mathbf{A}$ and a vectors $\mathbf{m}$ is written as $\mathbf{Am}$.When index notation is used, the summation convention is implied, unless otherwise stated. Superscripts T and -1 denote the transverse and inverse of a tensor, respectively.

The structure of this chapter is as follows: in section 3.2, the theory behind the single crystal plasticity model used is briefly explained. The slip system evolution equation and slip systems in Mg alloys are also presented in this section. Section 3.3 focuses on the methodology, particularly, the time-integration procedure and the interaction between finite elements and crystal plasticity. Section 3.4 points out some modifications made in the model, and, in Section 3.5, the modified model is verified for the case of Mg single-crystals with certain orientations and simple loadings.

3.2 CONSTITUTIVE EQUATIONS

The foundations of the single-crystal plasticity theory may be traced to the papers by Taylor (1938), Mandel (1965 and 1972), Hill (1965), Teodosiu (1970), Rice (1971), Teodosiu and Sidoroff (1976), Lee (1969), Asaro (1983), and Asaro and Needleman (1985), Kalidindi *et al*. (1992), Dawson *et al.* (1994), Bassani (1994), Wu *et al*. (1996), Neale *et al*. (2002), Anand (2004), and Van Houtte *et al*. (2005).

The general structure of the elasto-viscoplastic constitutive equations for single crystals is based on the kinematic decomposition of the deformation gradient into elastic and plastic components. In fact, the deformation of a single crystal is taken as the sum of two independent atomic mechanisms: (i) overall elastic distortion of the lattice, and (ii) a plastic deformation due to slip, that does not distort the lattice geometry. This decomposition introduces an intermediate configuration between the reference and current configurations which is obtained by elastically unloading the crystal to a stress-free state. Typically, both this relaxed configuration (e.g. Kalidindi *et al*., 1992) and the current configuration (e.g. Peirce *et al*., 1983) have been used to write the crystal constitutive equations. When elasticity is neglected, all descriptions reduce naturally to a rigid-viscoplastic constitutive model expressed in the current configuration. Following the work of Kalidindi *et al*. (1992), here the constitutive models are written in the relaxed configuration. The decomposition of the deformation gradient tensor, $\mathbf{F}$, can be stated as (Kroner, 1961; Lee, 1969)

$$\mathbf{F} = \mathbf{F}^{e}\mathbf{F}^{p}, \qquad \text{Eq. 3.1}$$

where $\mathbf{F}^{p}$ consists solely of the plastic deformation resulting from crystallographic slip, and $\mathbf{F}^{e}$ includes the elastic distortion of the lattice. The velocity gradient is obtained as

$$\mathbf{L} = \dot{\mathbf{F}}\mathbf{F}^{-1} = \mathbf{L}^{e} + \mathbf{F}^{e}\mathbf{L}^{p}\mathbf{F}^{e\,-1}; \text{ where} \qquad \text{Eq. 3.2}$$

$$\mathbf{L}^{e} = \dot{\mathbf{F}}^{e}\mathbf{F}^{e-1} \text{ and } \mathbf{L}^{p} = \dot{\mathbf{F}}^{p}\mathbf{F}^{p-1} \qquad \text{Eq. 3.3}$$

are elastic and inelastic distortion rates, respectively. Taking symmetric and skew-symmetric parts of the above relations leads to the elastic and plastic stretching and spin tensors:

$$\mathbf{D}^{e} = \text{sym}\ \mathbf{L}^{e}, \quad \mathbf{W}^{e} = \text{skw}\ \mathbf{L}^{e}, \qquad \text{Eq. 3.4}$$

$$\mathbf{D}^{p} = \text{sym}\ \mathbf{L}^{p}, \quad \mathbf{W}^{p} = \text{skw}\ \mathbf{L}^{p}, \qquad \text{Eq. 3.5}$$

so that

$$\mathbf{L}^{e} = \mathbf{D}^{e} + \mathbf{W}^{e} \ \text{ and } \ \mathbf{L}^{p} = \mathbf{D}^{p} + \mathbf{W}^{p}. \qquad \text{Eq. 3.6}$$

For metallic materials, the elastic stretches of single crystals are small. Hence, the constitutive equations for stress may be taken to be linear as

$$\mathbf{T}^{*} = \mathbb{C}\left[\mathbf{E}^{e}\right], \qquad \text{Eq. 3.7}$$

where $\mathbb{C}$ is a fourth-order anisotropic elasticity tensor; $\mathbf{E}^{e}$ and $\mathbf{T}^{*}$ are Green elastic strain measure and the symmetric second Piola-Kirchoff stress measure relative to the relaxed configuration, respectively. These measures are defined in the following equations. The elastic strain measure is defined as

$$\mathbf{E}^{e} = \frac{1}{2}\left\{\mathbf{C}^{e} - \mathbf{1}\right\}, \qquad \text{Eq. 3.8}$$

where $\mathbf{C}^{e}$ is the elastic right Cauchy-Green tensor, defined by

$$\mathbf{C}^{e} = \left(\mathbf{F}^{e}\right)^{T}\mathbf{F}^{e}. \qquad \text{Eq. 3.9}$$

On the other hand, the stress measure, $\mathbf{T}^{*}$, which is the work conjugate to the employed strain measure, is

$$\mathbf{T}^{*} = \mathbf{F}^{e^{-1}}\left\{\left(\det \mathbf{F}^{e}\right)\mathbf{T}\right\}\mathbf{F}^{e^{-T}}. \qquad \text{Eq. 3.10}$$

3.2.1 SLIP SYSTEMS EVOLUTION AND THE FLOW RULE

The total deformation of a polycrystal is achieved by imposing successive strain increments. When only slip systems are active, it can reasonably be assumed that each grain reorients gradually as a whole. It is assumed that plastic deformation of a crystal due to slip arises from a set of uniform shear increments occurring in small discrete volume-elements. The overall plastic deformation of a crystal is always inhomogeneous

at length scales associated with slip, and should be defined as an average over a volume element that must contain enough dislocation loops to result in an acceptably smooth process at the continuum level of interest. The volume of the smallest such volume element is denoted by V, which can be a small part of a crystal or its whole (Fig. 3.1).

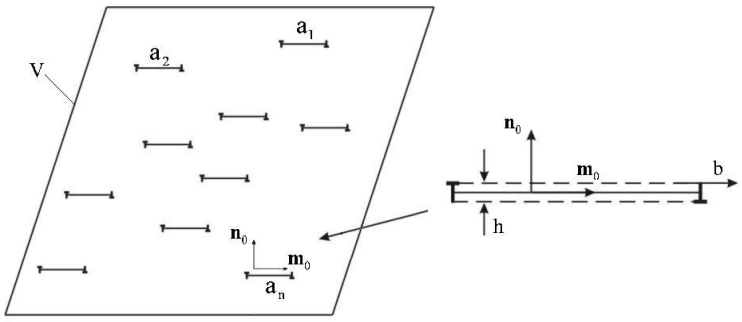

Figure 3.1 Volume-averaged incremental plastic gradient due to slip

Consider a single slip system characterized by a pair of orthonormal unit vectors $\mathbf{m}_0$ and $\mathbf{n}_0$ which define, respectively, the slip direction and the slip plane normal of a slip system. (a combination of slip plane and slip direction is called a slip system (Smith and Hashemi, 2004).) As proposed by Staroselsky (1998), at any given time, let there be n dislocation loops on such a slip system, and let a_k denote the area of the k-th dislocation loop, and let h (=const.) denote the spacing between the slip planes (Fig. 3.1). Then, at a given time, there exist n disk-like volume elements with principal planes normal to the unit vector $\mathbf{n}_0$, each of volume $v_k = h \times a_k$, which can potentially slip. The total volume of these disk-like volume elements is $v_{sl} = h \times \sum_1^n a_k$. Let $\gamma_{tr} = b/h$, with b denoting the magnitude of the Burgers vector in the slip direction $\mathbf{m}_0$, be the transformation shear strain associated with each such volume element. Then, an increment of plastic deformation resulting from slip may be visualized as being produced by an increment $\Delta v_{sl} = h \times \sum_1^n \Delta a_k$ of the volume of the disk-like elements, and the volume averaged incremental plastic deformation gradient for the crystal may be written as

$$F_t^p(\tau) = \mathbf{1} + \Delta\gamma_{sl}\ \mathbf{m}_0 \otimes \mathbf{n}_0, \text{ with } \Delta\gamma_{sl} = \frac{\Delta v_{sl}}{V}\gamma_{tr} = \frac{b\sum_1^n \Delta a_k}{V}, \qquad \text{Eq. 3.11}$$

where $\Delta\gamma_{sl}$ is the incremental shear due to slip which arises from the change in the entire area of the slip planes swept by mobile segments of the dislocation loops. $\mathbf{F}_t^p(\tau)$ is the plastic part of the deformation gradient in the multiplicative decomposition of deformation gradient from time t to τ. In writing the above, the assumption that the magnitude of the Burgers' vector, b, is the same for all the slip systems is used. Extending this idea for plastic deformation on multiple slip systems labeled by integer α, the kinematic expression for flow rule, $\mathbf{L}^p = \dot{\mathbf{F}}^p\mathbf{F}^{p-1}$, generalizes to

$$\mathbf{L}^p = \sum_\alpha \dot{\gamma}^\alpha \operatorname{sgn}(\tau^\alpha)\mathbb{S}_0^\alpha, \qquad \text{Eq. 3.12}$$

where $\dot{\gamma}^\alpha$ is the plastic shearing rate on the α-th slip system, and $\mathbb{S}_0^\alpha$ denotes the Schmid tensor for the slip system α defined by

$$\mathbb{S}_0^\alpha = \mathbf{m}_0^\alpha \otimes \mathbf{n}_0^\alpha. \qquad \text{Eq. 3.13}$$

The slip systems $(\mathbf{m}_0^\alpha, \mathbf{n}_0^\alpha)$ are assumed to be known in the reference configuration. It should be noted that $(\mathbf{m}_0^\alpha, \mathbf{n}_0^\alpha)$ remain constant throughout the deformation. The scalar value of the resolved shear stress, or the Schmid stress, on a slip system is obtained as follows

$$\tau^\alpha = \left\{\mathbf{C}^e\mathbf{T}^*\right\} : \mathbb{S}_0^\alpha. \qquad \text{Eq. 3.14}$$

For infinitesimal elastic stretches, the resolved shear stress may be approximated by

$$\tau^\alpha \cong \mathbf{T}^* : \mathbb{S}_0^\alpha. \qquad \text{Eq. 3.15}$$

The slip direction $\mathbf{m}^\alpha$ is taken to convect with the lattice, so that in the current state, we have $\mathbf{m}^\alpha = \mathbf{F}^e\mathbf{m}_0^\alpha$, while $\mathbf{n}^\alpha = \mathbf{n}_0^\alpha(\mathbf{F}^e)^{-1}$ remains orthogonal to $\mathbf{m}^\alpha$; their evolution is determined by

$$\dot{\mathbf{m}}^\alpha = \mathbf{L}^e\mathbf{m}^\alpha, \qquad \text{Eq. 3.16}$$

$$\dot{\mathbf{n}}^\alpha = -\mathbf{L}^{eT}\mathbf{n}^\alpha. \qquad \text{Eq. 3.17}$$

The next step is determining the value of shearing rates, $\dot{\gamma}^{\alpha}$, on slip systems. In rate-dependent crystal plasticity, the evolution equation for each microshear rate can be typically specified as follows (e.g., Anand, 2004),

$$\dot{\gamma}^{\alpha} = \dot{\gamma}_0 \left| \frac{\tau^{\alpha}}{s^{\alpha}} \right|^{\frac{1}{m}} \operatorname{sgn}\left(\tau^{\alpha}\right), \qquad \text{Eq. 3.18}$$

where τ^{α} is the resolved shear stress on the slip system, s^{α} is a strength-like internal variable representing the slip resistance, m is the strain rate sensitivity factor, and $\dot{\gamma}_0$ is a reference shear rate which is taken to be the same for all the slip systems and equal to 0.001 s^{-1}, unless otherwise stated. However, instead of considering a constant strain-rate sensitivity factor, m, a new strain-rate and temperature dependent formulation is used (m and $\dot{\gamma}_0$ are explained and discussed in Chapter 5). Balasubramanian and Anand (2002b) simulated the large deformation of polycrystalline materials with hexagonal crystal structure (titanium) at high homologous temperatures, using slip systems only by employing Eq. 3.18 as the evolution equation for shearing increments. As can be seen in this evolution equation (Eq. 3.18), like all rate-dependent models, although there is no specific critical value for the resolved shear stress, it is the ratio of the resolved shear stress, τ^{α}, to s^{α} that determines the activity of a slip system. For resolved shear stresses much smaller than s^{α}, the shearing increment on the slip system would be negligible, when $m << 1$ (Anand, 1982). Thus, s^{α} defines a threshold value which is a measure of the resistance to the dislocation on slip system α.

Different researchers have used different names for the term s^{α}. Some of these names include “slip resistance”, “slip hardness”, “threshold value for stress”, “reference slip stress”, “reference shear stress”, “reference stress”, “strength of slip system”, “current strength of slip system”, and CRSS (e.g. Raabe and Roters, 1991; Tome *et al*., 1998; Myagchilov and Dawson, 1999; Agnew and Duygulu, 2005). In this thesis, the most commonly used term “slip resistance” is used in referring to s^{α}.

3.2.2 HARDENING

The slip resistance values not only change from one slip system to the other, but also throughout the deformation. The evolution of these values during deformation is governed by hardening rules. Wu *et al*. (1996) reviewed and discussed some of the hardening rules reported in the literature. Some of these rules are briefly mentioned in what follows.

Asaro and Needleman (1985), among others, simply took the hardness of each slip system, s^{α}, to depend on the accumulated sum γ_a of the slips; i.e.,

$$s^{\alpha} = s^{\alpha}(\gamma_a), \quad \gamma_a = \int_0^t \left|\dot{\gamma}^{\alpha}\right| dt \ . \qquad \text{Eq. 3.19}$$

In a well-known approach for defining the hardening of slip systems, the slip system resistance, s^{α}, can be taken to evolve according to (e.g. Kalidindi *et al*., 1992)

$$\dot{s}^{\alpha} = \sum_{\alpha} h_{\alpha\beta}(t) \ \left|\dot{\gamma}^{\beta}\right|, \qquad \text{Eq. 3.20}$$

where the initial value of the hardness is defined for each slip system α as $s^{\alpha}(0)$. The values of $s^{\alpha}(0)$ for a specific temperature and strain-rate will be obtained by the relations that are introduced later in Chapter 5. $\dot{\gamma}^{\beta}$ is the shearing rate on slip system β, and the matrix $h_{\alpha\beta}$ describes the rate of increase of the deformation resistance on slip system α due to shearing on slip system β; it describes both self-hardening when $\alpha = \beta$ (diagonal terms), and latent hardening when $\alpha \neq \beta$ (non-diagonal terms). The use of the absolute value of $\dot{\gamma}^{\beta}$ in the hardening equation reflects the assumption that the hardening behavior is not significantly affected by the direction of shearing on a slip system. Each element $h_{\alpha\beta}$, in fact, depends on the deformation history. It is fair to state that the characterization of the hardening moduli, $h_{\alpha\beta}$, especially for hexagonal crystals is a formidable task. For example, in an HCP crystal deforming by three basal<a>, three

prismatic<a>, six pyramidal<a>, and the six pyramidal<c+a> slip systems, there are 324 elements in the $h_{\alpha\beta}$ matrix that need to be specified (Balasubramanian *et al*., 2002b).

The following form for the slip system hardening matrix $h_{\alpha\beta}$ is a simple tractable description of the crystal hardening (e.g. Staroselsky and Anand, 1998),

$$h_{\alpha\beta} = q_{\alpha\beta} h_{\beta}, \quad \text{with no sum on } \beta. \qquad \text{Eq. 3.21}$$

Here, h_{β} denotes the self-hardening rate of slip system β and $q_{\alpha\beta}$ is a matrix describing the latent hardening behavior of a crystal. In this work, $q_{\alpha\beta}$ is taken to be 1 for co-planar systems and 1.4 for the others. Different assumptions can be made in obtaining h_{β}. Based on strain-hardening measurements of Al single crystals by Chang and Asaro (1981), the following slip hardening rate was proposed by Asaro and co-workers (Harren *et al*., 1989):

$$h_{\beta} = h_s + (h_0 - h_s)\sec h^2 \left\{ \left(\frac{h_0 - h_s}{\tau_s - \tau_0} \right) \gamma_a \right\}, \qquad \text{Eq. 3.22}$$

where h_0 and h_s are the system's initial and asymptotic hardening rates, and τ_0 is the initial slip resistance value (or initial critical resolved shear stress) and is constant during the deformation. If $h_s = 0$, then τ_s represents the saturation value of the shear stress.

In an alternative approach, Wu *et al*. (1996) employed an exponential form for the hardening rate on all slip systems, i.e.

$$h_{\beta} = \frac{\tau_s - \tau_0}{\gamma_0} \exp\left(\frac{\gamma_a}{\gamma_0} \right). \qquad \text{Eq. 3.23}$$

Bassani and Wu (1991) proposed a particular multiplicative form in which each diagonal component is taken as the product of a self-hardening term h and an interactive hardening term G:

$$h_{\alpha\alpha} = h(\gamma_{\alpha}) G, \quad \text{with no sum on } \alpha. \qquad \text{Eq. 3.24}$$

It is clear that Asaro and co-workers as well as others have adopted a hardening description that is a special case of the above form, where $G = 1$. A form for G that equals unity when its arguments are all zero and approaches asymptotically to finite values when all slips are large is (Bassani and Wu, 1991)

$$G = 1 + \sum_{\beta \neq \alpha} f_{\alpha\beta} \tanh\left(\frac{\gamma_\beta}{\gamma_0}\right), \qquad \text{Eq. 3.25}$$

where γ_0 represents the amount of slip after which a given interaction between slip systems α and β reaches peak strength. Each $f_{\alpha\beta}$ represents the strength of the interaction and depends on the type of dislocation junction formed between the slip systems, which, in turn depends on the geometric relation between the two slip systems. A simple form for the self-hardening that gives a monotonically decreasing hardening rate at small strains and a finite rate of hardening at large γ_α is (Bassani and Wu, 1991)

$$h(\gamma_\alpha) = h_s + (h_0 - h_s)\operatorname{sech}^2\left\{\left(\frac{h_0 - h_s}{\tau_I - \tau_0}\right)\gamma_\alpha\right\}, \qquad \text{Eq. 3.26}$$

where τ_I is the so-called stage I stress and h_0 is the initial hardening rate, and h_s is assumed to depend on the total accumulated slip γ_a on all slip systems (Bassani, 1994).

Motivated by the work of Brown *et al*. (1989), Anand and co-workers (see e.g. Kalidindi *et al.,* 1992) considered the following power-law form:

$$h_\beta = h_{\beta 0}\left|1 - \frac{s^\beta}{s_s^\beta}\right|^n \operatorname{sign}\left(1 - \frac{s^\beta}{s_s^\beta}\right) \qquad \text{Eq. 3.27}$$

where $h_{\beta 0}$, n and s_s^β are slip system hardening parameters which are taken to be identical for all slip systems in their work. Unlike the Asaro or the exponential single slip hardening rate, in this hardening rule, h_β is directly related to the current hardness, s^β, of the slip system. In this thesis, this hardening rule is used after some modifications. $h_{\beta 0}$ and n are taken to be 50 MPa (discussed in Chapter 6) and 2.5 (Staroselsky, 1998), respectively. For high strain-rates and high temperatures, the saturation values, s_s^β,

cannot be taken constant. Following Balasubramanian and Anand (2002b), a phenomenological form has been adopted for the saturation value, s_s^β, as follows,

$$s_s^\beta = \tilde{s}^\beta \left(\frac{\dot{\gamma}^\beta}{\dot{\gamma}_0} \right)^{n'} \qquad \text{Eq. 3.28}$$

where $\tilde{s}^\beta$ and n' are additional slip system parameters. This equation was introduced by Anand (1982). Similar relations had also been suggested by Kocks (1976). In general, n' is a function of temperature, but here it is assumed to be constant and equal to 0.1 (Balasubramanian and Anand, 2002b). With the aim of reducing the number of parameters in the model, in the simulations done in this study, $\tilde{s}^\beta$ is considered to be a specific multiple of the initial hardness, $s^\beta(0)$, for all slip systems (Shahi and Nemes, 2007),

$$\tilde{s}^\beta = (n_{\tilde{s}}) s^\beta(0) \qquad \text{Eq. 3.29}$$

where $n_{\tilde{s}}$ is a multiplication factor, and is constant for all the slip systems. Here, it is taken to be 1.2. Eq. 3.28 plays an important role in controlling the value of saturation stress. In fact, Eq. 3.27 contains a hardening part and a softening part. The softening term, s^β / s_s^β, becomes more important with the increase in temperature and decrease in strain-rate. In other words, according to Eq. 3.28, with the decrease in strain-rate (and, consequently, the shearing rate on the slip system, $\dot{\gamma}^\beta$), the saturation stress decreases; in addition, with the increase in temperature, the initial slip resistance values decreases which in turn decreases the value of $\tilde{s}^\beta$ (Eq. 3.29) and, as a result, the saturation stress.

3.2.3 SLIP SYSTEMS IN MAGNESIUM ALLOYS

Slip is usually favored on close-packed planes where a lower shear stress is required for atomic displacement compared to less densely packed planes (Smith and Hashemi, 2004). The directions for easy crystallographic slip in HCP single crystals are the three $\langle 11\bar{2}0 \rangle$ or <a> directions (Fig. 3.2). The three dominant sets of planes which contain this slip direction are (1) the (0001) basal plane, (2) the three $\{1\,\bar{1}\,00\}$ prismatic planes and (3) the

six $\{1\bar{1}01\}$ pyramidal planes. Other than these <a> slip systems, the slip in the $\langle 11\bar{2}3\rangle$ direction (<c+a> direction) on the six $\{11\bar{2}2\}$ planes has been observed to be active in Mg alloys and will be considered in this work. Figure 3.2 shows the slip mechanisms common for Mg alloys.

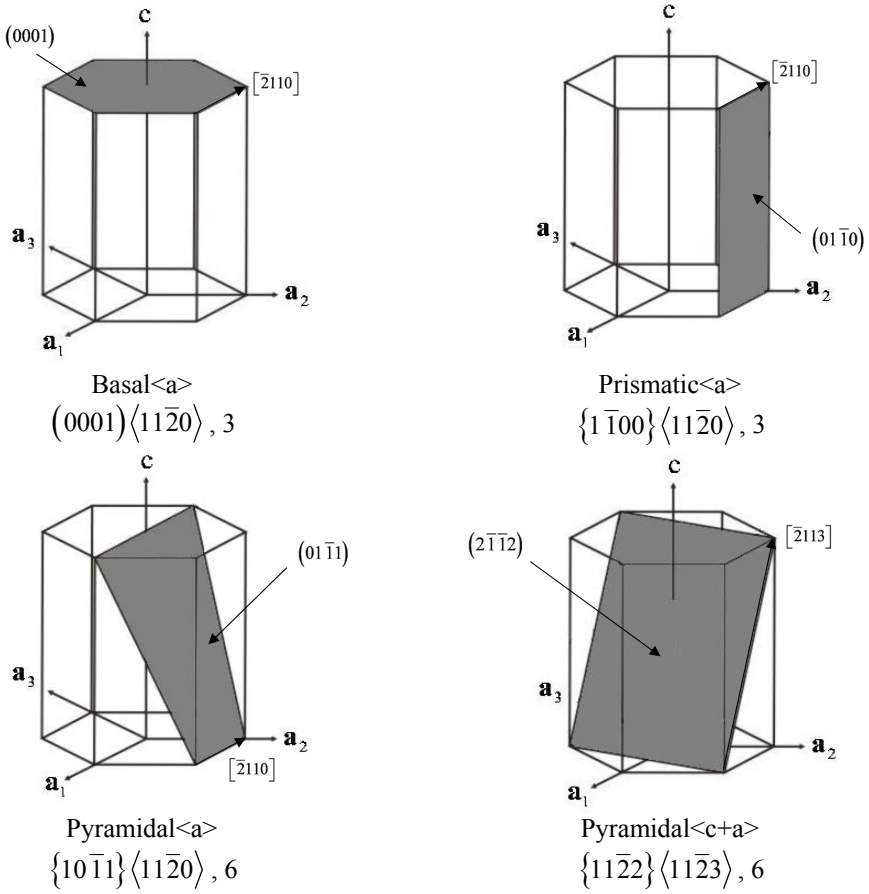

Figure 3.2 Slip systems mainly active in Mg alloys

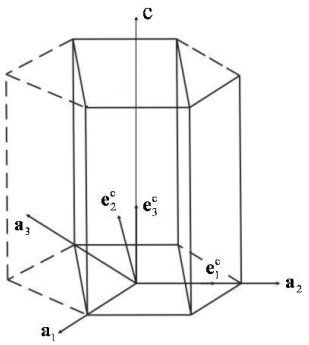

Figure 3.3 Orthonormal system used to describe slip systems

Table 3.1 Bravais indices and direction cosines for considered slip systems in Mg alloys

Slip Family	α	Bravais indices	$\mathbf{n}_0^\alpha$	$\mathbf{m}_0^\alpha$
basal<a> $(0001)\langle 11\bar{2}0\rangle$	1	$(0001)[11\bar{2}0]$	0 0 1	$\frac{1}{2}$ $-\frac{\sqrt{3}}{2}$ 0
	2	$(0001)[\bar{2}110]$	0 0 1	$\frac{1}{2}$ $-\frac{\sqrt{3}}{2}$ 0
	3	$(0001)[1\bar{2}10]$	0 0 1	$\frac{1}{2}$ $-\frac{\sqrt{3}}{2}$ 0
prismatic<a> $\{10\bar{1}0\}\langle 11\bar{2}0\rangle$	4	$(10\bar{1}0)[1\bar{2}10]$	0 1 0	1 0 0
	5	$(01\bar{1}0)[2\bar{1}\bar{1}0]$	$-\frac{\sqrt{3}}{2}$ $\frac{1}{2}$ 0	$\frac{1}{2}$ $\frac{\sqrt{3}}{2}$ 0
	6	$(\bar{1}100)[11\bar{2}0]$	$-\frac{\sqrt{3}}{2}$ $-\frac{1}{2}$ 0	$-\frac{1}{2}$ $\frac{\sqrt{3}}{2}$ 0
pyramidal <a> $\{10\bar{1}0\}\langle 11\bar{2}0\rangle$	7	$(10\bar{1}1)[1\bar{2}10]$	0.000 -0.882 0.471	1 0 0
	8	$(01\bar{1}1)[\bar{2}110]$	0.764 -0.441 0.471	$\frac{1}{2}$ $\frac{\sqrt{3}}{2}$ 0
	9	$(\bar{1}101)[\bar{1}\bar{1}20]$	0.764 0.441 0.471	$-\frac{1}{2}$ $\frac{\sqrt{3}}{2}$ 0
	10	$(\bar{1}011)[\bar{1}2\bar{1}0]$	0.000 0.882 0.471	-1 0 0
	11	$(0\bar{1}11)[2\bar{1}\bar{1}0]$	-0.764 0.441 0.471	$-\frac{1}{2}$ $-\frac{\sqrt{3}}{2}$ 0
	12	$(1\bar{1}01)[11\bar{2}0]$	-0.764 -0.441 0.471	$-\frac{1}{2}$ $-\frac{\sqrt{3}}{2}$ 0
pyramidal<c+a> $\{11\bar{2}2\}\langle 11\bar{2}3\rangle$	13	$(11\bar{2}2)[\bar{1}\bar{1}23]$	0.426 -0.737 0.524	-0.262 0.454 0.852
	14	$(\bar{1}2\bar{1}2)[1\bar{2}13]$	0.852 0.000 0.524	-0.524 0.000 0.852
	15	$(\bar{2}112)[2\bar{1}\bar{1}3]$	0.426 0.737 0.524	-0.262 -0.454 0.852
	16	$(\bar{1}\bar{1}22)[11\bar{2}3]$	-0.426 0.737 0.524	0.262 -0.454 0.852
	17	$(1\bar{2}12)[\bar{1}2\bar{1}3]$	-0.852 0.000 0.524	0.524 0.000 0.852
	18	$(2\bar{1}\bar{1}2)[\bar{2}113]$	-0.426 -0.737 0.524	0.262 0.454 0.852

The Bravais lattice notation is not convenient for numerical modeling because of the absence of orthogonality. The four-indice notations are, thus, transferred into Miller indices by definition of an orthogonal Cartesian system (Fig. 3.3).

Table 3.1 provides the detailed information about the Bravais indices as well as the direction cosines of the active slip systems in Mg alloys. For pyramidal<a> and pyramidal<c+a> slip systems, the slip plane normal and/or slip direction depend on the value of the c/a ratio of the HCP crystal. In hexagonal structures, the ideal c/a ratio (based on packing of hard spheres) is 1.633. However, in real materials, it varies from 1.567 for beryllium to 1.886 for cadmium. The increase in c/a ratio means that the distance between the adjacent basal planes increases, so they appear relatively more close-packed than alternative planes, for example, prismatic or pyramidal. The smaller the ratio c/a, the easier non-basal slip systems operate. The axial ratio for magnesium is close to the ideal value, and at room temperature is equal to 1.624 (Roberts, 1960), which is the value used in calculating the direction cosines in Table 3.1.

3.3 METHODOLOGY

3.3.1 THE INTERACTION BETWEEN FINITE ELEMENT (ABAQUS) AND CRYSTAL PLASTICITY (SUBROUTINE)

In combining the crystal plasticity model with finite element analysis, different approaches may be adopted. In this thesis, combining the crystal plasticity model and finite elements, two methods will be employed: in the first, each finite element represents a single crystal; in the second, each grain is divided into several finite elements. In both instances, each element, representing a crystal or part of a crystal, is described by the crystal plasticity constitutive model.

Crystal plasticity governs the constitutive equations at the micro-level, and provides the continuum relations of stress and/or strain in terms of slip system activity. Then finite element analysis is used for solving the field equations, in which equilibrium and compatibility are automatically satisfied between grains (or elements). In each increment,

for all integration points, the subroutine is called, where the values of stress and strain are updated and returned to the finite elements analysis.

In this thesis, the crystal plasticity constitutive relations are implemented in the commercial finite element software (ABAQUS) as a Material User-Subroutine (UMAT). This subroutine is written in the form of a FORTRAN code. Figure 3.4 presents a simple diagram of the interaction between finite element analysis (ABAQUS) and the crystal plasticity (UMAT), together with some other inputs and outputs to the simulations.

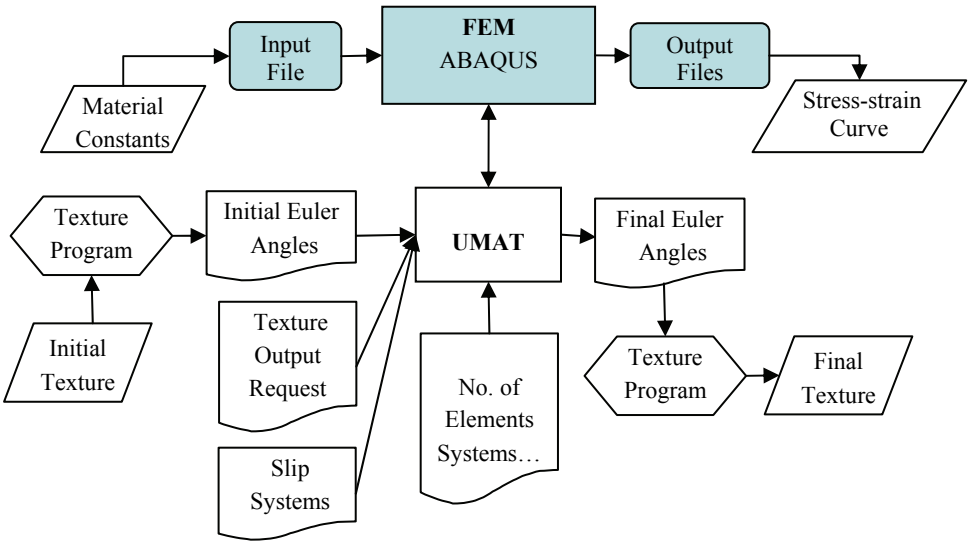

Figure 3.4 Interaction between finite element (ABAQUS) and crystal plasticity (UMAT)

Crystal plasticity simulation takes into account the initial texture of the material and its evolution during the deformation. As seen in Fig. 3.4, the initial texture of the material will be given to the subroutine as an input. This input is in the form of a series of non-weighted Euler angles sets. Each set of Euler angles defines orientation of a crystal. To define the Euler angles used in this work, let $\left\{\mathbf{e}_i^c \middle| i=1,2,3\right\}$ denote an orthonormal coordinate system associated with a crystal lattice, and $\left\{\mathbf{e}_i^g \middle| i=1,2,3\right\}$ be the orthonormal basis associated with a fixed global rectangular coordinate system. It can be shown (e.g. Anand, 2004) that the crystal system can always be aligned with the global system by three consequent rotations which are specified using Euler angles $0 \le \phi \le 2\pi$, $0 \le \theta \le \pi$ and $0 \le \omega \le 2\pi$. The sequence of rotations is as follows:

(i) rotate $\left\{\mathbf{e}_1^c,\ \mathbf{e}_2^c,\ \mathbf{e}_3^c\right\}$ about the $\mathbf{e}_3^c$-axis by angle ϕ to get $\left\{\mathbf{e}_1^{c'},\ \mathbf{e}_2^{c'},\ \mathbf{e}_3^c\right\}$;

(ii) then rotate the new system about $\mathbf{e}_1^{c'}$-axis by angle θ to get $\left\{\mathbf{e}_1^{c'},\ \mathbf{e}_2^{c''},\ \mathbf{e}_3^{c'}\right\}$;

(iii) finally, rotate $\left\{\mathbf{e}_1^{c'},\ \mathbf{e}_2^{c''},\ \mathbf{e}_3^{c'}\right\}$ about the $\mathbf{e}_3^{c'}$-axis by angle ω to get $\left\{\mathbf{e}_1^{c''},\ \mathbf{e}_2^{c'''},\ \mathbf{e}_3^{c'}\right\}$; this last system would be aligned with the global coordinate systems.

Each set of Euler angles will be assigned to one of the finite elements, which in turn can be the whole or part of a crystal. For an isotropic material, the initial texture is random, but as a result of the strong texture induced in Mg alloys after rolling or extrusion, the initial texture of samples can not be assumed to be random. Usually the textures are available in the form of ODF (orientation distribution function), pole figures, or weighted Euler angles, while in the CPFE simulations, non-weighted Euler angles are used to represent the orientation of individual grains. Therefore, texture software can be utilized to convert the initial texture of the specimens which are measured experimentally to the usable format. In this thesis, the Textools package (Resmat Co., 2002) is used which converts the experimentally measured textures (ODF or pole figures) to sets of Euler angles, which are part of the input to simulations. The evolving texture, which is again in the form of Euler angles, can be obtained at any stage of the deformation. Using the TexTools software, the numerical textures can be presented in the form of pole figures or other required formats.

3.3.2 ALGORITHM OF THE SUBROUTINE

In this thesis, the UMAT subroutine which was written for materials with cubic structure (Anand, 1992) is adopted. The subroutine is then modified for the case of HCP materials.

In all iterations of each time increment (from time t to τ), the subroutine is called for all integration points, which can represent a crystal or part of it. In each call to the subroutine, the values of $\left\{\mathbf{F}(t),\ \mathbf{F}(\tau)\right\}$, $\left\{\mathbf{T}(t),\ \mathbf{F}^p(t)\right\}$, and $\left\{\mathbf{m}_0^\alpha,\ \mathbf{n}_0^\alpha,\ s^\alpha(t)\right\}$ are known

from the previous step. $\mathbf{F}(\tau)$ is, in fact, an estimate of the deformation gradient at time τ which ABAQUS approximates. Then the incremental problem is to calculate $\{\mathbf{T}(\tau),\ \mathbf{F}^{p}(\tau)\}$, $\{\mathbf{m}^{\alpha}(\tau),\ \mathbf{n}^{\alpha}(\tau)\}$ and $\{s^{\alpha}(\tau)\}$ in the deformed configuration (at time τ). To solve this incremental problem, a time-integration procedure is used together with the governing equations, and the following steps are taken:

The first step is obtaining a trial estimate. A trial elastic strain is defined as follows:

$$\mathbf{F}^{e}(\tau)^{tr} = \mathbf{F}(\tau)\mathbf{F}^{p}(t)^{-1}; \qquad \text{Eq. 3.30}$$

$$\mathbf{C}^{e}(\tau)^{tr} = \left(\mathbf{F}^{e}(\tau)^{tr}\right)^{T}\mathbf{F}^{e}(\tau)^{tr}; \qquad \text{Eq. 3.31}$$

$$\mathbf{E}^{e}(\tau)^{tr} = (1/2)\left\{\mathbf{C}^{e}(\tau)^{tr} - \mathbf{1}\right\}. \qquad \text{Eq. 3.32}$$

Then, the trial stress is calculated by

$$\mathbf{T}^{*}(\tau)^{tr} = \mathbb{C}\left[\mathbf{E}^{e}(\tau)^{tr}\right], \qquad \text{Eq. 3.33}$$

Then we define $\mathbf{C}^{\alpha}$ as

$$\mathbf{C}^{\alpha} \equiv \mathbb{C}\left[\mathrm{sym}\left(C^{e}(\tau)^{tr}\,\mathbb{S}_{0}^{\alpha}\right)\right], \qquad \text{Eq. 3.34}$$

where

$$\mathbb{S}_{0}^{\alpha} = \mathbf{m}_{0}^{\alpha} \otimes \mathbf{n}_{0}^{\alpha}, \qquad \text{Eq. 3.35}$$

is the Schmid tensor for slip system α.

In the second step, the following system of coupled implicit equations are solved:

$$T^{*}(\tau) = T^{*}(\tau)^{tr} - \sum_{\alpha}\Delta\gamma^{\alpha}\mathbf{C}^{\alpha}, \qquad \text{Eq. 3.36}$$

$$s^{\alpha}(\tau) = s^{\alpha}(t) + \sum_{\beta}h^{\alpha\beta}(\tau)\left|\Delta\gamma^{\beta}\right|, \qquad \text{Eq. 3.37}$$

with

$$\Delta\gamma^{\alpha} \equiv \dot{\gamma}^{\alpha}\left(\tau\right)\Delta t\,. \qquad \text{Eq. 3.38}$$

Using a two-level iterative procedure (Anand, 2004), $T^{*}\left(\tau\right)$ and $s^{\alpha}\left(\tau\right)$ are obtained from the system above. Then, in the third step, the plastic deformation gradient is updated by

$$\mathbf{F}^{p}\left(\tau\right) \doteq \left\{\mathbf{1} + \sum \Delta\gamma^{\alpha} \text{sign}\left(\tau^{\alpha}\left(\tau\right)\right)\, \mathbb{S}_{0}^{\alpha}\right\} \mathbf{F}^{p}\left(t\right). \qquad \text{Eq. 3.39}$$

At this point, it should be checked that $\det \mathbf{F}^{p}\left(\tau\right) = 1$, within a tolerance. If not, $\mathbf{F}^{p}\left(\tau\right)$ is normalized by

$$\mathbf{F}^{p}\left(\tau\right) = \left[\text{def}\ \mathbf{F}^{p}\left(\tau\right)\right]^{-1/3} \mathbf{F}^{p}\left(\tau\right). \qquad \text{Eq. 3.40}$$

Then the elastic deformation gradient $\mathbf{F}^{e}\left(\tau\right)$ and the stress $\mathbf{T}^{*}\left(\tau\right)$ are calculated:

$$\mathbf{F}^{e}\left(\tau\right) = \mathbf{F}\left(\tau\right)\ \mathbf{F}^{p}\left(\tau\right)^{-1}, \qquad \text{Eq. 3.41}$$

$$\mathbf{T}^{*}\left(\tau\right) = \mathbb{C}\left[\mathbf{E}^{e}\left(\tau\right)\right]\,. \qquad \text{Eq. 3.42}$$

From which, the Cauchy stress can then be calculated as

$$\mathbf{T}\left(\tau\right) = \frac{1}{\det \mathbf{F}\left(\tau\right)} \mathbf{F}^{e}\left(\tau\right)\left\{\ \mathbf{T}^{*}\left(\tau\right)\right\}\ \mathbf{F}^{e}\left(\tau\right)^{T}. \qquad \text{Eq. 3.43}$$

Finally, the texture, $\left(\ \mathbf{m}_{\tau}^{\alpha},\ \mathbf{n}_{\tau}^{\alpha}\right)$, is calculated by

$$\mathbf{m}_{\tau}^{\alpha} = \mathbf{F}^{e}\left(\tau\right)\mathbf{m}_{0}^{\alpha}, \qquad \text{Eq. 3.44}$$

$$\mathbf{n}_{\tau}^{\alpha} = \mathbf{F}^{e}\left(\tau\right)^{-T}\mathbf{n}_{0}^{\alpha}. \qquad \text{Eq. 3.45}$$

The updated values are all returned to ABAQUS, which by taking into account the equilibrium condition proceeds to the next increment or alternatively defines a new iteration in the same increment.

3.4 MODIFICATIONS MADE

As mentioned previously, the main goal of this work is not the development of a new constitutive framework, but rather to modify the available framework of the CPFE model to utilize it in studying Mg alloys mechanical response.

To carry out the objectives of this work, the UMAT subroutine originally written for FCC materials is adopted (Anand, 1992). The subroutine incorporates the rate dependent crystal plasticity model with a single hardening law for all the slip systems. Texture can be computed at any time (increment) during the deformation, which is in the form of non-weighted Euler angles. The model was verified for cases of single and poly-crystal FCC structure, with a random initial texture, for both hardening and non-hardening models by comparing the results to the available data (Anand and Kalidindi, 1994).

In order to use the subroutine for the case of materials with HCP structure, the subroutine has been modified in several ways. As a necessary first step, the algorithms of the constitutive equations were modified to be used for HCP materials. The lower symmetry of the HCP structure affects the modeling in several aspects. The number of independent elastic moduli is increased from 3 to 5; i.e. due to symmetry, out of 21 elastic constants for a general anisotropic material, hexagonal single crystals have five independent elastic moduli C_{11}, C_{12}, C_{13}, C_{33}, and C_{55}; with $C_{22} = C_{11}$, $C_{23} = C_{13}$, $C_{44} = C_{55}$, and $C_{66} = \frac{1}{2}(C_{11} - C_{12})$, and all other elements zero. These five constants are defined as follows:

$$
\begin{aligned}
C_{11} &= \left(\mathbf{e}_1^c \otimes \mathbf{e}_1^c\right) : \mathbb{C}\left[\mathbf{e}_1^c \otimes \mathbf{e}_1^c\right] \ ; \\
C_{12} &= \left(\mathbf{e}_1^c \otimes \mathbf{e}_1^c\right) : \mathbb{C}\left[\mathbf{e}_2^c \otimes \mathbf{e}_2^c\right] \ ; \\
C_{13} &= \left(\mathbf{e}_1^c \otimes \mathbf{e}_1^c\right) : \mathbb{C}\left[\mathbf{e}_3^c \otimes \mathbf{e}_3^c\right] \ ; \\
C_{33} &= \left(\mathbf{e}_3^c \otimes \mathbf{e}_3^c\right) : \mathbb{C}\left[\mathbf{e}_3^c \otimes \mathbf{e}_3^c\right] \ ; \\
C_{55} &= \left(\mathbf{e}_1^c \otimes \mathbf{e}_3^c\right) : \mathbb{C}\left[2\mathrm{sym}\left\{\mathbf{e}_1^c \otimes \mathbf{e}_3^c\right\}\right] \ .
\end{aligned}
\qquad \text{Eq. 3.46}
$$

Careful determination of the elastic constants for magnesium has been carried out by Long and Smith (1957) using an ultrasonic technique. The change in the number of elastic constants, in turn, affects the constitutive relation (algorithm) for stress. The necessary changes are made in the subroutine.

The next concern in modeling the HCP structure is the inhomogeneity inherent in slip systems. It is well-established that the slip resistance values vary greatly for different slip systems. The subroutine is modified to take into account the activity of different slip system families present in the Mg alloys. In addition, the relations governing the hardening of different slip systems are modified. Minor modifications are made in the hardening relations taken from the literature and implemented in the subroutine. As a result of these changes, the number of material constants is increased from 10 to 21.

One of the demanding issues in the CPFE modeling is determination of the parameters present in the model. The model parameters are divided into several groups and will be determined in different ways. Some parameters are known characteristics of the material and can be obtained from the literature. Among them are the elastic moduli mentioned above. Elastic constants are taken as (Simmons and Wang, 1971):

$$C_{11} = 58 \text{ GPa};\ C_{12} = 25 \text{ GPa};\ C_{13} = 20.8 \text{ GPa};$$
$$C_{33} = 61.2 \text{ GPa};\ \text{ and } C_{55} = 16.6 \text{ GPa}. \qquad \text{Eq. 3.47}$$

Another important parameter, the strain-rate sensitivity factor is taken to be equal to its macroscopic value. The definition of the strain-rate sensitivity factor and its effect on the deformation behavior of Mg alloys, together with a study on the values of this factor are presented in Chapter 5. Also in this chapter, the effects of change in the reference shearing rate are discussed. Some other parameters, including the hardening parameters, are usually obtained by curve-fitting. It is important to note that in order to arrive at a physically-based model, the curve-fitting should be done only for one of the basic deformation modes; the resulting parameters in this case should give satisfactory results for other modes of deformation. Of utmost importance are the slip resistance values. Chapter 5 discusses these values for different slip systems.

3.5 CPFE MODELING OF Mg (ALLOYS) SINGLE CRYSTAL

As a first step in verifying the crystal plasticity models, simulations are done on a single crystal; the initial orientation (texture) of a single crystal is defined by a set of Euler angles and is given to the model as an input. Then, during the deformation, crystal plasticity provides the change in the orientation of this crystal.

In this section, in order to verify the employed crystal plasticity model and the activity of different slip systems, simulations are done on a single crystal of Mg. (The effect of strain-rate sensitivity on the response of a single crystal is discussed in Chapter 5.) In these simulations, the single crystal is assumed to be one finite element. The correct activity of different slip systems are verified by assuming specific initial orientations for the single crystal and thus activating specific slip systems, and then comparing the results with the theoretically expected ones.

3.5.1 TENSION TESTS ON A SINGLE Mg CRYSTAL

The deformation of a crystal is composed of an elastic part and a plastic part, which is the result of the activity of different slip systems. It is expected that in the absence of slip system activity, the response of a single crystal be elastic. On the other hand, with the activity of slip systems, different material behaviors are expected with the change in the slip resistance values, and, especially, with the switch between <a> and <c+a> families.

In the first step, a series of simulations is done on a single crystal of Mg with the tension loading along the c-axis; i.e. tension is applied in the third direction, and the initial orientation of the crystal is assumed to be [0, 0, 0] in terms of Euler angles. Here, all the Euler angles are defined according to Bunge's convention. The cube considered for the simulation of Mg single crystal is shown in Fig. 3.5. The element type is considered to be of reduced integration type, C3D8R (8 node solid brick element with one Gaussian integration point). All the nodes on the plane $X_3 = 0$ (nodes 1-4) have zero displacements in the 3- direction. Node 1 has zero displacement in all directions. All of the nodes on the top X_3 face (nodes 5-8) are displaced in the 3-direction at a constant velocity.

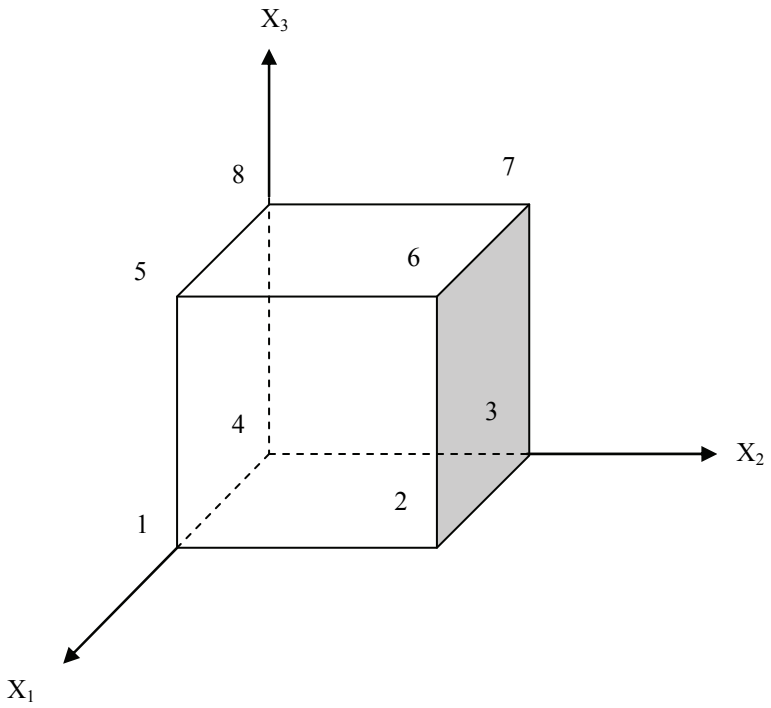

Figure 3.5 The cube considered for the simulation of Mg single crystal

Figures 3.6-3.8 show the stress-strain curves for these tension tests with the loading along the c-axis, while different slip systems are assumed to be active. As can be seen in Figs. 3.6 and 3.7 (which show the same plots on different scales), when no slip system is active, as expected, the material shows an elastic behavior with an elastic modulus of approximately 60E3 MPa which is in agreement with the assumed C_{33} component of the stiffness tensor. Performing tension tests in other directions with no slip system active gives different elastic moduli, as expected for an anisotropic single crystal of Mg.

Regarding the slip systems, it is known that all the <a> slip systems (basal<a>, prismatic<a>, and pyramidal<a>) provide dislocations only in the <a> direction which lies in the basal plane, normal to c-axis; in other words, none of these systems can provide deformation along the c-axis. This theoretical observation is verified by the stress-strain curves obtained in Fig. 3.6.

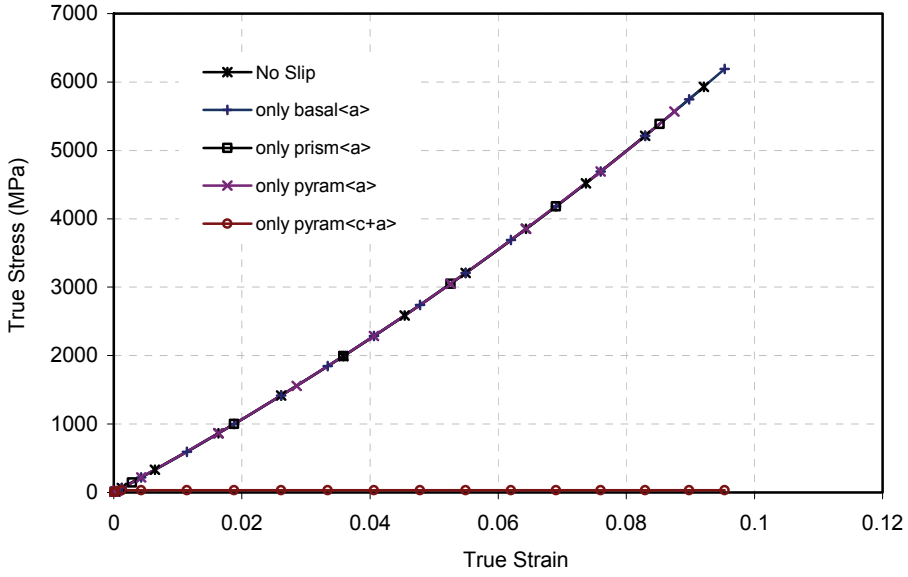

Figure 3.6 Stress-strain curves for a Mg single crystal loaded along the c-axis, while assuming different slip systems to be active

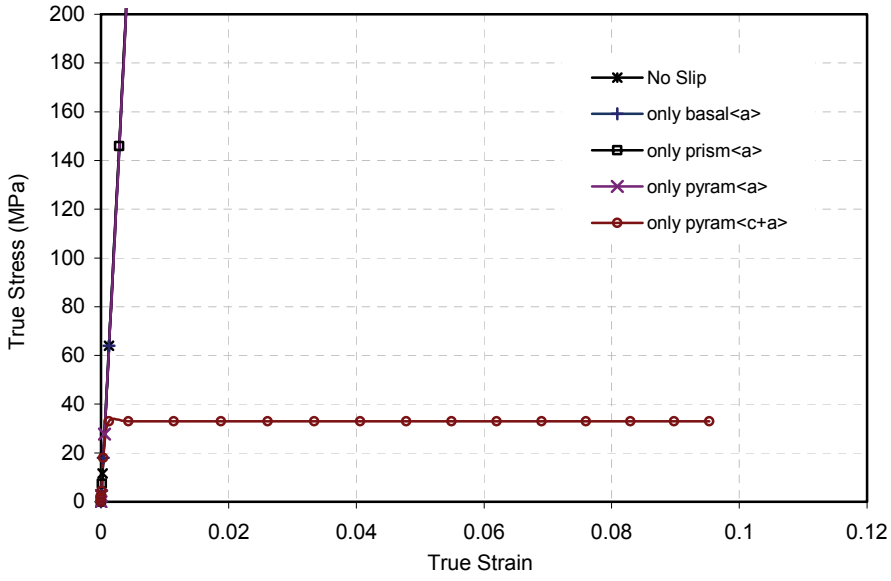

Figure 3.7 Stress-strain curves shown in Fig. 3.6 on a different scale

As shown in Fig. 3.6, with the loading along the c-axis, <a> slip systems are not active, the stress level does not change, and, basically, the crystal behavior remains elastic. More precisely, in these loading cases (with only <a> slip systems active), the applied stress would be normal to the slip plane, and, therefore, the resolved shear stress will be zero, which gives a zero shearing increment on that slip system, and keeps the slip system inactive. Figures 3.6 and 3.7 also show the stress-strain curve of the crystal with the pyramidal<c+a> slip system active. As mentioned before, this system enables the crystal to deform plastically in the c-direction as well as in the a-direction. For this system, the resolved shear stress is not zero, which causes the level of stress to decrease considerably with plastic deformation.

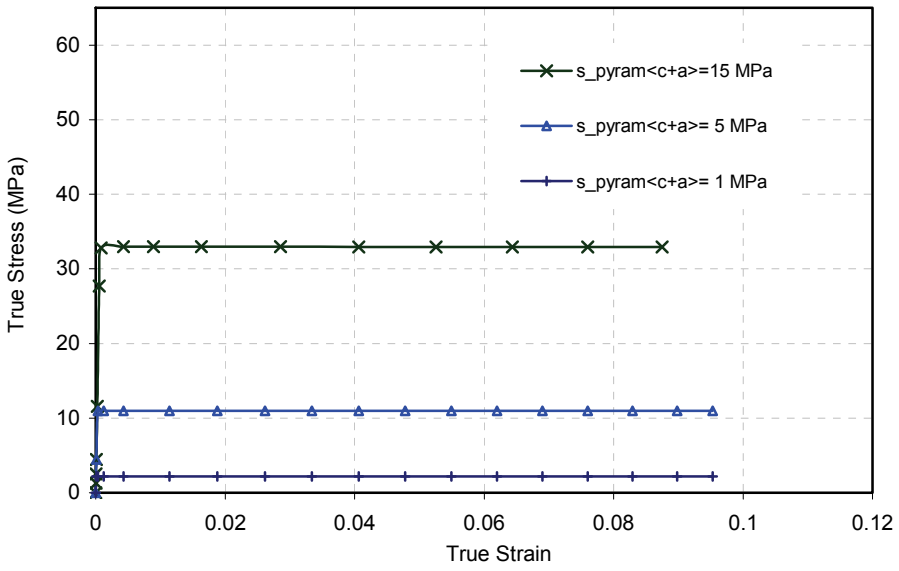

Figure 3.8 Stress-strain curves for a single Mg crystal loaded along the c-axis, with different slip resistance values for active systems; $s_{basal} = 5$ MPa

Figure 3.8 shows the stress-strain curves for the same crystal orientation and loading direction with varying slip resistance values assumed for pyramidal<c+a> slip system. As shown, with the decrease in the slip resistance of this system, the stress level decreases for the single crystal.

Another important aspect of the model that should be verified is the orientation-dependence of the crystal response. Figure 3.9 shows the stress-strain curves and the deformed shapes of two single crystals (each with one finite element) with different initial orientations. Crystal A is assumed to have the previously defined [0, 0, 0] orientation and Crystal B has an initial orientation of [45, 45, 45]. Unlike crystal A, for crystal B, tension will not be along the c-axis. As can be seen in Fig. 3.9, the change in the initial orientation of the crystal (A to B) affects both the stress level and the deformed shapes significantly.

The simulations done for crystal A are repeated for crystal B, and the stress-strain curves and final deformations of the crystal are shown in Figs. 3.10 and 3.11, respectively. In this case, unlike the results shown in Fig. 3.8, it can be seen that adding, for example, basal<a> to pyramidal<c+a> slip system reduces the stress level. Also, with the decrease in the slip resistance of basal<a> from 5.0 MPa to 0.5 MPa, the stress level decreases, which is the expected response. However, adding the activity of prismatic<a> slip system with a slip resistance value of 15.0 MPa (while basal<a> is active with a slip resistance of 5.0 MPa) does not change the level of stress. While the deformed shapes obtained for the crystal A with different slip systems are quite similar (not shown), this is not the case for crystal B (Fig. 3.11). It is noteworthy that a crystal can deform plastically without significant change in its orientation, depending on the assumed boundary conditions.

Another interesting observation in Fig. 3.10 is that, although the hardening is set to zero for all the slip systems, in case 3, with the prismatic<a> slip system active, stress-strain curve shows an overall hardening. In other words, while there is no micro-hardening on the slip systems, macro-hardening does exist. This macro-hardening results as the orientation of the crystal changes, causing a decrease in the resolved shear stress on the slip system, which causes the hardening in the overall stress-strain curve.

Overall, the results obtained for Mg single crystals are compatible with the theoretical considerations, which demonstrates the basic capabilities of the model that will be used in the remainder of this thesis.

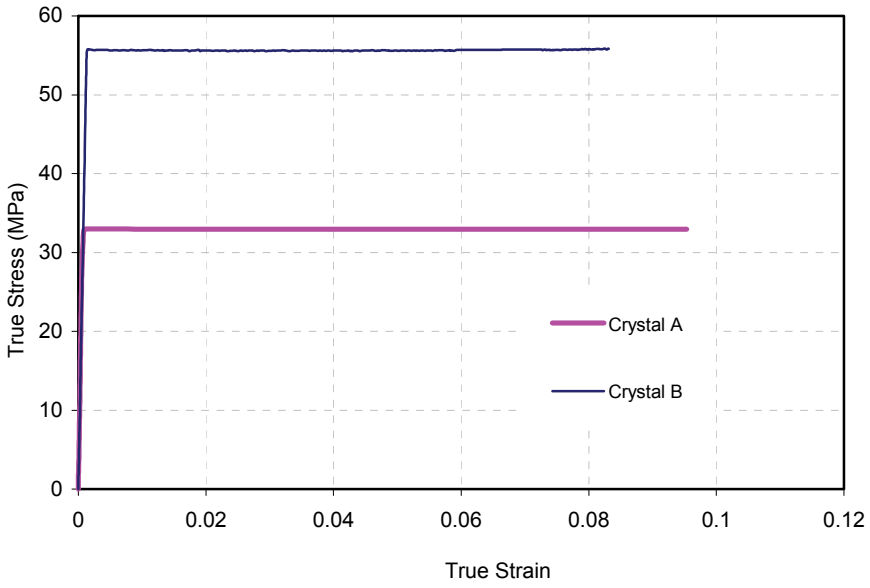

(a)

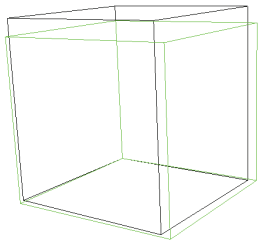

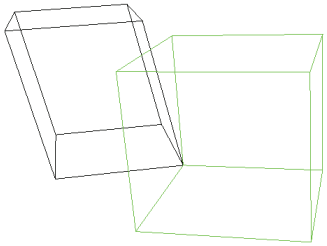

(b) (c)

Figure 3.9 Tension tests on a Mg single crystal with only pyraml<c+a> slip system active and two different initial orientations (a) stress-strain curves (b) deformed crystal A (c) deformed crystal B

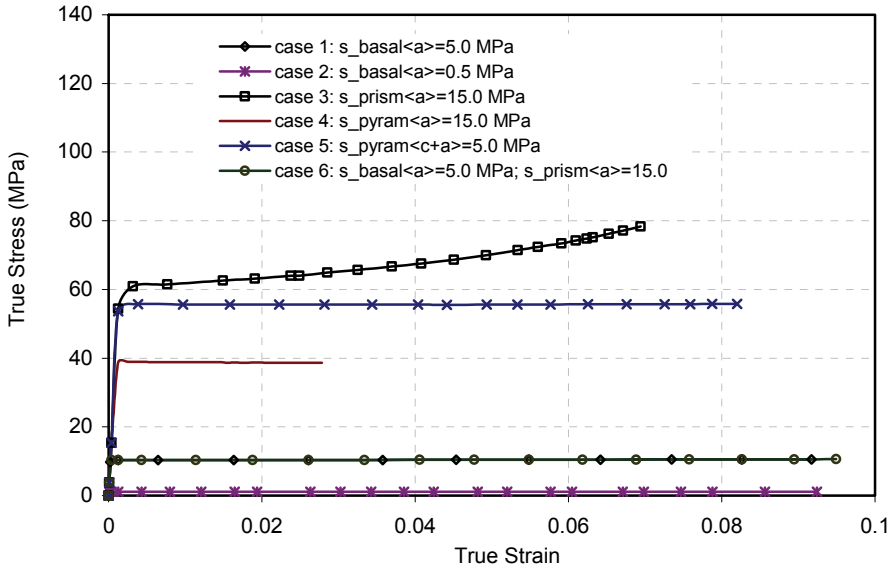

Figure 3.10 the stress strain curves for a tension test on a single crystal assuming different slip resistance values

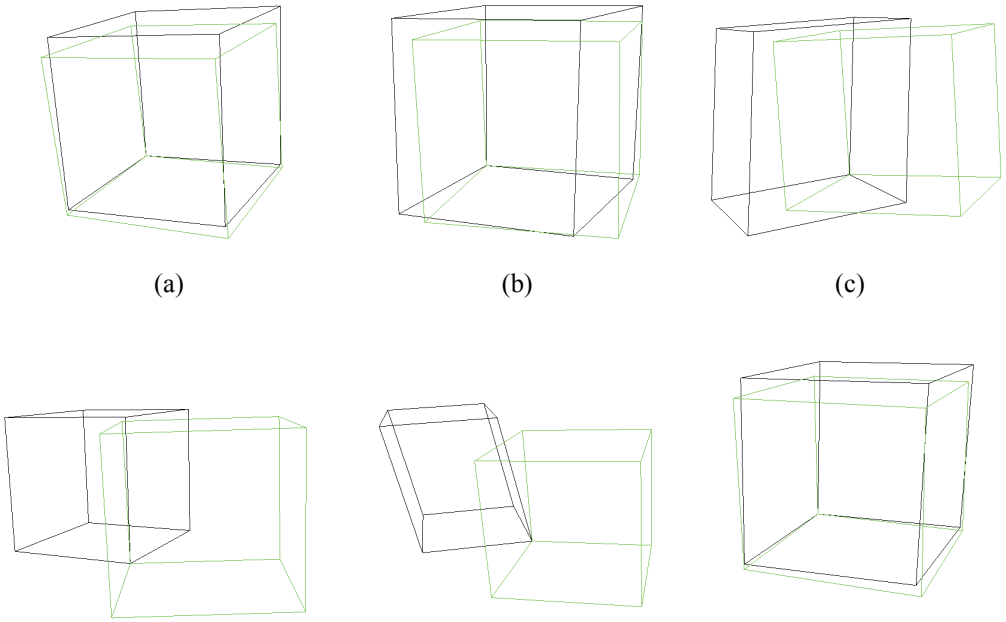

(a) (b) (c)

(d) (e) (f)

Figure 3.11 Deformed shapes of a Mg single crystal under tension for the cases shown in 3.10 (a-f) corresponding to case 1 to 6, respectively

Chapter 4
The RVE Size and Grain Inhomogeneity in the CPFE Modeling of Mg Alloys

4.1 INTRODUCTION

The overall distribution of grain orientations in a polycrystal represents the initial (as well as the evolving) texture of the material. Because of computational limitations, CPFE models do not use a complete geometrical depiction of an entire polycrystal, which usually consists of billions of grains. Instead, they use a representative volume element (RVE), large enough to have the average properties of the polycrystalline material. This RVE usually consists of a few thousand grains, chosen in such a way that it offers a suitable representation of a macroscopic RVE. Another limiting factor is that lattice orientations, locations of grains with given orientations, grain shapes and grain size, and orientation of grain boundaries are chosen randomly from a real micro-structure in a representative way (Van Houtte *et al*., 2005). Despite these limitations, it should be noted that other crystal plasticity models are more limited, as they utilize averaging schemes, such as the Taylor model.

In this regard, a pre-requisite for using CPFE modeling is to study the role of the factors mentioned above, and to obtain the appropriate RVE size. In simulations, there should be

enough grains present to sufficiently model the evolving texture without excessive variation from one simulation to another for the same initial texture. Another factor is the degree of inhomogeneity in each grain. This inhomogeneous behavior can be modeled by dividing each grain into several elements. It is expected that increasing the number of grains and elements per grain increases the precision and consistency of the simulation. However, with an increase in the number of elements, computational cost will increase, and there is always a compromise in making this choice. The effect of grain shapes and the role of grain boundary should also be added to these parameters for investigation.

The objective of this chapter is to obtain the optimum size of the RVE or optimum number of grains (Section 4.2) and number of elements per grain (Section 4.3) that should be used in the crystal plasticity modeling of magnesium alloys. Also, the effect of grain shape on the overall behavior of the material is studied (Section 4.4). In Section 4.5, the effect of considering grain boundaries is explored. A summary of the obtained results is presented in Section 4.6.

4.2 THE RVE SIZE (EFFECT OF TOTAL NUMBER OF GRAINS)

There are two effects that are expected to be seen when the total number of grains in the model is increased. First, the material texture is represented more precisely (assuming that the specimen is made up of thousands of grains), and more representative results are expected. Second, with the increase in the number of grains, there will be more grain boundaries, and more interaction between grains, which can lead to different stress levels.

To study the effect of total number of grains, and to obtain the optimum size for the RVE, a series of simulations is performed for the simple compression of a magnesium cube with a height-to-width ratio of 1.5. In the simulations, only three families of <a> slip systems are assumed, namely basal<a>, prismatic<a> and pyramidal<a>, with slip resistance values of 0.55 MPa, 105 MPa, and 105 MPa, respectively; no hardening is assumed for the slip systems in this preliminary study. Each grain is taken to be one element (this is discussed in detail in the next section) of reduced integration type,

C3D8R (8 node solid brick element with one Gaussian integration point), and the initial texture of the material is assumed to be random. All the nodes on the planes $X_1 = 0$, $X_2 = 0$, and $X_3 = 0$ have zero displacements in the 1-, 2-, and 3- directions, respectively. All of the nodes on the top X_3 face are displaced in the 3-direction at a constant velocity (Fig. 4.1). Simulations are done at a nominal strain rate of 0.001 s^{-1}. The strain-rate sensitivity factor is assumed to be 0.012. The results are obtained for different total number of grains, from a cube divided into 8 grains $(2 \times 2 \times 2)$ to a cube with 3375 grains $(15 \times 15 \times 15)$. The simulations are done up to a nominal strain of 0.14.

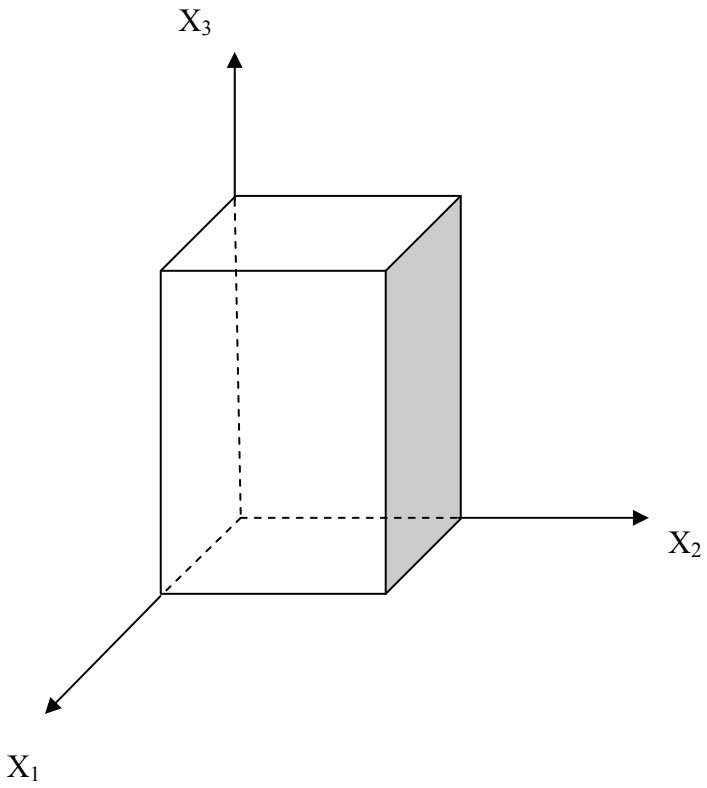

Figure 4.1 Magnesium specimen under compression

Throughout this thesis, the stress-strain curves are presented as averages over grains. In other words, each data point used for plotting the curves is obtained by averaging the true stress and true strain values obtained for all the grains in specimen at a certain time during the deformation. This averaging, which is done on the obtained stress/strain values, should not be confused with the averaging schemes which can be used in obtaining the stress and/or strain values.

To observe the effects of change in the total number of grains on the computed material response, the repeatability of the simulation results using a fixed number of grains with different initial random orientations is studied. The simulation for the case of 125, 216, 343, 512, and 1000 grains are repeated using different sets of random Euler angles as the initial random texture. For example, Fig. 4.2 shows the results of simulations for a cube with 125 grains $(5\times5\times5)$, but different random initial orientations. As can be seen, with the change in random initial orientations, the stress level changes. This indicates the insufficiency of 125 grains for representing a real random texture. Figures 4.3-4.6 show the same test for larger number of grains. In each case, the closer the curves are to each other, the better is the representation of random texture.

By observing Figs. 4.2-4.6, it can be seen that the repeatability of the simulations, as expected, improves with the increase in number of grains. For the case of the cube with 1000 grains $(10\times10\times10)$, the results are quite repeatable. In other words, 1000 grains can simulate the initial random texture of the material reasonably well, in that all the simulations give the 'same' flow curve.

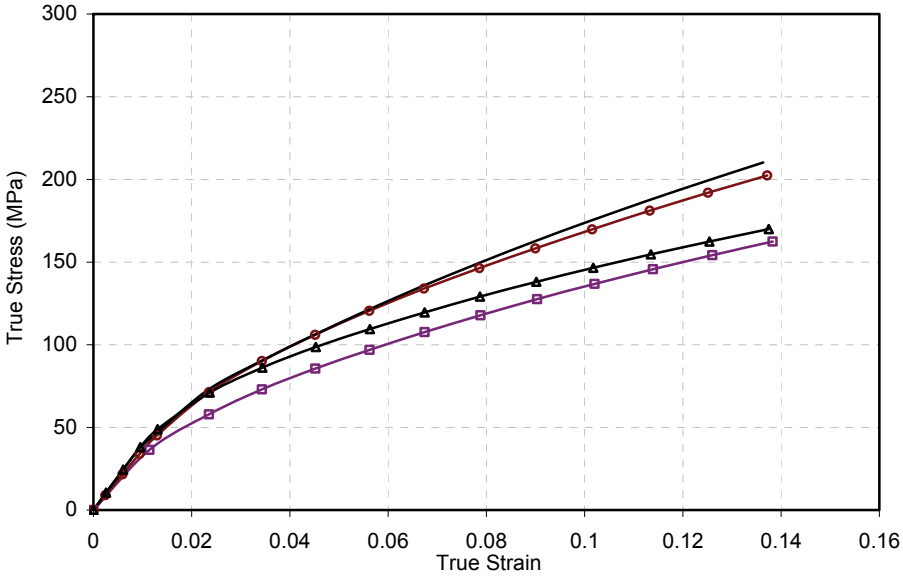

Figure 4.2 Simple compression of Mg cube using 125 grains for 4 different initial random textures

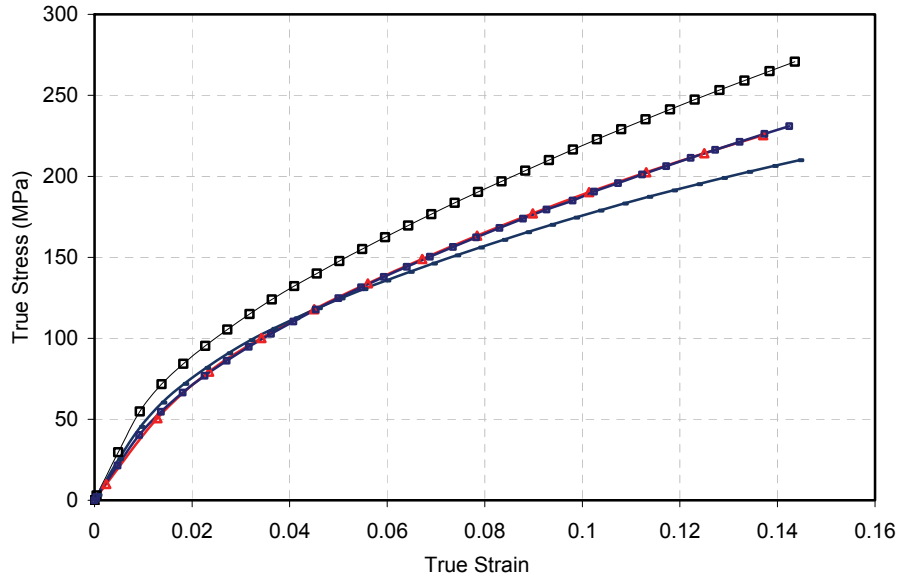

Figure 4.3 Simple compression of Mg cube using 216 grains for 4 different initial random textures

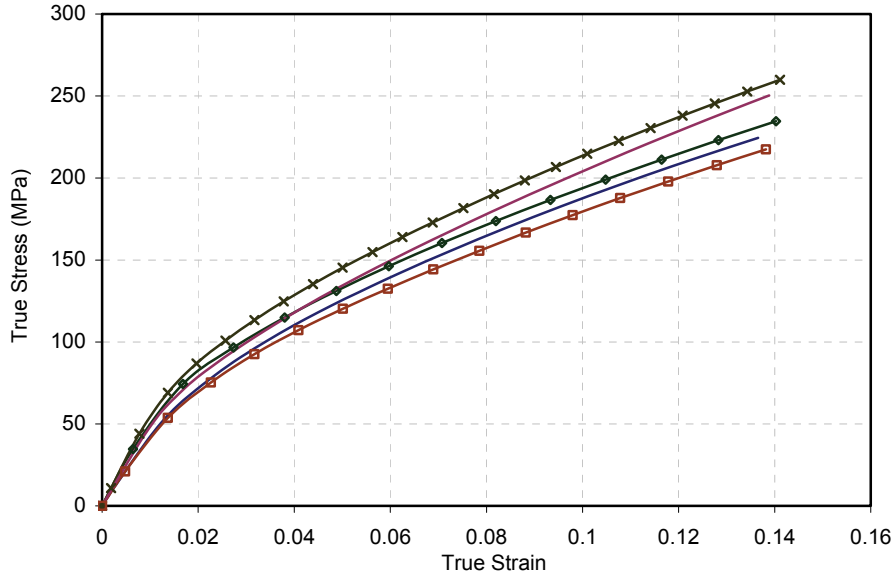

Figure 4.4 Simple compression of Mg cube using 343 grains for 5 different initial random textures

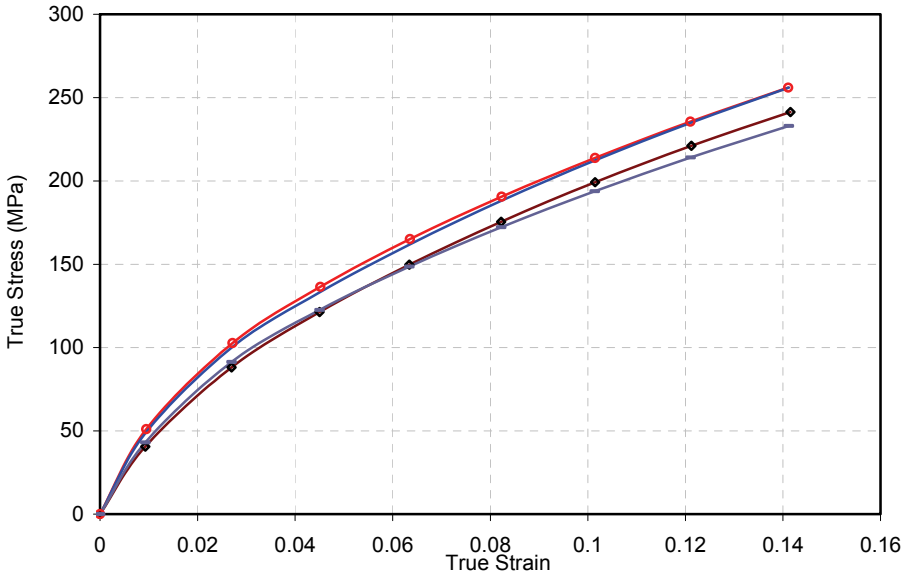

Figure 4.5 Simple compression of Mg cube using 512 grains for 4 different initial random textures

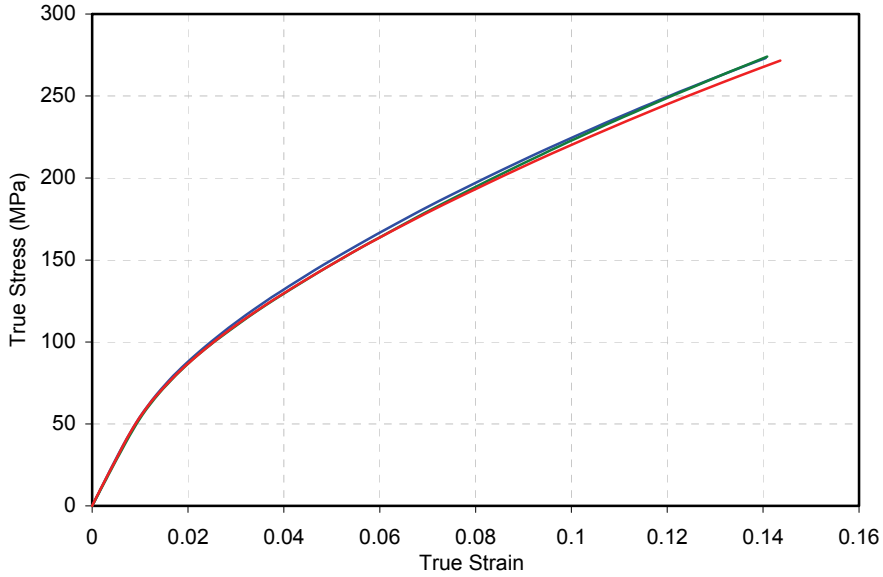

Figure 4.6 Simple compression of Mg cube using 1000 grains for 3 different initial random textures

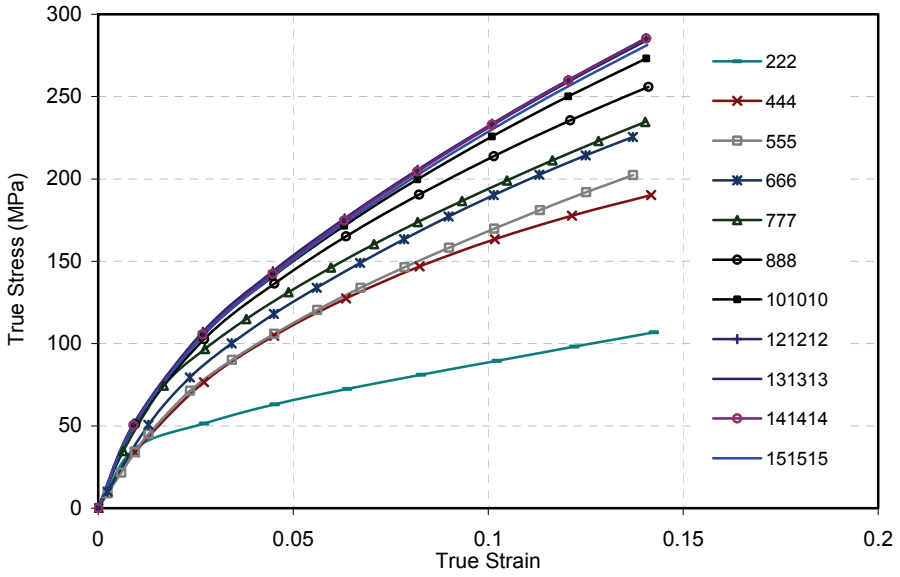

Figure 4.7 Stress-strain curves in simple compression of Mg cube for different number of grains

Summarizing Figs. 4.2-4.6, Fig. 4.7 shows the change in the stress-strain curve with the increase in the total number of grains. As can be seen, the stress level increases with the increase in the total number of grains. For cubes with the total number of grains above 1000, the results are very close to each other. Each curve in Fig. 4.7 is the average of the stress-strain curves obtained for that specific total number of grains. For example, the curve reported for $(5\times5\times5)$ is the average of the curves shown in Fig. 4.2 (at each strain the average of the stress values is plotted).

Using the curves in Fig. 4.7, the stress at strain of 0.14 versus total number of grains is plotted in Fig. 4.8. As seen in this figure, with the increase in number of grains the curve rises and then reaches a plateau (for a total number of grains more than 1000), where an increase in the total number of grains does not have a significant effect on the simulation results.

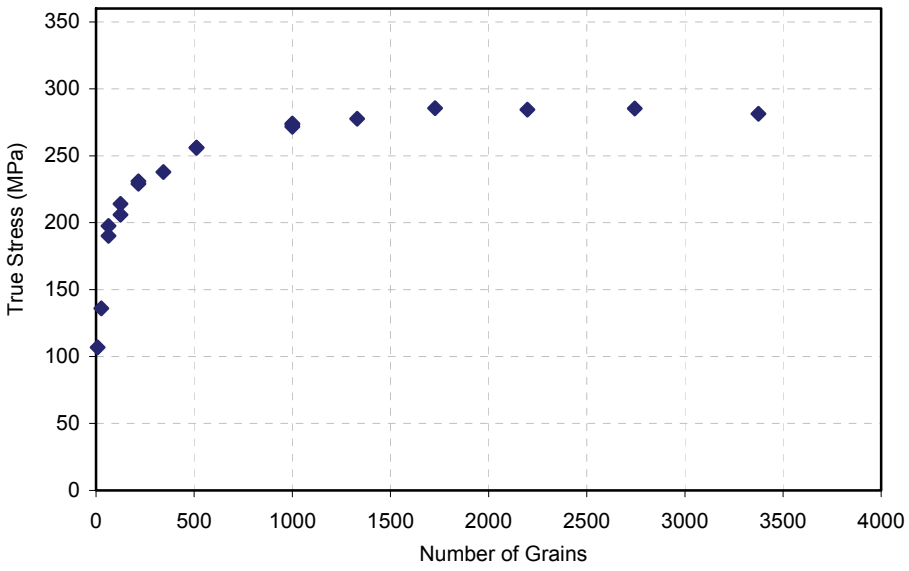

Figure 4.8 Stress at $\varepsilon = 0.14$ vs. different number of elements

Having done the simulations, the optimum size of the RVE (number of grains) for crystal plasticity simulations of HCP crystals should be chosen. Introducing the optimum number of grains to be used in this type of analysis is always a compromise, given that increase in precision requires higher computational cost. Based on Figs. 4.6-4.8, it can be said that the ideal case is to consider at least 1000 grains. For an RVE with this number of grains, not only is the simulation quite repeatable, but also, regarding the result from

Fig. 4.8, the stress level is less than 3 percent different from the plateau level. In fact, if the number of grains is sufficient to represent the texture, with different initial random orientations assigned to grains, the same results should be obtained, which is nearly the case in Fig. 4.6. In this thesis, then, all the simulations are done using an RVE size containing, at least, 1000 grains (with most of them done using about 1500 grains).

4.3 THE GRAIN INHOMOGENEITY EFFECT

Improving the CPFE modeling results by assigning multiple elements per grain instead of one element per grain has been investigated by a number of researchers (e.g. Anand and Kalidindi, 1994; Mika and Dawson, 1998; Van Houtte *et al.*, 2002; Dawson *et al.*, 2002). It has been shown that the accuracy of the prediction for certain aspects of material behavior can be improved by assigning multiple elements per grain. In particular, for texture predictions during forming processes such as cold rolling or predictions on the micro-scale such as micro-shear band formation and growth (Anand and Kalidindi, 1994), assigning multiple elements per grain has been shown to be useful.

In this section, the effect of considering intra-granular inhomogeneity on the overall behavior of the material is studied. In crystal plasticity simulations combined with finite element analysis, each grain can be divided into several elements to take into account the inhomogeneous grain behavior. In such simulations, the elements in each grain have the same initial orientation, but during the deformation, can adopt different orientations. The goal is to obtain the number of elements per grain that is sufficient to represent the inhomogeneity of a grain to correctly simulate the overall behavior of the material.

To study the effect of inhomogeneous behavior within grains on the overall stress-strain curve, the cube used in the previous section is utilized in a series of simulations assuming the same element type and boundary conditions. First, the number of grains is fixed at 125, but the simulation is performed using different numbers of elements per grain (El/Gr), from 1 to 12. Figure 4.9 shows the stress-strain results for the simple compression of this Mg cube for different numbers of elements per grain. As seen in Fig. 4.9, with an increase in the number of elements per grain, the level of stress goes down. To better see the change in stress level with the increase in the elements per grain

number, the stress at a strain of 0.14 versus the number of elements per grain is plotted in Fig. 4.10.

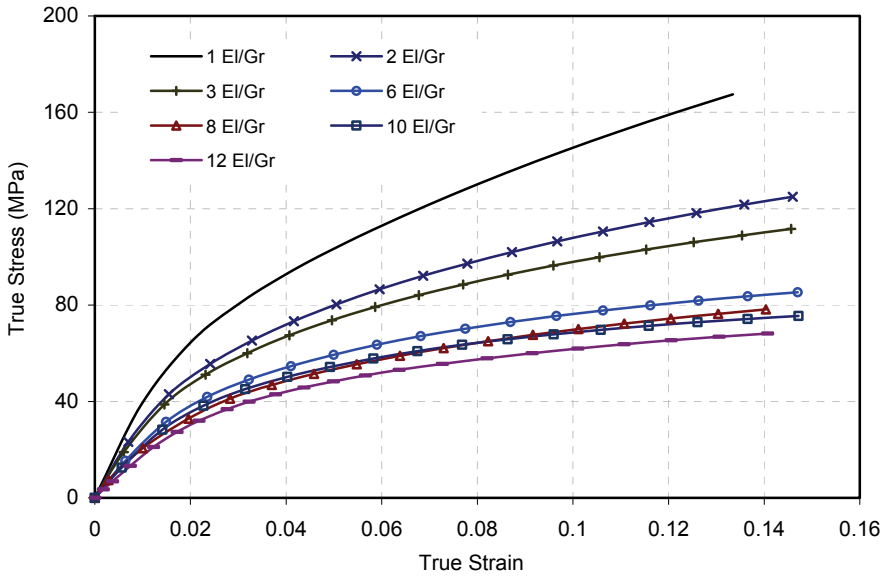

Figure 4.9 The change in stress vs. strain with the number of elements per grain (125 grains)

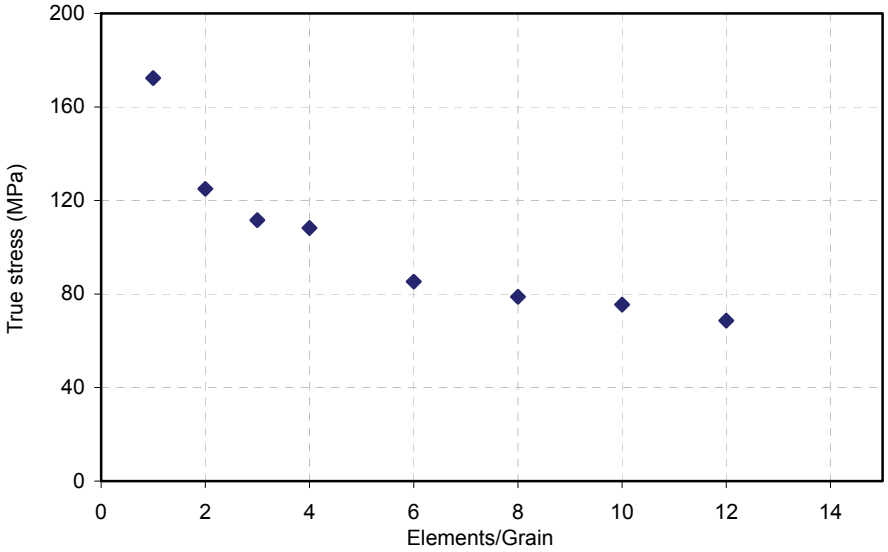

Figure 4.10 The change in level of stress at a strain of 0.14 vs. the number of elements per grain (125 grains)

It is seen that there is a difference of approximately 50 percent between the results of simulation with six El/Gr and one El/Gr (while a total of 125 grains is assumed). In fact, the main drop occurs with an increase from one El/Gr to six El/Gr. Beyond six to eight elements per grain, further division of grains leads only to minor changes in the level of stress. Therefore, with a low number of grains (125), eight El/Gr would be sufficient for predicting the overall behavior of the material. It should be noted that the discretization needed to fully capture the inhomogeneous deformation at the grain scale is expected to be substantially higher than eight El/Gr (Li *et al*., 2004). However, in this work the effect on the overall behavior of the material is sought.

It should be emphasized that in both cases, i.e. increasing totally number of grains and increasing number of elements per grain, the number of elements is increasing, while in one case the stress level increases and in the other decreases. The drop in the stress level can be explained by the fact that for multiple elements per grain the texture inhomogeneity is allowed in each grain; the higher inhomogeneity means lower constraint and more degrees of freedom which leads to a lower level of stress. This drop in the stress level has been reported, to various degrees, in the literature (Boyle and Curtin, 2005; Buchheit *et al*., 2005; Dawson and Tong-Seok, 2007). The drop in the stress level is also a manifestation of the absence of length scale in the model; a missing length scale is grain size, known to play an important role in hardening in polcrystalline materials (Buchheit *et al*., 2005).

To further study the intra-granular inhomogeneity effect, the change in the overall stress-strain curve with the increase in elements per grain number is plotted in Figs. 4.11 and 4.12, for a total number of grains of 343 and 1000 grains, respectively. It is seen in Fig. 4.11 that with the increase in the total number of grains from 125 to 343, the effect of grain inhomogeneity is greatly decreased. While for the case of 125 grains, the increase in El/Gr from 1 to 8 decreases the level of stress (at a strain of 0.1) by about 60%, for 343 grains, this decrease is about 25%. Figure. 4.12 shows the simulation results with 1000 grains assumed. It is seen that with 1000 grains, the difference between the stress-strain

curves for 1 El/Gr and 8 El/Gr is further reduced, and is negligible compared to the difference observed in Fig. 4.9.

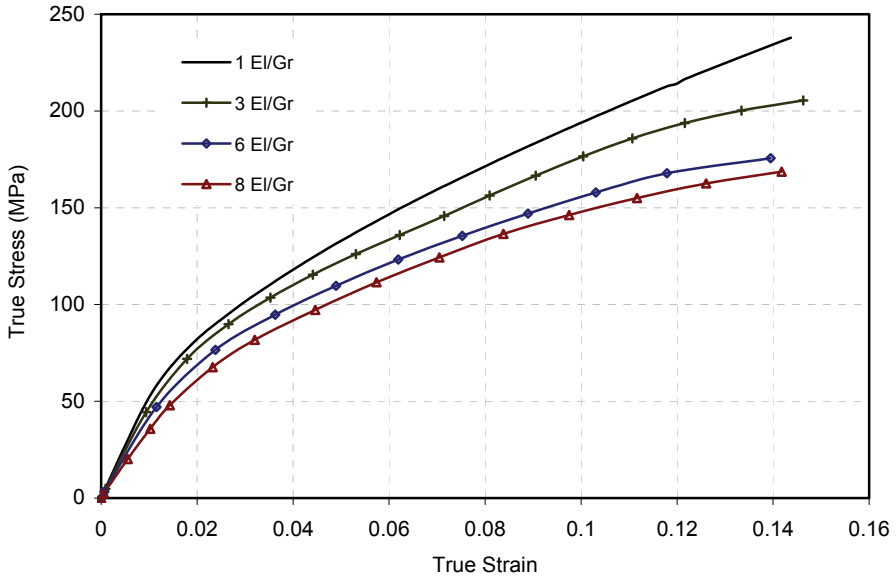

Figure 4.11 The change in stress vs. strain with the number of elements per grain (343 grains)

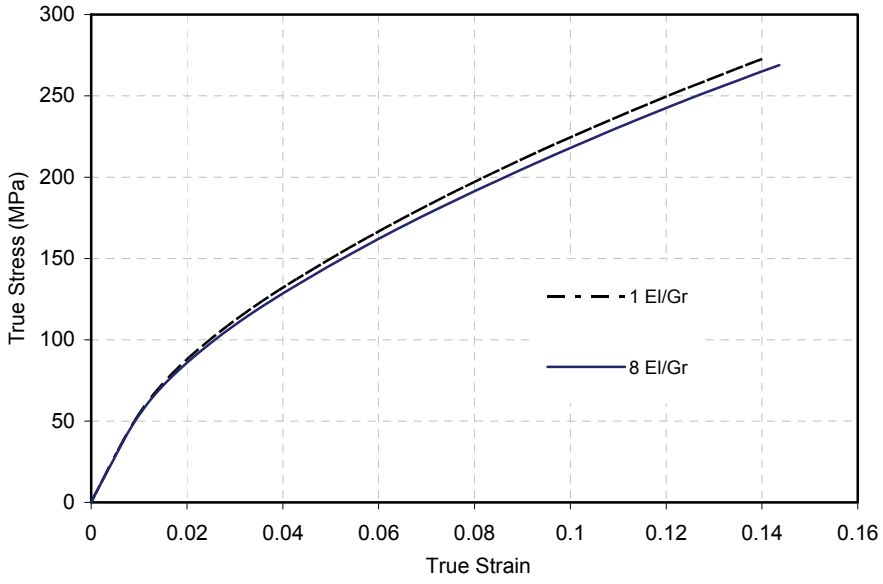

Figure 4.12 The change in stress vs. strain with the number of elements per grain (1000 grains)

Comparing Figs. 4.9-4.12, it seems that with a sufficient number of grains assumed in the model, the necessity of using multiple elements per grain is reduced for simulating the overall behavior of the material. In other words, each grain can be confidently assumed to be one single element in simulating the overall response of the material. It is acknowledged that a coarse mesh with only one El/Gr cannot give an accurate description of intragranular fields. However, this type of mesh is able to give a good estimation of the macroscopic stress–strain curve.

Using one element per grain in simulations has been extensively used in the literature, and has shown to provide very good results, in agreement with experimental measurements (e.g. Kalidindi *et al*., 1992; Sarma and Dawson, 1996; Bachu and Kalidindi, 1998; Staroselsky, 1998; Barbe *et al*., 2001; Van Houtte *et al*., 2002; Balasubramanian and Anand, 2002a; Neale *et al*., 2003; Wu *et al*., 2004; Diard *et al*., 2005), even for complex crystal plasticity laws, including phase transformation or twinning (e.g. Gall *et al*., 2000; Staroselsky and Anand, 2003). Therefore, in the simulations done in this thesis, each grain is assumed to be one single finite element.

4.4 GRAIN SHAPE EFFECT

Another important parameter that is of special interest in the CPFE modeling is the effect of grain shape. It is well known that grains are not of cubic shape. Thus, it is important to know the deviation in results caused by using idealized cubic grains instead of the more realistic shaped grains.

As a first study of the grain shape effect, the simple compression simulation is done on a Mg cube which is divided into five layers with 25 grains in each layer (Fig. 4.13a). The configuration of the first layer is repeated for the other layers. The grains are of different sizes and shapes. As a result, the number of elements per grain is not the same for all the grains. The average value of elements per grain is calculated to be around 11 elements per grain (4.13a).

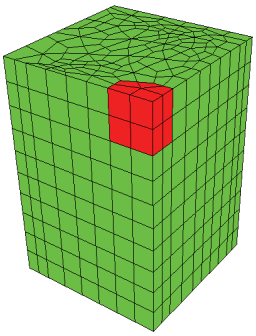

(a)

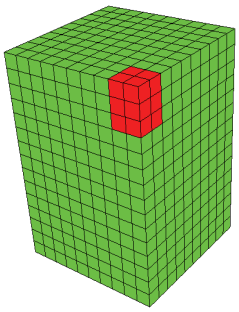

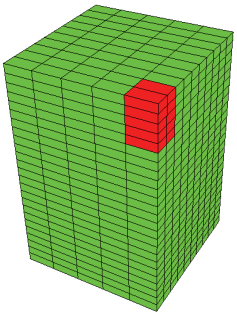

(b) (c)

Figure 4.13 Comparison between specimens with cubic grains and irregular shaped grain

(a) specimen with irregular shaped grains (average of 10.88 El/Gr (b) cubic grains with 10 El/Gr

(c) cubic grains with 12 El/Gr

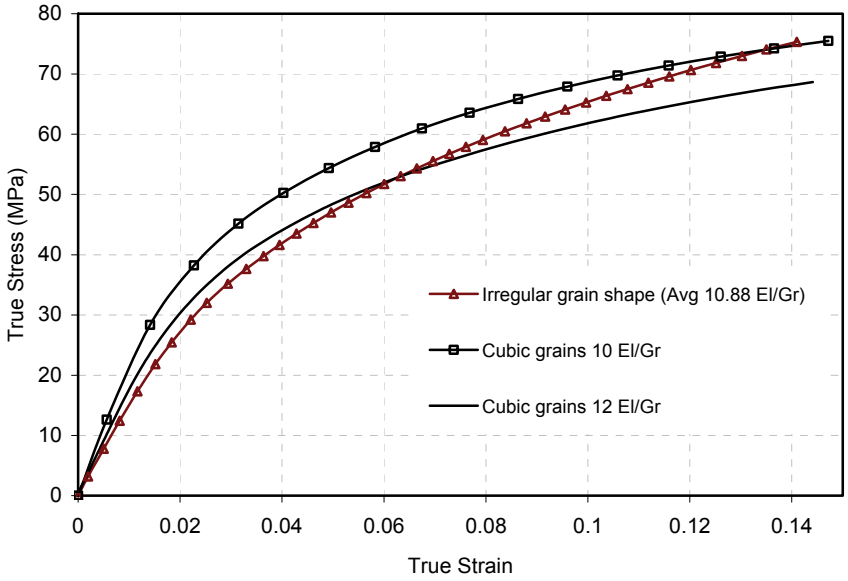

Figure 4.14 The effect of grain shape on material behavior

Figure 4.14 shows the result of the simple compression test using the cube with irregularly shaped grains shown in Fig. 4.13a. For the sake of comparison, the results of simple compression test using cubic grains with 10 elements per grain and 12 elements per grain (also shown in Fig. 4.13b-c) are shown in Fig. 4.14. It should be mentioned that the number of grains in all three cases is 125.

As can be seen in Fig. 4.14, the stress-strain curve for the cube with irregular shaped grains (10.88 elements per grain) is close to the 12 elements per grain case initially, but then follows the curve for 10 elements per grain case. It indicates that the change in shape of the grains does not impose a significant rise or drop in the stress level, although there are some slight changes in the curve shape. Constructing models with grains of irregular shape can sometimes be time-consuming and cumbersome. Considering this result and following the extensively-used approach in the literature, it may be concluded that in most cases, the grains can be considered as cubic shape. However, further studies are needed concerning the role of grain shape in the crystal plasticity modeling. One approach is to see the effect of grain shape when the grain boundary is included. In such a case, in different layers of the model, different patterns can be used for grains (such a model is presented in the next section).

4.5 GRAIN BOUNDARIES

To take into account the effects of the grain boundary, in general, some methods have been proposed in the literature. To consider the effect of grain boundary sliding in the deformation of Mg alloys, Staroselsky and Anand (2003) added a term to the constitutive equation for stress in each crystal. They assumed the stress in each grain to be a volume average of the stress from the crystal plasticity model in certain percentage of the grain and an isotropic model in the rest of the grain. In this method, they did not consider the topology of the boundary region. Wei and Anand (2004) coupled a crystal-plasticity model for the grain interiors with a new elastic–plastic grain-boundary interface model to simulate the effects of grain boundaries in polycrystalline materials. They used this new computational capability to study the deformation and fracture response of nanocrystalline FCC nickel.

In a preliminary study in this section, a new approach is proposed for investigating the effects of grain boundaries in the deformation of Mg alloys. To take into account the effect of the grain boundary, the geometry is divided into two distinct regions, namely grains and grain boundaries. The ratio of the grain boundary thickness to the average grain dimension is assumed to be 0.04. Considering the average grain dimension to be 20 μm, the grain boundary thickness would be 1 μm. This assumed thickness is higher than the actual thickness of grain boundaries; in fact, it includes both the grain boundary thickness and thickness of the region inside grains adjacent to it which shows abundant slip system activity. The crystal plasticity model has been assigned to the elements inside the grains; whereas for the elements in the grain boundary region, an isotropic elastic–plastic material model has been employed.

To study quantitatively the effects of grain boundaries, a material model must be defined. However, determining the values of material parameters for the grain boundary, by no means, is a straightforward task. Thus, a range of material properties is defined and examined for grain boundaries. Figure 4.15 shows three hardening behaviors assumed for the grain boundary region, namely HB-1, HB-2 and HB-3. These material behaviors have been defined as a first-step in studying the role of grain boundaries, but are obviously not exact models of grain boundaries. By combining these hardening behaviors and considering different values of elastic modulus, different material properties can be defined. A series of simulations is done with the aim of considering the effects of grain boundaries in the modeling. Each grain is assumed to be one finite element, and the initial texture is assumed to be random. In general, a finer mesh is used for the grain boundaries.

Figure 4.16 shows a sample deformed shape together with the undeformed shape of the Mg cube. The sliding at the grain boundaries can be clearly seen in the deformed shape. In Fig. 4.17, the stress distribution in the whole specimen (Fig. 4.17a) and the grain boundaries (Fig. 4.17b) can be observed. As can be seen, the distribution of stress is inhomogenous, particularly at the grain boundaries.

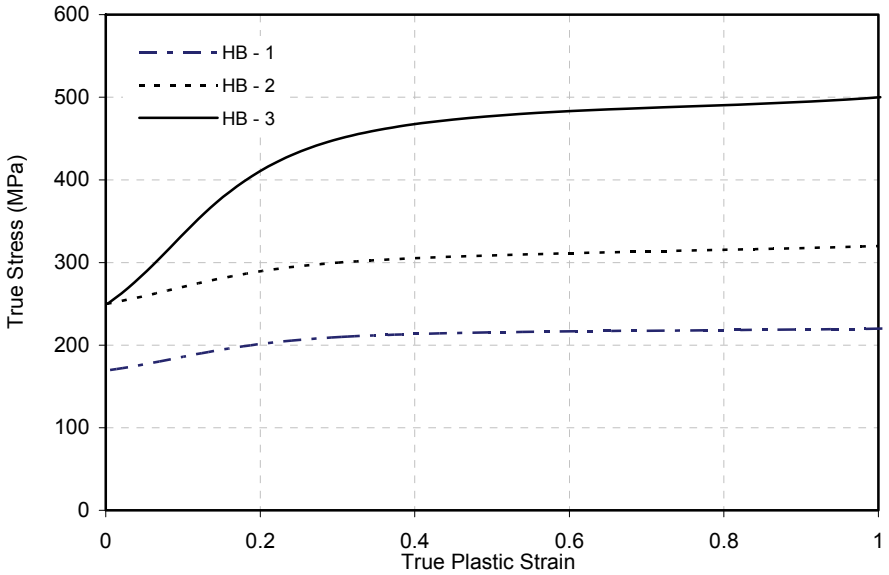

Figure 4.15 Different hardening behaviors defined for grain boundary

Figure 4.16 Deformed and undeformed shape of Mg cube; grains and grain boundaries

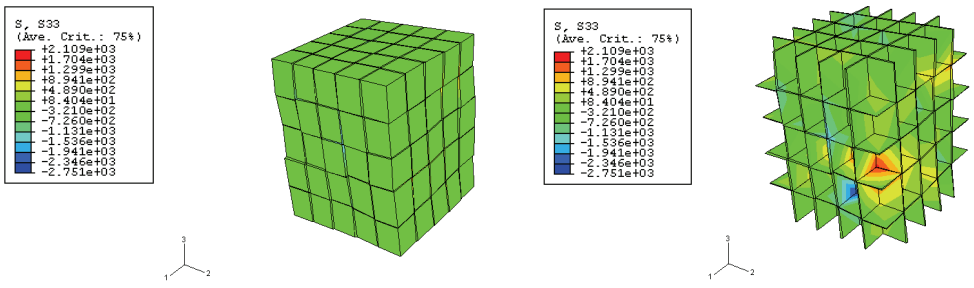

(a) (b)

Figure 4.17 The stress distribution (in MPa) in (a) specimen and (b) grain-boundary region

In Fig. 4.18, the stress-strain curves for a specimen having different grain boundary properties (using the same crystal plasticity model for grains) are plotted. In all the simulations, the deformation of the grains are described by the crystal plasticity model with three basal <a> slip system and six pyramidal <a> slip systems, with slip resistance

values of 0.55 and 105 MPa, respectively. For comparison, the case of simple compression without grain boundaries is also included.

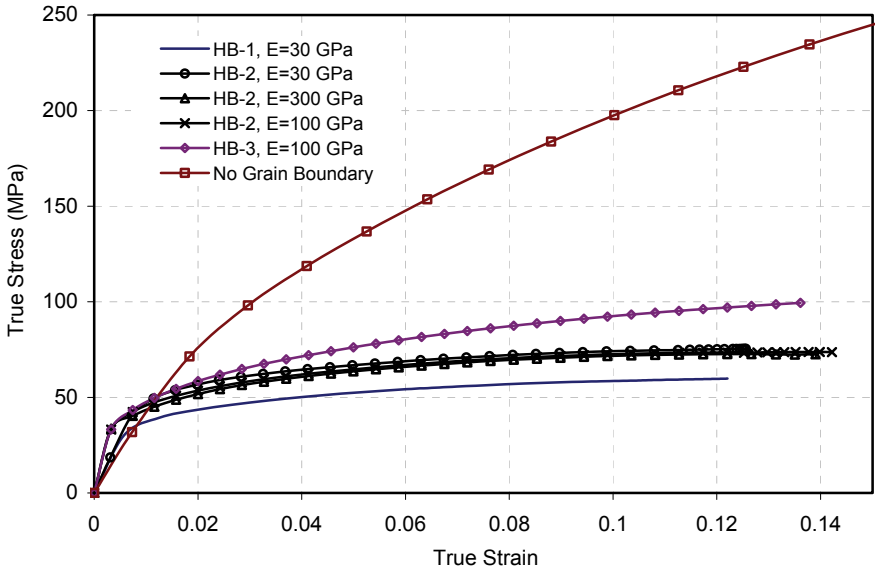

Figure 4.18 Stress-strain curve for Mg cube, considering the effects of grain boundaries using the hardening behaviors defined in Fig. 4.15.

The stress-relieving role that the grain boundary can play in deformation of Mg alloys can be clearly seen in Fig 4.18. Also, it is seen that a higher level of stress in the hardening behavior assumed for the grain boundary causes a higher level of stress in the overall behavior of the specimen. It is noteworthy that the volume fraction of the grain boundary region is only 5-8% of the whole specimen.

Other than studying the effects of flow stress level, in order to investigate the effect of elastic modulus of the grain boundaries, three different values of elastic modulus are used with the HB-2 hardening behavior to form different material models for the grain boundary. As can be observed, even a large change in elastic modulus does not change the overall behavior of the specimen, considerably.

To take the effects of grain boundaries into account, such as grain boundary sliding, models with grain boundaries and irregular shaped grains can be considered. An example of these models is shown in Fig. 4.19. In this model the cube is divided into grain layers and grain boundaries. In each layer the pattern for the shape of grains is different, which gives a more realistic picture of the microstructure. However, due to the large number of

elements necessary for such models, the computational cost would be higher than models without grain boundaries.

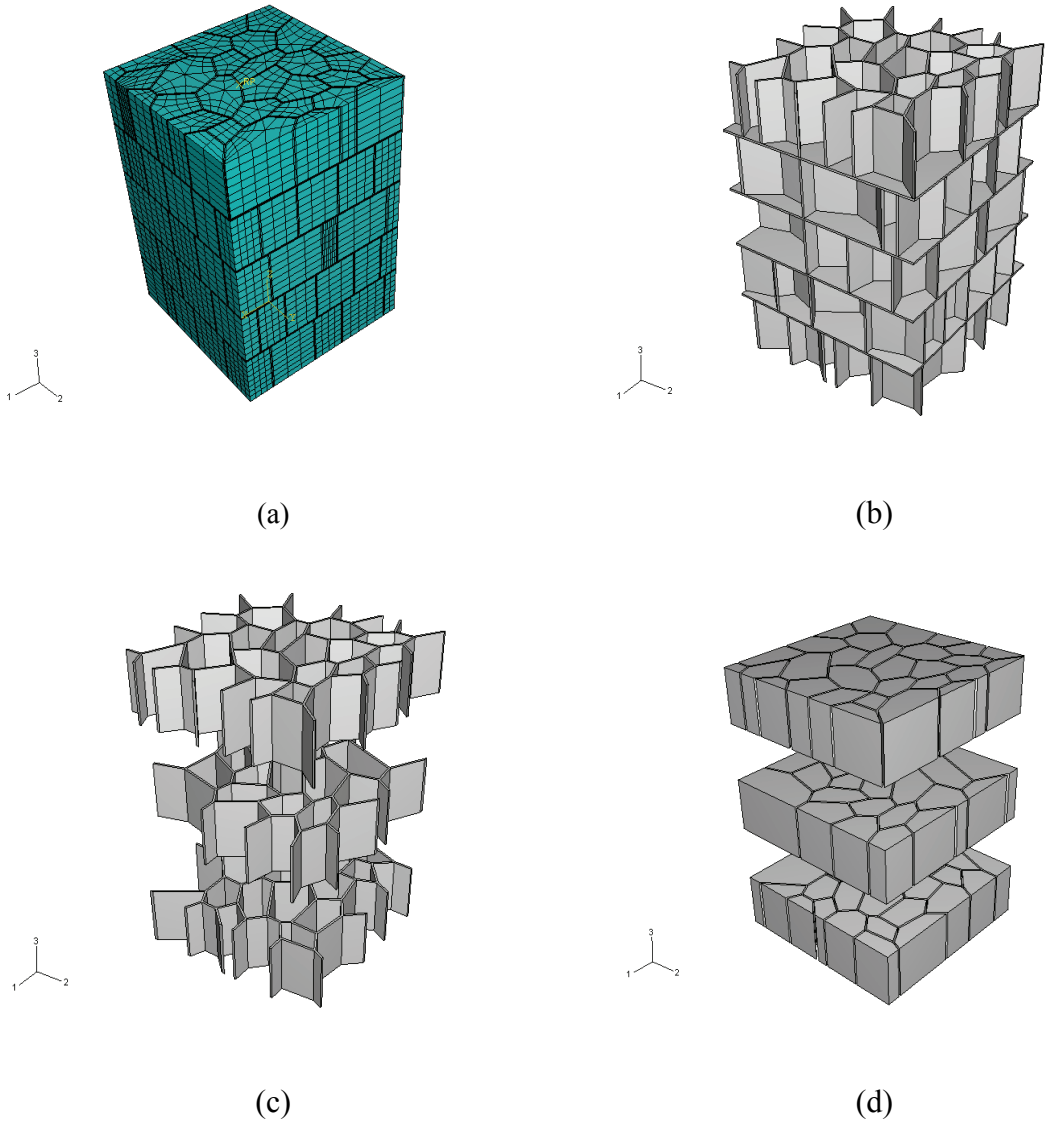

Figure 4.19 Cube divided into grains and grain boundaries with different grain shape in each layer; (a) the whole model (b) all the GBs (c) GB in layers 1, 3 and 5 (d) grains in layers1, 3 and 5

It should be noted that the stress-strain curves in the models with grain boundaries (Fig 4.18) are obtained using the assumed material properties for the grain boundary area, which are not physically measured. Therefore, the drop in the stress level when grain boundaries are taken into account is due to the assumed values. Studying the behavior of the grain boundary area and grain interactions requires more complicated models. In

addition, admittedly, a comprehensive model which is designed to accurately model the mechanical response of Mg alloys over a range of temperatures and strain-rates should take into account grain boundary sliding as well as twinning and DRX, in addition to slip. However, as mentioned in previous chapters, this thesis focuses on the role of slip systems in Mg alloys, and detailed discussion of the role of grain boundaries is not considered as part of this thesis. Interactions between grains are simulated by simple interactions between finite elements, satisfying both equilibrium and compatibility between the grains. This approach has been extensively used and verified in the literature, and does not limit conclusions regarding the role of slip systems.

4.6 SUMMARY

There are some prerequisites for the CPFE modeling that play important roles in obtaining realistic results. Among these are the RVE size (total number of grains), the degree of inhomogeneity in grains (number of elements per grain), and the grain shape effect.

Different simulations were performed to give an overall picture of these effects. As a result of these simulations, it is concluded that increasing the number of grains increases the level of stress until it reaches a plateau. On the other hand, increasing the number of elements per grain (for low number of grains), lowers the level of stress, until it reaches a plateau.

Regarding the RVE size, for consistent modeling of texture, at least 1000 grains are ideally needed. With this number of grains, the stress-level is less than 3 percent different from the plateau level. However, in situations where the computational cost is of great importance, half of this amount, 512 grains, may be sufficient; in which case, the difference would be around ten percent.

Considering the intra-grain inhomogeneity effect, it was observed that, for a low number of grains, dividing grains into more elements decreases the stress level until the point that it reaches a plateau. It was observed that the main change happens by increasing the inhomogeneity from one element per grain to six (or eight) elements per grain; thus, 6 to 8 elements per grain will be sufficient for simulating the overall behavior of the material

even with a low number of grains. The drop in the stress level for multiple elements per grain decreases with the increase in total number of grains. For 1000 grains, assigning multiple elements per grain does not affect the overall behavior of material significantly. It is concluded that for simulations at a macro-level, 1 El/Gr is certainly sufficient for predicting the overall behavior of the material.

For observing the grain shape effect on the overall behavior of the material, a comparison was done between a cube with well-ordered cubic grains and layers of arbitrarily shaped grains. Comparing the results, it is seen that the difference as a result of the shape change is not significant. Thus, although further study is recommended for a firm conclusion, in simulations of this thesis, cubic grains are used.

Chapter 5

Slip Systems and Strain-rate Sensitivity in Mg Alloys

5.1 INTRODUCTION

In many studies on magnesium, the ultimate goal is finding ways to achieve high levels of formability, especially at warm temperatures (75°C to 250°C). As mentioned in Chapter 1, other than the usual methods for increasing formability, recently, some innovative methods such as activating particular slip systems are being considered as possible alternative options. The prerequisite for using these methods is a thorough understanding of the role that each slip system plays in the deformation of Mg alloys. In addition, the effect of strain-rate sensitivity (SRS) on the activity of slip systems and the overall behavior of the material should be understood.

It has been reported in the literature that depending on the model, different approximations of the slip resistance values can be obtained for different slip systems in Mg alloys at room temperature (see e.g. Burke and Hibbard, 1952; Reed-Hill and Robertson, 1957; Kelly and Hosford, 1968; Staroselsky and Anand, 2003; Kleiner and Uggowitzer, 2004; Barnett *et al.*, 2005; Agnew and Duygulu, 2005; Brown *et al.*, 2005; Levesqus *et al.*, 2006; Lou *et al.*, 2007). For the deformation of Mg alloys at higher temperatures, the available data for the slip resistance values is even less consistent and

scarcer, and there are more unanswered questions related to the active slip systems, and evolution of their slip resistance with temperature. Despite the apparent contradictions in the reported values of slip resistances (using different methods), the trends that are obtained by employing various methods are of particular interest. General conclusions that these methods propose are crucial to the correct modeling of magnesium alloy behavior. The main objective of this chapter is to understand the role of different slip systems in Mg alloys and the effect of strain-rate sensitivity (SRS) on slip systems activity and the overall behavior of the material using the CPFE method. Then slip resistances and SRS values are proposed in an inverse approach using the CPFE method and experimental data for a Mg alloy (AZ31). This understanding leads us to a prediction of the behavior of Mg alloys at warm temperatures.

The chapter is divided into three main parts; in the first part (Section 5.2), the effect of individual slip systems on the mechanical response of material is studied. Several series of simulations are done to simulate the behavior of Mg alloys polycrystals employing different potentially active slip systems and different values of slip resistances. The first series of simulations is performed using random initial texture. In the next simulations, initial textures were assigned to be that of hot-rolled plates, obtained from experimental measurements. The pole-figures of these textures are shown and discussed in the following sections. Simulations are performed with loading in the normal (ND), rolling (RD), and transverse (TD) directions.

In the second part, Section 5.3, SRS and its effect on the macro- and micro-scale response of the material, and the concept of the reference shearing rate (RSR) are studied. Next, the effect of SRS on the slip systems activity is investigated. Finally, some experimental data regarding the SRS values in Mg alloys are collected and analyzed.

In the third part, Section 5.4, the mechanical behavior of Mg alloy (AZ31) over the range of warm temperatures is simulated. There are certain issues that should be considered at higher temperatures, among which are the change in the slip resistance values of different systems and the strain-rate sensitivity factor. First, by considering the obtained trends regarding the effect of each slip system, a series of relations are proposed for the change of slip resistance values versus temperature and strain-rate. Second, considering the

results obtained in Section 5.3, a new relation for the change in the SRS factor with the change in temperature and strain-rate is developed. Then, a series of simulations is performed to simulate the mechanical behavior of Mg alloys at different temperatures. The simulations are performed with loading in the rolling direction, RD, and the transverse direction, TD. The stress-strain curves and r-values are obtained and results are compared to the experimental results of Agnew and Duygulu (2005). The chapter finishes with some concluding remarks in Section 5.5.

5.2 ROLE OF INDIVIDUAL SLIP SYSTEM IN Mg ALLOYS

A series of simulations are performed for the tension and compression of samples with different initial textures, i.e., random initial texture, and texture of hot-rolled plates. For the hot-rolled samples, the loading in the normal direction (ND), the rolling direction (RD), and the transverse direction (TD) is considered.

5.2.1 RANDOM TEXTURE

To study the effects of slip resistance values (excluding the effect of initial texture), a set of compression simulations are performed on a cube sample with a random initial texture. The random texture is produced using the TexTools software (Resmat Co., 2002) and a random orientation distribution function (ODF) file as its input. Compression simulations are performed assuming the cube to be composed of 1728 grains, each of which is represented by a single element of reduced integration type, C3D8R (8 node solid brick element with one Gaussian integration point). Different sets of simulations are performed to observe the effects of change in the activity of slip systems on the overall behavior of material. Simulations are done at a nominal strain rate of 0.001 s^{-1}. In all the simulations done in this thesis, the slip resistances of slip systems are chosen to be in the range of values proposed by different researchers and collected in the work of Lou *et al.* (2007). Some of these values are reproduced in Table 5.1.

In studying the effects of slip systems, one issue is whether to consider the ratio of the slip resistances of different systems or their absolute values. Special attention is usually paid to the ratio of slip resistance of different systems to that of the basal<a> slip system. Lou *et al.* (2007) report that different values, ranging from 0.45 MPa to 45 MPa (with

most values between 1 MPa to 10 MPa), have been proposed by different researchers for the slip resistance of the basal<a> slip system in Mg alloys. They also report different s_{prism}/s_{basal} ratios, ranging from 1 to 87. With these in mind, the simulations in this section are done for two different slip resistance values for basal<a>: $s_{basal<a>} = 1$ MPa and $s_{basal<a>} = 10$ MPa . The ratio of slip resistance values of different slip systems to that of the basal<a> slip system varies from 100 to 1.

Table 5.1 Slip resistance values reported for pure magnesium and AZ31B (Lou *et al.*, 2007)

Metals	Conditions	$s_{basal<a>}$ (MPa)	$s_{prism<a>}$ (MPa)	$\frac{s_{prism<a>}}{s_{basal<a>}}$
Mg	SC	0.81; 0.76; 0.45; 0.65; 0.52	39.2	48-87
AZ31B	PC, VPSC, XRD	45	110	2.4
AZ31B	PC, EPSC, ND	10	55	5.5
AZ31B	PC, Taylor, XRD	-	-	1-2.4
AZ31B	PC, TEM	-	-	1.1

SC: single crystal; PC: polycrystal; XRD, X-ray diffraction; ND: neutron diffraction; VPSC: visco-plastic self-consistent model; EPSC: elastic-plastic self-consistent model; TEM: transmission electron microscopy

Figure 5.1 shows the change in the computed stress-strain curves with the change in the slip resistance of prismatic<a>. In this case, the only active slip system other than prismatic<a> is basal<a> with slip resistance of 1 MPa. As can be seen in this figure, the presence of prismatic<a> slip systems, even with the high s_{prism}/s_{basal} ratio of 100, greatly reduces the level of stress compared to the case when only basal<a> is active (about 65% at strain of 0.15). However, the change in the values of $s_{prism<a>}$ from 100 MPa to 1 MPa, i.e. the change in ratio from 100 to 1, only changes the level of stress by about 20% at strain of 0.2. The simulations are repeated with $s_{basal<a>} = 10$ MPa and the same s_{prism}/s_{basal} ratios from 100 to 1 (Fig. 5.2). Comparing the two figures, two observations should be noted: first, the results for the same slip resistance ratios are different in Figs. 5.1 and 5.2; second, the change in the stress level from slip resistance

ratio of 100 to 1 is noticeably larger in this case. It is interesting that in both cases, a lower bound for the stress-strain curve is observed. This lower bound seems to be independent of the basal<a> slip resistance; i.e. in both cases, the stress level of the lower bound at strain of 0.3 is about 280 MPa. This lower bound can be attributed to the ratio of slip resistance of prismatic<a> to that of basal<a>.

It seems that the values of slip resistances, not their ratios, determine the level of stress. On the other hand, it is expected that the slip resistance ratios govern the texture evolution. Both the basal<a> and prismatic<a> families provide dislocations on three slip systems; although the latter is active on three different planes compared to one for the former. In addition, with random initial texture, there are no favorable orientations for the activity of specific systems. Therefore, when, for example, the slip resistance ratio is 100, the level of activity of the prismatic<a> system is expected to be very low, and the texture evolution resulted by the activity of this system should be negligible. Nevertheless, this low activity affects the level of stress significantly.

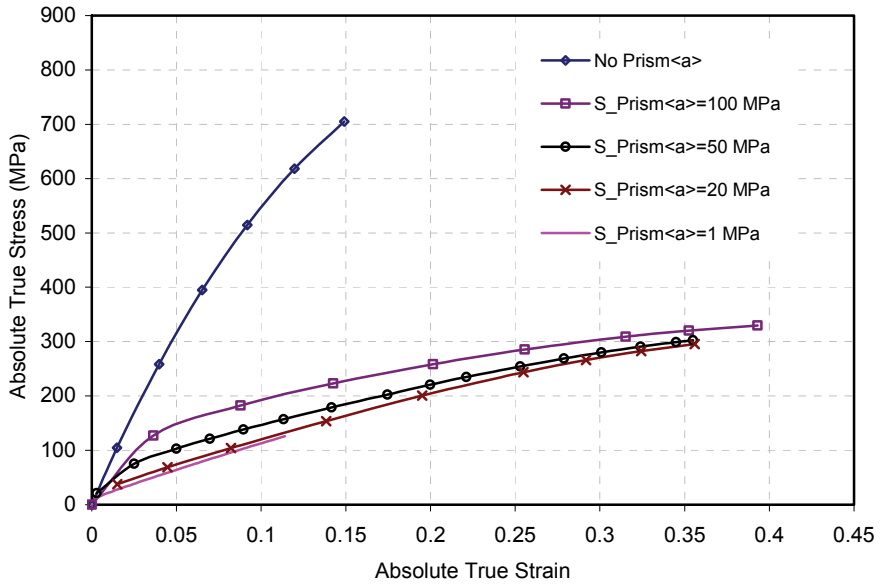

Figure 5.1 The effect of prismatic<a> slip resistance on the stress-strain curves for specimens under compression; pyramidal<a> and pyramidal<c+a>: not active; $s_{basal<a>} = 1$ MPa

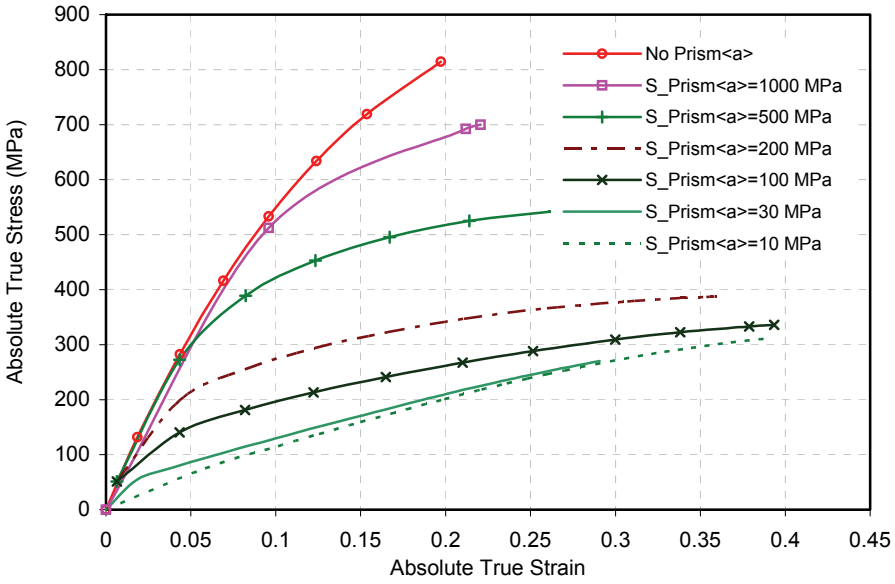

Figure 5.2 The effect of prismatic<a> on the stress-strain curves for specimens under compression; pyramidal<a> and pyramidal<c+a>: not active; $s_{basal<a>} = 10$ MPa

Regarding the effect of pyramidal<a> slip systems, results obtained for the effect of this system on the stress-strain curve are quite similar to those of the prismatic<a> slip system. Figure 5.3 shows the results for $s_{basal<a>} = 1$ MPa , where the trends are much like the ones seen in Fig. 5.1.

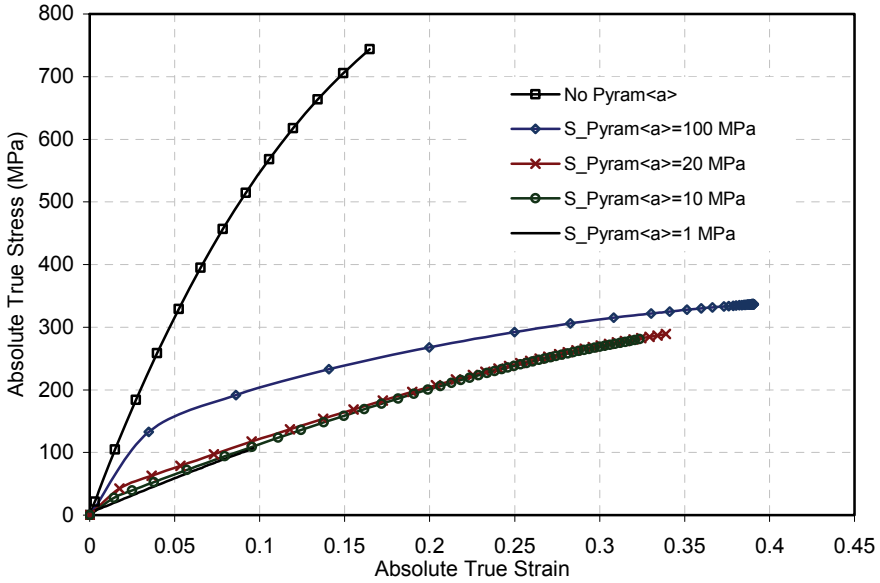

Figure 5.3 The effect of pyramidal <a> slip resistance on the stress-strain curves for specimens under compression; prismatic <a> and pyramidal<c+a>: not active; $s_{basal<a>} = 1$ MPa

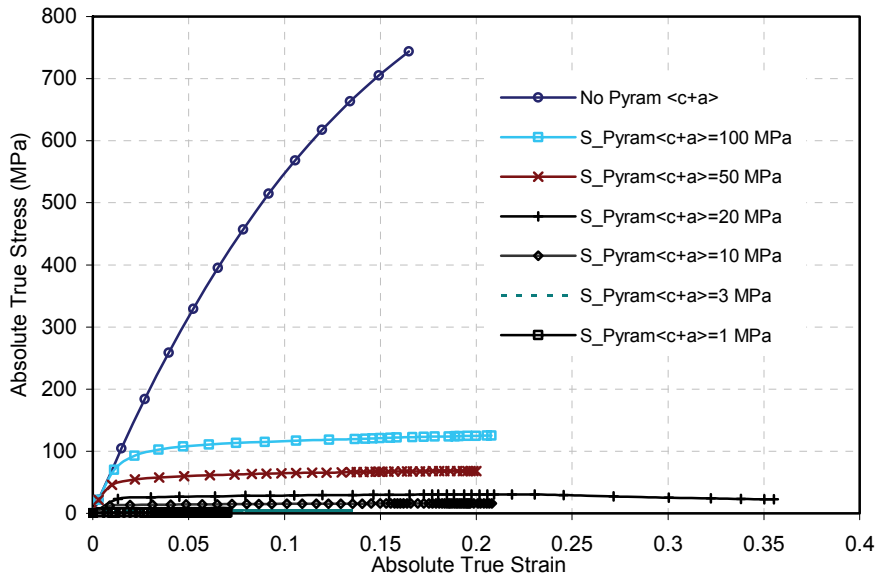

Figure 5.4 The effect of pyramidal<c+a> slip resistance on the stress-strain curves for specimens under compression; pyramidal<a> and prismatic<a>: not active; $s_{basal<a>} = 1$ MPa

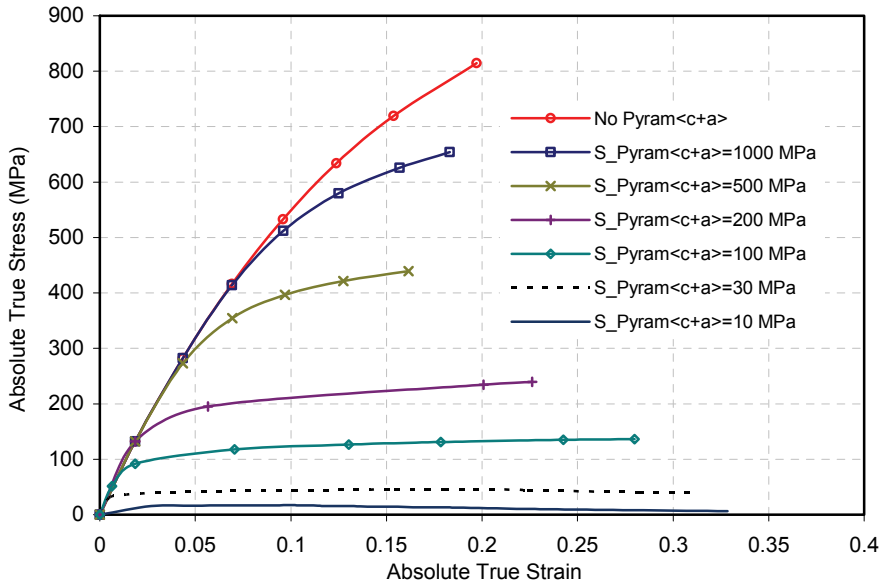

Figure 5.5 The effect of pyramidal<c+a> slip resistance on the stress-strain curves for specimens under compression; pyramidal<a> and prismatic<a>: not active; $s_{basal<a>} = 10$ MPa

The next family of slip systems considered is the pyramidal<c+a> slip system. Simulations are done for two different slip resistances values assumed for the basal<a> slip system, 1 MPa and 10 MPa; the results are shown in Figs. 5.4 and 5.5, respectively. The most important aspect of these graphs is the constant decrease in the level of stress with the decrease in the slip resistance value of pyramidal<c+a> slip system. The lower bound observed for the prismatic<a> and pyramidal<a> slip systems does not exist here. In general, the flow stress and the slip resistance of pyramidal<c+a> slip system have the same order of magnitude. This can be attributed to the unique characteristic of the pyramidal<c+a> slip system. As shown for the case of Mg single crystals in Section 3.5, pyramidal<c+a> is the only system that provides deformation along the c-axis of the crystal other than deformation in the basal planes; other slip systems provide deformation only in the <a> directions. This characteristic intensifies the effect of the <c+a> system on material response, in particular, the stress level.

5.2.2 TENSION AND COMPRESSION IN THE ND

In this section, the simulations are done for samples with the texture of hot-rolled plates, with specimens loaded in the normal direction (ND). Tension and compression simulations are performed using different slip resistance values for different systems, and the effect of change in the activity of each system is considered separately through a series of simulations.

Figure 5.6 shows a typical specimen cut from a hot-rolled plate and loaded in the ND. In the simulations, because of the symmetry, the modeled specimen is only one-eighth of the original one. This specimen is simulated using a cube with the height to width ratio of 1.5, and is considered to be composed of 1000 grains. Each grain is considered to be one single element of C3D8R type. All the nodes on the planes $X_1 = 0$, $X_2 = 0$, and $X_3 = 0$ have zero displacements in the 1-, 2-, and 3- directions, respectively. All of the nodes on the top X_3 face are displaced in the 3-direction at a constant velocity. Simulations are done at a nominal strain rate of 0.001 s^{-1}.

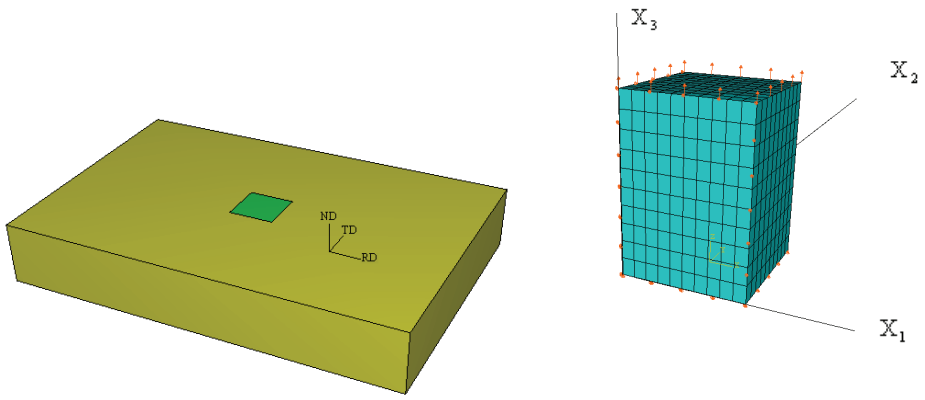

(a) (b)

Figure 5.6 (a) The hot-rolled plate and the corresponding specimen (b) specimen (1000 grains)

The initial texture is assigned to be that of a hot-rolled plate, taken from measurements obtained at McGill University. (Details of texture measurements and a study on the texture gradient in Mg alloy AZ31 sheets is presented in Appendix A.) The initial $\{0\,0\,0\,2\}$ and $\{1\,0\,\bar{1}\,1\}$ pole figures of this plate are shown in Figs. 5.7(a) and 5.7(b), respectively. It should be noted that as a result of the inhomogeneities inherent in the rolling process, hot-rolled plates of Mg alloys show a surface to mid-plane texture gradient. The pole figures, shown in Fig. 5.7, are an average of hot-rolled plate texture. The needed discreet orientations for 1000 grains, in the form of 1000 sets of Euler angles, were obtained by using the TexTools software (Resmat Co., 2002), and by inputting the experimentally measured ODF file.

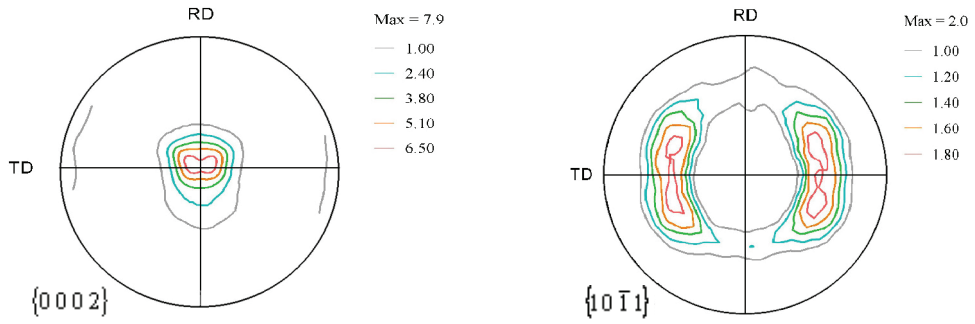

(a) (b)

Figure 5.7 Initial texture of the specimen (rolled plate) (a) $\{0\,0\,0\,2\}$ pole figure (b) $\{1\,0\,\bar{1}\,1\}$ pole figure

Figures 5.8, 5.9 and 5.10 show the results of simulations of tension and compression tests for varying values of slip resistances for basal<a>, prismatic<a> and pyramidal<c+a> slip systems, respectively, while the slip resistance of other slip systems are kept constant. In this section, no hardening is assumed for the slip systems. The first observation in Figs. 5.8-5.10 is that for some tension simulations, yielding is followed by softening. Computationally, the softening is manifested by localization of the strain to particular grains, oriented to favor the activity of slip systems with a lower slip resistance level (localization will be discussed in more detail in Chapter 6).

The second observation in Figs. 5.8-5.10 is the difference between the stress-strain curves in tension and compression tests for some combinations of slip resistances. This phenomenon should not be misinterpreted as a prediction of Mg alloys anisotropic yielding behavior in tension/compression tests which is a result of the twinning activity and its directionality. In these simulations, twinning is not included, and, as expected, the yield anisotropy is negligible. Therefore, the difference between the curves is a result of different degrees of activity for slip systems in tension and compression, which will be discussed later in this section.

Considering the effect of individual slip systems separately, the change in s_{basal} from 10 MPa to 0.55 MPa does not change the level of stress or the difference between tension and compression curves significantly (Fig. 5.8). With the loading in the ND (parallel to the general c-axis orientation and normal to the basal plane), basal slip is inhibited greatly. Therefore, it is not surprising that basal slip resistance has little effect on macro-behavior.

The decrease in the slip resistance of prismatic<a> system decreases the stress level both in tension and compression (Fig. 5.9); nevertheless, the drop in the stress level is more pronounced in tension than in compression. For $s_{prism<a>} = 500$ MPa, the stress-strain curves are similar in form in tension and compression, with the stress level of former higher than that of the latter. With the increase in the activity of prismatic<a>, the stress level after yielding tends to drop lower in tension than in compression. In addition, the stress-strain curves show different forms in tension and compression. It seems that the

high activity of prismatic<a> compared to pyramidal<c+a> (the slip resistance of which is assumed to be 105 MPa) is the reason behind the tension-compression anisotropy. This will be investigated more in what follows.

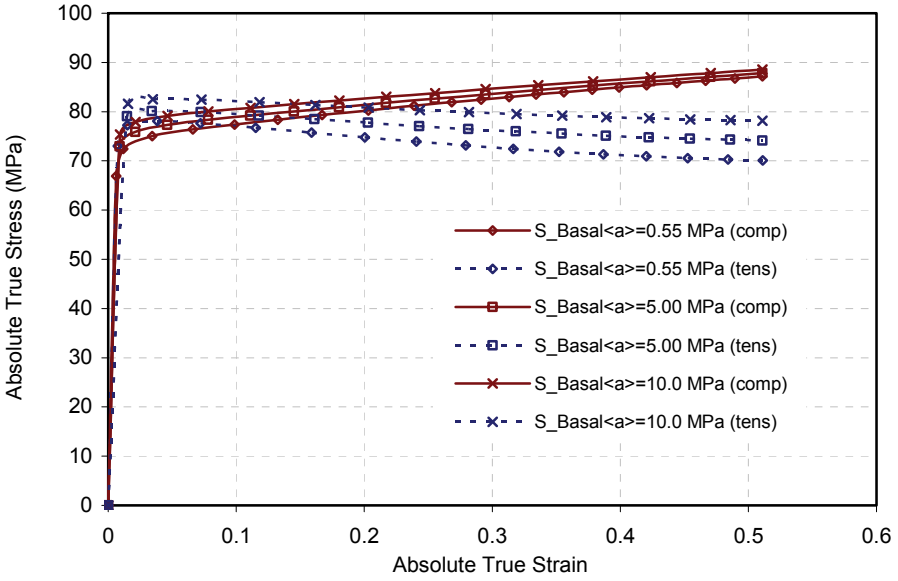

Figure 5.8 Effect of basal<a> slip system in the tension and compression tests; pyramidal<a>: not active; $s_{prism<a>} = 105$ MPa , $s_{pyram<c+a>} = 105$ MPa

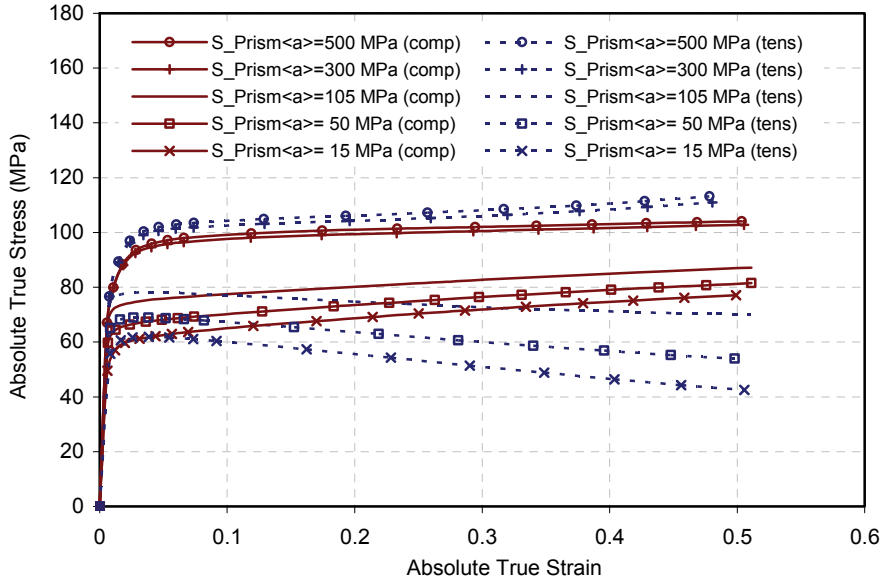

Figure 5.9 Effect of prismatic<a> slip system in the tension and compression tests; pyramidal<a>: not active; $s_{basal<a>} = 0.55$ MPa , $s_{pyram<c+a>} = 105$ MPa

Fig. 5.10 shows the results for the effect of the pyramidal<c+a> slip system. According to this figure, higher activity of pyramidal<c+a> slip systems (lower slip resistance values) not only decreases the stress level more than the basal<a> or prismatic<a> systems, but also reduces the difference between tension and compression curves, which is a result of the unique characteristic of <c+a> system in providing deformation in both the c- and a-directions. In compression simulations, the change in $s_{pyram<c+a>}$ from 500 MPa to 10 MPa can reduce the stress value at strain of 0.2 from 320 MPa to 10 MPa.

It can be seen that the flow stress has the same order of magnitude as the slip resistance of the pyramidal<c+a> slip system, regardless of assumed slip resistances for other systems. Also, while for $s_{Pyram<c+a>} = 500$ MPa the stress level at large strains is higher in compression than in tension, there is negligible difference between tension and compression curves when $s_{pyram<c+a>}$ is 50 MPa or 10 MPa. Considering that $s_{prism<a>}$ is assumed to be 105 MPa, it is seen that lower slip resistances of prismatic<a> compared to pyramidal<c+a> causes the difference between tension and compression.

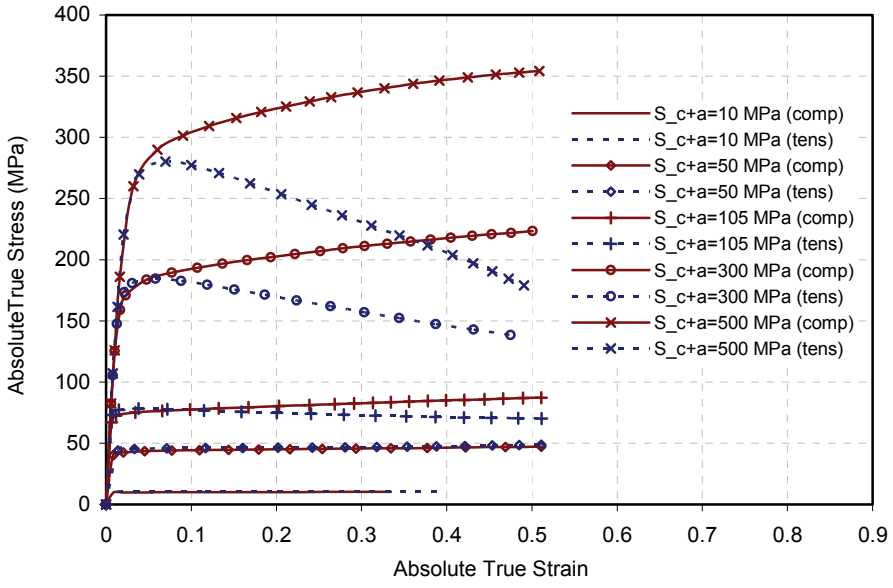

Figure 5.10 Effect of pyramidal<c+a> slip systems in the tension and compression tests; pyramidal<a>: not active; $s_{basal<a>} = 0.55$ MPa , $s_{prism<a>} = 105$ MPa

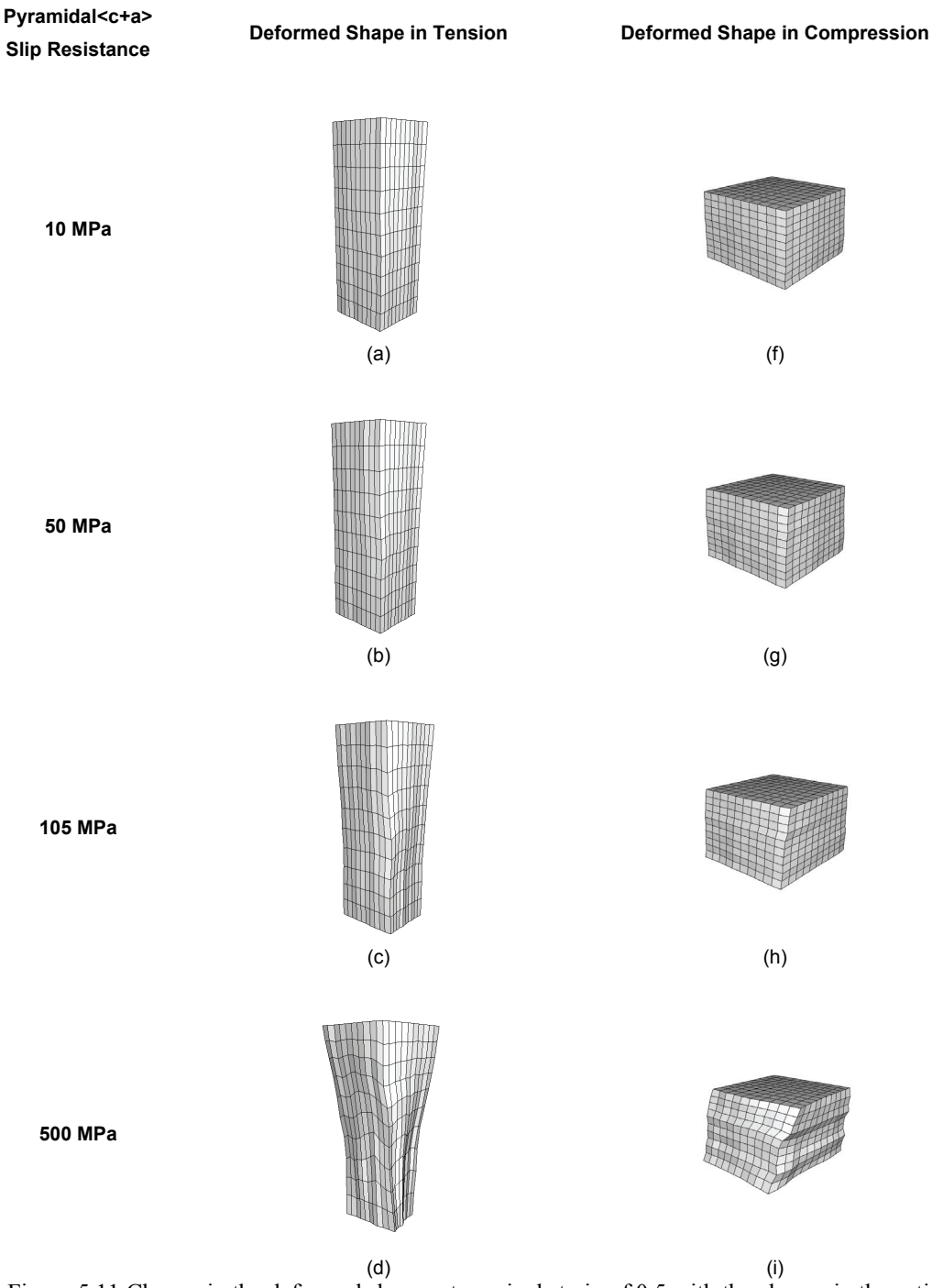

Figure 5.11 Change in the deformed shapes at nominal strain of 0.5 with the change in the activity of the pyramidal<c+a> under tension (a-e) and compression (f-j); the activity of pyramidal<c+a> decreases from top to bottom; pyramidal<a>: not active; $s_{basal<a>} = 0.55$ MPa , $s_{prism<a>} = 105$ MPa

Figure 5.11 shows the deformed shapes of samples under tension and compression with different slip resistance values assumed for the pyramidal<c+a> system. It is seen that with the decrease in the activity of this system, deformed shapes tend to be more

heterogeneous. When pyramidal<c+a> is highly active, the material behaves more isotropic. In general, the activation of pyramidal<c+a> slip system not only lowers the stress level but also reduces the degree of anisotropy of material (the difference between tension and compression curves). Since at higher temperatures, a lower level of stress and a lower anisotropy are expected for Mg alloys, the simulation results strongly support the idea of pyramidal<c+a> being more active at higher temperatures. It should be mentioned that although the results regarding the effect of each system are, to some extent, dependent on the relative slip resistance values of other systems, the obtained trends are independent of these values.

It was observed in both Figs. 5.9 and 5.10 that when the slip resistance value of pyramidal<c+a> is relatively higher than that of prismatic<a>, stress-strain curves in tension and compression would be different. Stress-strain curves of ideally isotropic materials are identical in tension and compression; therefore, this anisotropy should be the result of different slip system activity in tension and compression. To further study this issue, samples with three sets of slip resistance values, TC01-TC03 as defined in Table 5.2, are considered. Figures 5.12 and 5.13 show the stress-strain curves in tension and compression with the slip resistances defined in Table 5.2. As expected, for sample TC01, which assumes lower slip resistance values for pyramidal<c+a> compared to prismatic<a>, the curves are similar in tension and compression (Fig. 5.12). On the other hand, for samples TC02 and TC03, which assume higher pyramidal<c+a> slip resistance values compared to prismatic<a>, the stress level tends to be significantly higher in compression (5.13).

Table 5.2 Slip resistance values assumed for different systems for samples TC01-TC03

Sample	$S_{basal<a>}$ MPa	$S_{prism<a>}$ MPa	$S_{pyram<c+a>}$ MPa
TC01	1	105	10
TC02	1	105	300
TC03	1	15	300

To investigate the reasons behind the difference in tension-compression curves, the final texture and slip system activity for samples TC01-TC03 are plotted in Figs. 5.14-5.19. Figure 5.14 shows the final $\{0001\}$ and $\{10\bar{1}1\}$ pole figures of the sample TC01. As seen in this figure, the simulated final textures of these samples are quite similar in tension and compression. In Fig. 5.15, the accumulated shearing increments on different slip families are plotted for sample TC01 in tension and compression. The accumulated shear on each slip system family, f, is calculated using the following relation,

$$\left(\gamma^{acc}\right)^{f} = \int_{0}^{t_1} \left(\sum_{1}^{nf} \dot{\gamma}^{\alpha} \right) dt , \qquad \text{Eq. 5.1}$$

where nf shows the number of slip systems in the family f, and $\dot{\gamma}^{\alpha}$ shows the shearing rate on slip system α at time t. It is observed that except for basal<a>, slip systems show similar activity levels in tension and compression; basal<a> shows higher activity in tension. In short, for sample TC01, the texture evolution and slip system activity are similar in tension and compression, which result in similar stress-strain curves.

Figures 5.16 and 5.17 show the final pole figures and accumulated shearing increments on various slip families for sample TC02, which shows anisotropy in tension and compression. It is seen that both the final textures and slip system activity are quite different in tension and compression. Figure 5.17 shows that the activity of pyramidal<c+a> is higher in compression (which results in a more basal texture), while the activity of basal<a> and prismatic<a> is higher in tension; the activity of pyramidal<a> is negligible in both tension and compression for this case.

Final pole figures and slip system activity for sample TC03 are shown in Figs. 5.18 and 5.19, respectively. The trends observed for sample TC02 are repeated here. It is obvious that different activity levels of various system, particularly pyramidal<c+a>, which results in different final textures, is the main reason behind different responses in tension and compression.

It should be mentioned that the small difference observed for the yield stress values in tension and compression can be attributed to the activity of slip systems. It can be seen in

Figs. 5.15, 5.17, and 5.19 that for some slip systems, the activity is non-zero and different in tension and compression from the very low strain values (≈ 0.01). The different slip system activity in tension and compression at small strains might be related to the micro-yielding on a few grains which occurs differently in tension and compression.

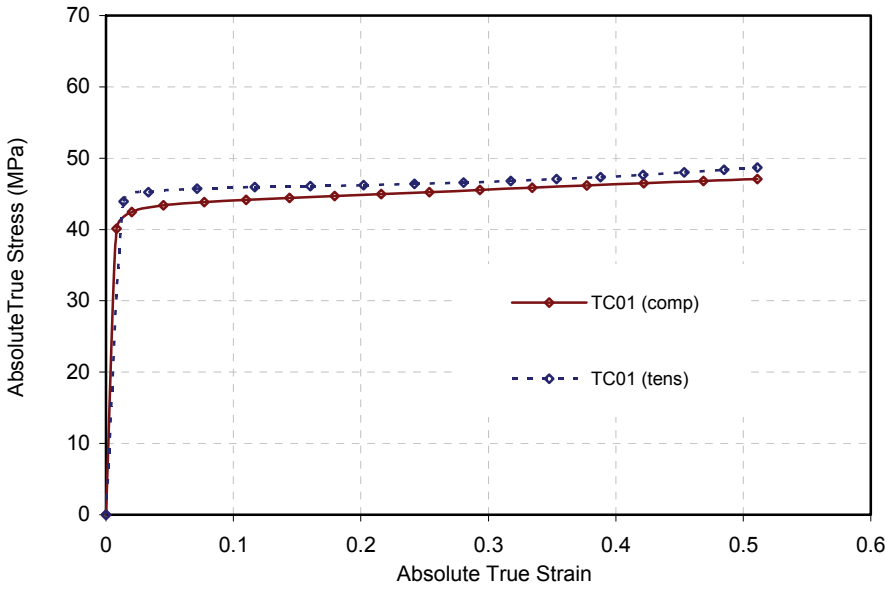

Figure 5.12 Stress-strain curves of sample TC01 in tension and compression

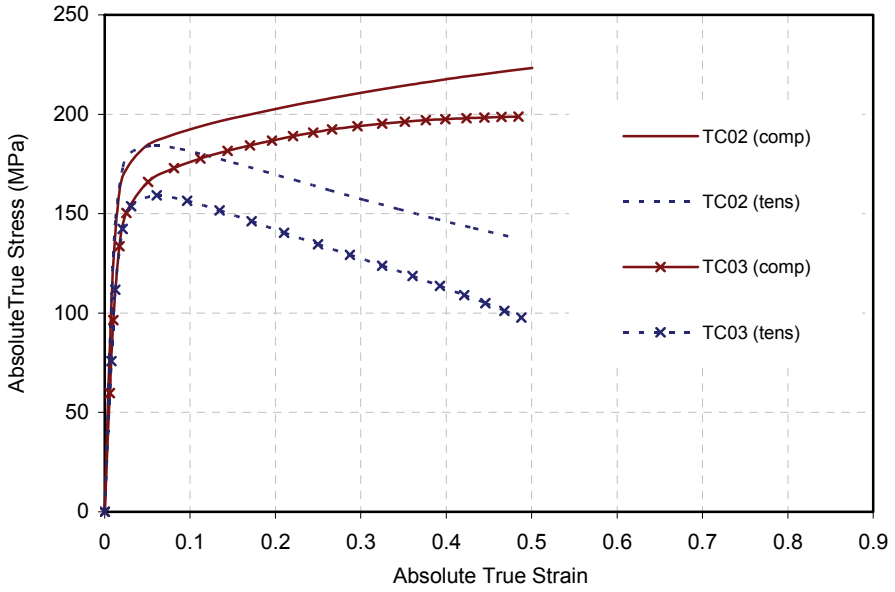

Figure 5.13 Stress-strain curves of sample TC02 and TC03 in tension and compression

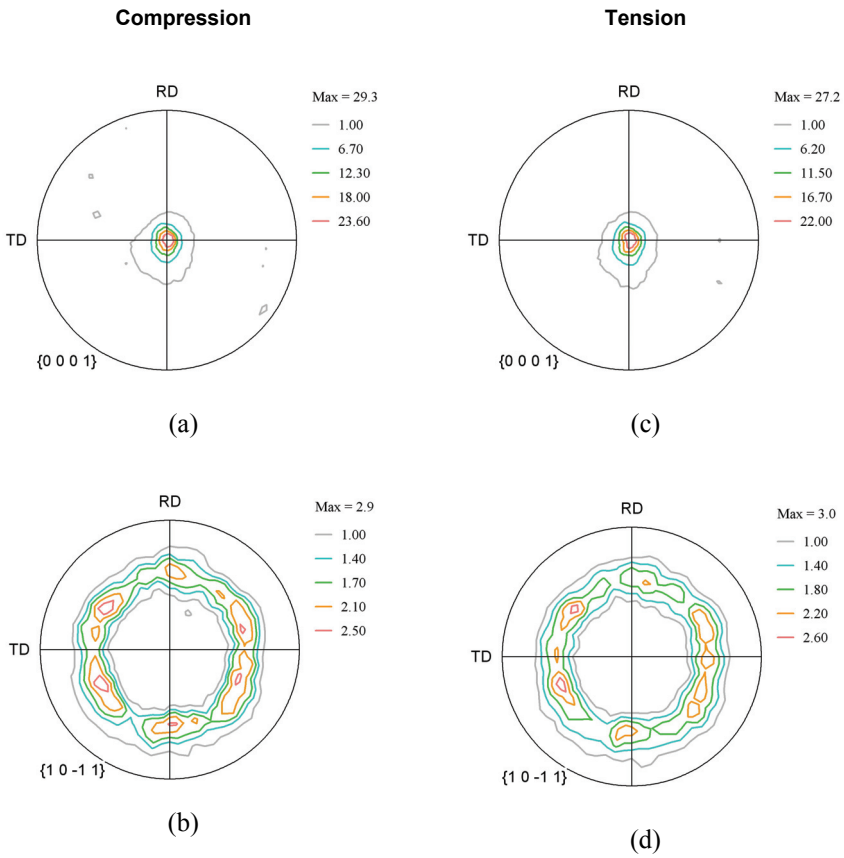

Figure 5.14 Final $\{0001\}$ and $\{10\bar{1}1\}$ pole figures of sample TC01 in (a-b) tension and (c-d) compression

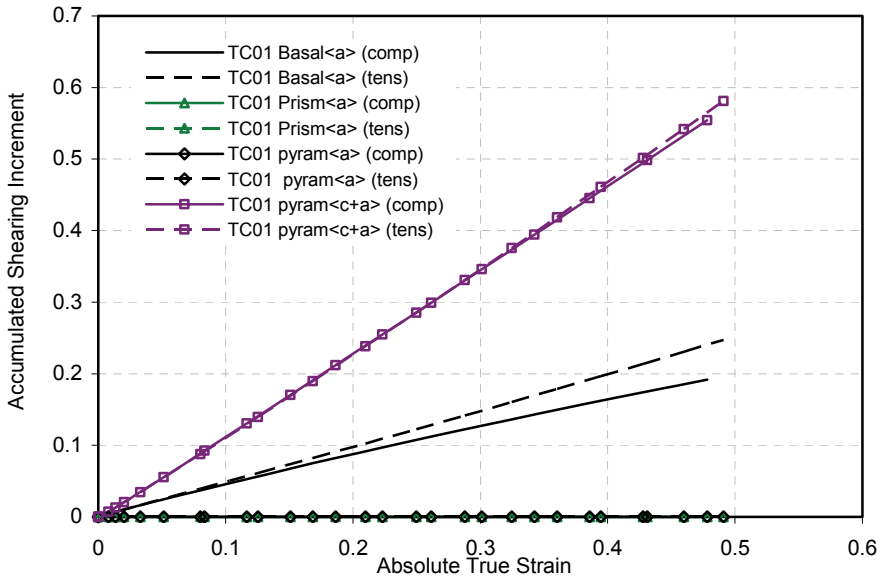

Figure 5.15 Accumulated shearing increment on different slip systems for sample TC01 in tension and compression

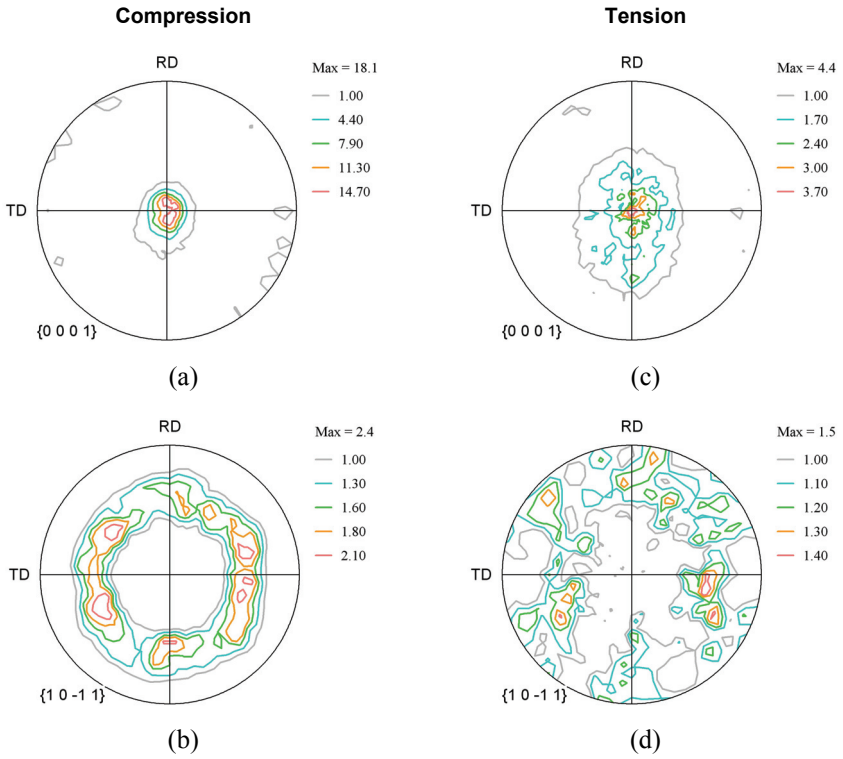

Figure 5.16 Final $\{0001\}$ and $\{10\bar{1}1\}$ pole figures of sample TC02 in (a-b) tension and (c-d) compression

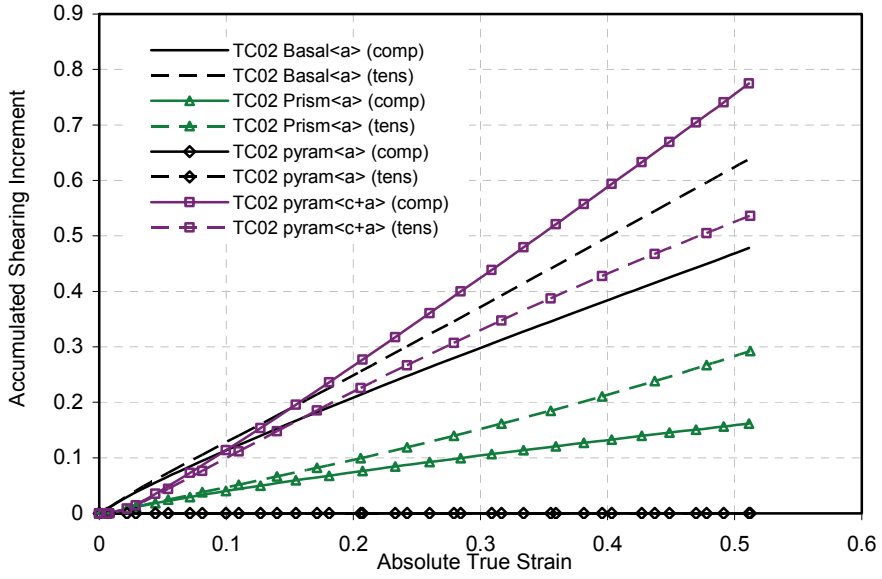

Figure 5.17 Accumulated shearing increment on different slip systems for sample TC02 in tension and compression

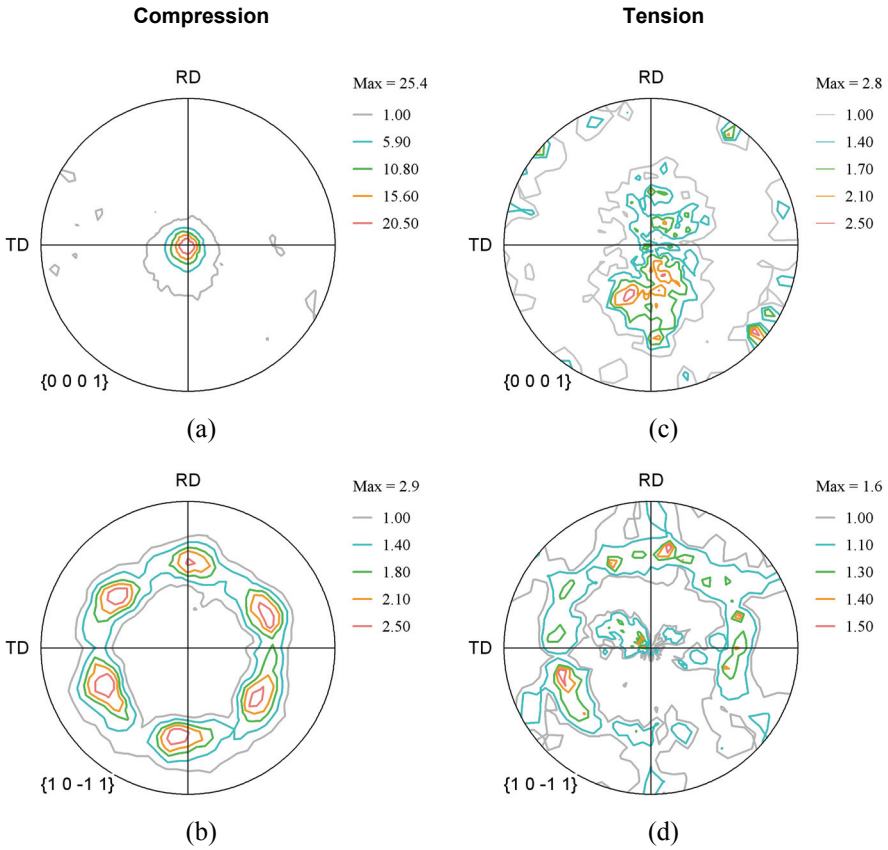

Figure 5.18 Final $\{0001\}$ and $\{10\bar{1}1\}$ pole figures of sample TC03 in (a-b) tension and (c-d) compression

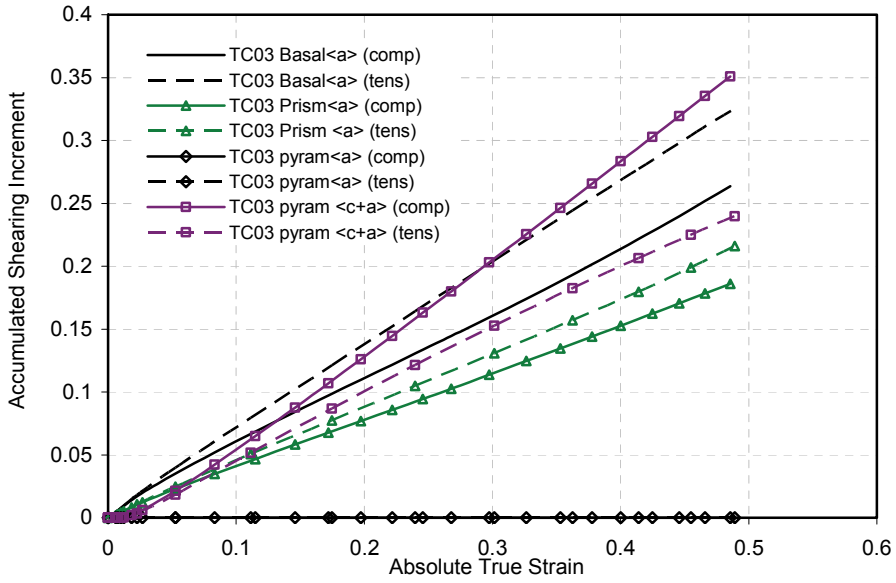

Figure 5.19 Accumulated shearing increment on different slip systems for sample TC03 in tension and compression

5.2.3 TENSION IN THE RD

As mentioned in Section 5.2.1, one of the main factors in determining the response of Mg alloys is the initial texture of the specimen and its evolution with loading. Sometimes, a difference in initial texture can greatly affect the overall behavior of the material. On the other hand, the change in the loading direction for a textured material can have similar effects on material response as that of a different initial texture. To study the effect of slip systems for a sample with different distribution of grain orientations with respect to the loading axis, a series of tension simulations are performed. The simulations use a texture corresponding to hot-rolled plate, and are loaded in the RD.

These samples are simulated using a cube with the ratio of length to width to height of 25 to 6 to 3.2 (compatible with the experiments reported in the literature and used for comparison purposes in Section 5.4.3). Due to symmetry, only one-eighth of the sample is modeled. The modeled specimen is divided into 1440 elements of C3D8R type; each of which represents one single grain. The $\{0\,0\,0\,2\}$ and $\{1\,0\,\bar{1}\,1\}$ pole figures of the initial texture are plotted in Figs. 5.20(a) and 5.20(b), respectively. The textures show basal texture (average c-axis–normal to basal planes–parallel to ND), which is typical of Mg alloy rolled-plates (e.g. Roberts, 1960, Agnew *et al.*, 2001, Yukutake *et al.*, 2003, Styczynski *et al.*, 2004). The 1440 required sets of Euler angles are obtained using the TexTools software. The simulations are performed up to the divergence point, which is usually the strain at which the localization reaches a threshold in one or some of the elements (see Chapter 6) at a nominal strain rate of 0.005 s^{-1}. The stress-strain curves as well as the r-values are obtained for the whole deformation range. The r-value, which indicates the degree of anisotropy, is a measure of the resistance of the sheet to thinning, and can be defined as follows,

$$r = \frac{\varepsilon_w}{\varepsilon_t};\quad r = \frac{\varepsilon_{TD}}{\varepsilon_{ND}} \text{ for loading in the RD};\quad r = \frac{\varepsilon_{RD}}{\varepsilon_{ND}} \text{ for loading in the TD};} \qquad \text{Eq. 5.2}$$

where ε_w represents the strain in the width direction and ε_t is the through thickness strain. When deformation is isotropic, the r-value is one. With the introduction of anisotropy in deformation, r-values move away from one. High r-values are reported to

promote good deep-drawability in many metals (Cheng *et al.*, 2007). However, this observation is not ubiquitous among all classes of metals. Strong variations in r-value within the sheet plane (i.e. in-plane or planar anisotropy) can cause forming problems such as earing (e.g. Inal *et al.*, 2000; Raabe and Roters, 2004).

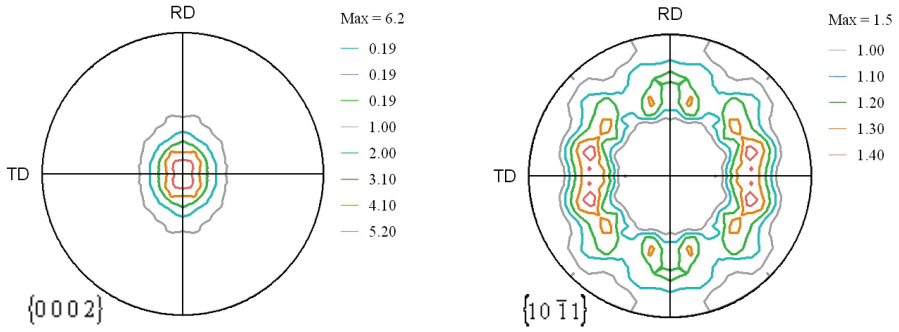

Figure 5.20 Initial texture of the specimens (hot-rolled plate)

By convention, r-value measurements are usually performed on samples strained to an elongation of 20% or at the limit of uniform elongation, whichever is smaller. In this study, the r-values are obtained directly from the results of simulation and are available for the whole range of strain. To take into account the inhomogeneity of deformation through the length of the specimen, the r-values are obtained by using the average values of strain over all the elements in the specimen. This method basically takes into account the variation of r-value along the length of the specimen. For most of the simulations, the r-value increases with strain in the loading direction, attains a maximum at a relatively low strain, and then drops gradually. In Section 5.4, results are compared with experimental ones, and, therefore, for consistency, the r-values are calculated at a strain of 0.11.

The effect of change in the slip resistance of different systems on the stress-strain curves and the calculated r-values are shown in Figs. 5.21 to 5.28. Figures 5.21 and 5.22 show the effects of basal<a> slip systems. As can be seen in Fig. 5.21, the change in stress level as a result of the change in slip resistance of basal<a> system is negligible. Even a decrease in the slip resistance from 50 MPa to 0.4 MPa does not have a significant effect on the stress level. Nevertheless, the higher activity of basal<a> increases the strain level at which localization occurs in the material, as the localization strain increases from about

0.45 to 0.58. Looking at Fig. 5.22, it seems that the change in the activity of basal systems can change the r-values significantly; however, this is only true for the slip resistance values greater than 10 MPa. In the more realistic range of basal<a> slip resistance values, between 0.4 MPa and 10 MPa, the change in r-values is again negligible.

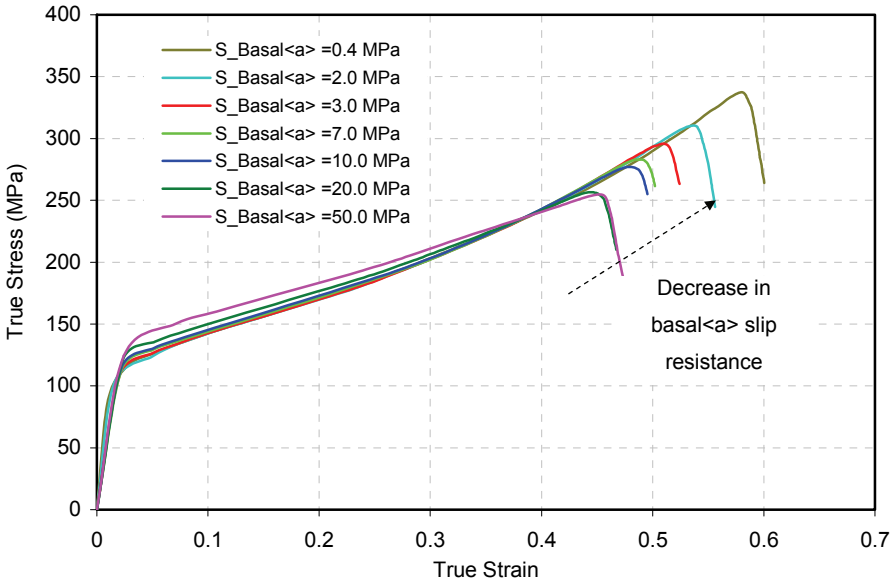

Figure 5.21 The effect of change in basal<a> slip resistance on the tension stress-strain curve; $s_{prism<a>} = 100$ MPa, $s_{pyram<a>} = 100$ MPa, $s_{pyram<c+a>} = 100$ MPa

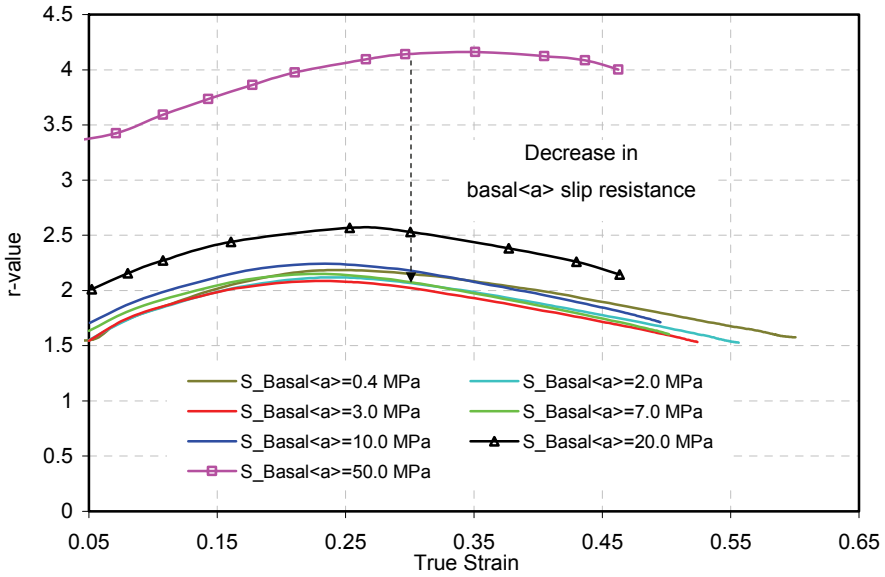

Figure 5.22 The effect of change in basal<a> slip resistance on r-values; $s_{prism<a>} = 100$ MPa, $s_{pyram<a>} = 100$ MPa, $s_{pyram<c+a>} = 100$ MPa

Unlike the basal<a> slip system, the change in the slip resistance of prismatic<a> slip system can greatly change the mechanical response in simulations (Figs. 5.23 and 5.24). The change in slip resistance of prismatic<a> slip system changes the stress level (Fig. 5.23) and r-values (Fig. 5.24), and can shift the threshold of localization (Fig. 5.23) significantly. These results are obtained at such slip resistance values for prismatic<a> that are comparable to the ones for pyramidal<c+a> slip systems.

The decrease in the prismatic<a> slip resistance from 100 MPa to 5 MPa (while $s_{pyram<c+a>} = 15$ MPa and $s_{basal<a>} = 2$ MPa) decreases the level of stress from 35 MPa to about 13 MPa at a strain of 0.05, and increases the localization strain from 0.05 to about 0.6. In addition, unlike the effect of basal systems, the decrease in the slip resistance of prismatic systems increases the r-values. Agnew and Duygulu (2005), using a visco-plastic self-consistent (VPSC) model, also showed that a decrease in the ratio of prismatic<a> to basal<a> slip resistances increases r-value. For this loading condition, the crystal c-axis is, on average, normal to the loading direction; therefore, it is expected that the effect of non-basal systems become more dominant in determining the overall macro response of the material.

The next family of slip systems considered is the pyramidal<a> slip system. The effects of change in the slip resistance of pyramidal<a> slip systems on the stress level (Fig. 5.25), r-values (Fig. 5.26), and the change in the localization strain (Fig. 5.25) are much like those of prismatic slip systems. However, the major effect of the change in the value of pyramidal<a> slip resistance occurs in the strain range from approximately 0.03 to 0.05. In this range, the decrease in slip resistance from 300 MPa to 20 MPa reduces the level of stress by about 50%, and doubles the r-values, whereas for the strain values out of this range, the difference between the curves for different values of slip resistance is much less. Less difference outside this range of strains is a result of reorientation of crystals in this range, which brings the crystals to such orientations which are less favorable for the activity of pyramidal<a> slip system.

The last slip system considered is the pyramidal<c+a> slip system. Previous results indicated a strong effect from this slip system on the response of the material. Two sets of simulations are done with the goal of excluding the effect of slip resistance of prismatic<a> on the results, one with $s_{prism<a>} = 100$ MPa (results are not presented here due to similarity) and the second one with $s_{prism<a>} = 50$ MPa (Figs. 5.27 and 5.28). For both series, it was observed that the decrease in the slip resistance of pyramidal<c+a> slip system causes a significant decrease in the level of stress and r-values. This, again, supports the higher activity of pyramidal<c+a> slip systems at higher temperatures. The current results, obtained by using the CPFE model, confirm that an increased activity of non-basal<c+a> dislocations provides a consistent explanation for the observed changes in the anisotropy with increasing temperature.

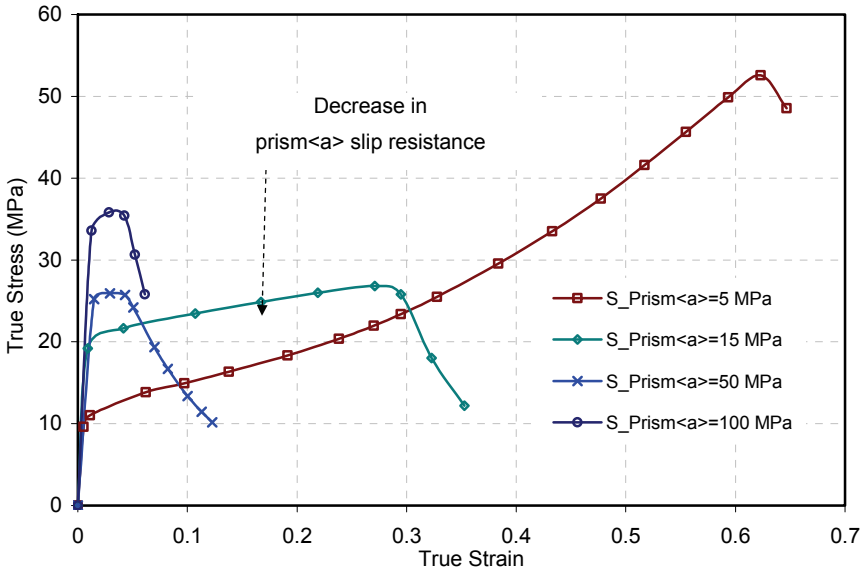

Figure 5.23 The effect of change in prismatic<a> slip resistance on tension stress-strain curve; $s_{basal<a>} = 2$ MPa , $s_{pyram<c+a>} = 15$ MPa

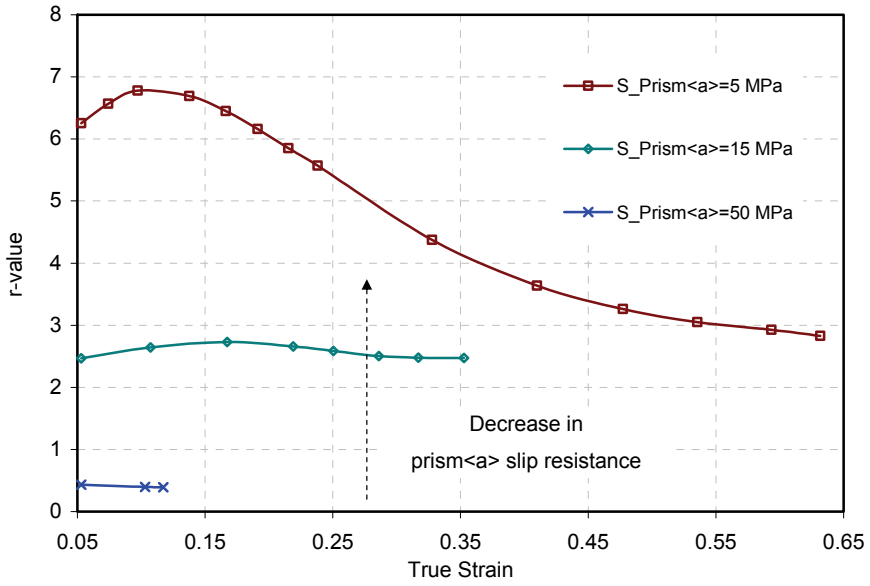

Figure 5.24 The effect of change in prismatic<a> slip resistance on r-values;

$s_{basal<a>} = 2$ MPa , $s_{pyram<c+a>} = 15$ MPa

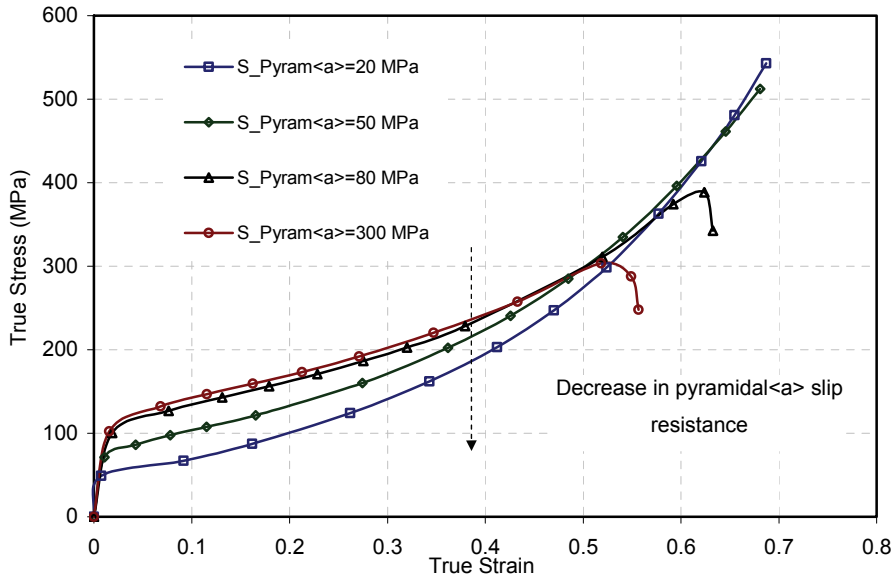

Figure 5.25 The effect of change in pyramidal<a> slip resistance on the tension stress-strain curve;

$s_{basal<a>} = 2$ MPa , $s_{prismatic<a>} = 100$ MPa

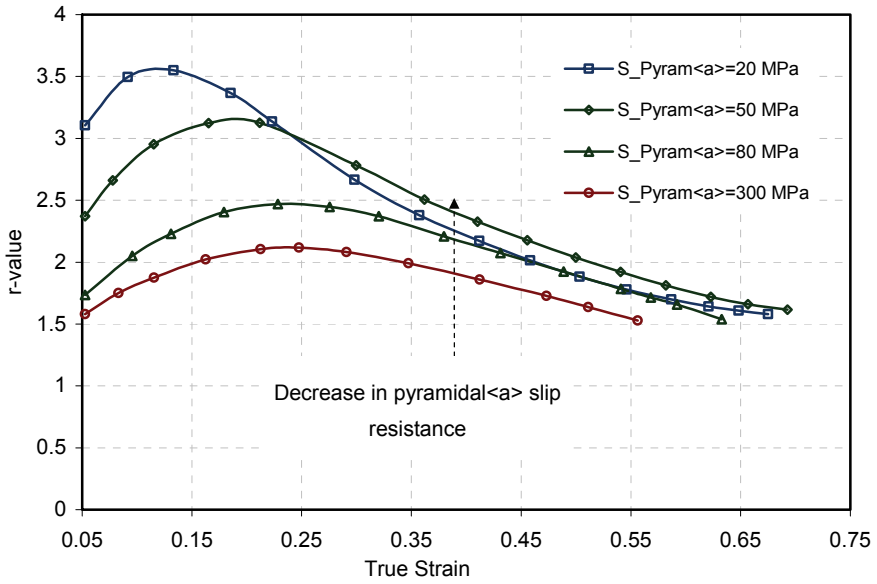

Figure 5.26 The effect of change in pyramidal<a> slip resistance on r-values;

$s_{basal<a>} = 2$ MPa , $s_{prism<a>} = 100$ MPa

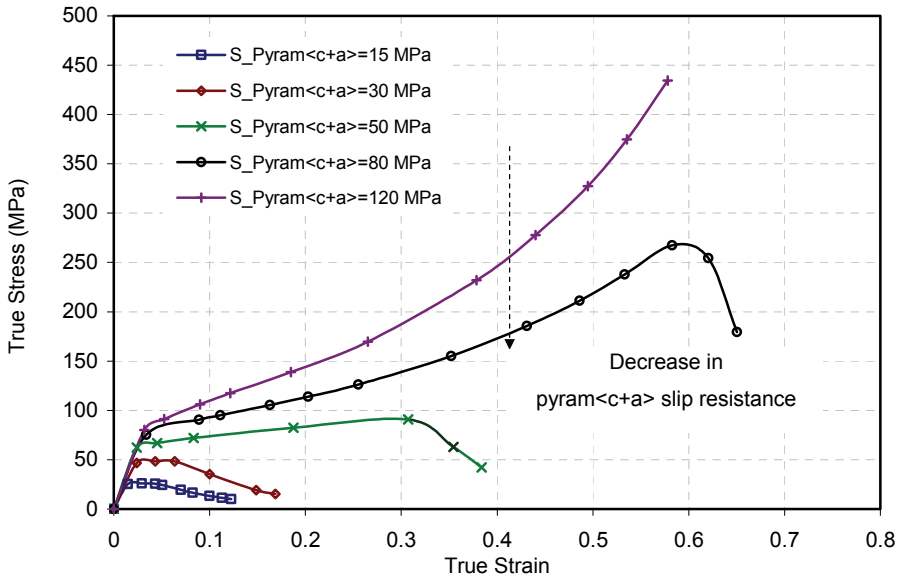

Figure 5.27 The effect of change in pyramidal<c+a> slip resistance on the tension stress-strain curve;

$s_{basal<a>} = 2$ MPa , $s_{prism<a>} = 50$ MPa , $s_{pyram<a>} = 100$ MPa

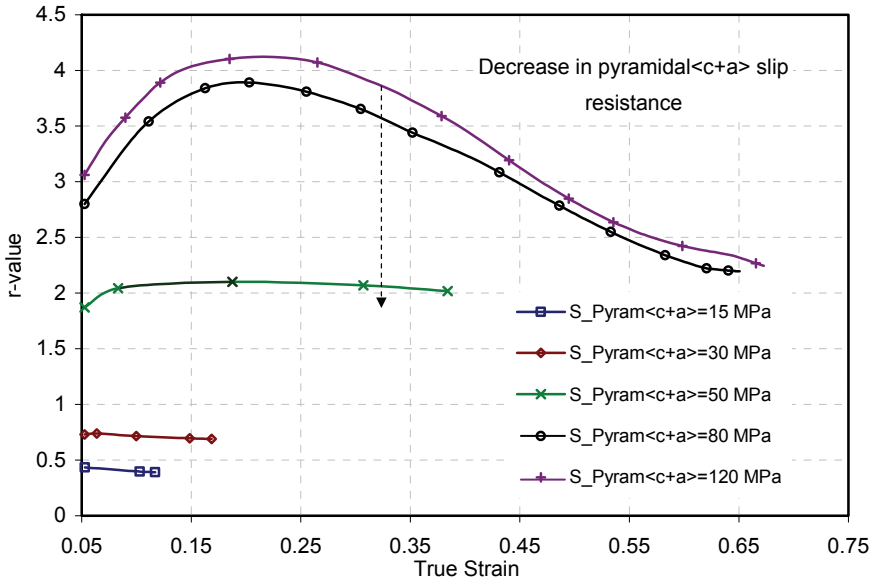

Figure 5.28 The effect of change in pyramidal<c+a>slip resistance on r-values;

$s_{basal<a>} = 2$ MPa , $s_{prism<a>} = 50$ MPa , $s_{pyram<a>} = 100$ MPa

5.3 STRAIN-RATE SENSITIVITY IN Mg ALLOYS

In this section the concept of strain-rate sensitivity and its effect on the mechanical response of Mg alloys at the micro- and macro-scale are studied. First, in Section 5.3.1, the definition of strain-rate sensitivity at the macro-scale is presented. In the following section, strain-rate sensitivity on the micro-scale is defined, and its relation with the macro-scale definition is investigated. In Section 5.3.3, the concept of reference shearing increment and its relation with the strain-rate sensitivity is explained. Section 5.3.4 is devoted to the effect of strain-rate sensitivity on the slip system activity. Finally, in Section 5.3.5, the strain-rate sensitivity values for Mg and Mg alloys are discussed.

5.3.1 STRAIN-RATE SENSITIVITY ON THE MACRO-SCALE

In studying the mechanical behavior of metals at higher temperatures, the two parameters

$$Q = \partial \ln \dot{\varepsilon}^{p}(\sigma,\theta)/\partial(-1/k\theta), \qquad \text{Eq. 5.3}$$

with k denoting Boltzmann's constant, θ indicating temperature, $\dot{\varepsilon}^{p}$ defining the plastic strain rate, and

$$m = \left(\partial \ln \dot{\varepsilon}^{p}\left(\sigma,\theta\right)/\partial \ln \sigma\right)^{-1}, \qquad \text{Eq. 5.4}$$

called the "activation energy" and the "strain-rate sensitivity", respectively, are used to interrelate $\dot{\varepsilon}^{p}, \theta,$ and σ (Kocks *et al.*, 1975). Compatible with Eq. 5.4, when the elastic part of the strain rate is small , the increase in flow stress with strain rate at a constant strain can be approximated by

$$\sigma = C\dot{\varepsilon}^{m}, \qquad \text{Eq. 5.5}$$

where C is a constant or a function of strain (Hosford and Caddell, 1993). Considering this relation, the flow stress values at two different strain-rates at the same strain are compared as follow,

$$\frac{\sigma_2}{\sigma_1} = \left(\frac{\dot{\varepsilon}_2}{\dot{\varepsilon}_1}\right)^{m}, \quad \text{or} \quad m = \ln\left(\frac{\sigma_2}{\sigma_1}\right) \Big/ \ln\left(\frac{\dot{\varepsilon}_2}{\dot{\varepsilon}_1}\right), \qquad \text{Eq. 5.6}$$

If σ_2 is not much greater than σ_1, then

$$\frac{\Delta\sigma}{\sigma} \approx m \ln \frac{\dot{\varepsilon}_2}{\dot{\varepsilon}_1} = 2.3\ m \log \frac{\dot{\varepsilon}_2}{\dot{\varepsilon}_1}. \qquad \text{Eq. 5.7}$$

As defined, m is a measure of the strain-rate sensitivity of the material which shows how the material response changes with change in strain-rate; for example, if m=0.01, an increase in strain-rate by a factor of 10 increases the level of stress by approximately 2%; for m=0.15 this increase would be approximately 40%.

To determine m-values from experiments, two different methods can be used (depending on the available data). In the first method, continuous stress-strain curves are obtained at different strain rates, and then the stress values are obtained at a specific strain. Then Eq. 5.6b is used for determining m-values. In the second method, an abrupt jump is made in the strain-rate during a tension test. The corresponding level of stress and the change in the stress value, $\Delta\sigma$, are subsequently used in Eq. 5.7 for obtaining m. At higher strain rates, usually the strain hardening is greater, which results in higher values of m. Thus, the first method gives higher values of strain-rate sensitivity than the second method

which uses the flow stresses for the same structure (Hosford and Caddell, 1993). The second method has the advantage of using only one specimen for different strain rates.

5.3.2 STRAIN-RATE SENSITIVITY ON THE MICRO-SCALE

In crystal plasticity modeling, different assumptions can be made for the evolution equation of the shearing increments on different slip systems. One commonly used relation of this type, introduced in Chapter 3, is the following power law utilized for evolution of plastic shearing rates on slip systems (e.g. Hutchinson, 1976; Asaro and Needleman, 1985; Toth *et al.*, 1988; Neale *et al.*, 1990; Van de Giessen *et al.*, 1992)

$$\dot{\gamma}^{\alpha} = \dot{\gamma}_0 \left| \frac{\tau^{\alpha}}{s^{\alpha}} \right|^{1/m} \operatorname{sign}\left(\tau^{\alpha}\right), \qquad \text{Eq. 5.8}$$

where $\dot{\gamma}^{\alpha}$ is the shearing increment on slip system α, $\dot{\gamma}_0$ is the reference shearing increment, τ^{α} is the resolved shear stress on slip system α, s^{α} is the slip resistance value of slip system α, and m is the strain-rate sensitivity on the micro-scale.

The relation between the macro-scale values of strain rate sensitivity (Eq. 5.5) and the micro ones (Eq. 5.8), which are assumed in the simulations for the shearing rates of different slip systems, has rarely been discussed in the literature. However, it seems that there is a direct link between the rate sensitivity on the macro- and micro-scales. Asaro (1983) assumed the same value for microscopic and macroscopic strain-rate sensitivities. Kalidindi and Anand (1994) also took the slip rate sensitivity parameter, m, to be equal to the macroscopic strain rate sensitivity, and determined its value from a strain rate jump experiment. The validity of this assumption has not been directly examined in the above mentioned sources. In order to verify this assumption, simulations are done using the CPFE model; during which the obtained macroscopic values of m are compared to the ones which are assumed for the slip system activity. Simulations are done for both multiple stress-strain curves at different strain rates and the strain rate jump test. Material parameters are assumed as defined in Section 3.2. The macroscopic values of m are obtained using Eq. 5.6.

Table 5.3 shows a summary of the results obtained in these tests. It can be seen that although the obtained value of m at the macro-level increases with the increase in the strain, the difference between the obtained macro values and the assumed micro ones is, in all cases, less then 6.2%. In the strain-rate jump test, on the micro-level, a value of 0.14 is assumed for m in the simulation. The jump in the strain-rate is applied at a strain of 0.11 from 0.0001 s^{-1} to 0.01 s^{-1}. Using the obtained stress-strain curve (Fig. 5.29), the macroscopic value of m for the strain-rate jump test is calculated to be 0.1386 (using Eq. 5.6), which is less than 1% difference from the assumed value of m on the micro-level. In short, it can be concluded that in the crystal plasticity simulations and, in particular, in the employed CPFE model, the strain-rate sensitivity parameter can be taken to be equal to the macroscopic strain-rate sensitivity values obtained from the experiments with reasonable confidence.

Table 5.3 Comparison of the computed macroscopic SRS values vs. values assumed in simulations

Test Type	ε Strain	σ_1 (MPa)	σ_2 (MPa)	$\dot{\varepsilon}_1$ (1/s)	$\dot{\varepsilon}_2$ (1/s)	m (micro/ assumed)	m (macro/ computed)	Difference %
Compression multi-curve	0.1	28.3	58.3	0.0001	0.01	0.1600	0.1568	2.00
Compression multi-curve	0.3	31.6	67.5	0.0001	0.01	0.1600	0.1650	3.13
Tension multi-curve	0.1	38.1	79.0	0.0001	0.01	0.1600	0.1583	1.04
Tension multi-curve	0.3	74.3	162.4	0.0001	0.01	0.1600	0.1699	6.17
Compression (Jump Test)	0.11	28.2	53.3	0.0001	0.01	0.1400	0.1386	0.97

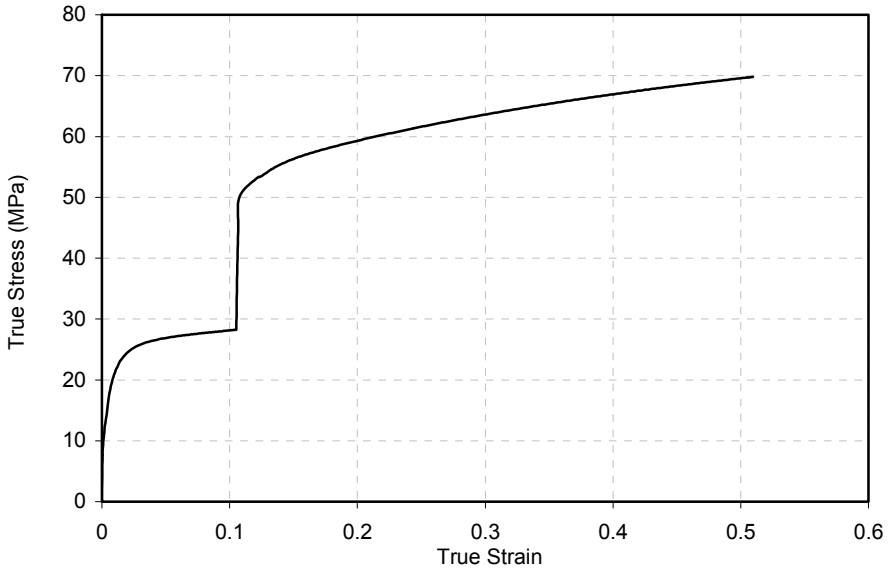

Figure 5.29 Change in the stress-level with the change in strain-rate from 0.0001 s^{-1} to 0.01 s^{-1}

5.3.3 STRAIN RATE SENSITIVITY (SRS) AND REFERENCE SHEARING RATE (RSR)

Different approaches can be followed for simulating the change in the activity of slip systems in Mg alloys at higher temperatures. One approach (used in Section 5.4) is to define the slip resistance values of different slip systems as functions of temperature (and strain-rate). An alternative approach that has been used in the literature is to consider changes in the evolution equation of shearing increments on slip systems with change in temperature (and strain-rate). In particular, the change in the reference shearing rate and strain-rate sensitivity has been used.

The effect of change in the strain rate sensitivity (SRS), m, and the reference shearing rate (RSR), $\dot{\gamma}_0$, has not been addressed fully in the literature. In particular, the discussions on the definition and the effect of the reference shearing rate have rarely been presented. Hutchinson (1976) for the first time introduced Eq. 5.8 for the shearing increments on the slip systems. In the definition of $\dot{\gamma}_0$, he states that "$\dot{\gamma}_0$ is any convenient reference creep-rate which could, without loss in mathematical generality, be taken to be unity (s^{-1}) but will be carried along explicitly for ease of application of

subsequent results." Several researchers have used this equation with different values of the RSR. Very frequently RSR is taken to be 0.001 s^{-1} without sufficient justification.

To study the effect of change in the SRS and RSR values and their relation with the effect of strain-rate, a series of simulations are performed. Compression tests on magnesium specimens at different strain-rates are simulated, employing two different values for SRS and RSR ($m = 0.14$ and 0.05; $\dot{\gamma}_0 = 0.001\ s^{-1}$ and $\dot{\gamma}_0 = 0.01\ s^{-1}$). The initial texture of the specimens is assumed to be that of a hot-rolled plate, with loading in the rolling direction (RD). The stress-strain curves obtained are shown in Figs. 5.30 and 5.31.

There are some observations regarding the effects of both the SRS and the RSR. First, it can be seen that, as expected, the decrease in the SRS value from 0.14 to 0.05 decreases the effect of strain rate in changing the level of stress. In other words, it reduces the strain rate sensitivity of the material. Second, the reduction in m-value decreases the localization strain, which is in agreement with the theory behind the SRS. Hosford and Caddell (1993) state that high values of SRS promote large elongations without extensive localization.

Regarding the role of RSR, it can be seen in Fig. 5.30 that the curves are basically spread about the curve with the stain rate of $\dot{\varepsilon} = 0.001\ s^{-1}$ (which is equal to the reference shearing rate); and with the increase or decrease in m, only the difference between curves changes. Therefore, when m approaches zero (and material becomes practically rate-independent), the stress-strain curve will be that of $\dot{\varepsilon}$ corresponding to the RSR. This behavior is repeated in Fig. 5.31 where the RSR is 0.01 s^{-1}, and the curves are spread about the curve for $\dot{\varepsilon} = 0.01\ s^{-1}$.

It should also be noted that, without any change in other material parameters, the simulated behavior of the material at $\dot{\varepsilon} = 0.001\ s^{-1}$ when $\dot{\gamma}_0 = 0.001\ s^{-1}$ (Fig. 5.30) is the same as the simulated behavior of material at $\dot{\varepsilon} = 0.01\ s^{-1}$ when $\dot{\gamma}_0 = 0.01\ s^{-1}$ (Fig. 5.31). Thus, it can be concluded that the reference shearing rate should be interpreted as the reference strain-rate at which material constants (such as slip resistances) are determined.

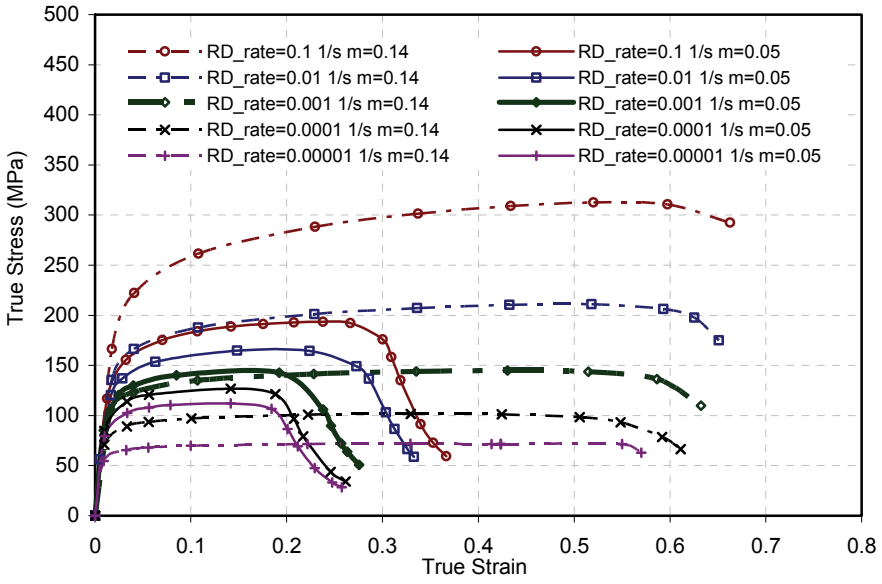

Figure 5.30 Change of mechanical behavior with change in SRS and strain-rate $\dot{\gamma}_0 = 0.001\ s^{-1}$

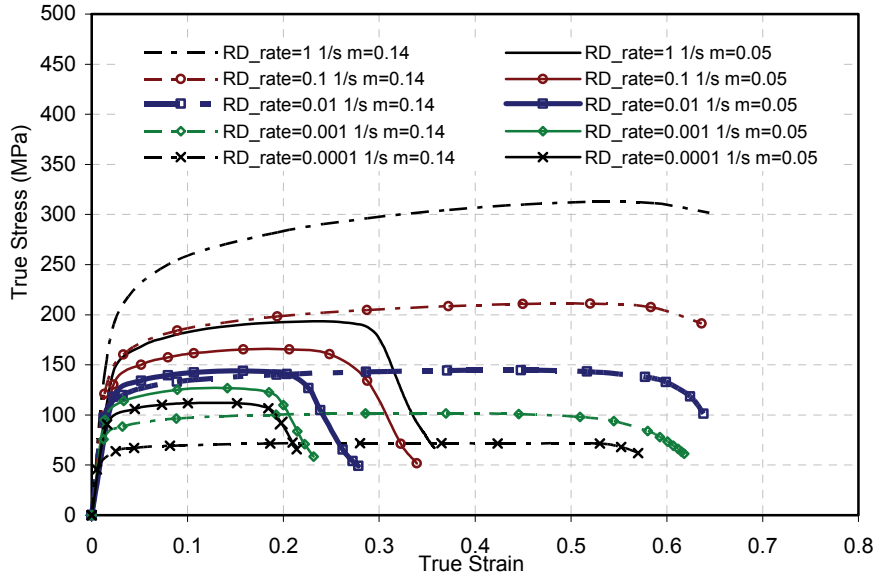

Figure 5.31 Change of mechanical behavior with change in SRS and strain-rate $\dot{\gamma}_0 = 0.01\ s^{-1}$

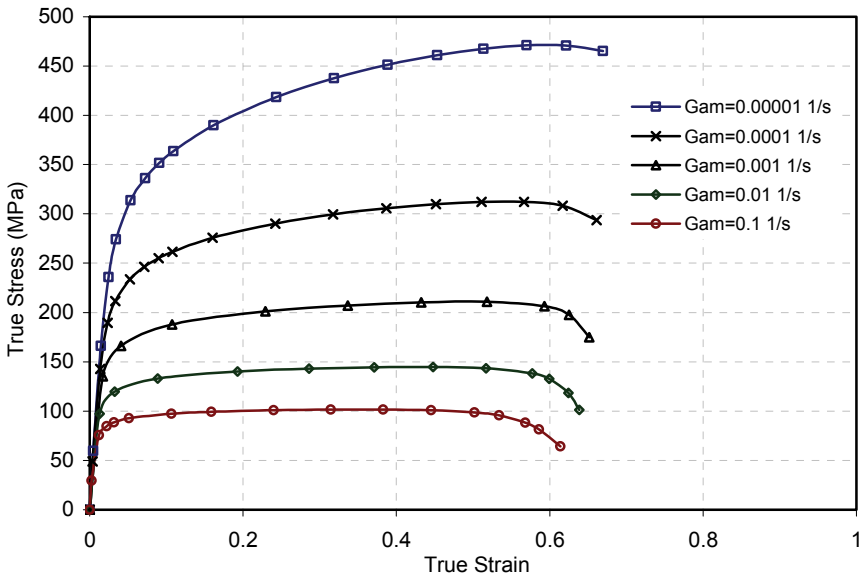

Figure 5.32 The effect of change in the reference shearing rate $\dot{\varepsilon}_{nominal} = 0.01\ s^{-1}$

Finally, it should be mentioned that the change in the RSR can greatly change the computed material behavior. Figure 5.32 shows the change in stress-strain curve with the change in the reference shearing rate from 10^{-6} s^{-1} to 1 s^{-1}. It can be seen that with the decrease in the RSR, the stress level increases. Therefore, an increase in temperature can be modeled by an increase in the RSR. Some researchers have used this concept to model the change in material behavior with temperature by changing the value of $\dot{\gamma}_0$ accordingly (e.g. Lee and Zaverl, 1978; Anand, 1982).

5.3.4 STRAIN-RATE SENSITIVITY AND SLIP SYSTEM ACTIVITY

In FCC materials, the distribution of shear rates is very uneven between the slip systems for low values of m; an increase in strain rate sensitivity promotes a more even spread of the shearing rates (Canova *et al.*, 1988). Therefore, high strain-rate sensitivity values may increase the total number of significantly active slip systems.

To study the effect of strain-rate sensitivity on slip system activity in Mg alloys, tension simulations with different m-values are performed for a single crystal of Mg. The initial orientation of the crystal is defined by an Euler angle set of [170, 20, 110], and the slip resistance value of all slip systems is assumed to be equal (5 MPa). The accumulated shearing increments on different slip system families at a strain of ~0.1 are shown in

Table 5.4 for different values of m. As can be seen in this table, for $m = 0.01$, <c+a> is the only slip system with significant activity. However, with the increase in m, the activity of other slip systems increases, and a more uniform distribution of accumulated shearing increments (Eq. 5.1) is observed. With $m = 1$, all the slip families, are significantly active. Although the slip systems which are active at low m-values and the shearing increment obtained are dependent on the assumed crystal orientation, the obtained results regarding the effect of m are independent of the initial orientation considered. Therefore, for the case of HCP crystals, a higher m-value leads to a more uniform distribution of shearing increments on slip systems which, in turn, leads to less anisotropy in deformation.

Table 5.4 Change in accumulated shearing increments with the change in m;
a Mg single crystal under tension (strain of 0.1)

m	$\left(\gamma^{acc}\right)^{basal}$	$\left(\gamma^{acc}\right)^{prism}$	$\left(\gamma^{acc}\right)^{pyram<a>}$	$\left(\gamma^{acc}\right)^{pyram<c+a>}$
0.01	6.627E-19	0.000E+00	0.000E+00	1.940E-01
0.05	3.989E-06	5.532E-21	2.813E-11	1.969E-01
0.1	5.490E-04	1.641E-11	1.851E-06	2.050E-01
0.2	7.434E-03	1.155E-06	5.608E-04	2.039E-01
0.4	2.730E-02	3.653E-04	9.857E-03	2.007E-01
0.6	4.054E-02	2.430E-03	2.480E-02	1.953E-01
1	5.442E-02	1.058E-02	5.126E-02	1.870E-01

5.3.5 SRS VALUES IN Mg ALLOYS

The SRS value is a material characteristic which varies with many factors including change in the material preparation process. In addition, it changes with the change in temperature and strain rate. In general, for values of m less than 0.01, the material is relatively rate-insensitive. For most metals at room temperature, the magnitude of m is

quite low, between 0 and 0.03 (Hosford and Caddell, 1993), but even the low values of m at room temperature can be important in determining uniform elongation. For pure FCC materials like aluminum, m is on the order of 0.01, and the material response often displays an apparent rate-insensitivity (Asaro, 1983). At hot-working temperatures, m typically rises to 0.10 to 0.20, so rate effects are more significant than at room temperatures. The higher values of strain rate sensitivity at higher temperatures are attributed to the increased rate of thermally activated processes such as dislocation climb and grain boundary sliding. For the superplastic deformation of some materials, m-values as high as 0.7 have been observed (Hosford and Caddell, 1993). Many authors have reported that with an increase in strain-rate, strain rate sensitivity may differ (increase or decrease) depending on whether the material is deformed beyond or below a given strain rate, characteristic for the material.

Agnew and Duygulu (2005) report that the SRS value in magnesium alloy (AZ31) increases with the increase in temperature from about 0.01 at room temperature to about 0.15 at 250°C. However, no consistent set of data has been presented for the SRS values of magnesium alloys at different temperatures and strain-rates to the knowledge of the author. Because of the lack of explicit data on the SRS values in Mg alloys in the literature, SRS values can be obtained from the stress-strain curves reported at different strain rates and temperatures.

Here, the reported stress-strain curves of various Mg alloys at different strain-rates and temperature (Prasad and Sasidhara, 1997) are used. Then, Eq. 5.6 is used for computing the SRS values from the stress-strain curves, at different temperatures and strain-rates. The SRS values are calculated at strain of 0.2. Typical graphs of the change in the SRS values vs. temperature and strain rate are shown in Figs. 5.33 and 5.34, respectively; these curves show the SRS values of pure as-cast magnesium. As can be seen, there exists no clear trend in the change in the SRS values whether with the change in temperature at a certain strain rate or with strain rate at a certain temperature.

To obtain a better overview of the reported results, the SRS values at each strain-rate are obtained by averaging the SRS values at that strain-rate and different temperatures, and are plotted in Fig. 5.33. On the other hand, for each temperature, the average of SRS values at different strain rates is shown in Fig. 5.34. Considering these average curves for

as-cast magnesium, it is seen that with the increase in strain-rate, SRS reaches a maximum and then decreases, which confirms the statement by Hosford and Caddell (1993) in which they indicate that SRS values reach a maximum at a strain rate which is a characteristic of a material. In contrast, with the increase in temperature, a constant increase in SRS values is observed (Fig. 5.34).

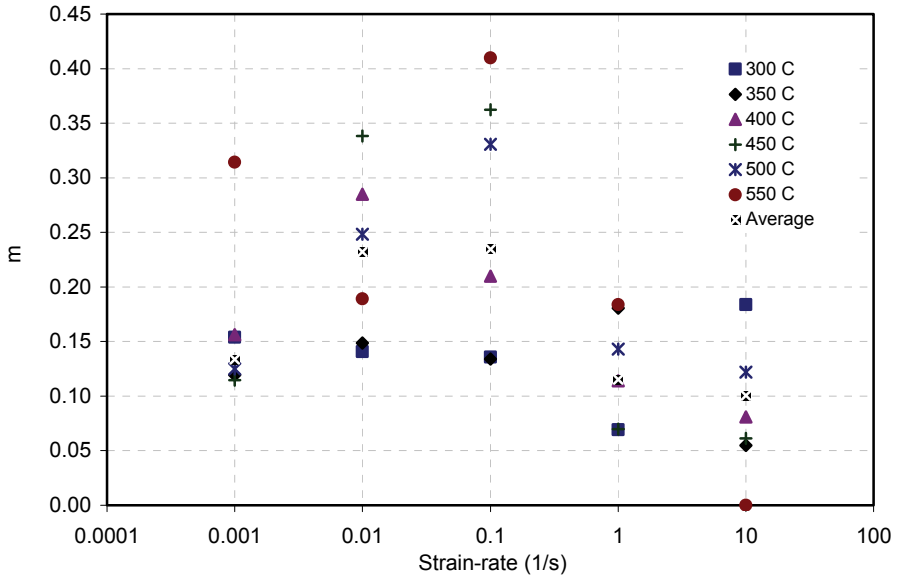

Figure 5.33 Measured change in SRS with strain-rate at different temperatures for as-cast magnesium; values computed from stress-strain curves taken from Prasad and Sasidhara (1997)

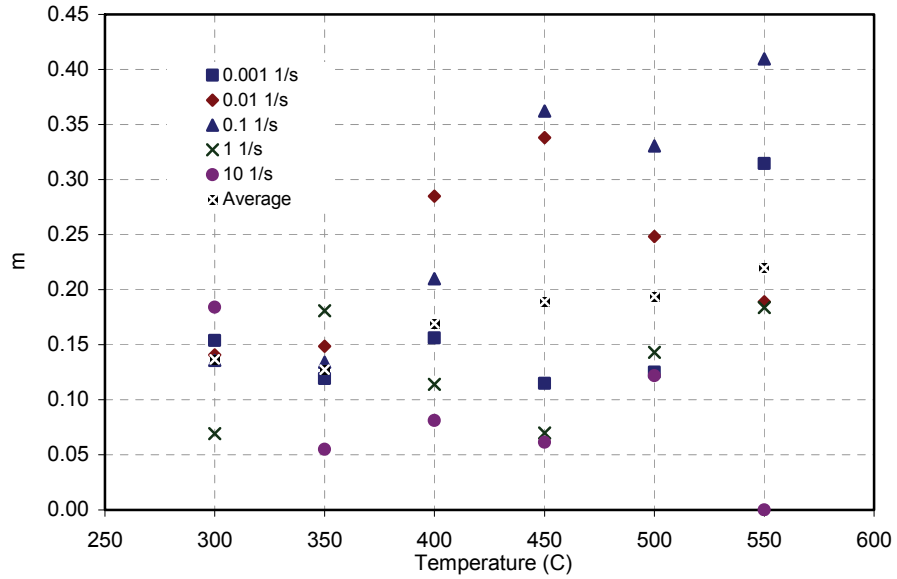

Figure 5.34 Change in SRS with temperature at different strain-rates for as-cast magnesium; values computed from stress-strain curves taken from Prasad and Sasidhara (1997)

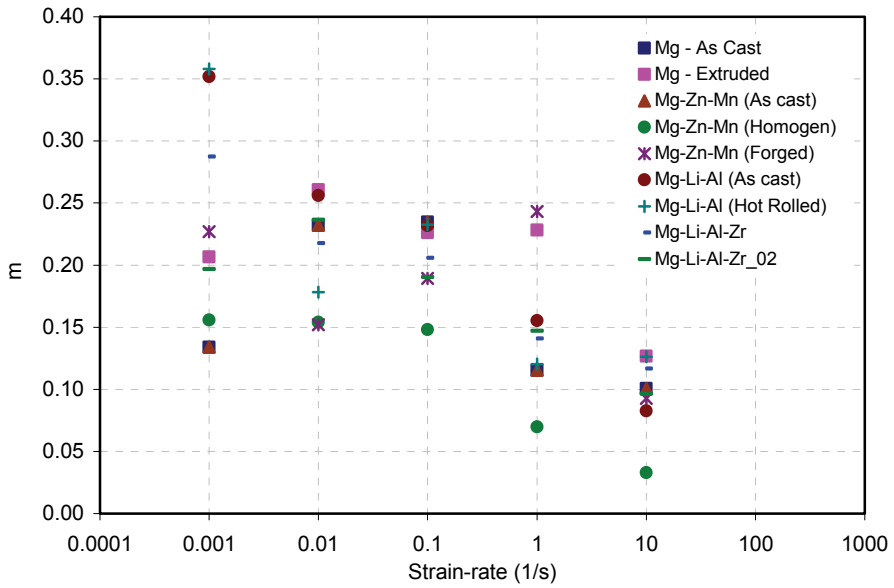

Figure 5.35 Values of SRS (m) for different magnesium alloys vs. strain-rate (average of the values at different temperatures); values computed from stress-strain curves taken from Prasad and Sasidhara (1997)

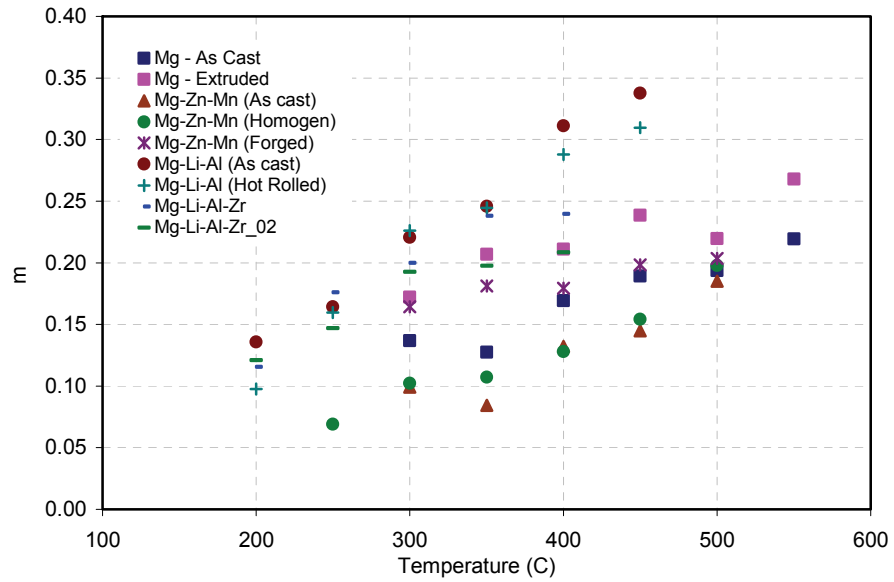

Figure 5.36 Values of SRS (m) for different magnesium alloys vs. temperature (average of the values at different strain-rates); values computed from stress-strain curves taken from Prasad and Sasidhara (1997)

With the method explained above, SRS values were obtained at different strain rates and temperatures for different magnesium alloys. Average curves (values) similar to the ones shown in Figs. 5.33 and 5.34 are obtained for all the considered alloys and are shown in Figs. 5.35 and 5.36. These results in general, confirm the trends obtained regarding the

change in SRS values with the change in temperature and strain-rate for the case of as-cast magnesium.

To state the change in strain-rate sensitivity factor with the change in strain-rate and temperature, the Zener-Hollomon parameter, Z, can be used ($Z = \dot{\varepsilon}\exp(Q/RT)$, where R is the gas constant, Q is the effective activation energy for deformation, and T is the temperature). In magnesium, the effective activation energy for deformation, Q, is actually a function of temperature, but it has been found that an average value of 147,000 J/mol can be employed (Barnett, 2001). It is proposed in this thesis that a linear function of $\ln Z$ may be able to predict reasonably well the change in the SRS values of a specific Mg alloy with change in temperature and strain-rate. This is verified by plotting the experimentally obtained SRS values vs. $\ln Z$. The SRS values collected are plotted for the verification of this assumption (Figs. 5.37 and 5.38). It is seen in these figures that the change in m with change in temperature and strain-rate can be reasonably approximated by a linear function of ln Z. However, this linear function (particularly the slope of the line) changes from one Mg alloy to the others, and also it differs for the same alloy with different preparation histories.

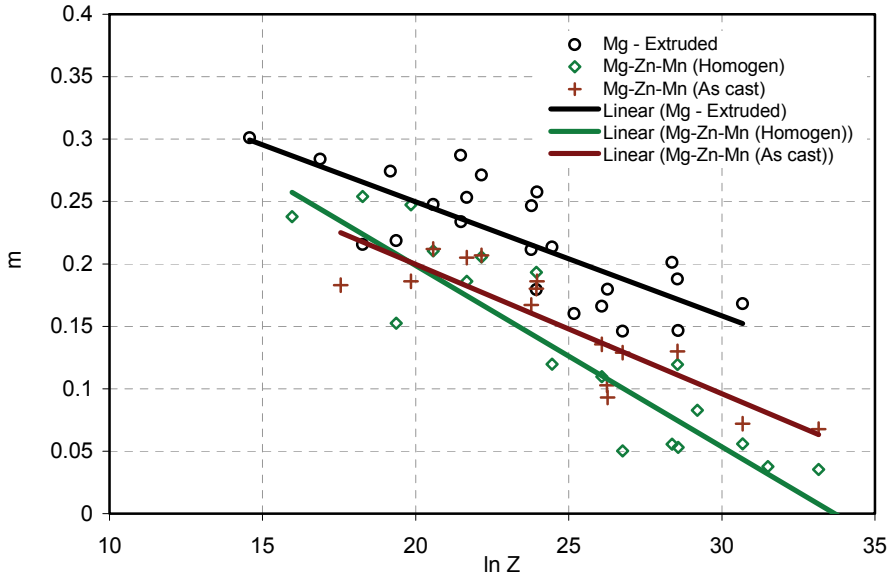

Figure 5.37 Values of SRS (m) for different magnesium and its alloys (Mg-Zn-Mn) vs. ln Z; stress-strain curves taken from Prasad and Sasidhara (1997)

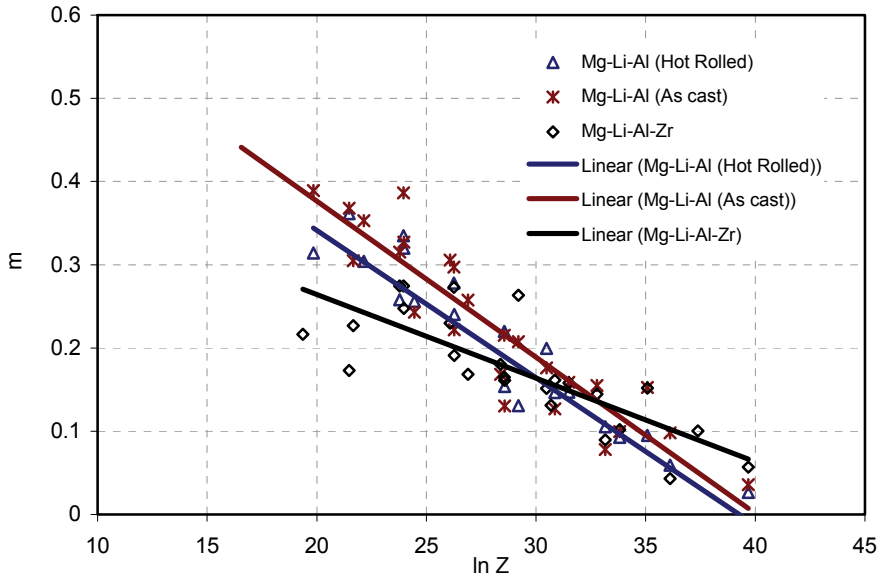

Figure 5.38 Values of SRS (m) for different magnesium alloys (Mg-Li-Al) vs. ln Z; stress-strain curves taken from Prasad and Sasidhara (1997)

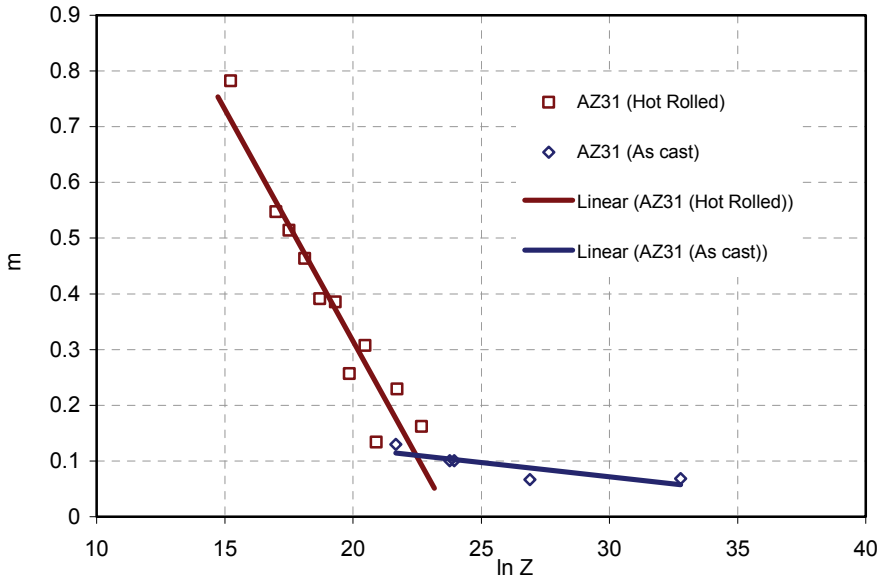

Figure 5.39 Approximating the strain-rate sensitivity as a linear function of lnZ for two Mg alloy AZ31 (Zarandi *et al.*, 2007)

Figure 5.39 shows results of measured SRS values for two different AZ31 Mg alloys (Zarandi *et al.*, 2007), which is the alloy being simulated in this work. In all, it is observed that for all the materials considered, SRS can be approximated by a linear

function of $\ln Z$; the coefficient of the linear relation should be specifically determined for the material being modeled.

5.4 MODELING THE CHANGE IN SLIP RESISTANCE VALUES AND STRAIN-RATE SENSITIVITY

In simulating the mechanical behavior of magnesium alloys at higher temperatures, several issues should be considered. Active slip systems, change in the slip resistances of different slip systems and increase in the strain-rate sensitivity are among the main factors, and will be considered in this section. For the change in slip resistance values with temperature and strain-rate, some new relations are proposed. Also, the change in the strain-rate sensitivity with strain-rate and temperature is taken into account.

5.4.1 MODELING THE CHANGE IN THE SLIP RESISTANCE VALUES

The change in slip resistance values of different slip systems affects the level of activity of each slip system. The trend for this change with increase in temperature can be obtained through a systematic series of simulations, and then by deriving the results on the micro-scale from the ones observed on the macro-scale. The evolution of slip resistance values with temperature should yield reasonable results on the macro-scale not only for the stress-strain curves, but also for the other measurable data such as texture evolution or anisotropic behavior quantified by r-values. In this section, this approach is used, while the trends observed for the effects of slip systems in Section 5.2 are carefully considered.

It is known that in Mg alloys, the increase in ductility with temperature is accompanied by a decrease in the flow stress, an increase in the strain-rate sensitivity, and a decrease in the normal anisotropy. Non-basal<a> slip mechanisms were observed at high temperatures (>180^{o}C) by some investigators (Wonsiewicz and Backofen, 1967), and, thus, were widely held responsible for the good elevated temperature ductility of magnesium and its alloys. Decreasing the slip resistance ratio between non-basal<a> and basal<a> slip systems for elevated temperature simulations seems justified by slip resistance data obtained from single crystal studies of Reed-Hill and Robertson (1957). However, as mentioned in Section 5.2, this leads to an increase in r-value, and the

experimental results show a decrease in r-values with temperature, not an increase. Therefore, other mechanisms such as non-basal dislocations with <c+a> direction should be active within magnesium. Concurrent with the increase in <c+a> activity, there is a drop in r-value along both the RD and TD.

During recent years, different researchers have proposed different values of slip resistance for slip systems active in magnesium alloys at room and warm temperatures. Some of these values are an order of magnitude higher than the others. Barnett (2003) proposed linear relations between the slip resistance values of AZ31 slip systems and the natural logarithm of the Zener-Hollomon parameter. He concludes that using a Taylor-type model together with the following relations for the slip resistances of different slip systems yields reasonable results, regarding the flow curves, over a range of temperatures from 150°C to 450°C,

$$\begin{aligned} s^{\alpha}(0) &= s_{basal<a>} = 5\ (\text{MPa}), && \alpha = 1,\ 2,\ 3; \\ s^{\alpha}(0) &= s_{prism<a>} = 2.5\ln(Z) - 38\ (\text{MPa}), && \alpha = 4,\ 5,\ 6; \\ s^{\alpha}(0) &= s_{pyram<c+a>} = 2.1\ln(Z) - 32\ (\text{MPa}), && \alpha = 7,..,\ 12. \end{aligned} \qquad \text{Eq. 5.9}$$

As mentioned earlier, it seems that different modeling methods yield different approximations of the slip resistance values of slip systems in Mg alloys and their evolution with temperature. A series of simulations is done using the CPFE method to examine the proposed relations by Barnett for the slip resistance values (Eq. 5.9). To compare the results and validate the relations, simulations are performed to model the experimental work of Agnew and Duygulu (2005). Tension simulations are performed using samples with a texture of hot-rolled plate, loaded in the transverse direction. It should be noted that the loading conditions simulated in this section, i.e. tensile loading on specimens cut in the rolling direction (and transverse direction) of a hot-rolled plate, are the least favored loading conditions for twinning activity. It is known that while an in-plane compression activates twinning, an in-plane extension does not (e.g. Reed-Hill and Abbaschian, 1994; Lou *et al*., 2007).

The obtained results are compared to the experimental results in Fig. 5.40. The results show that using the above-mentioned relations for the evolution of slip resistances in the

CPFE predicts stress levels which are much different from the ones seen in the experiments, and therefore indicates the need for new relations. This shortcoming may be attributed to usage of a Taylor-type model in Barnett's work. It is expected that an averaging scheme, such as the Taylor model, is not able to fully capture the response of the anisotropic Mg single crystals. In addition, the CPFE method, which takes into account the material micro-structure (such as slip system activity) more precisely, should yield more accurate approximations of the slip resistance values.

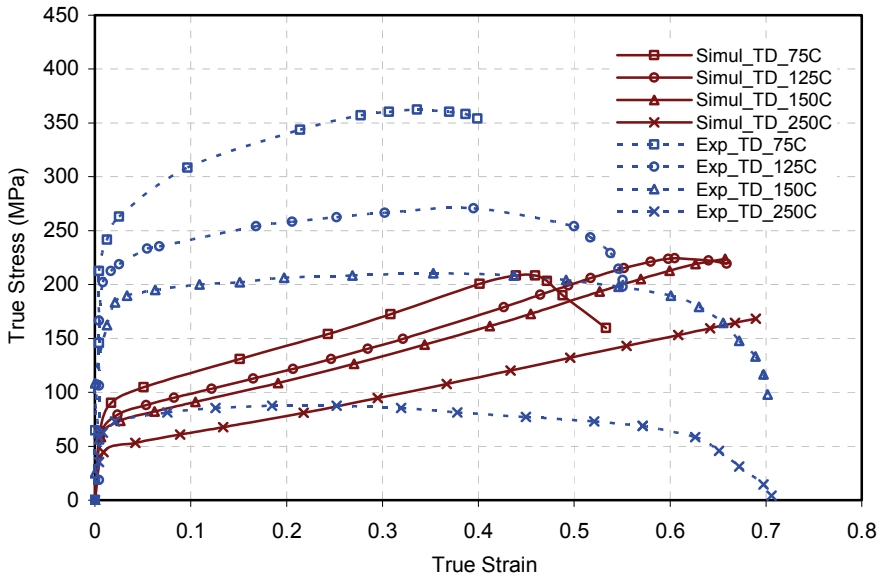

Figure 5.40 Predicted and experimental (Agnew and Duygulu, 2005) stress-strain curves in the TD vs. temperature using Eq. 5.9

To address the above shortcoming, new relations are proposed for the slip resistance evolution of different systems in Mg alloy (AZ31) as a function of Z. In this stage, the pyramidal<a> slip system is assumed to be inactive. By trial and error, new relations are proposed for evolution of the slip resistance values. In doing so, the slip resistance values presented in Table 5.1 are also considered. In addition, the trends observed in Section 5.2 were taken into account. It was observed in that section that the change in the basal<a> slip resistance has less effects on the overall behavior of the material compared to those of the prismatic<a> or pyramidal<c+a> slip systems. Therefore, the value of the basal<a> system over the range of temperatures is considered to remain independent of

temperature and strain-rate and equal to 15 MPa; which is in the range of values previously presented in Table 5.1. The proposed relations are as follows,

$$\begin{aligned} s^{\alpha}(0) &= s_{basal<a>} = 15\ (\text{MPa}), && \alpha = 1,\ 2,\ 3; \\ s^{\alpha}(0) &= s_{prism<a>} = 6.0\ln(Z) - 70\ (\text{MPa}), && \alpha = 4,\ 5,\ 6; \\ s^{\alpha}(0) &= s_{pyram<c+a>} = 8.7\ln(Z) - 200\ (\text{MPa}), && \alpha = 7,..,\ 12. \end{aligned} \qquad \text{Eq. 5.10}$$

The change in the slip resistance values proposed in Eq. 5.10 versus ln Z are shown in Fig. 5.41. It is seen that with the decrease in Z (decrease in strain rate and/or increase in temperature), the pyramidal<c+a> slip system becomes more dominant. For ease of comparison, relations proposed in Eq. 5.9 are also plotted in this figure. The results of simulations employing the above relations are shown and discussed in Section 5.3.3.

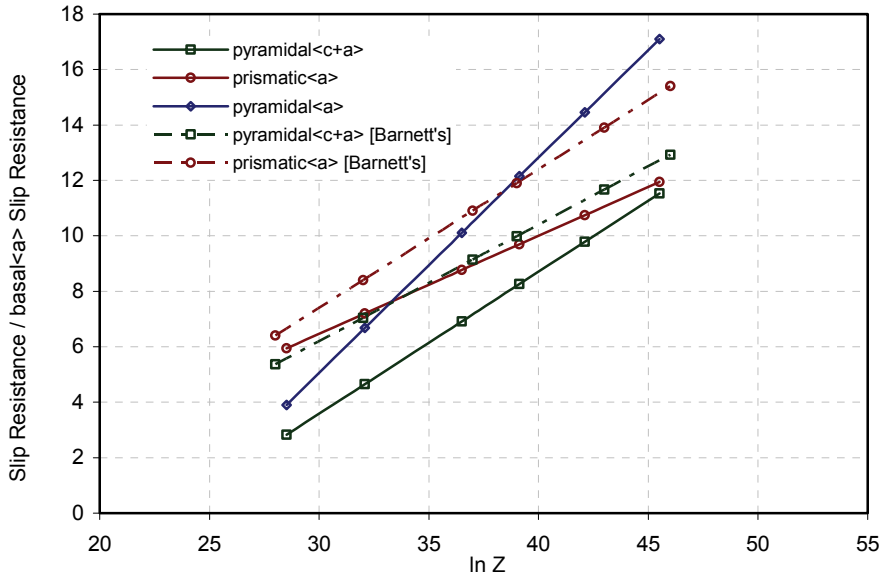

Figure 5.41 Change in the slip resistance values vs. ln Z

Some observations (explained in section 5.3.3) encouraged inclusion of the pyramidal<a> slip system activity, whose slip resistance is taken as,

$$s^{\alpha}(0) = s_{pyram<a>} = 13.2\ln(Z) - 310\ (\text{MPa}), \qquad \alpha = 13,..,\ 18. \qquad \text{Eq. 5.11}$$

The change in the pyramidal<a> slip resistance versus ln Z, Eq. 5.11, is also shown in Fig. 5.41. The results obtained using the proposed relations are presented and discussed in Section 5.4.3.

5.4.2 MODELING THE CHANGE IN THE STRAIN-RATE SENSITIVITY

As mentioned in Section 5.1, an important consideration in modeling the behavior of magnesium alloys at warm temperatures is the change in the strain-rate sensitivity factor. The observed increase in rate sensitivity with temperature is common among many metals. It was proposed in Section 5.3.5 that SRS values of a Mg alloy can be approximated by a linear function of ln Z. As a result, to take into account the change in strain-rate sensitivity, a new relation is proposed, where the increase in strain-rate sensitivity from $m = 0.01$ to 0.15 as the temperature is increased from RT to 200°C (Agnew and Duygulu, 2005) is considered for calibrating the relation. The strain-rate sensitivity factor is stated as a function of strain-rate and temperature (a linear function of $\ln Z$) as

$$m = 0.35 - 0.0068 \ln(Z) \quad . \qquad \text{Eq. 5.12}$$

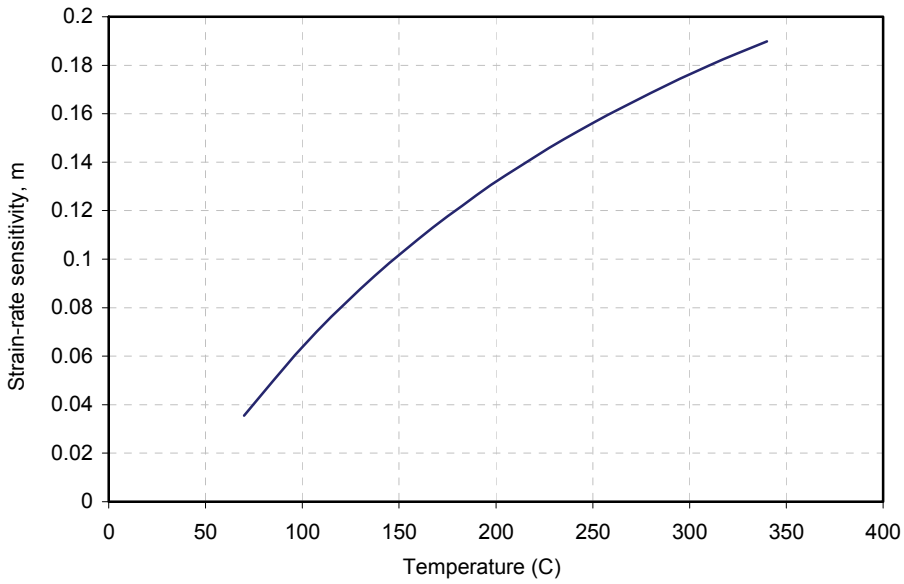

Figure 5.42 Strain-rate sensitivity vs. temperature at strain-rate of 0.001 s^{-1}

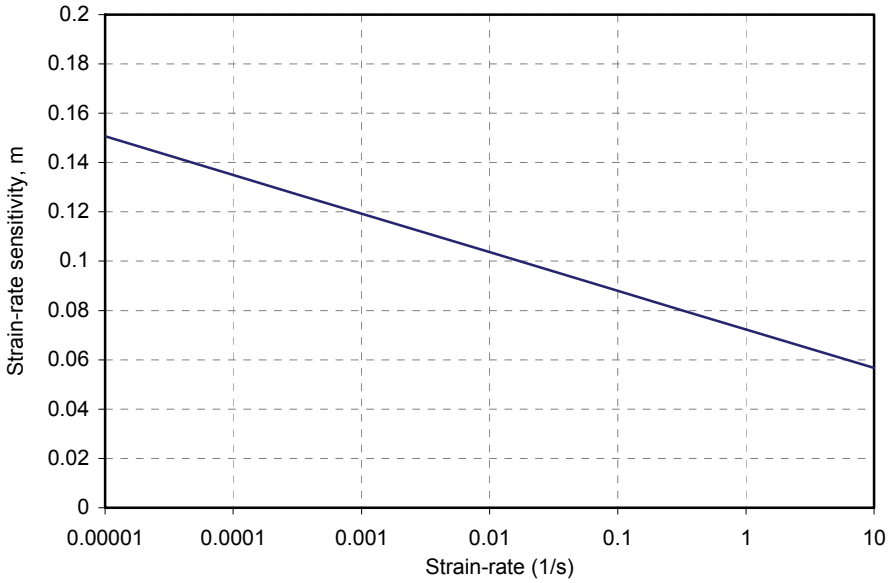

Figure 5.43 Strain-rate sensitivity vs. strain-rate at 160^{o}C

The change in this parameter with the change in temperature (at a nominal strain-rate of 0.001 s^{-1}) can be seen in Fig. 5.42. Also, the dependence of m on the strain-rate is depicted in Fig. 5.43 at a temperature of 160^{o}C. As can be seen in these figures, the proposed strain-rate sensitivity factor increases with the increase in temperature and decrease in strain-rate, which in turn results in a better ductility. At high temperatures and low strain-rates, the material is theoretically super-plastic; at 200^{o}C and strain-rate of 10^{-4} s^{-1}, an elongation of 260% has been measured for magnesium (Duygulu and Agnew, 2003).

5.4.3 RESULTS

The results obtained for the stress-strain curves in the RD and TD and also the r-values in both directions, using the relations proposed in Eqs 5.10 and 5.12, are depicted in Figs. 5.44, 5.45 and 5.46, respectively. For comparison, the experimental results are also shown on the graphs. In the simulations, a nominal strain-rate of 0.005 s^{-1} is used, similar to that in the experiments. The loading conditions simulated in this section, i.e. tensile loading on specimens cut in the RD and the TD of a hot-rolled plate, are the least favored loading conditions for twinning activity. The main twinning system in Mg alloys is active while the crystal is under tension along its c-axis; but the crystals in a rolled plate tend to orient themselves such that their c-axis is aligned normal to the rolling plane, and, thus,

under a tension load in the RD or TD, the crystal has a lower tendency of twinning. Therefore, in-plane tension for samples cut from hot-rolled plates can be simulated only using slip systems with reasonable confidence.

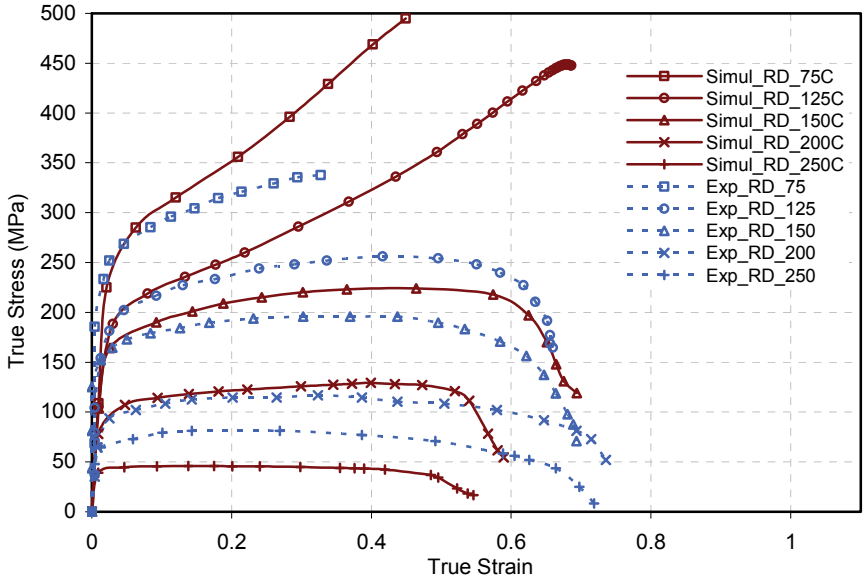

Figure 5.44 Predicted and experimental (Agnew and Duygulu, 2005) stress-strain curves in RD vs. temperature using 5.10

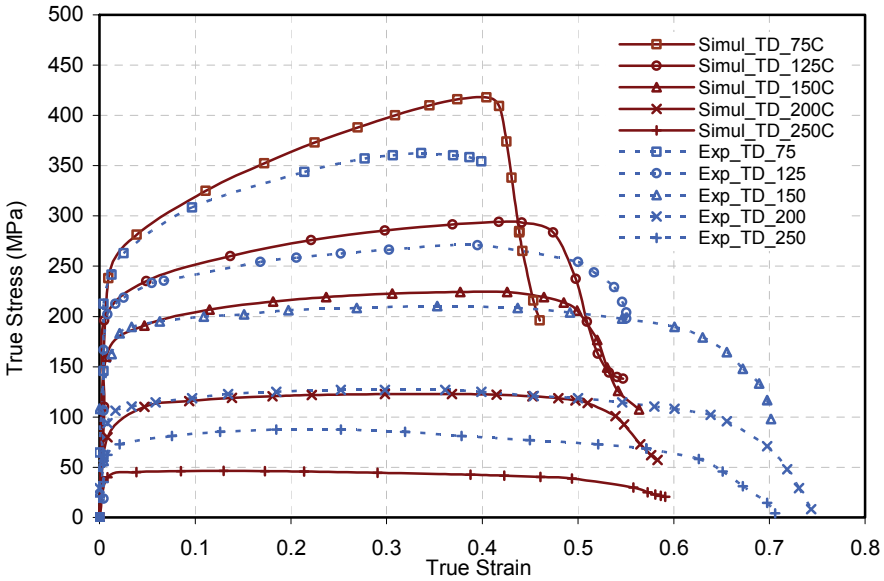

Figure 5.45 Predicted and experimental (Agnew and Duygulu, 2005) stress-strain curves in TD vs. temperature using 5.10

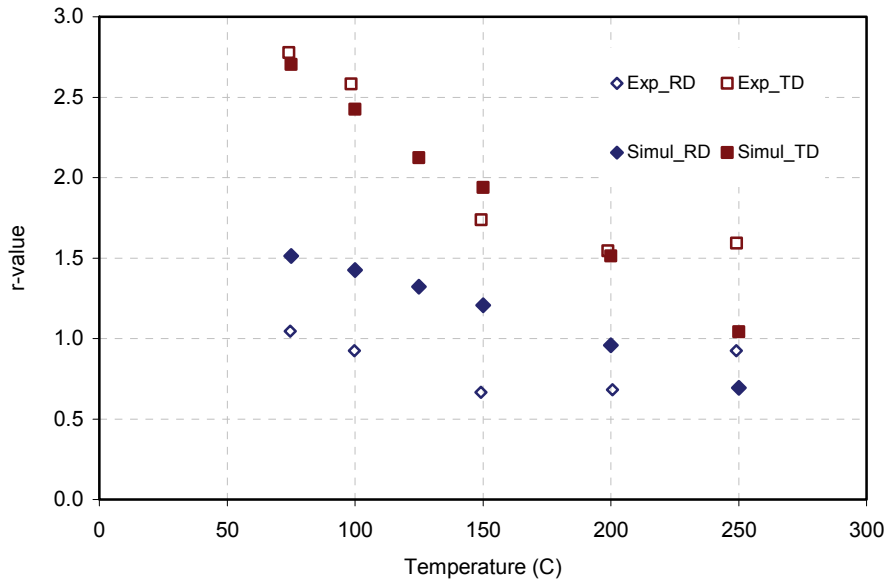

Figure 5.46 Predicted and experimental (Agnew and Duygulu, 2005) r-values in RD and TD vs. temperature using 5.10

There are three main aspects of the material behavior that are captured in these simulations: first, the higher r-values in the TD than the RD; second, the decrease in the level of stress for both the RD and TD with increase in temperature; third, the decrease in the difference between r-values in RD and TD with the increase in temperature, or the decrease in the in-plane anisotropic deformation.

Also it is noted that, in general, the predicted results for both stress-strain curves and r-values are closer to the experimental ones for the TD. The results for the RD are significantly different from the experimental ones for some temperatures. For the TD, both the curve shapes and stress level are closer to the experiments. This can be attributed to the difference in the assumed and real initial textures of the specimen. In the experiments, the peaks in the basal pole figures of initial specimens were not co-linear with the ND, rather they were tilted towards the rolling direction by approximately 7–8^{o}. The initial texture of the specimen used here, although that of a hot-rolled plate, is different from the one used in the experiments[1]; in particular, the tilt in basal pole figure

[1] The initial texture used in the experiments of Agnew and Duygulu (2005) was available to the author only in the printed pole figure format, which could not be converted to the required discreet orientations needed as input for the simulations. This led to use of a similar but not identical initial texture in the simulations.

from the ND toward the RD is much less, and the peaks are closer to the normal direction. This difference yields the more realistic results in the TD than the RD. A spreading of the basal pole along the RD allows easier activation of basal slip by RD tension. The strong basal texture in TD requires activation of non-basal slip, which increases the yield stress. The higher incidence of non-basal<a> slip, relative to basal<a> slip, during TD tension is responsible for the higher r-value of TD than that of RD and 45°. The same reasoning as that stated above may explain why the difference between the TD and the RD is not captured in the stress-strain curves properly.

It can be seen that at 200^{o}C, where the stress-strain curve is close to that of the experimental results, the r-values are also close to the experimental ones. Figs. 5.44 and 5.45 also show that the stress level of the simulated curves for temperatures up to 200°C are comparable to the experimental results. However, the predicted results at 250°C are offset from the experimental data by a large margin. This raises the possibility of the activation of some other deformation mechanisms, such as grain boundary sliding, at some point between 200°C and 250°C. At the other end, the curve for 75°C shows a large difference with the experimental result, which may be attributed to the lower activity of slip systems and dominance of twinning at this temperature (even with its low level of activity) which has not been considered. Therefore, it can be concluded that at some point between 75°C and 100°C, twinning loses its significance as an active deformation mechanism.

As can be seen in the experimental results of Fig. 5.46, with the increase in temperature, the r-value decreases, but with the increase in temperature above 175°C, the r-values tend to remain constant and even to increase slightly. However, in the simulations this phenomenon is not captured. According to the results obtained in Section 5.2, the trend in the predicted r-values can be improved by increasing the activity of either the prismatic<a> or the pyramidal<a> slip systems, as both of them increase the r-values. In fact, the same strains and plastic rotations are achievable by basal slip in combination with the slip of <a> dislocations on the prismatic or pyramidal planes. Thus, it is difficult to discriminate between the various permutations (prismatic or pyramidal slip only or combinations of both) with the current modeling approaches. However, to keep the

relations linear and consistent, instead of introducing a non-linear relation for prismatic<a>, the pyramidal<a> system activity is included by introducing Eq. 5.11. Adding the pyramidal<a> slip system using the above equation affects the r-values in particular. Figure 5.47 shows the updated results for the r-values at different temperatures, while the pyramidal<a> slip is included. As can be seen, the plateau or the gradual increase in the r-values above 175°C is captured in this case. Nevertheless, attaining relations for predicting the correct r-values and stress-strain curves quantitatively demands further study.

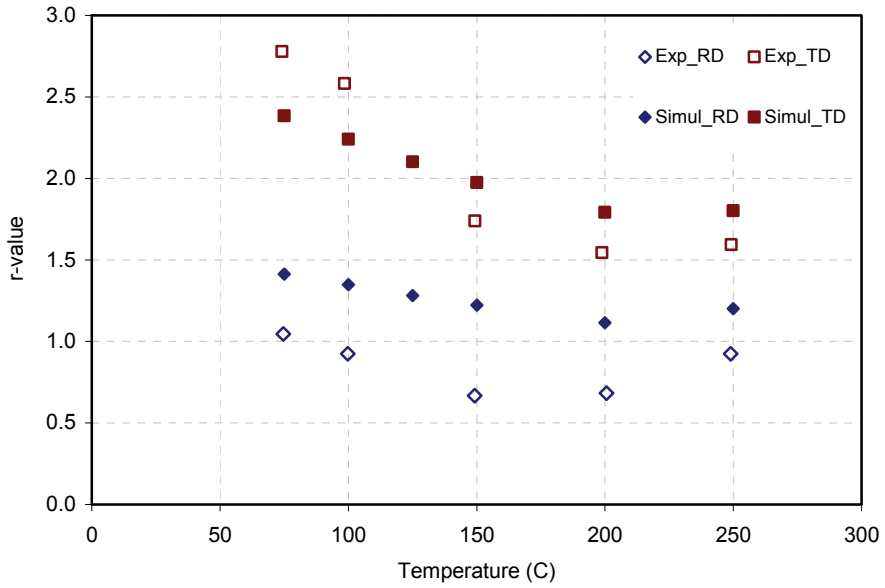

Figure 5.47 Predicted and experimental (Agnew and Duygulu, 2005) r-values in RD and TD vs. temperature using Eq. 5.10 and Eq. 5.11

Although the work in this chapter was focused mainly on the simulation of Mg alloy (AZ31) behavior over a range of temperatures, the modeling should correctly predict the mechanical behavior of material at different strain rates as well. Figure 5.48 shows the change in stress-strain curves with the change in the strain-rate for tension in the TD at 75°C. Using the relations introduced, particularly the new relation for strain-rate sensitivity, the two main effects of strain-rate are captured; the decrease in level of stress and the increase in the localization-strain with the decrease in strain-rate. However, verifying the capability of the model to predict the results at different strain-rates requires further experimental and computational work.

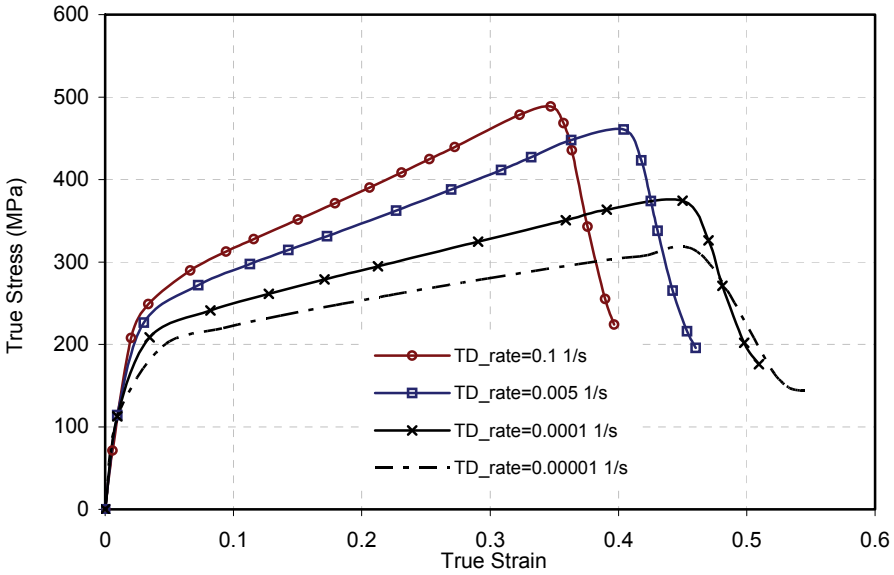

Figure 5.48 The simulated change in stress-strain curve with the change in strain-rate

5.5 CONCLUSIONS

With the aim of gaining a good knowledge of active slip systems and their role in the deformation of magnesium alloys at different temperatures (the effect of individual slip systems), a series of simulations were performed. Tension and/or compression simulations were performed for magnesium samples having a texture of hot-rolled plate and loaded in the RD, TD and ND direction. Some simulations were also done using a sample with random initial texture. The trends regarding the effects of activity of each slip system on the overall behavior of magnesium alloys are stated in Table 5.5 (it should be noted that decrease in the slip resistance values of a system usually leads to higher activity of that system).

Decrease in the slip resistance of the slip systems lowers the overall level of stress, except for the case of basal<a> slip system which has a negligible effect for the initial textures and loading cases considered in this work. Considering the effect of slip systems on r-values (for in-plane tension), the increase in the activity of the prismatic<a> and the pyramidal<a> slip systems increases the r-values, while increasing activity of the pyramidal<c+a> slip system decreases the r-values. Basal<a> has negligible effect in the realistic range of slip resistance values. The activity of the pyramidal<c+a> slip systems at higher temperatures not only lowers the level of stress, but also decreases the r-value;

this strongly supports the postulated increase in the activity of the <c+a> slip systems at higher temperatures.

Table 5.5 The effects of higher activity of each slip system on the overall behavior of the material

	flow stress	Anisotropy	
		r-value (RD and TD)	Tens/comp difference
basal<a>	no significant change (for the conditions considered in this work)	no significant change (for reasonable range of slip resistances)	no significant change
prismatic<a>	decrease	increase	increase
pyramidal<a>	decrease	increase	increase
pyramidal<c+a>	decrease (significantly)	decrease	decrease (significantly)

As a result of the initial texture of the material, the mechanical response is different for the loading in the RD or TD direction. The summary of the simulation results in the RD and TD directions are as follows,

- From RD to TD
    - Flow stress
        - Increases (slightly)
    - Strain at which localization occurs
        - Decreases (slightly)
    - r-value
        - Increases (significantly)

Regarding the effect of strain-rate in the simulations, it can be concluded that decrease in strain-rate decreases the level of flow stress, and increases that localization strain.

It was seen that the strain-rate sensitivity factor increases greatly with the increase in temperature. The change in the SRS with the change in strain-rate was observed to be less monotonic. SRS tends to increase with decrease in strain-rate, but often shows a peak and decreases afterwards. It was observed that the increase in SRS value leads to a more

uniform distribution of shearing increments on slip systems, leading to a more homogenous deformation. This will postpone the localization and, thus, enhances the forming properties of the material.

Using the results obtained in the first and second parts, the activity of different slip systems present in Mg alloys at warm temperatures was modeled. Also the change in the strain-rate sensitivity with the change in temperature was included. A series of relations was proposed for the evolution of the slip resistance values and the strain-rate sensitivity factor at warm temperatures. The proposed relations were implemented in the CPFE model and were used in the finite element simulations of magnesium alloys behavior. The results obtained using the CPFE model confirm general trends predicted by other models. However, being more physically-based compared to other methods, the CPFE proposes different values for slip resistances of different systems, which seems to be more accurate.

The use of the relations introduced for the evolution of the slip resistance values and the strain-rate sensitivity factor (stated below), results in qualitatively correct predictions of the trends for the change in the stress-strain curves, and r-values with temperature.

$$
\begin{aligned}
s^{\alpha}(0) &= s_{\text{basal<a>}} = 15 \text{ (MPa)}, && \alpha = 1,\ 2,\ 3; \\
s^{\alpha}(0) &= s_{\text{prism<a>}} = 6.0\ln(Z) - 70 \text{ (MPa)}, && \alpha = 4,\ 5,\ 6; \\
s^{\alpha}(0) &= s_{\text{pyram<c+a>}} = 8.7\ln(Z) - 200 \text{ (MPa)}, && \alpha = 7,..,\ 12; \\
s^{\alpha}(0) &= s_{\text{pyram<a>}} = 13.2\ln(Z) - 310 \text{ (MPa)}, && \alpha = 13,..,\ 18; \\
m &= 0.35 - 0.0068\ln(Z)\ .
\end{aligned}
\qquad \text{Eq. 5.13}
$$

In particular, using the proposed relation for the strain-rate sensitivity in the simulations leads to a decrease in the stress-level and an increase in the localization-strain with the decrease in the strain-rate, which is in agreement with the experimental results. The more quantitative comparisons can be done using a more exact initial texture and re-evaluation of the proposed relations. Further experimental and computational study is needed for developing a model capable of predicting the correct r-values and the stress-strain curves quantitatively.

Chapter 6
Localization in Mg Alloys

6.1 INTRODUCTION

The problem of strain localization (necking) has been of interest for many years (a comprehensive review was presented in Section 2.4). The early work on localization was done primarily using the tension test on cylindrical specimens (e.g. Davidenkov and Spiridonova, 1946; Swift, 1952; Hill, 1958; Thomason, 1969; Chen, 1971; Needleman, 1972; Rice, 1977; Burke and Nix, 1979). The concept of localization in sheet metals has also been extensively studied. The necking point specifies the forming limit of the sheet metal, and the width of the necking zone specifies the ductility of the post-localization behavior. Thus, a full understanding of localization and post-localization behavior is important for the purpose of formability prediction (Keeler, 1968; Mikkelsen, 1997; Daly *et al.*, 2007). In Mg alloys, therefore, with the low formability, studying the localization and post-localization behavior is critical to improving the forming process. In this chapter, localized necking phenomenon in Mg alloy sheets is studied in detail. In particular, the conditions that lead to localization and the affecting parameters are investigated.

In general, there are two different sources of inhomogeneity in sheet metal: material inhomogeneity, which is due to an inhomogeneous spatial orientation distribution and

geometrical inhomogeneity, which is associated with the initial surface topography (Wu *et al.*, 2007). In most investigations on localization in sheet metals, the concept of the forming limit diagram (FLD) has been used to represent conditions for the onset of sheet necking (e.g. Hecker, 1975). Most theoretical and numerical FLD analyses utilize the M–K approach. This approach, introduced by Marciniak and Kuczynski (1967) and further investigated by Hutchinson and Neale (1977), is based on existence of a geometric defect (see Chapter 2).

Within the M–K framework, the influence of various constitutive features on FLDs has been explored using phenomenological plasticity models (see e.g. Neale and Chater, 1980; Wu *et al.*, 2003; Stoughton and Zhu, 2004; Matin and Smith, 2005; Stoughton and Yoon, 2006; Vegter and Van der Boogaard, 2006) and crystal plasticity models (e.g. Zhou and Neale, 1995; Wu *et al.*, 1998; Knockaert *et al.*, 2002; Inal *et al.*, 2002b, Wu *et al.*, 2005b). Nevertheless, the M–K approach requires the value of an artificial initial imperfection parameter which cannot be directly measured by physical experiments, and has to be estimated by fitting the FLD prediction to the corresponding experimental data (Wu *et al.*, 2007). As pointed out by Tvergaard (1978), attempts to correlate predictions based on the M–K approach with experiments have shown that an unrealistically large initial imperfection must be assumed in order to get agreement between the limit strains.

Wu *et al.* (2007) demonstrated that by utilizing the CPFE modeling, the need for the artificial initial imperfection necessitated by the macroscopic M–K approach can be omitted. Studying localized necking in a commercial Al alloy sheet under in-plane plane-strain tension using a 2D CPFE model, they concluded that the initial surface imperfections have only a small effect on the strain to necking, and the initial texture and its spatial orientation distribution are predominant factors for the development of localized necking.

However, 2D models have some shortcomings; in studying localization, 2D finite element analysis will give a physically unrealistic mesh sensitive solution, where the necking zone occupies the smallest possible area allowed by the mesh (Mikkelsen, 1997). In such analyses, potential out-of-plane shears are restrained and spatial variations behind or in front of the model plane are neglected, which can affect the deformation field and

texture evolution (Becker, 1998). Tvergaard (1993) stated that both the delay of the onset of localization and the post-necking behavior of an imperfect thin sheet are determined by three-dimensional effects. Using a 3D model in this work, the limitations of two dimensional models are overcome.

There are also some problems inherent in the use of rate-independent models for studying localization. Rate-independent models exhibit an inherent mesh dependence in solving localization problems (e.g. Tvergaard and Needleman, 1981; Pietruszczak and Mroz, 1981; Tvergaard, 1982; Belytschko and Bazant, 1986). For rate-dependent solids, the mesh sensitivity associated with numerical solutions is eliminated. In addition, the rate-dependent models are well adapted to handle the post-localization behavior since the instability is delayed due to the introduced viscosity and the stabilizing effect of strain-rate sensitivity (Hutchinson and Neale, 1977; Needleman, 1988; Daly *et al.*, 2007).

In this chapter, localized necking phenomenon (referred to as localization frequently) is investigated using a 3D rate-dependent CPFE model. The 3D, rate-dependent model removes the problems inherent in 2D analyses and rate-independent models for studying localization. The effects of local texture (spatial distribution of orientations over finite elements) and slip system activity on localization and post-localization behavior of Mg alloys are studied. The plastic deformation resulting from the activity of slip systems only is considered. Localization behavior is predicted for a typical Mg alloy (AZ31B) under different circumstances. By tracking slip system activity and texture evolution in the necked area, a hypothesis linking the localization phenomenon with slip system activity and local texture in the necked area is proposed. The findings explain some phenomena including different post-localization softening behaviors observed for Mg alloys in terms of slip system activity. These phenomena have been conventionally attributed to the activity of some other deformation mechanisms (such as DRX) or to the presence of cavities.

The outline of the chapter is as follows. Section 6.2 is devoted to the effects of spatial distribution of texture and existence of hardening on the localization behavior of Mg alloy polycrystals. In section 6.3, the stress state in the localized area is discussed. These two sections, explaining the effects of spatial distribution of texture and hardening on slip

systems, provide the necessary background for the following sections; i.e., they clarify the role that these parameters play in the localization phenomenon and the extent to which they affect it. In Section 6.4, local texture and slip system activity in the necked area are studied. The interaction between the activity of different slip systems and localization is investigated in Section 6.5. The chapter finishes with some concluding remarks in Section 6.6.

6.2 LOCAL TEXTURE AND LOCALIZATION

One of the main factors in determining the response of Mg alloys is the initial texture of the specimen and its evolution with loading which has been well addressed in the literature. However, less discussed in the literature is the effect of texture distribution throughout the specimen on the overall material response. In this section, the relation between the spatial distribution of orientations in the specimen and the localization phenomenon is investigated. A series of tension simulations are performed on specimens with a texture corresponding to hot-rolled plates, loaded in the rolling direction (RD). The experimentally measured $\{0001\}$ and $\{10\bar{1}1\}$ pole figures of the initial texture are plotted in Figs. 6.1(a) and 6.1(b), respectively.

To simulate the tension samples, the cube geometry used in Chapter 5 is considered. It should be mentioned that, in this part, the model represents the tensile deformation of a 0.6 mm sheet. Figure 6.2 shows the location of the modeled region in the tension specimen. Due to symmetry, only one-fourth of the specimen is shown. Also due to symmetry, the modeled region is assumed to have a thickness half that of the specimen. (Assuming the grains to have an average size of 50 μm, the sheet would have a thickness of 0.6 mm.) The model is divided into 1440 elements of C3D8R type, each of which represents one single grain. The 1440 required sets of Euler angles are obtained using the TexTools software, which takes the experimentally measured ODF file as its input.

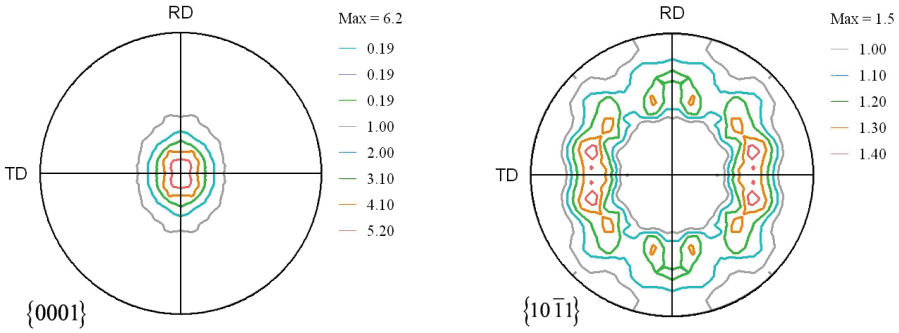

(a) (b)

Figure 6.1 Initial texture of the specimens (hot-rolled plate).

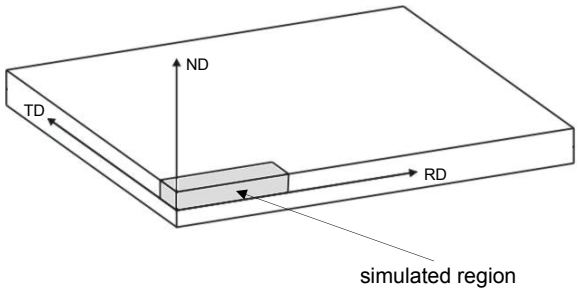

Figure 6.2 The location of the simulated region in the specimen (one-fourth of the specimen)

To start, three groups of material parameters with different hardening parameters are defined in Table 6.1. In the first group, NH, no hardening is assumed on the slip systems. In the second, LH, and the third, HH, hardening is assumed on the slip systems, with a higher initial hardening rate assumed in the latter. In each set, four different pairs of strain-rate sensitivity and reference shearing rate values are used. The parameters in corresponding simulations in two different groups (e.g. NH 01 and LH01 or HH01) differ only in the assumed initial hardening rate, $h_{\beta 0}$ (Section 3.2.2). As seen in Table 6.1, the slip resistance values are normalized with respect to $s_{basal<a>}$. Consistent with this approach, the figures presented in this chapter use stress values normalized by the same value as well. It should be mentioned that the goal is to study localization and the effect of different parameters on this phenomenon rather than obtaining the exact stress-strain curves or comparing the obtained values with experiments; thus, conclusions are independent of the material parameters chosen.

Figure 6.3 shows the stress-strain curves for the first two sets of parameters, LH01-LH04 and NH01-NH04, with and without hardening assumed on the slip systems, respectively. By examining the simulation results with and without work hardening on the slip systems, it is observed that the peak stress disappears for the case of non-hardening slip systems (the existence of a peak stress and the drop in the stress thereafter is discussed in Section 6.3). However, the results for both hardening and non-hardening cases, independent of whether a peak stress exists or not, predict that the specimen localizes at some point (Fig. 6.3). Also, both the strain-localization intensity and the post-localization slope of the flow stress decrease when hardening is assumed on the slip systems.

Table 6.1 Material parameters assumed for non-hardening , hardening with low initial hardening rate (LH), and hardening with high initial hardening rate cases

	Set Name	$\frac{s_{prism<a>}}{s_{basal<a>}}$	$\frac{s_{pyram<a>}}{s_{basal<a>}}$	$\frac{s_{pyram<c+a>}}{s_{basal<a>}}$	$\dot{\gamma}_0 \left(s^{-1}\right)$	m	$\frac{h_{\beta 0}}{s_{basal<a>}}$
Group #1	NH 01	15	15	5	5E-7	0.1	0
	NH 02	15	15	5	1E-6	0.1	0
	NH 03	15	15	5	1E-5	0.12	0
	NH 04	15	15	5	1E-4	0.12	0
Group #2	LH 01	15	15	5	5E-7	0.1	25
	LH 02	15	15	5	1E-6	0.1	25
	LH 03	15	15	5	1E-5	0.12	25
	LH 04	15	15	5	1E-4	0.12	25
Group #3	HH 01	15	15	5	5E-7	0.1	50
	HH 02	15	15	5	1E-6	0.1	50
	HH 03	15	15	5	1E-5	0.12	50
	HH 04	15	15	5	1E-4	0.12	50

The conditions that initiate the observed localization are the focus of this chapter. The first issue investigated is the probability of a particular local texture leading to the global localization. In other words, it is proposed that a certain distribution of grain orientations over the finite elements in the necked area is triggering the start of localization. In order to verify this, simulations are done for the specimens with the same overall initial texture,

but different spatial distributions. The orientations generated by TexTools software are assigned randomly to finite elements. Then, simulations are repeated with different random redistributions of the generated Euler angles over the finite elements (without any change in the overall initial texture). Distinction should be made between the random distributions which are used here from homogenous ones. During consecutive random redistribution of orientations over finite elements, although the *overall* texture of the specimen remains constant, the *local* textures change.

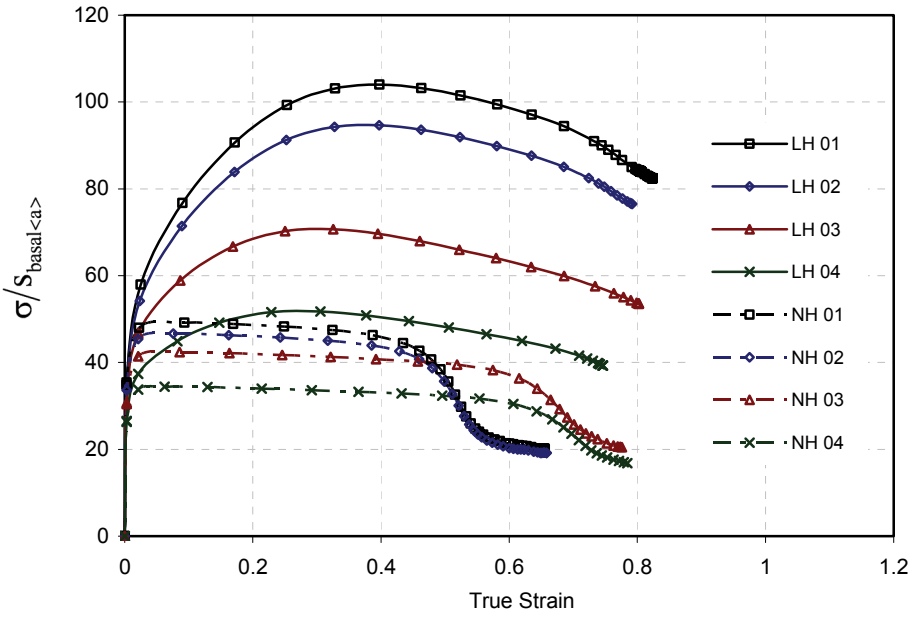

Figure 6.3 Comparison between the stress-strain curves for the hardening (LH) and non-hardening cases

To investigate the effects of local texture, the first series of simulations is done with no hardening on the slip systems. The simulations are done using the parameters defined in Table 6.1 as NH01. Figure 6.4 shows the stress-strain curves and the deformed shapes for four specimens with four different distributions of orientations over the finite elements, but the same overall initial texture and material parameters.

As can be seen in Fig. 6.4, localization occurs regardless of how the crystal orientations are distributed among the finite elements. Nevertheless, redistribution of orientations affects the strain at which localization occurs; localization strain varies from 0.3 to 0.55 with redistributions. The location of the necked area also changes with the change in the

orientation redistributions over finite elements. This interesting observation raises the idea that a specific local texture which relocates by redistribution of orientations is triggering the localization.

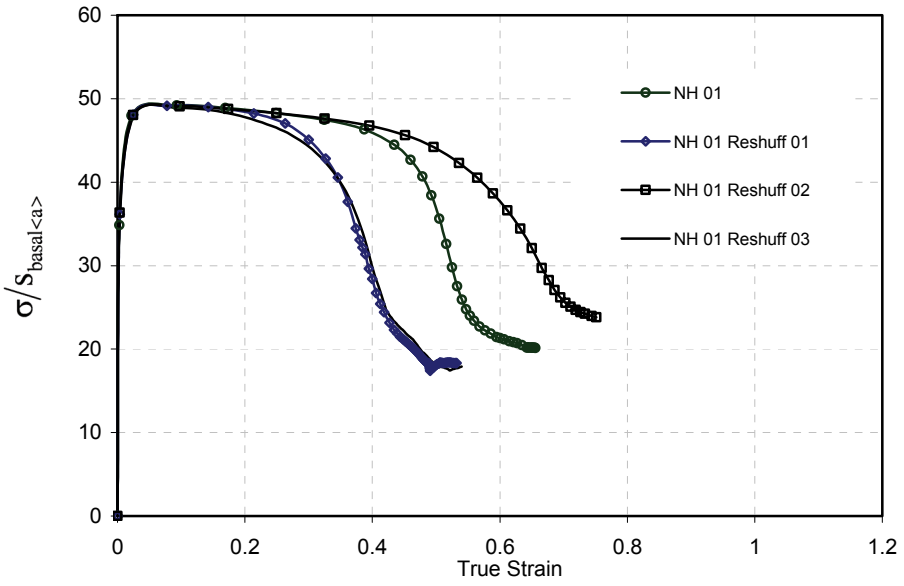

(a)

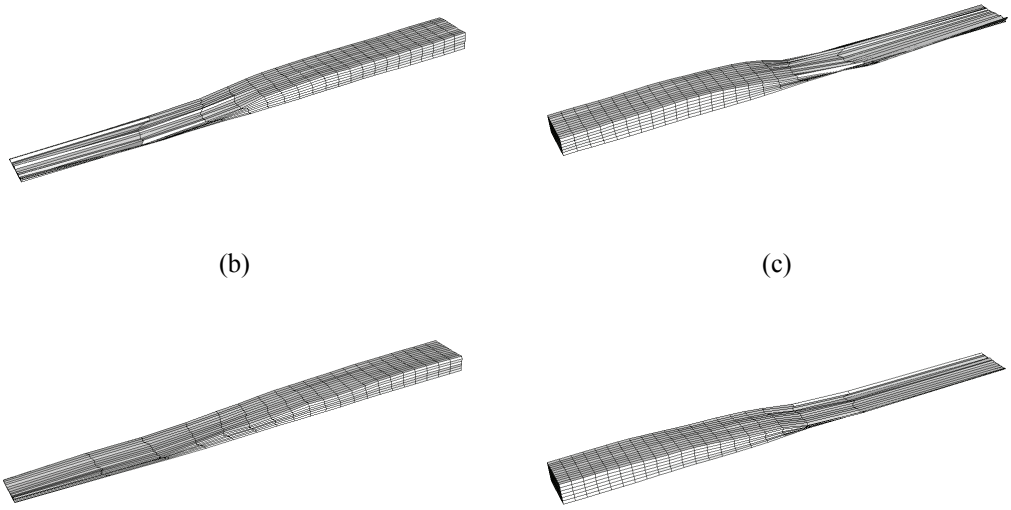

(b) (c)

(d) (e)

Figure 6.4 Using different random distribution of orientations over finite elements; no hardening on the slip systems (a) difference in the true stress-true strain curves (b) the reference distribution (c) redistribution Reshuffled 01 (d) redistribution Reshuffled 02 (e) redistribution Reshuffled 03

The local texture in the necked area is studied in Section 6.4. However, other than local texture, other parameters may affect pre- and post-localization behavior of Mg alloys; among which are the assumed active slip systems and hardening rates. In this section, the effect of change in the hardening rate on the localization behavior of Mg alloys is investigated. The effect of active slip systems is discussed in Section 6.5.

To study the hardening effect, the simulations done for the non-hardening case (Fig. 6.4) are repeated with hardening assumed on the slip systems for the sample labeled LH01. Figure. 6.5 shows the stress-strain curve and deformed shapes of sample LH01 with different redistribution of orientations; the ratio of the initial hardening rate to basal<a> slip system is $h_{\beta 0}/s_{basal} = 25$. As seen in Fig. 6.5, in this case, all the curves overlap each other up to the peak stress (UTS) point; but thereafter, with the start of localization, the curves show different softening slopes.

The simulations are repeated in Fig. 6.6 for sample HH01, with higher initial hardening rate ($h_{\beta 0}/s_{basal} = 50$). The trends in the stress-strain curves observed in Fig. 6.5 are repeated for this case, and the curves show a difference only after the UTS point. Moreover, the softening slopes of different curves are closer to each other compared to the curves of Fig. 6.5. It is observed in both Fig. 6.5 and Fig. 6.6 that, regardless of the initial hardening rate, with redistribution of local textures, the localization area occurs at different points along the specimen. This observation confirms the important effect of spatial distribution of orientations.

Considering Figs. 6.4-6.6, it is observed that redistributing the crystal orientations over the finite elements does not affect the existence of localization or the UTS point, but affects the post-localization softening slope for all the cases, and the strain at which localization occurs in the non-hardening case. When hardening is present, the curves show the same behavior before localization but different behavior in the post-localization zone. In all cases, the location of the neck also changes with the change in the spatial distribution of orientations.

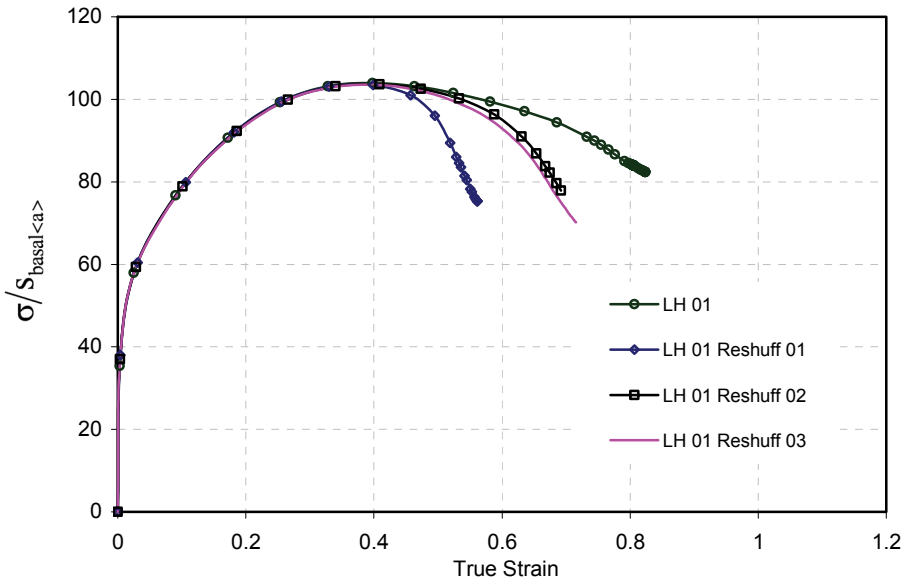

(a)

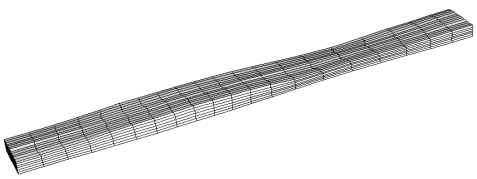

(b)

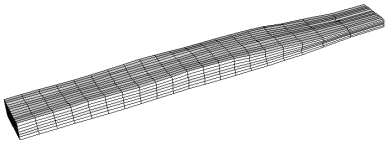

(c)

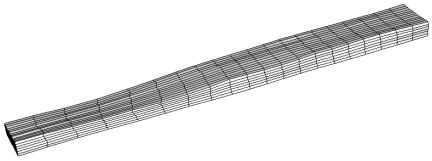

(d)

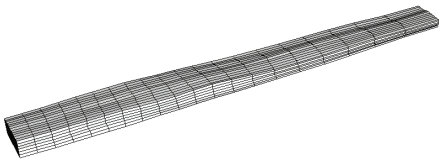

(e)

Figure 6.5 Using different random distribution of orientations over finite elements; hardening is assumed (LH) on the slip systems (a) Difference in the true stress-true strain curves (b) the reference distribution (c) redistribution Reshuffled 01 (d) redistribution Reshuffled 02 (e) redistribution Reshuffled 03

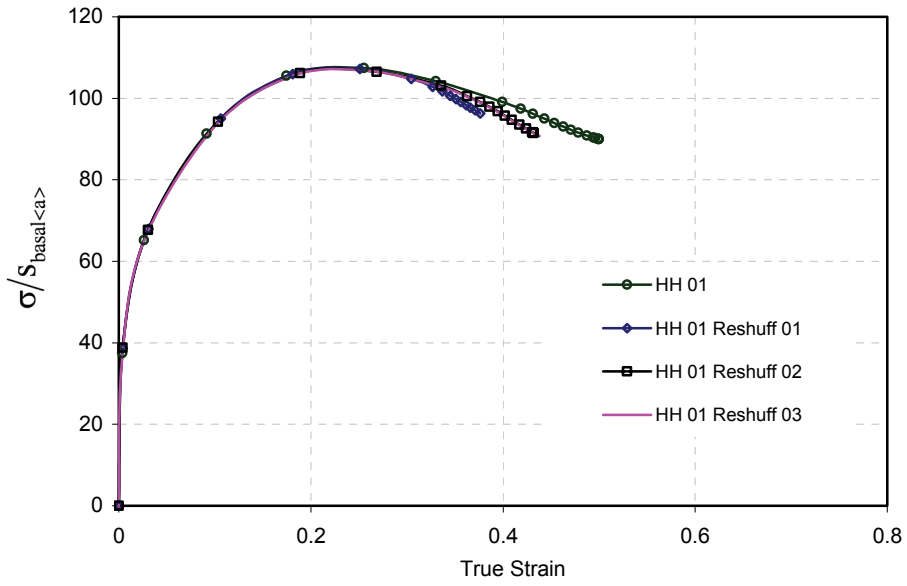

(a)

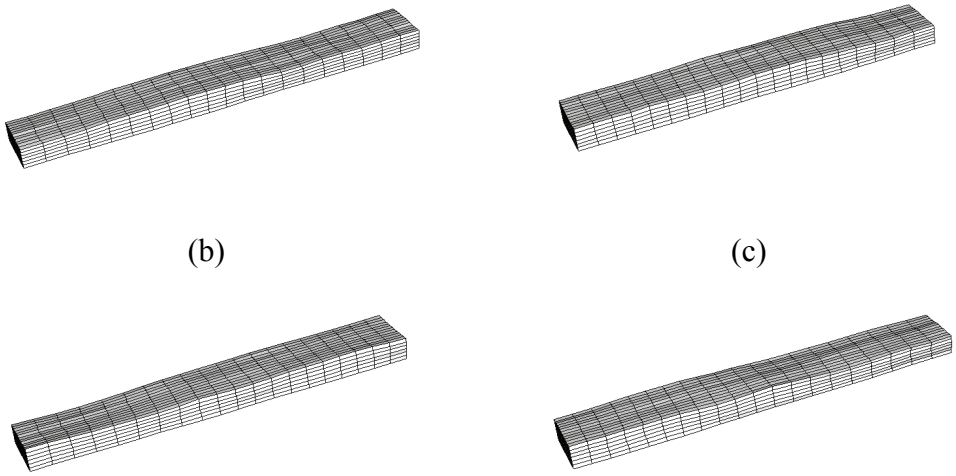

(b) (c)

(d) (e)

Figure 6.6 Using different random distribution of orientations over finite elements; higher initial hardening rate assumed on the slip systems (a) Difference in the true stress-true strain curves (b) the reference distribution (c) redistribution Reshuffled 01 (d) redistribution Reshuffled 02 (e) redistribution Reshuffled 03

The difference between the curves obtained for specimens with exactly the same overall initial texture but different distributions of it over the finite elements has significant implications. In the first place, the results indicate that different stress-strain curves may be obtained for specimens with the same initial texture; i.e., samples with the same measured initial texture can behave differently. In addition, considering the fact that in real situations, hardening does exist on the slip systems, Figs. 6.5 and 6.6 are expected to give more realistic results. In these figures, the post-localization behavior is different for samples with different distributions of orientations while the pre-localization behavior is the same for all. In general, it is clearly seen that other than the initial texture, local textures (or spatial distribution of texture) can greatly affect the localization strain, post-localization behavior, and the location of the neck. In the following sections, the stress state, texture evolution, and slip system activity in the localized area are studied in detail.

6.3 STRESS IN THE LOCALIZED AREA

The drop in the true stress-true strain curve, after it reaches its peak at the onset of localization (seen in Figs. 6.4-6.6), raises a question regarding its physical interpretation; in fact, the drop in the true stress for the localized material seems to be unrealistic as there is no softening mechanism in the constitutive equations (explained in Sections 3.1-3.4). To explain this, it should be recalled that the stress-strain curves are obtained by averaging the true stress and true strain values obtained for all the grains in the specimen at a certain time during the deformation. This averaging, which is done on the obtained stress/strain values, should not be confused with the averaging schemes which can be used in obtaining the stress and/or strain values. It is expected that this averaging is the reason behind the drop in the curves for the whole specimen, and, therefore, the true stress in the localized region does not show a peak, but rather increases monotonically.

Wu *et al.* (2007) state that after localized necking, the applied deformation is almost all concentrated in the neck; this deformation concentration results in unloading of the materials outside the localized neck, which in turn results in decreasing true stress. To gain a better insight, the stress state in the localized area is closely studied in the tension

simulations. The true stress-true strain curves are plotted not only for the whole specimen, but also for the parts of the specimen that show strain-localization.

Figure 6.7 shows the true stress-true strain curves obtained for specimen LH 01 (Fig. 6.7b) as well as some localized areas of this specimen which are chosen as shown in Figs. 6.7c to 6.7e. By moving from Fig. 6.7b to Fig. 6.7e, the geometry considered becomes more confined to the elements with the highest degree of strain localization. As can be clearly seen, as the inspected region becomes more limited to the grains located in the localized area, the softening disappears, and no drop in the stress level is observed, even after localization.

It should be noted that defining the localized area and its boundaries is by no means a straightforward task. The localized area can be defined as the collection of points at which the strain (or strain rate) reaches a certain multiple of the average strain (or strain rate) in the whole specimen. Alternatively, and in particular for sheet metals, localized area can be defined according to the sheet thickness at various points.

In this thesis, no attempt is being made to define the localized area boundaries precisely, as it is not the main objective of the work. For example, in discussing the stress state in the localized area, the goal is not to obtain the exact stress-strain curve for the necked region, but to show the increasing value of stress with strain in this region. Although the stress-strain curve of the localized area would be dependent on the elements chosen to define the boundary of the necked region, it does not affect the conclusions regarding constant increase in the stress level in the necked area.

The verification is repeated for different redistributions of orientations over finite elements. Figure 6.8 shows the results for the same sample shown in Fig. 6.7, but with a different spatial orientation distribution. This verification was also repeated for several other samples (including LH02, LH03, and NH02), the results of which are not shown here due to similarity of trends. In all cases, no drop in the stress level was observed in the localized area, and the trends seen in Fig. 6.7 were repeated. Therefore, the material in the necked area itself is hardening and the overall softening is due to geometric effects caused by thickness variations throughout the sheet.

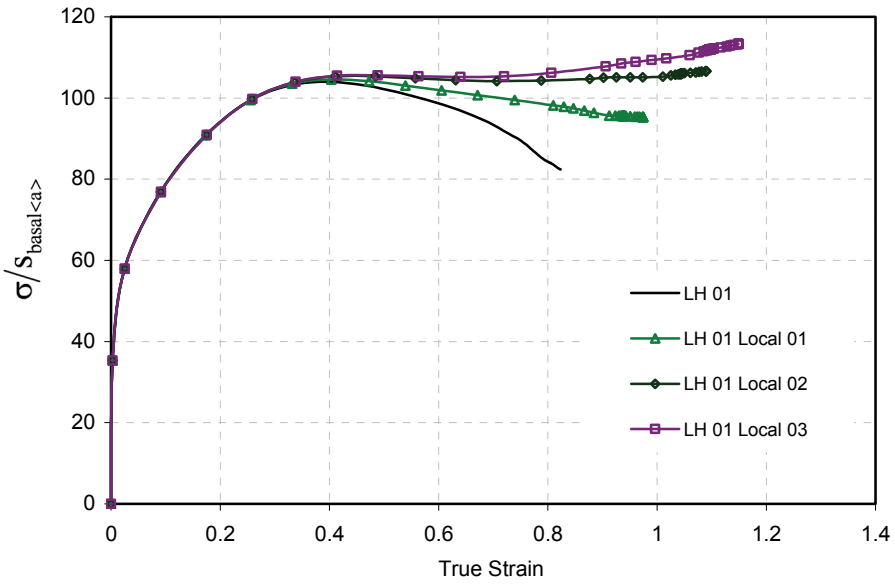

(a)

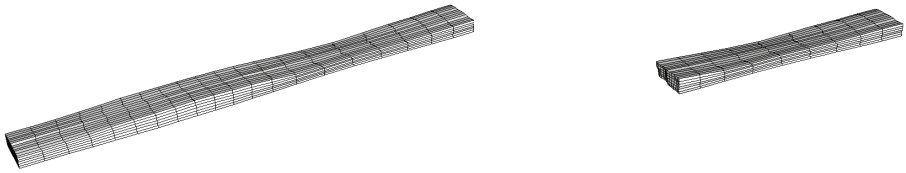

(b)

(c)

(d)

(e)

Figure 6.7 Difference in the true stress-true strain curves of the localized area and the whole specimen comparison of the curves (b) the whole specimen (c) localized area labeled by local 01 (d) localized area labeled by local 02 (e) localized area labeled by local 03

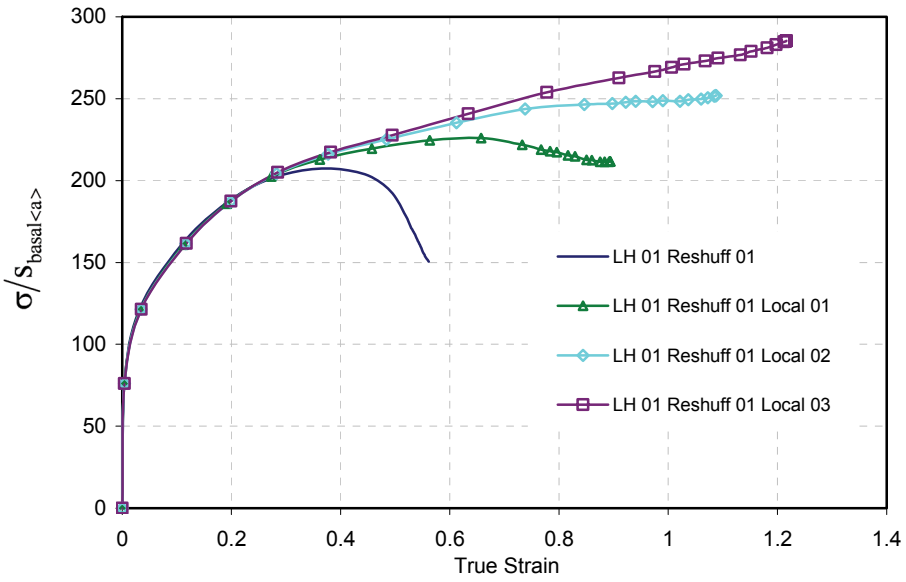

(a)

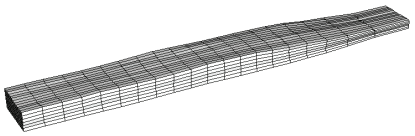

(b)

(c)

(d)

(e)

Figure 6.8 Difference in the true stress-true strain curves of the localized area and the whole specimen comparison of the curves (b) the whole specimen (c) localized area labeled by local 01 (d) localized area labeled by local 02 (e) localized area labeled by local 03

6.4 TEXTURE EVOLUTION AND SLIP SYSTEM ACTIVITY IN THE LOCALIZED AREA

In this section, the link between the start of localization, the texture evolution in the necked area, and slip system activity is investigated. It is expected that the initial texture in the localized area and its evolution with deformation differ from those of the whole specimen. Simulations are done with the texture evolution tracked in both the localized area as well as in the whole specimen. The first series of simulations is performed for sample with low initial hardening rate, LH 01. For ease of reference, the average stress in the localized area and in the whole specimen is presented with respect to time in Fig. 6.9. Figure 6.10 shows the accumulated shearing increments on different slip system families in the localized area and the whole specimen. The accumulated shear for each family, f, is calculated using the following relation,

$$\left(\gamma^{acc}\right)^{f} = \int_{0}^{t_1} \left(\sum_{1}^{nf} \dot{\gamma}^{\alpha} \right) dt , \qquad \text{Eq. 6.1}$$

where nf shows the number of slip systems in the family f, and $\dot{\gamma}^{\alpha}$ shows the shearing rate on the slip system α at time t. The simulations are all done at a nominal strain rate of 0.1 s^{-1} and for duration of 15 s or 30 s, or up to the divergence of the simulation.

Figure 6.10 shows that with the assumed slip resistance values for slip systems, shown in Table 6.1, the pyramidal<c+a> system has the highest activity among the slip system families. Also, it is seen that the average activity of all the slip systems, especially the pyramidal<c+a>, is higher in the localized area, which shows the inhomogeneity of slip system activity throughout the specimen. In addition, the first slip system that shows a higher activity in the localized area is the <c+a> slip system at $t \approx 2$ s (nominal strain of 0.2). It is only at $t \approx 5$ s that basal<a> shows localization in the necked area, followed by pyramidal<a> ($t \approx 8$ s) and prismatic<a> ($t \approx 9$ s). It is seen in Fig. 6.9 that average stress values are different for the localized area only after $t \approx 4$ s. Thus, with assumed slip resistance values and initial texture, the higher activity of <c+a> slip system seems to be triggering the localized activity of other systems which finally leads to strain-localization.

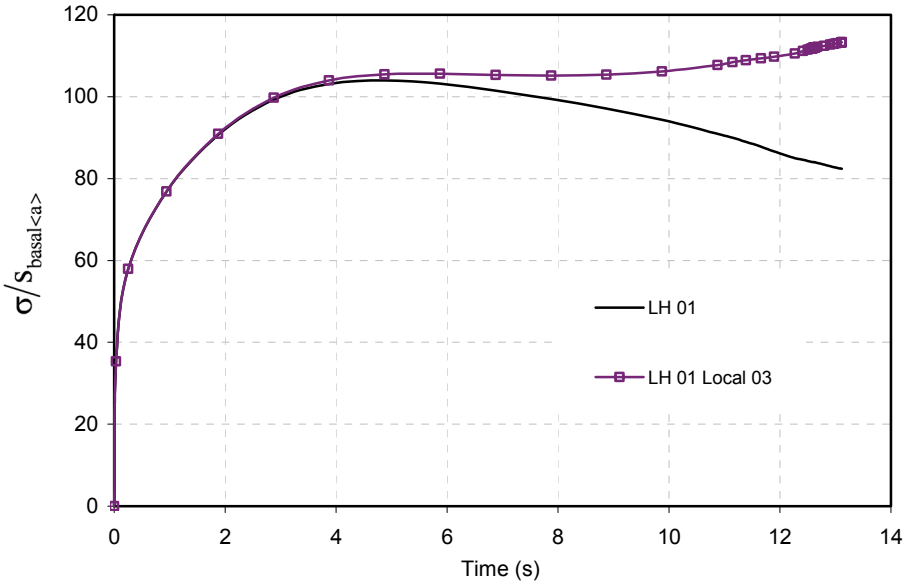

Figure 6.9 Comparing the change in the true stress (averaged over the elements) for the whole specimen and the localized area (LH 01)

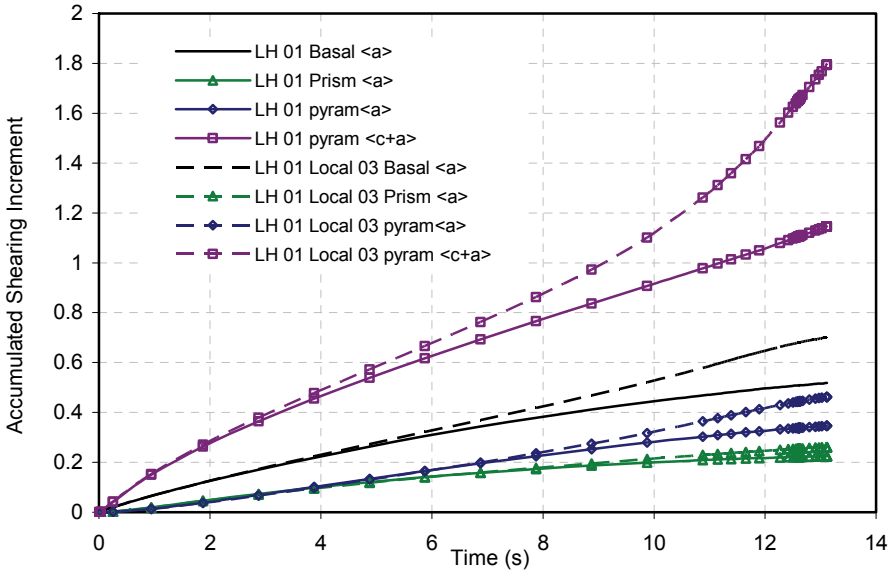

Figure 6.10 Comparing the activity of different slip system families for the whole specimen and the localized area (LH 01)

To further study the localized area, texture evolution in this area and the whole specimen are calculated and plotted at several times during deformation. Figure 6.11 compares the $\{0001\}$ pole figures of the whole specimen and the localized area at t = 0, 4 and 13s; initial texture, texture at peak stress and final texture, respectively (see Fig. 6.9).

Comparing the initial pole figures of the whole specimen and the localized area, shown in Figs. 6.11a and 6.11d, it is noticed that initially the basal pole figure has a higher maximum intensity in the localized area. At the onset of localization (Figs. 6.11b and 6.11e), as a result of the prior texture evolution, the basal texture is replaced by a bipolar texture with average c-axis tilted toward the RD and the maximum intensity higher in the localized region.

After the start of localization, it seems that further change in the basal pole figure in the localized area is negligible, while it continues in the whole specimen. Interestingly, in terms of maximum intensity in the basal pole figure, the final texture is more intense for the whole specimen compared to the localized area. It is speculated that this texture localization, in particular, the higher intensity of basal texture in the localized area, is the reason behind the occurrence of necking at this point. However, this particular orientation triggers the localization with the assumed set of active slip systems and the considered spatial distribution of orientations. Therefore, this hypothesis should be verified for other cases and combinations of slip systems as well.

To verify the occurrence of localization at a certain location due to a specific local texture, the comparison made in Figs. 6.9-6.11, between the localized area and the whole specimen, is repeated for the following cases: (i) a different redistribution of orientations which creates a different spatial distribution of texture (for sample LH 01 Reshuff 01, previously shown in Fig. 6.5c); the results for this case are shown in Figs. 6.12 to 6.14; (ii) no hardening on the slip systems (sample NH 01), with the results reported in Figs. 6.15 to 6.17; (iii) a higher initial hardening rate considered for the slip systems (sample HH 01), with the results shown in Figs. 6.18 to 6.20.

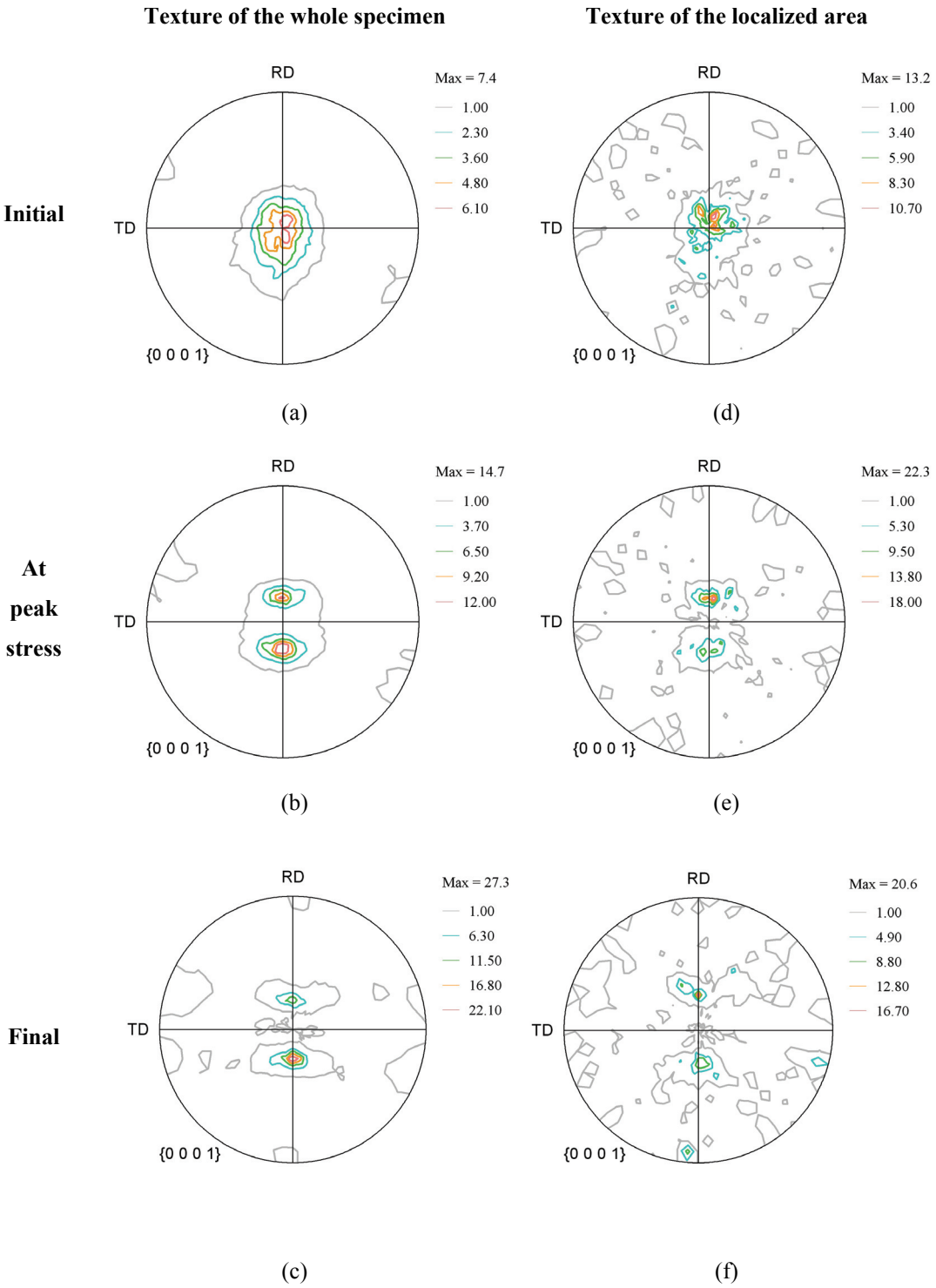

Figure 6.11 Comparing the texture evolution in the whole specimen and the localized area (LH 01)

Figures 6.12 to 6.14 show the results for a sample with the same material parameters as the ones considered for the sample in Figs. 6.9-6.11, but with a different spatial distribution of texture (LH01 Reshuff 01). It is seen in Fig. 6.13 that similar to the previous case (LH01), the activity of all slip systems is higher in the localized area. Pyramidal<c+a> not only shows a notably higher activity in the localized area (especially after the start of strain localization), but also exhibits a localized activity before all the other systems and before strain localization, as well. In fact, <c+a> shows a localized activity as early as $t \approx 0.5$ s; followed by basal<a>, pyramidal<a>, and prismatic<a> at $t \approx 2$ s, $t \approx 4$ s, and $t \approx 5$ s, respectively. For this case, UTS occurs at $t \approx 4$ s (Fig. 6.12).

Regarding the $\{0001\}$ pole figures (Fig. 6.14), it is seen that the initial maximum intensity of the basal pole figures is higher in the localized area. Similar to Fig. 6.10, at the onset of localization ($t \approx 4$ s), the basal pole figure shows its maximum intensity, which is still higher than that of the whole specimen. The final $\{0001\}$ pole figure of the localized area shows a maximum intensity lower than that of the whole specimen. In short, it is observed that the overall trends remain the same when a different spatial distribution of texture is used. Therefore, the conclusions regarding the texture in the localized area are independent of the spatial distribution of orientations.

Figures 6.15 to 6.17 show the results obtained with no hardening assumed on the slip systems (sample NH 01). In this case, both the slip system activity and its localization in the necked area are higher for the pyramidal<c+a> and basal<a> slip systems compared to the pyramidal<a> and prismatic<a> slip systems. Also, the delay between the localization of pyramidal<c+a> and the overall strain localization is nearly removed (both seem to occur at $t \approx 2.5$ s). Thus, hardening of slip systems enhances the overall forming limit of the material, as expected. Without hardening, the overall strain-localization starts with the onset of slip system activity.

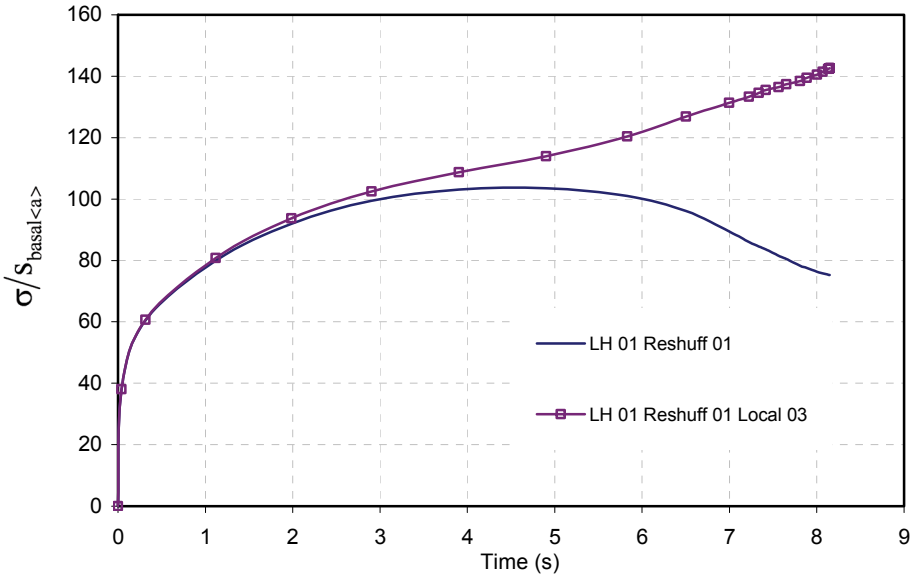

Figure 6.12 Comparing the change in the true stress (averaged over the elements) for the whole specimen and the localized area (LH 01Reshuff 01)

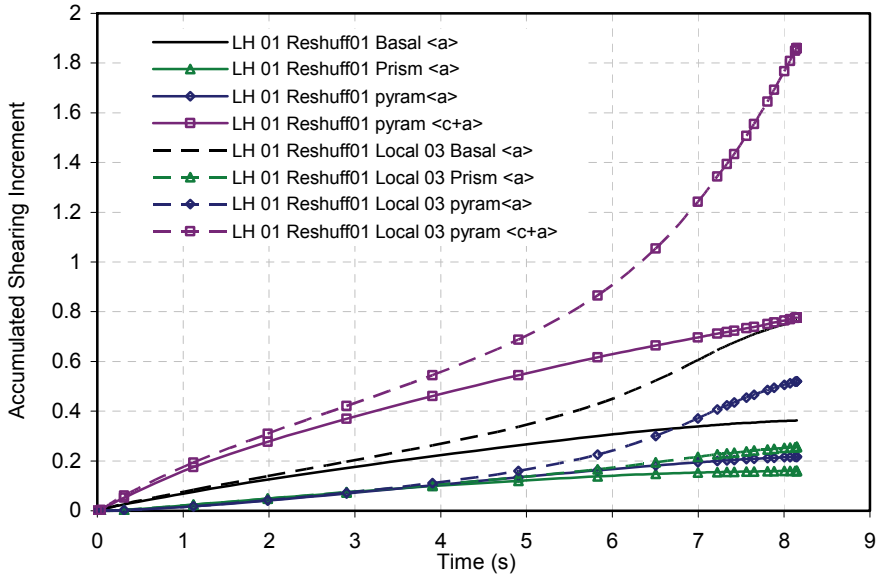

Figure 6.13 Comparing the activity of different slip system families for the whole specimen and the localized area (LH 01Reshuff 01)

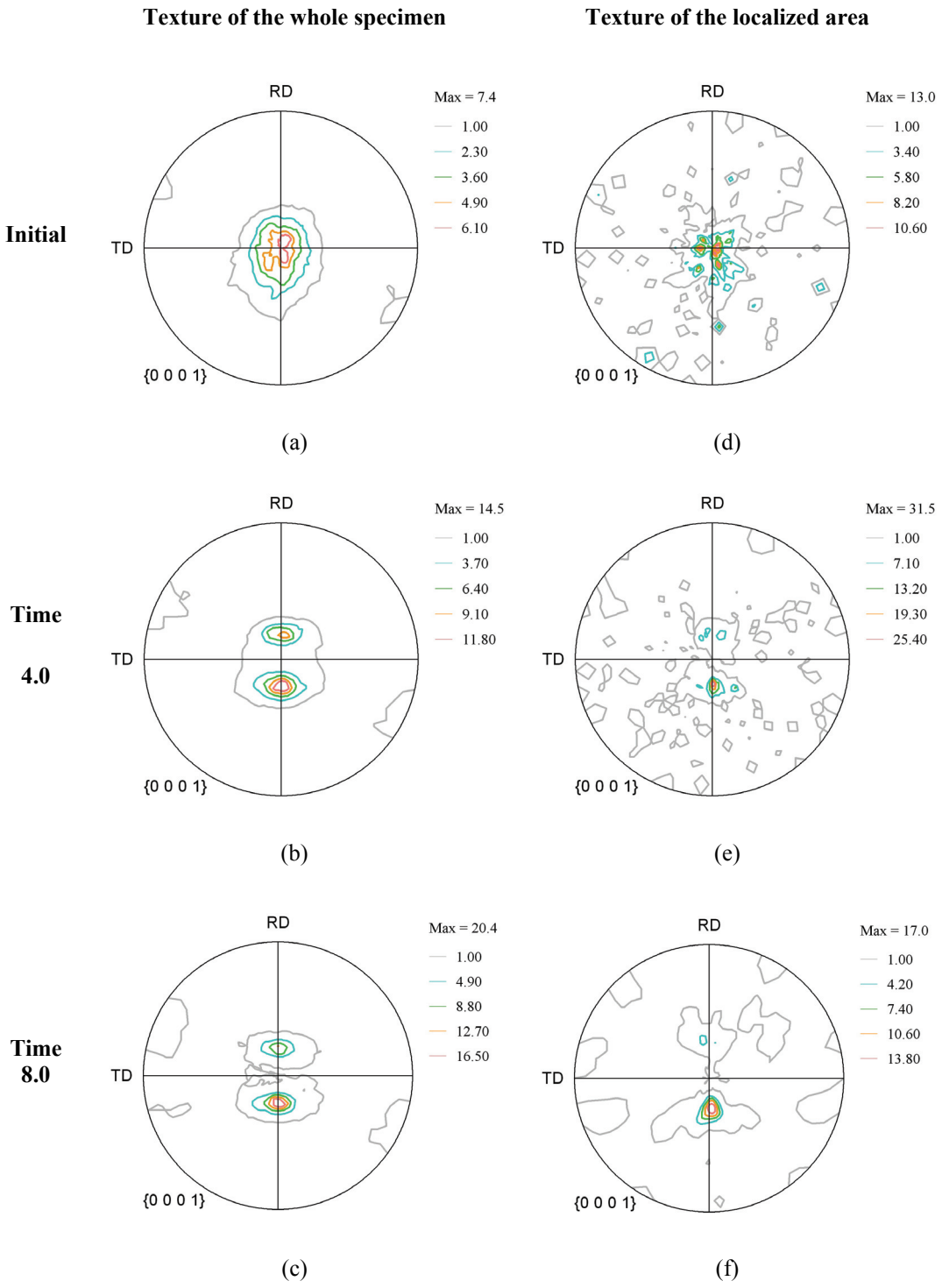

Figure 6.14 Comparing the texture evolution in the whole specimen and the localized area (LH 01Reshuff 01)

In Fig. 6.16, similar to the previous case (Fig. 6.13), slip system activity shows localization first in the pyramidal<c+a> and basal<a> followed by the pyramidal<a> and prismatic<a> slip systems. Regarding the texture evolution, it is seen in Fig. 6.17 that the higher maximum intensity of basal texture in the localized area, initially and at peak stress, is repeated for this case as well. However, in this case, unlike the hardening one (LH 01), the final basal pole figure in the localized area still shows a higher maximum intensity compared to that of the entire specimen. This implies the high degree of localization that occurs both in the strain and slip system activity in the localized area after the UTS. The high degree of localization was also observed in the deformed shapes of this case, shown in Fig. 6.4.

Figures 6.18 to 6.20 show the results for the sample with higher initial hardening rate assumed on slip systems (HH01). The results are very similar to the original sample (LH01, Figs. 6.9-6.11). This shows the independence of the results of the assumed hardening rate. In this case, however, the difference in the slip system activity in the localized area and the whole specimen is milder. Due to this lower slip system activity localization, the difference in maximum intensity of $\{0001\}$ pole figure in the localized area and the whole specimen is also less at peak stress.

In general, the observed trends for the initial local texture and its evolution throughout the deformation compared to those of the whole specimen are repeated in all the above simulations (Figs. 6.9-6.20). In other words, with the assumed set of slip resistances, the localized area consistently shows a local texture with a higher intensity of basal texture at the start of the experiments. Simulation results proved to be independent of the defined hardening rates and the assumed distribution of texture throughout the specimen. Maximum intensity in the basal pole figure increases for both the localized area and the whole specimen up to the onset of localization, where localized area reaches its maximum intensity of tilted basal texture. It is concluded that with the assumed slip system activity, this tilted orientation is a stable orientation for average grains in the localized area. After the onset of localization, the texture evolution in the localized area seems to be slower than that of the whole specimen in terms of the change in {0001} pole figure. In all the cases considered, localization in the activity of <c+a> slip system occurs before that of the other systems. The activity of all the slip systems remains higher in the localized area.

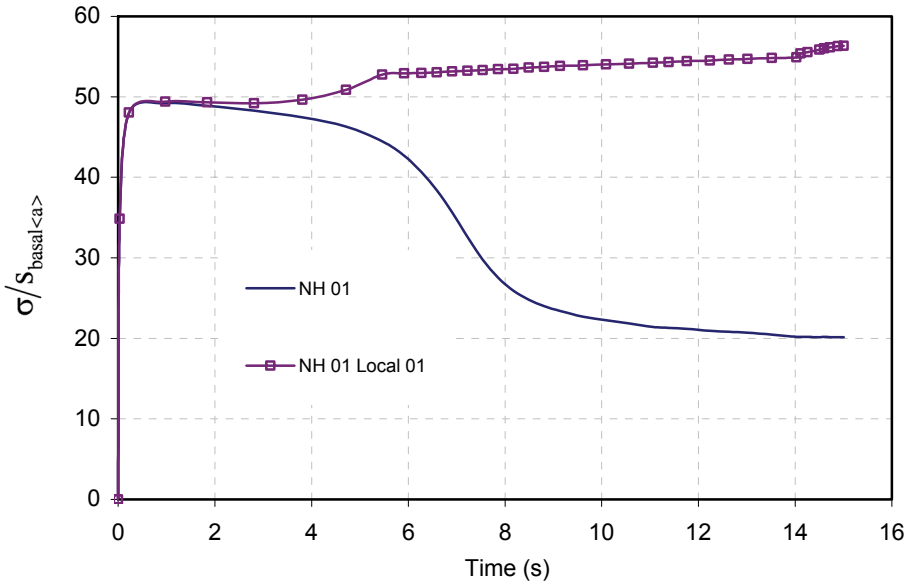

Figure 6.15 Comparing the change in the true stress (averaged over the elements) for the whole specimen and the localized area (NH 01)

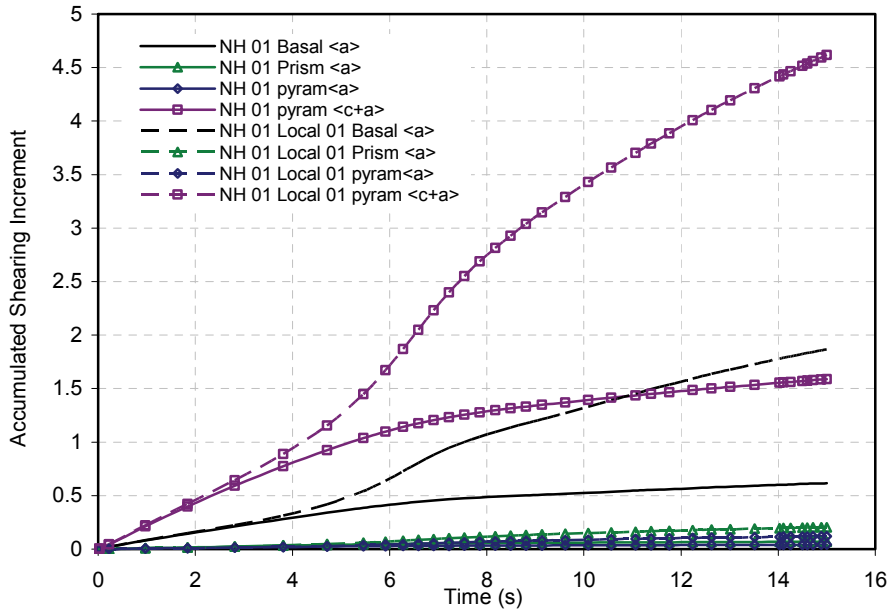

Figure 6.16 Comparing the activity of different slip system families for the whole specimen and the localized area (NH 01)

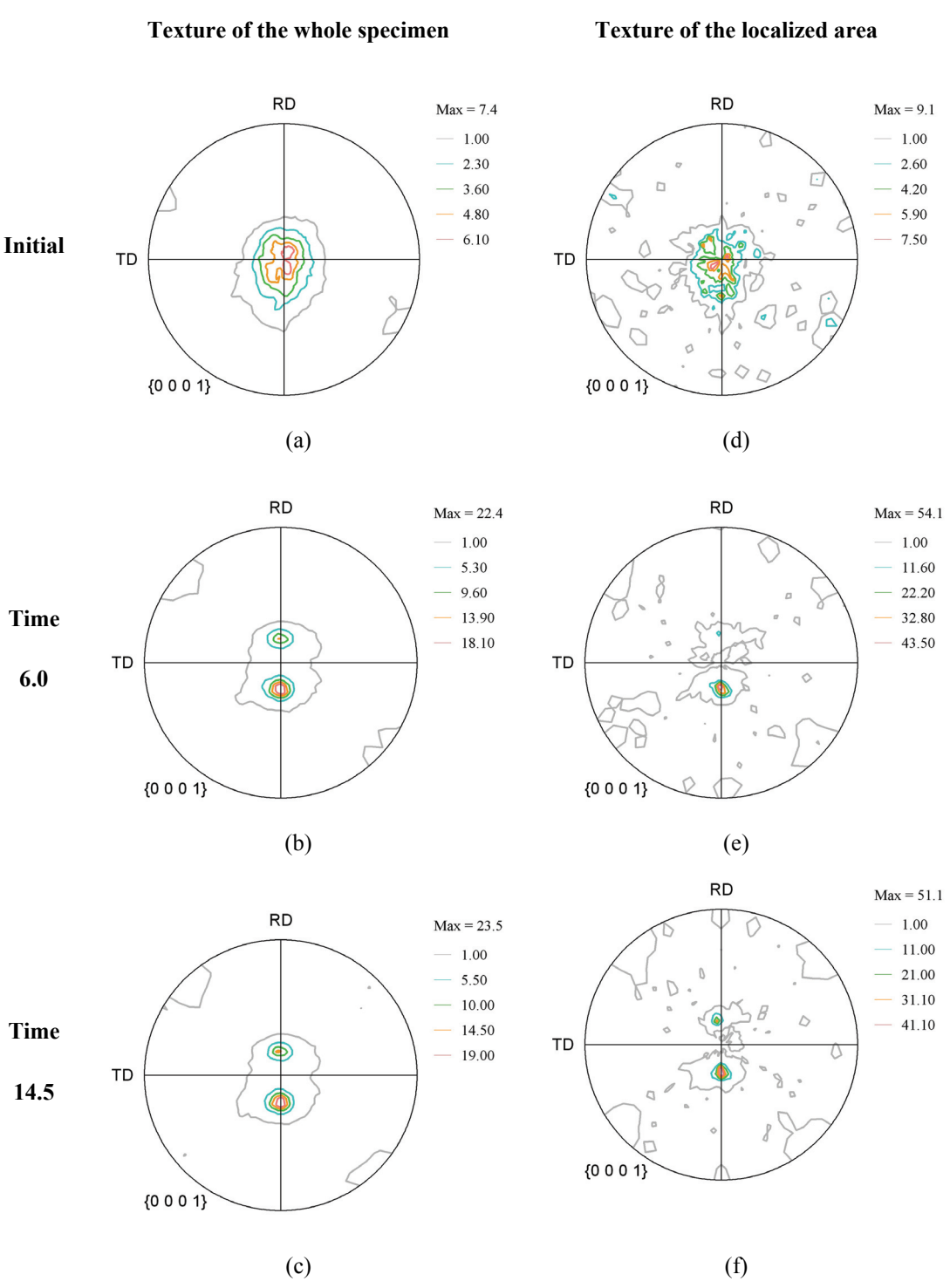

Figure 6.17 Comparing the texture evolution in the whole specimen and the localized area (NH 01)

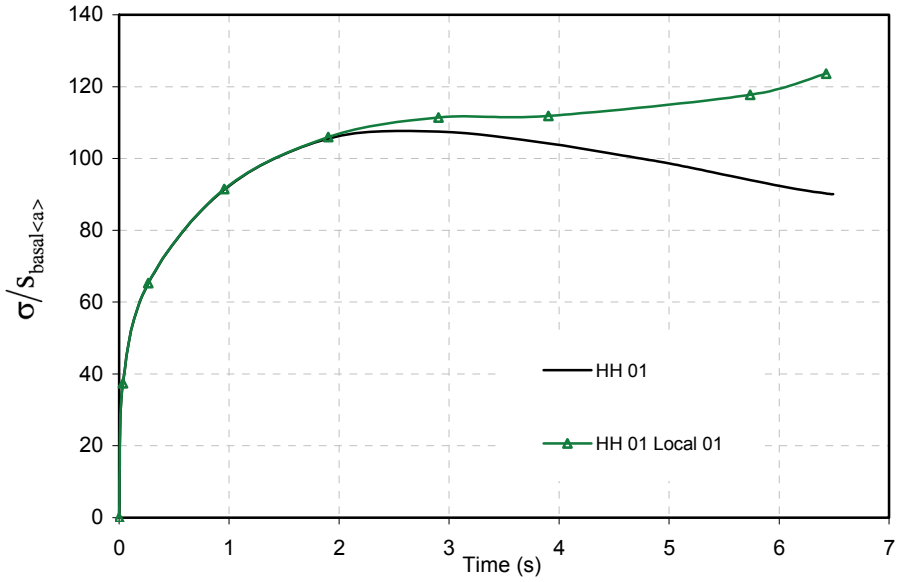

Figure 6.18 Comparing the change in the true stress (averaged over the elements) of the whole specimen and the localized area (HH 01)

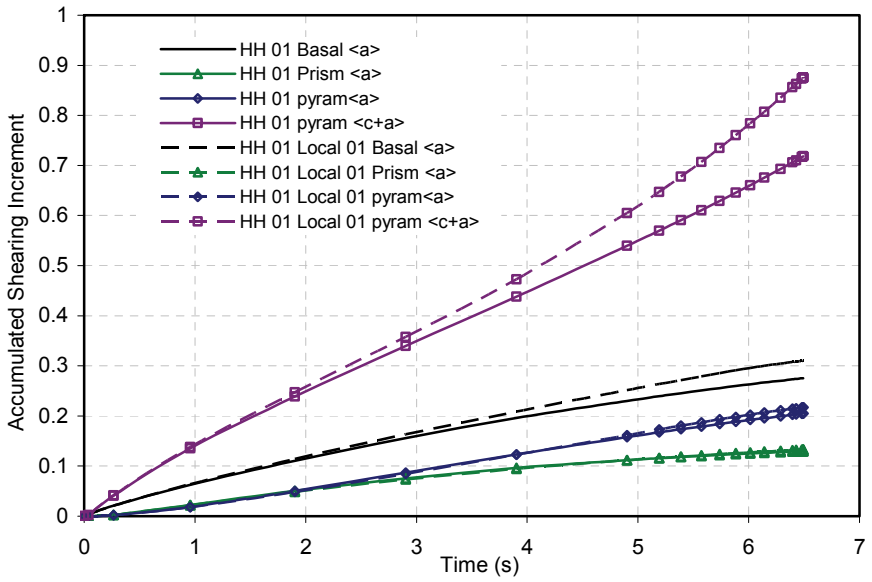

Figure 6.19 Comparing the activity of different slip system families for the whole specimen and the localized area (HH 01)

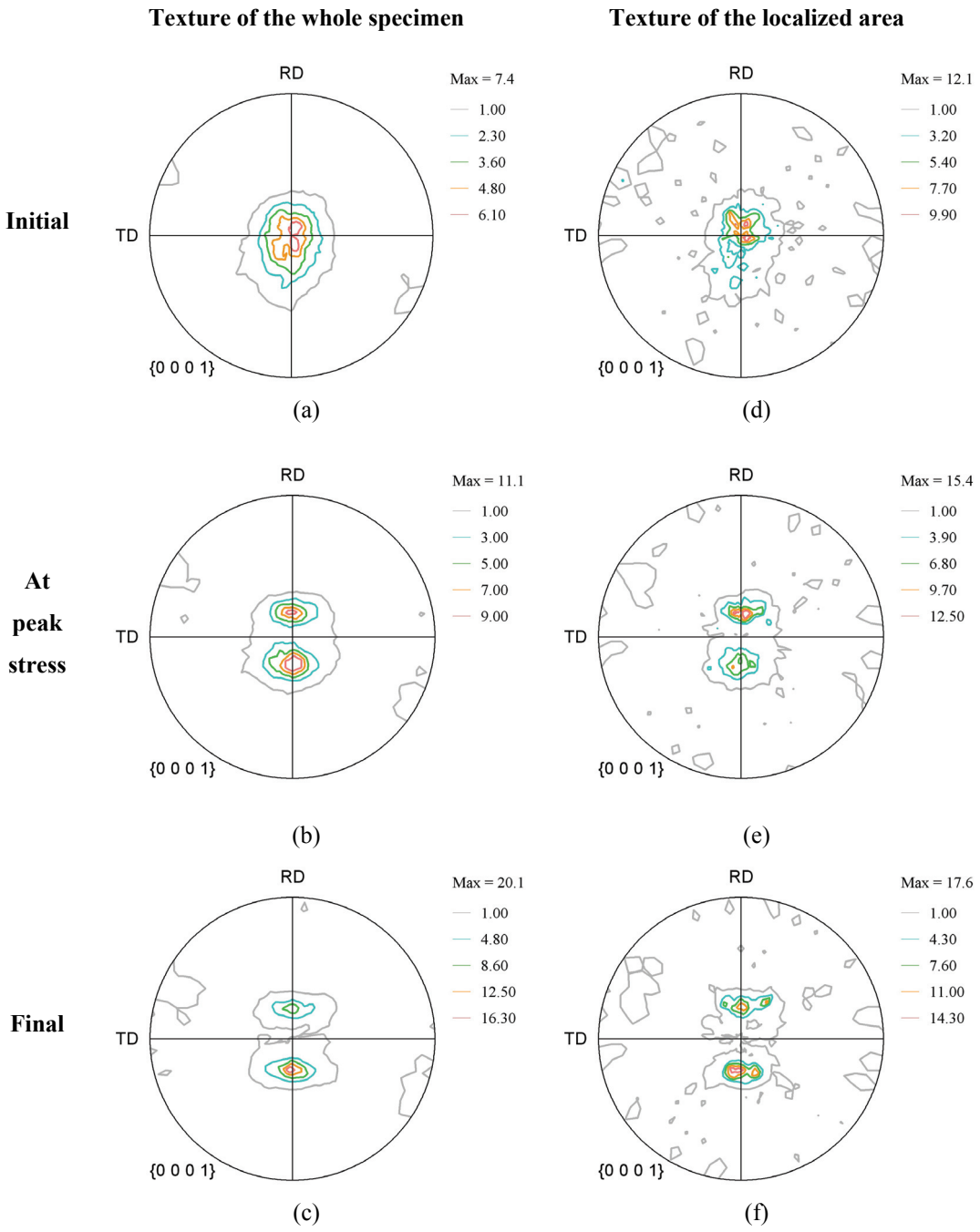

Figure 6.20 Comparing the texture evolution in the whole specimen and the localized area (HH01)

It is observed that a specific local texture in the necked area, caused by texture inhomogeneity, is the reason behind localization. The position of the neck changes with the change in the spatial distribution of texture, but the form of the initial texture of the necked area remains constant. It is, therefore, expected that a specimen with a more homogenized texture should show a better formability. In an attempt to visualize the

deformation of a specimen with a more uniform texture, an artificial texture distribution is created (using the texture of sample LH01 Reshuff01). This is done by assigning the texture of the localized area (and its distribution) to all parts of the specimen. Figure 6.21 compares the stress-strain curves and the deformed shapes of the specimen with the artificially generated texture (homogenized) and the original one. The new specimen shows a smoother deformed shape with a more diffused neck area (6.21c), which consequently leads to a more desirable stress-strain curve in the post-localization zone (Fig. 6.21a). It is obviously seen that the created texture greatly enhances the forming limit of the specimen. Therefore, a more uniform (homogenous) texture would be desirable during a forming process.

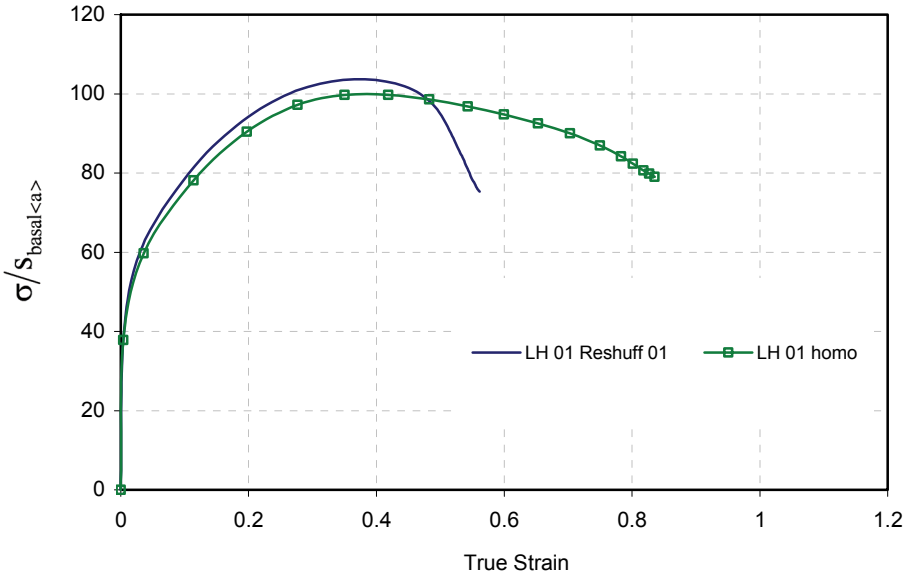

(a)

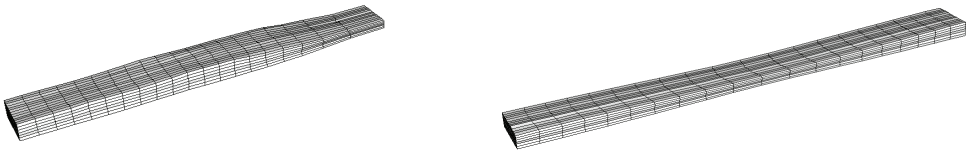

(b) (c)

Figure 6.21 (a) Comparing the stress-strain curves for specimens (b) with a basal texture and (c) with a "homogenized" texture

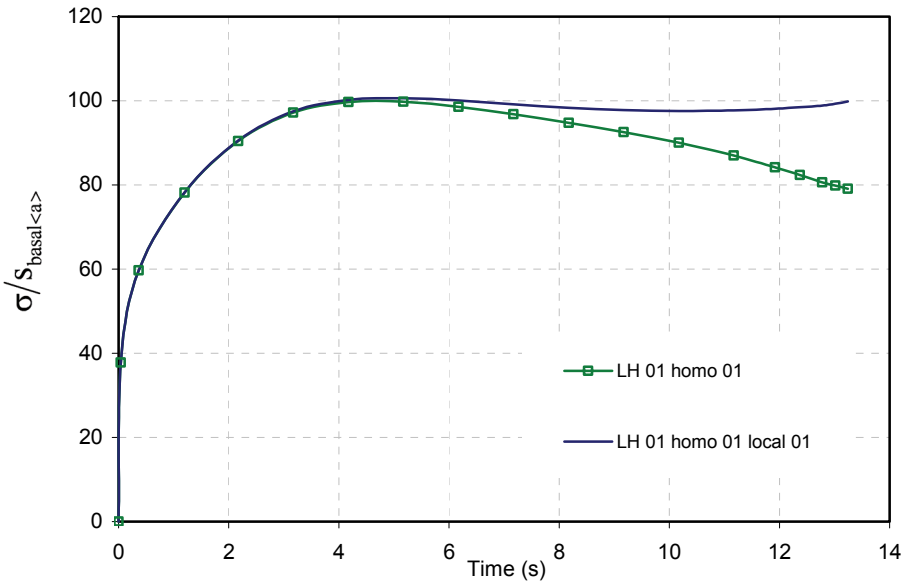

Figure 6.22 Comparing the change in the true stress (averaged over the elements) of the whole specimen and the localized area (LH 01 homo 01)

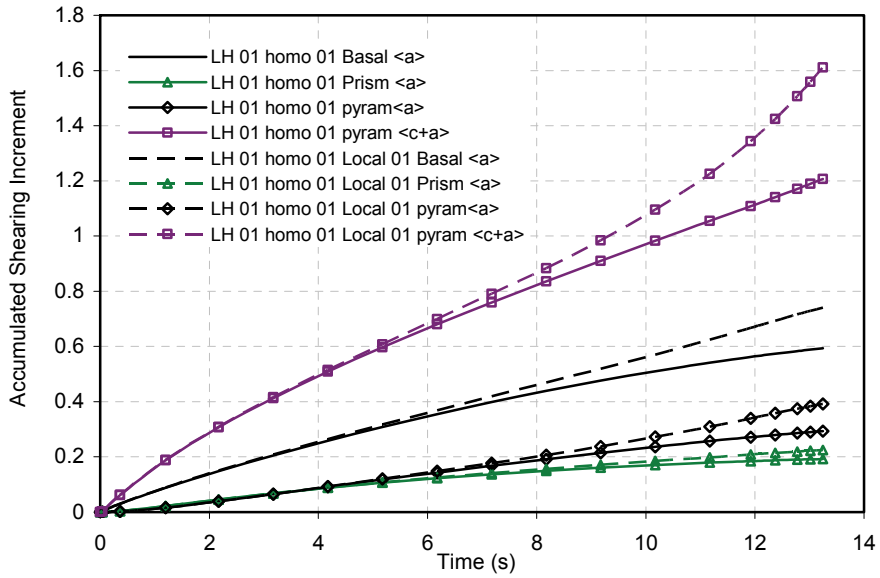

Figure 6.23 Comparing the activity of different slip system families for the whole specimen and the localized area (LH 01 homo 01)

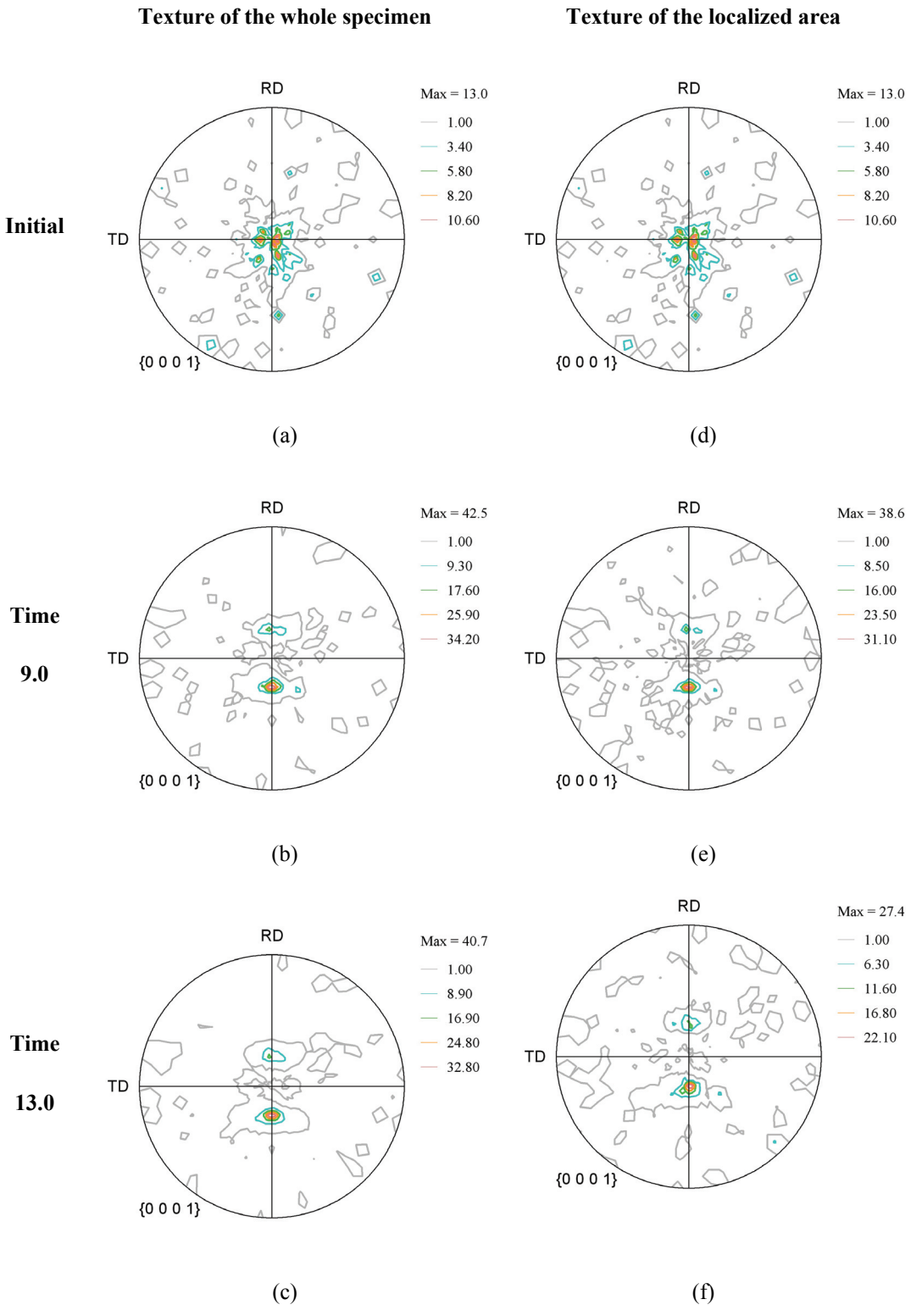

Figure 6.24 Comparing the texture evolution in the whole specimen and the localized area (LH 01 homo 01)

Figures 6.22-6.24 show the slip system activity and texture evolution in the localized area and the whole specimen for the "homogenized" specimen. As planned, the initial texture of the localized area and the whole specimen are exactly the same, but their evolutions are obviously different from each other, and also different from the non-homogenous case. It is interesting that in this case, the onset of localization for slip system activity (Fig. 6.23) is simultaneous with the strain localization (6.22). However, localization of slip system activity starts only at $t \approx 5$ s. The activity of pyramidal<c+a> is still seen to be higher than that of the other systems.

6.5 ACTIVE SLIP SYSTEMS AND LOCALIZATION

The role of slip systems in the overall behavior of Mg alloys has been previously discussed (see Chapter 5). Besides other aspects, slip resistance values affect the texture evolution and, as a result, the localization phenomenon in Mg alloys. In fact, a constant interaction occurs between the slip system activity and localization phenomenon, in which both sides affect each other. In this section, the interaction between slip system activity and the localization phenomenon is investigated. In Section 6.4, it was observed that a specific local texture would be observed in the necked area, regardless of the spatial distribution of orientations and hardening rate. This local texture is further investigated with different activity levels for slip systems.

It was seen in Chapter 5 that in Mg alloys, among other slip systems, the pyramidal<c+a> slip system plays a key role during the deformation, especially at higher temperatures. Therefore, in this section special attention is paid to the role of <c+a> slip systems. A series of simulations is performed with different slip resistance values assumed for the pyramidal<c+a> relative to other slip systems. The slip resistance values assumed in the simulations are listed in Tables 6.2 and 6.3; stress-strain curves are shown in Figs. 6.25 and 6.26, respectively. In Table 6.2, the slip resistance of <c+a> systems is assumed to be constant while different values of prismatic<a> and pyramidal<a>, which are taken equal, are considered. In contrast, in Table 6.3, the value of <c+a> slip resistance is changing and the other two are assumed to be constant. Except for the slip resistance values, the other parameters are taken to be the same as those defined for LH01 in Table 6.1. In all

the simulations, $s_{pyram<a>}/s_{prism<a>}$ is taken to be one. It can be seen in Figs. 6.25 and 6.26 that the largest strain to localization is predicted for the case of $s_{pyram<c+a>}/s_{prism<a>}=1$; as this ratio moves away from 1 in either direction, the localization strain decreases.

Table 6.2 Slip resistance values of different families; change in prismatic<a> and pyramidal <a>

	$\frac{s_{prism<a>}}{s_{basal<a>}}$	$\frac{s_{pyram<a>}}{s_{basal<a>}}$	$\frac{s_{pyram<c+a>}}{s_{basal<a>}}$	$\frac{s_{pyram<c+a>}}{s_{prism<a>}}$
SS 01 (LH 01)	15	15	5	1/3
SSE 02	5	5	5	1
SSE 03	2.5	2.5	5	2

Table 6.3 Slip resistance values of different slip families; change in pyramidal<c+a>

	$\frac{s_{prism<a>}}{s_{basal<a>}}$	$\frac{s_{pyram<a>}}{s_{basal<a>}}$	$\frac{s_{pyram<c+a>}}{s_{basal<a>}}$	$\frac{s_{pyram<c+a>}}{s_{prism<a>}}$
SSE 03	2.5	2.5	5	2
SSE 04	2.5	2.5	7.5	3
SSE 05	2.5	2.5	15	6

To gain a better insight into the relation between slip system activity and the localization phenomenon, the results of the above-mentioned simulations are more closely studied. The deformed shapes and the texture in the whole specimen and in the localized area are shown in Figs. 6.27-6.31 at several points during the deformation for the different simulations listed in Tables 6.2 and 6.3. The simulation results for LH01 (SSE 01), previously presented in Fig. 6.10, is repeated in Fig. 6.27 for ease of reference. This figure depicts the case of $s_{pyram<c+a>}/s_{prism<a>}=1/3$. The features of the texture evolution in this case were discussed before.

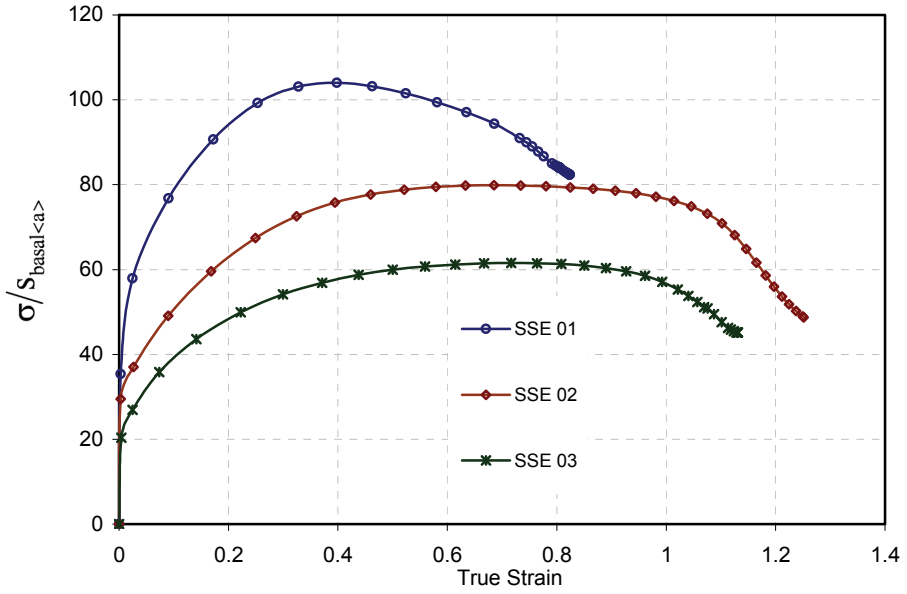

Figure 6.25 The change in the localization strain with the change in the relative activity of <c+a> to other slip systems (slip resistances defined in Table 6.2)

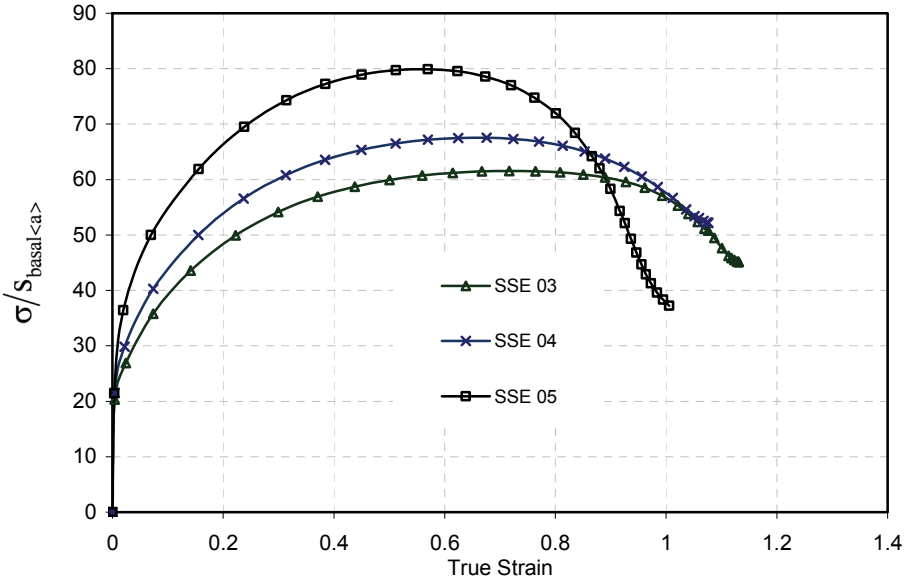

Figure 6.26 The change in the localization strain with the change in the relative activity of <c+a> to other slip systems (slip resistances defined in Table 6.3)

In Figs. 6.28 to 6.31, the assumed ratio, $s_{pyram<c+a>}/s_{prism<a>}$, increases from 1 to 2, 3, and 6, respectively. Figure 6.28 shows the case of $s_{pyram<c+a>}/s_{prism<a>}=1$. In this case, initially the maximum intensity of the basal pole figure in the necked area is 15.8 compared to 7.4 for the whole specimen. This higher intensity (and increase in that) is observed up to the onset of localization, where a split in the basal pole figure is observed. This split remains for the whole specimen as well as the localized part throughout the deformation. An interesting observation regarding the deformed shape is the shift in the deformation mode in the localized area, compared to the ones observed in previous sections. While in the previous cases (e.g. LH01 in Fig. 6.4), the main thinning in the necked area was seen to be in the ND; in this case, it occurs both in the ND and TD (Fig. 6.28i and 6.28m).

Figure 6.29 shows the case of $s_{pyram<c+a>}/s_{prism<a>}=2$, with the activity of <c+a> further lowered. In this case, the initial texture of the necked area still shows a higher intensity of basal texture compared to the whole specimen. The texture evolution follows a trend similar to the previous ones, except for the fact that in the final basal pole figures, the average c-axis is tilted less towards the RD. Also, the difference in maximum intensities between the localized area and the whole specimen at the onset of localization is less pronounced. The final deformed shape (6.29m) clearly shows that the thinning has become stronger in the TD compared to the ND, which is in agreement with the discussion presented for Fig. 6.28.

With further decrease in the activity of the pyramidal<c+a> slip system in Fig. 6.30 ($s_{pyram<c+a>}/s_{prism<a>}=3$), the tilt in the final pole figures is nearly removed (Fig. 6.30j and k), and the thinning is even more apparent in the TD rather than the RD (Fig. 6.30m).

Finally, Fig. 6.31 shows the case of $s_{pyram<c+a>}/s_{prism<a>}=6$. In this case, the main feature of the pole figures previously observed is still present: the higher intensity of the basal pole figure for the necked area, initially and up to the localization point. The tilt in the final pole figure is totally removed in this figure. Moreover, the thinning in the ND compared to the TD becomes negligible.

Comparing the final textures of the whole specimen in Figs. 6.28 to 6.31, it is observed that with the decrease in the activity of the <c+a> slip system, the tilt in the basal texture toward the RD decreases and finally disappears in Fig. 6.31. As mentioned in Appendix A, a distinct tilt is observed in the experimentally measured $\{0001\}$ pole figures at the mid-plane of AZ31B hot-rolled plates. This tilt disappears at the surface. This can be attributed to the higher activity of <c+a> slip systems at the mid-plane compared to the surface, which is justified by the higher temperatures at the mid-plane during the rolling. It is expected that the surface cools down at much faster rates than the inner points located at the mid-plane, and, thus, has a lower temperature. (it should be noted that the deformation mode also changes from the mid-plane to the surface and affects the results.)

In general, and by comparing Figs. 6.28 to 6.31, it is seen that with the activity of different systems, the location of the neck changes. Also, depending on the active systems, the deformation mode changes, and the main thinning may occur in either the RD or the TD. However, it is seen that the trend observed in the previous section regarding the higher intensity of basal texture in the localized area compared to the whole specimen holds true for all cases. This difference becomes more distinct when the <c+a> is more active compared to the other systems. In other words, with higher activity of <c+a> slip systems, a basal texture would act as a trigger for localized deformation. Despite the initial texture in the localized area, its evolution greatly changes when <c+a> slip systems are less active (e.g. Fig. 6.31). In fact, although the higher initial intensity of basal texture exists in the localized area regardless of the assumed slip systems, the form of texture evolution changes with the assumed slip resistances. Overall, it is expected that the intensity of a certain local texture will be higher in the localized area and serve as the trigger for the strain-localization. In studying the in-plane tension of Mg alloy specimens cut from hot-rolled plates, this local texture seems to be one with higher intensity of basal texture. This knowledge would be of great help in identifying critical points, which can be the trigger for strain-loclaization, in the forming processes.

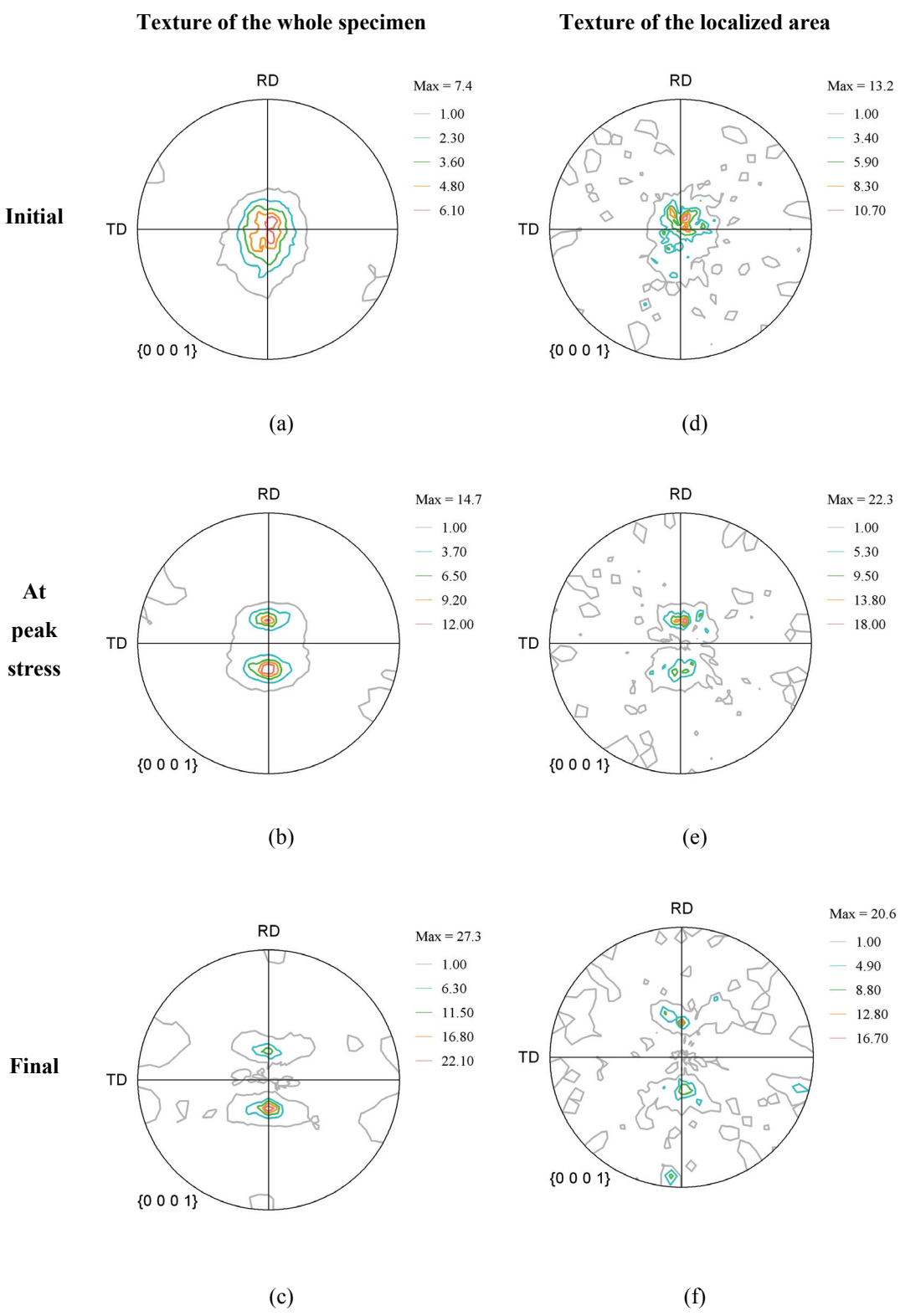

Figure 6.27 Comparing the texture evolution in the whole specimen and the localized area (LH 01)

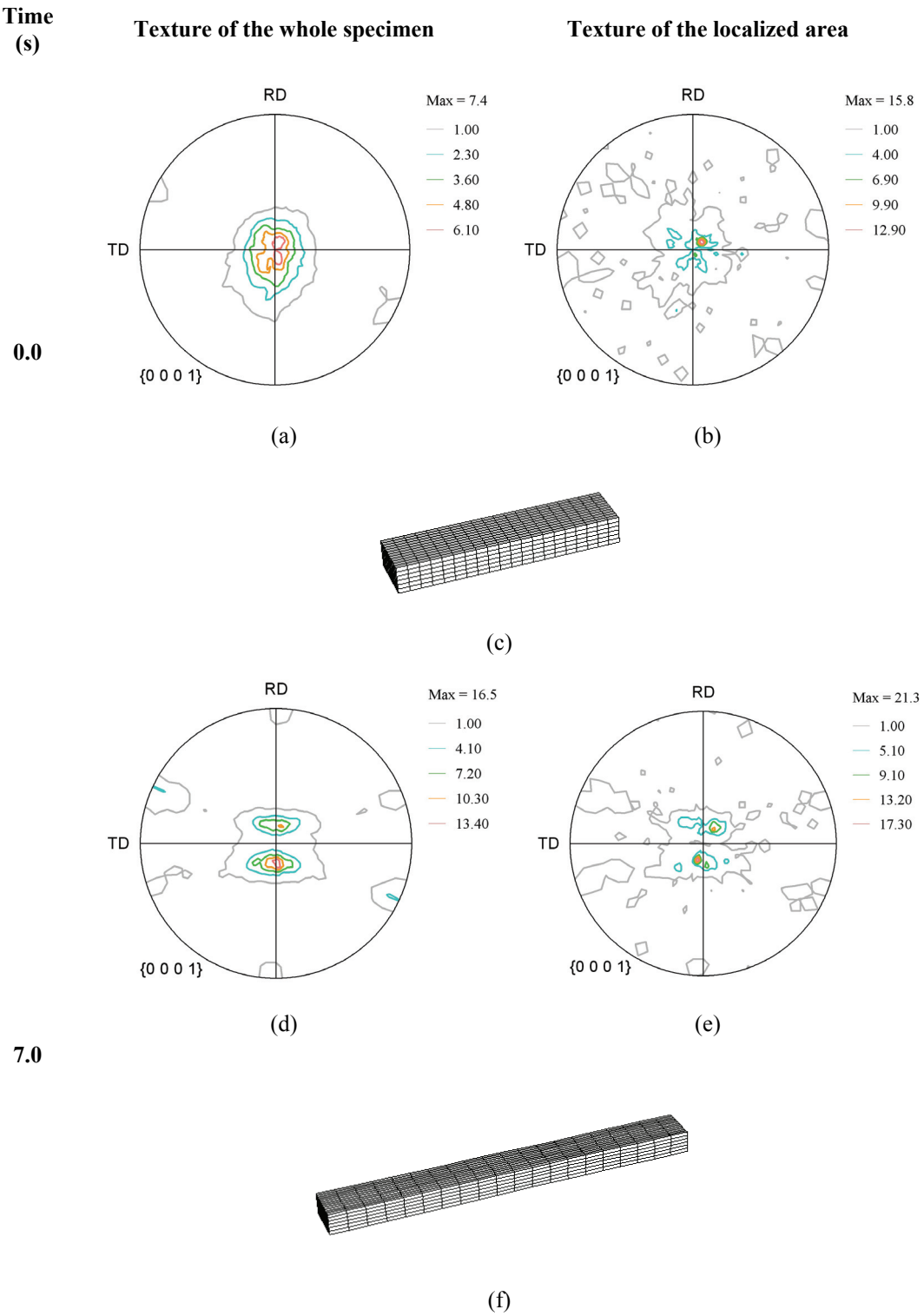

Figure 6.28 Comparing the texture evolution in the whole specimen and the localized area (SSE 02)

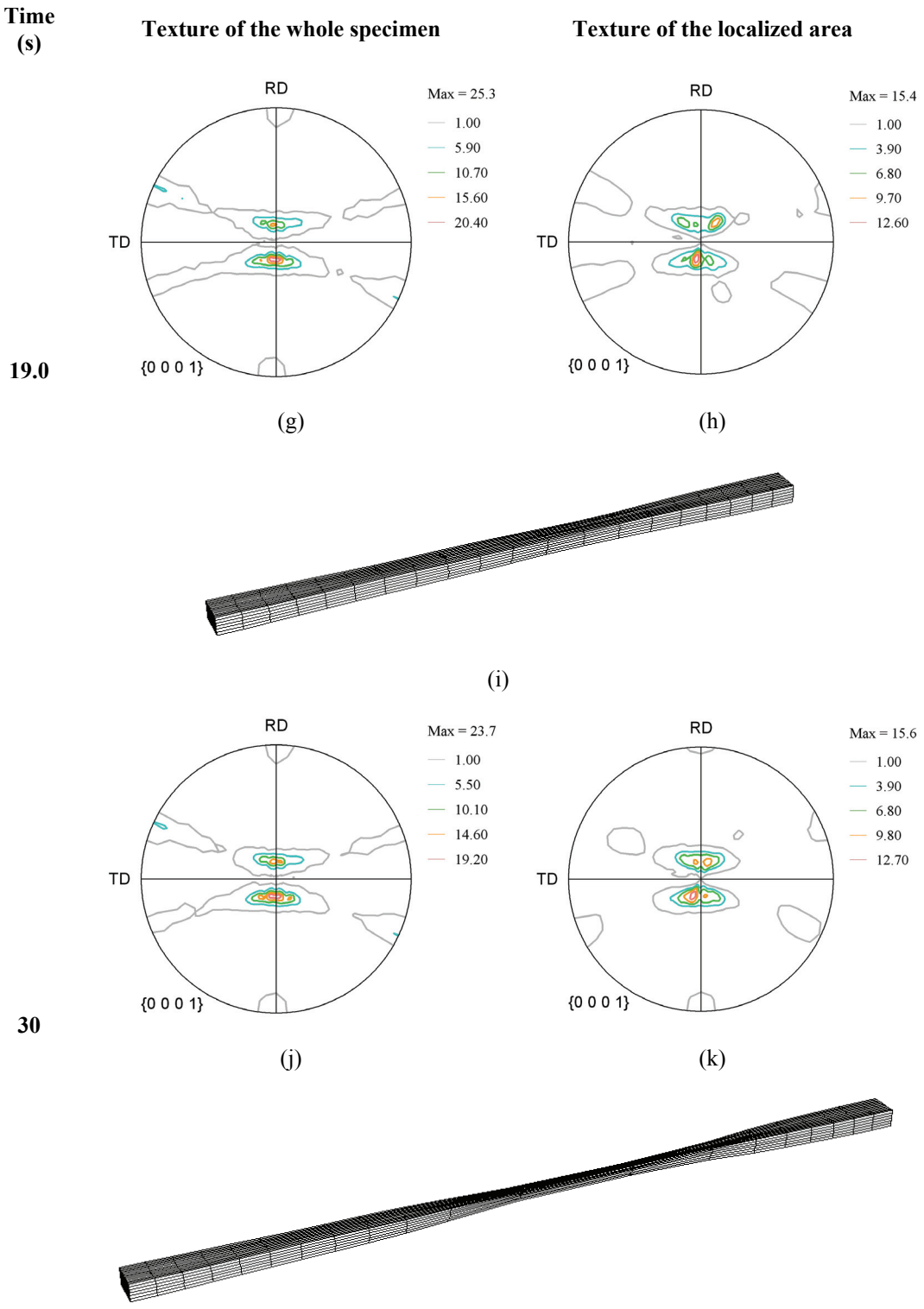

Figure 6.28 (cont'd) Comparing the texture evolution in the whole specimen and the localized area (SSE 02)

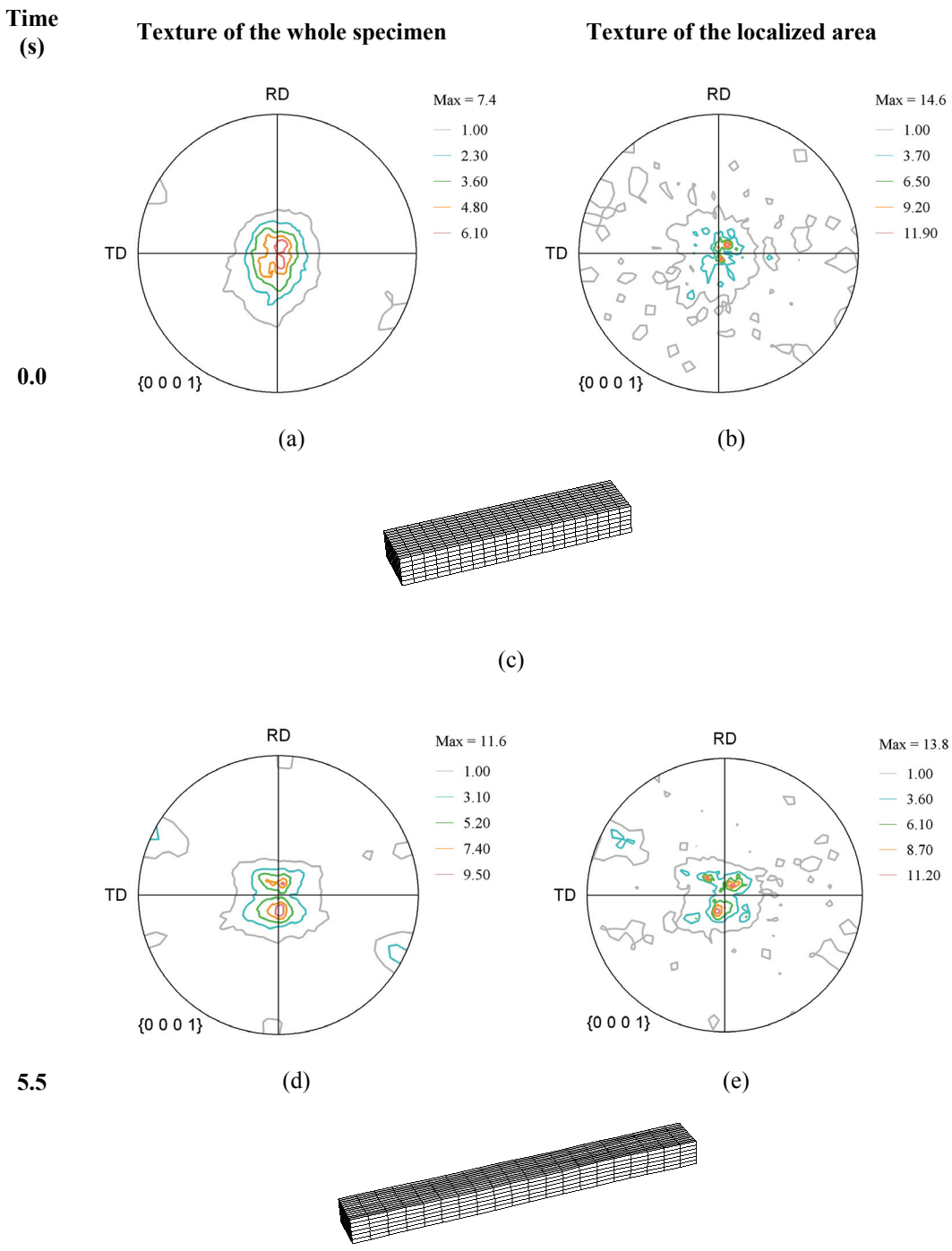

Figure 6.29 Comparing the texture evolution in the whole specimen and the localized area (SSE 03)

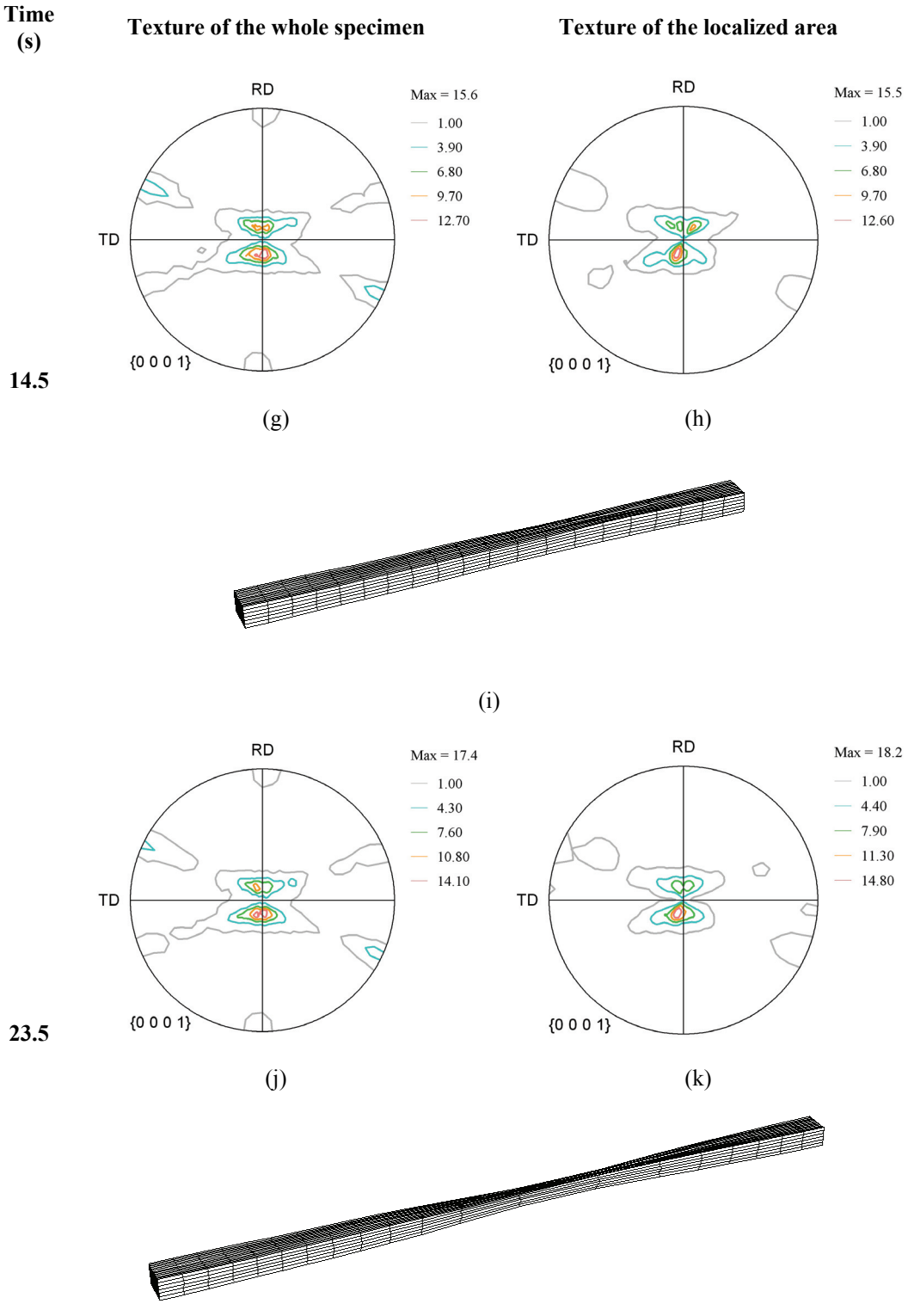

Figure 6.29 (cont'd) Comparing the texture evolution in the whole specimen and the localized area (SSE 03)

Time (s)	Texture of the whole specimen	Texture of the localized area
0.0	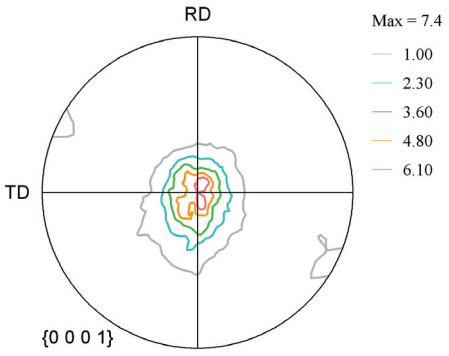 (a)	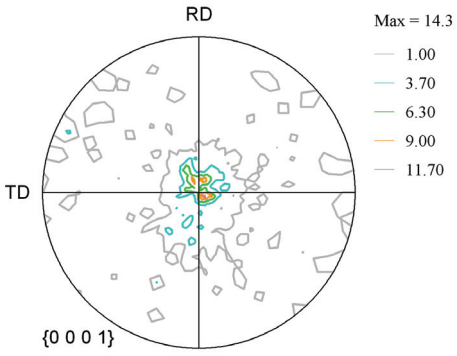 (b)
	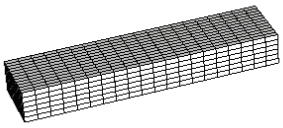 (c)	
5.5	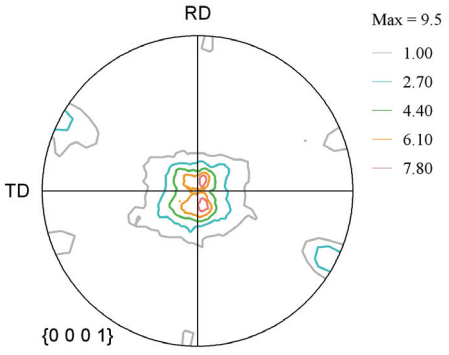 (d)	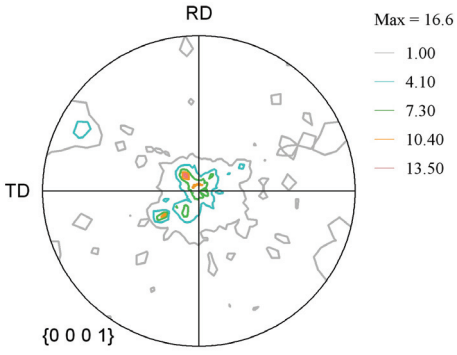 (e)
	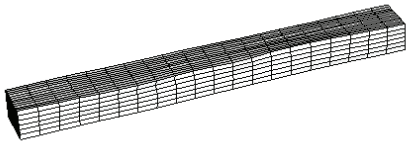 (f)	

Figure 6.30 Comparing the texture evolution in the whole specimen and the localized area (SSE 04)

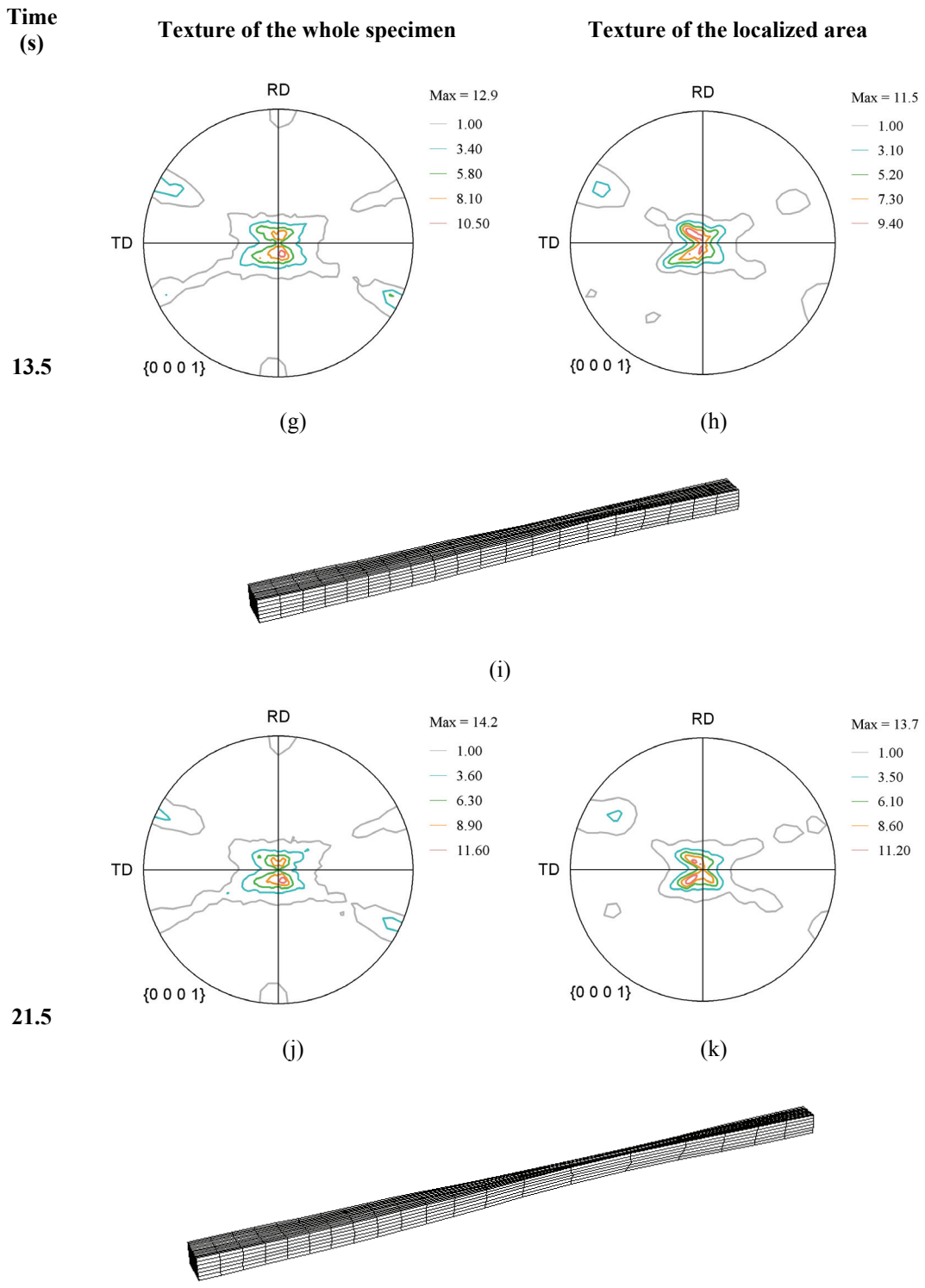

Figure 6.30 (cont'd) Comparing the texture evolution in the whole specimen and the localized area (SSE 04)

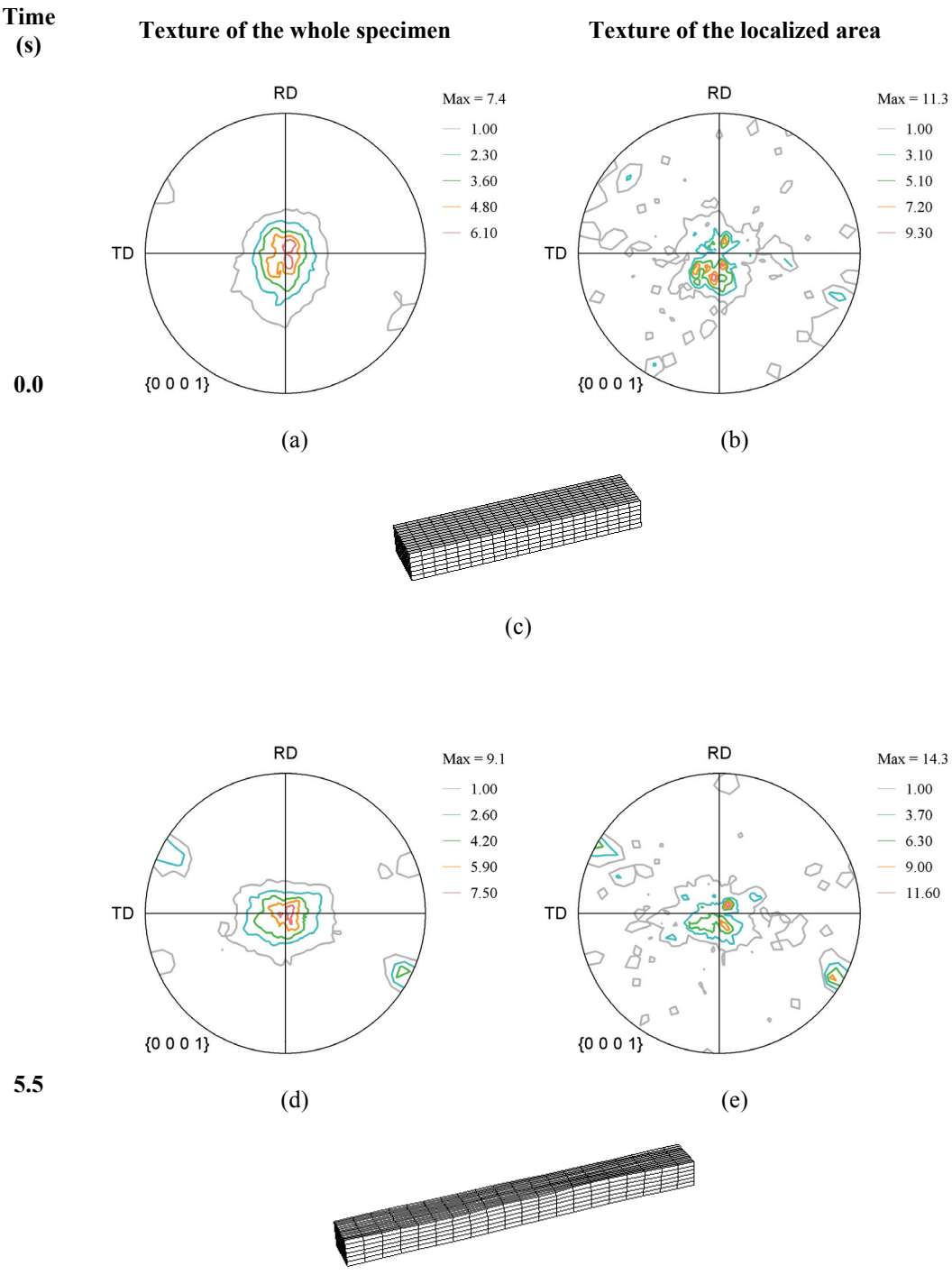

Figure 6.31 Comparing the texture evolution in the whole specimen and the localized area (SSE 05)

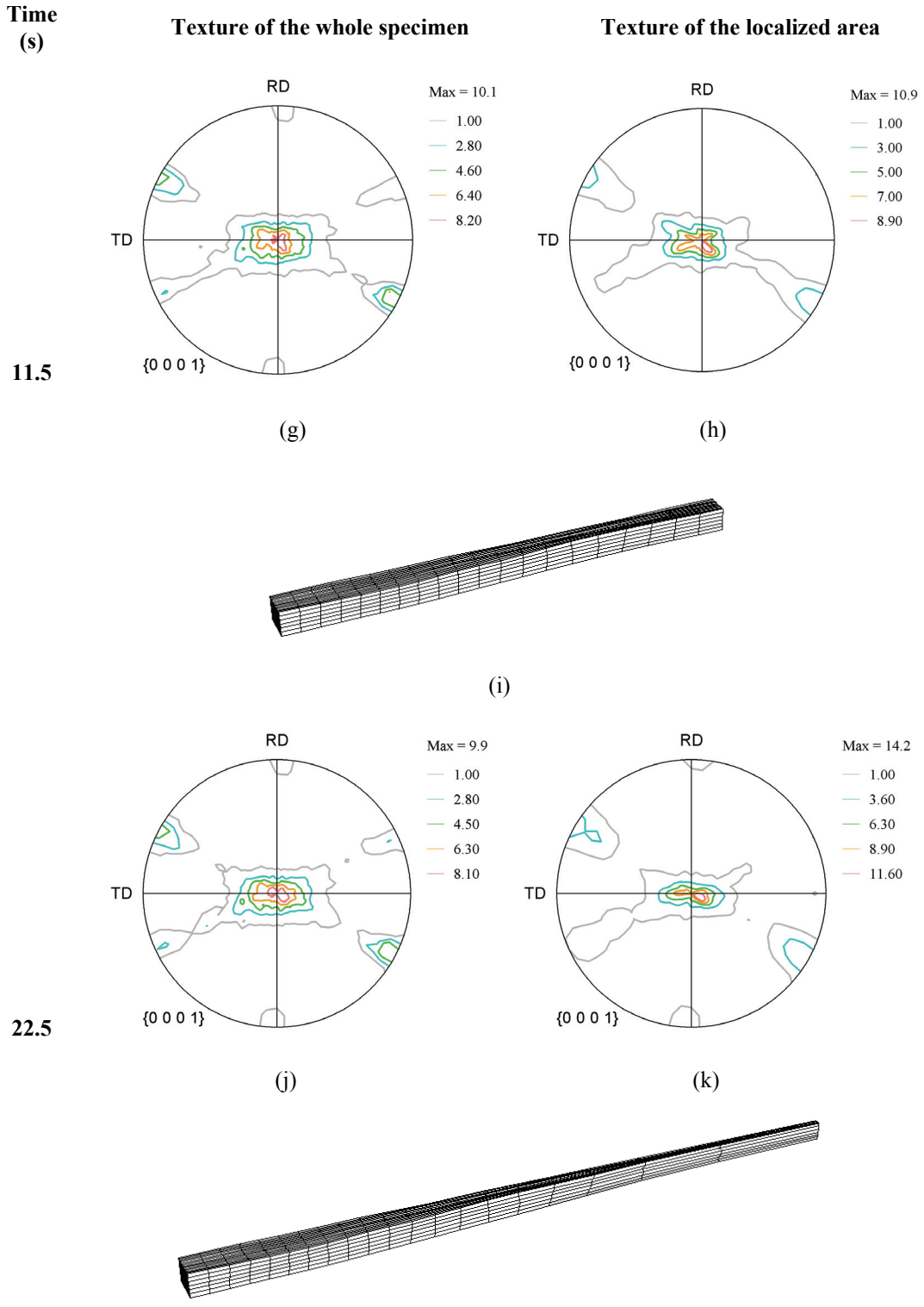

Figure 6.31 (cont'd) Comparing the texture evolution in the whole specimen and the localized area (SSE 05)

6.6 CONCLUSIONS

Using 3D rate-dependent CPFE modeling, the localization and post-localization behavior of Mg alloys has been studied. The link between local texture and slip system activity with localization phenomenon was investigated. Simulations were performed for Mg alloy specimens with the texture of a hot-rolled plate loaded under tension in the RD. Determining the effect of local texture, simulations were repeated with random redistribution of crystal orientation over the elements, keeping the overall initial texture constant. It was observed that some random distribution of the Euler angles can lead to local textures that accommodate localization at a lower strain compared to other distributions. In addition, for the reasonable hardening values incorporated in the model, the difference between the stress-strain curves was observed only in the post-localization area. Therefore, other than overall initial texture, distribution of orientation over the specimen (spatial distribution of texture) greatly affects the post-localization behavior.

The localized area was closely studied by tracking the texture evolution and slip system activity inside the localized area during the deformation and comparing them with the texture evolution and slip system activity of the specimen as a whole. It is observed that localization is triggered by the higher intensity of particular textures in the localized area. Therefore, the location of necking changes with the change in the distribution of orientations, which changes the location of that specific texture. The assumed set of active slip systems and their slip resistance values determine the expected form of texture evolution in the localized area. For in-plane tension of Mg alloy specimens cut from hot-rolled plates, this local texture is concluded to be one with a higher intensity of basal texture.

Chapter 7
Conclusions

7.1 INTRODUCTION

In this thesis, micro- and macro- mechanical behavior of Mg alloys, particularly at warm temperatures, was extensively investigated using crystal plasticity finite element (CPFE) modeling. The roles of strain-rate sensitivity and individual slip systems (slip resistance values) on the micro- and macro-levels were investigated and new relations were proposed for their dependence on temperature and strain-rate. Also, localization phenomenon observed in the simulations and experiments were studied in detail, and the relationship between the onset of localization and specimen characteristics were established. The findings greatly enhance our knowledge of slip system activity in the pre- and post-localization zones in Mg alloys, and can be used in improving the formability of these materials at different temperatures and strain-rates.

This chapter summarizes and concludes the thesis. The plan of the chapter is as follows. In the next section, Section 7.2, the work done is briefly reviewed, and the results obtained and the conclusions found are summarized. Section 7.3 is devoted to some contributions of this thesis to the knowledge. Finally, in Section 7.4 some recommendations are made for future work.

7.2 THE WORK DONE: RESULTS AND CONCLUSIONS

An exhaustive literature review was performed on the modeling methods available for anisotropic materials including Mg alloys. A summary of this review was presented in Chapter 2, where different crystal plasticity models were explained. Studying the advantages and shortcomings of different methods led to the choice of the crystal plasticity finite element (CPFE) approach for the purpose of modeling in the current project. Not only does this method take into account the initial texture of the material and its evolution with deformation, but it can also be used for solving complex loading cases which is common in forming processes. A review of the work done on the CPFE modeling (and modeling of slip systems and localization phenomenon in Mg alloys) was also presented in this chapter.

For modeling Mg alloys, a crystal plasticity model (in the form of a user-defined material subroutine, UMAT, originally written for the FCC materials) was then adopted, the theory of which was presented in Chapter 3. As a necessary first step, the algorithms of the constitutive equations were modified to be used for HCP materials. The subroutine was then modified to take into account the activity of different slip system families present in Mg alloys, and also the relations governing the hardening of different slip systems. Modifications were made both in the relations for the slip resistance values and strain-rate sensitivity, and in the hardening relations, all of which were implemented in the subroutine. The modifications were presented in Chapters 3 and 5. The modified subroutine was implemented in the commercial finite element software (ABAQUS). To verify the modified algorithms, some benchmark simulations were done for the case of magnesium single crystals with specific initial orientations and loading cases; the results were reported in Chapter 3.

Chapter 4 was devoted to the investigation of modeling issues for using the CPFE appropriately. In particular, the optimum size of the RVE (the effect of total number of grains), and the effects of grain inhomogeneity (number of elements per grain) and grain shape were considered. It was observed that in simulations, there should be a sufficient number of grains present to accurately model the texture without excessive variation from one simulation to another. It was concluded that increasing the number of grains

increases the level of stress until it reaches a plateau at approximately 1000 grains. Therefore, for consistent modeling of the texture in simulations, at least 1000 grains are ideally needed. With this number of grains, the stress-level variation from one simulation to another is less than 3 percent. On the other hand, for a small number of grains, increasing the number of elements per grain (El/Gr), or allowing inhomogeneity inside each grain, lowers the level of stress, until it reaches a plateau. It was observed that the main change happens by increasing the inhomogeneity from one element per grain to six (or eight) elements per grain; thus, 6 to 8 elements per grain will be sufficient for simulating the overall behavior of the material even with a small number of grains. The drop in the stress level for multiple elements per grain decreases with the increase in total number of grains. For 1000 grains, assigning multiple elements per grain does not affect the overall behavior of material significantly. It was concluded, therefore, that for simulations at a macro-level, 1 El/Gr is certainly sufficient for predicting the overall behavior of the material. Regarding the effect of grain shape on the overall behavior of the material, it was seen that the difference due to different grain shapes was not significant. Thus, it was concluded that cubic grains would be efficient for the purpose of this project. However, further studies are recommended in the future work section for a firm conclusion. The conclusions regarding the minimum RVE size and the required number of elements per grain are valid for HCP metals in general, and must be considered in the CPFE modeling of these materials.

In Chapter 5, the roles of slip systems and strain-rate sensitivity (SRS) in the deformation of Mg alloys were studied. The stress-strain curves and r-values (a measure of anisotropy of deformation) were obtained through a detailed computational study of slip systems under different conditions using the CPFE modeling. The results obtained on the role of slip systems in Mg alloys can be directly used for proposing more accurate models to simulate the mechanical behavior of these materials. Tension and/or compression simulations were done for magnesium specimens with random initial texture and also a texture of hot-rolled plate, loaded in the RD, TD and ND directions. It was observed that the decrease in the slip resistance value of the slip systems lowers the overall level of stress, except for the case of basal<a> slip system which has a negligible effect. Considering the effect of slip systems on r-values (in the in-plane tension simulations), it

was concluded that the increase in the activity of the prismatic<a> and the pyramidal<a> slip systems increases the r-values, while increasing the activity of the pyramidal<c+a> slip system decreases the r-values. Basal<a> slip had negligible effects in a range of reasonable slip resistance values. It was shown that higher activity of the pyramidal<c+a> slip system not only lowers the level of stress, but also decreases the r-value, which strongly supports the postulated increase in the activity of the <c+a> slip systems at higher temperatures. Findings regarding the role of different slip systems, in particular the pyramidal<c+a>, are not only utilized for proposing more accurate models for Mg alloys, but also can be used to improve the formability of these materials by intentional activation of specific slip systems. For instance, the addition of certain alloying elements which decrease the c/a ratio of Mg alloys crystal can increase the activity of pyramidal<c+a> slip systems.

Strain-rate sensitivity was shown to be an important factor which affects the behavior of Mg alloys both on the micro- and macro-levels. The values of strain-rate sensitivity for Mg alloys at different temperatures and strain-rates were presented in Chapter 5; it was observed that the strain rate-sensitivity factor, m, varies between about 0.01 at room temperatures to around 0.4-0.6 at high temperatures and low strain rates. Then the effect of this parameter on the micro- and macro-scale behavior of the material was discussed and its effects in the crystal plasticity modeling of Mg alloys were investigated. It was shown that there is a direct link between the strain-rate sensitivity assumed at the micro-scale and the computed values at the macro-scale. This is particularly important in assigning the strain-rate sensitivity values for the slip systems on the micro-scale using the experimentally measured values at the macro-level. It was shown that on micro-level, the increase in the strain-rate sensitivity leads to a more uniform distribution of the shearing increments on the slip systems. In other words, with the increase in m-value, more slip systems become active, leading to a more uniform, homogeneous deformation. On the macro-level, this increase in the uniformity of shearing increment distribution on slip systems causes a higher strain to localization, which leads to better formability of the material.

Also in Chapter 5, a series of relations were proposed for the change in the strain-rate sensitivity and slip resistance values of different systems with the change in temperature and strain rate. The proposed relations were implemented in the CPFE model and were used in the finite element simulations of Mg alloy behavior. Stress-strain curves and r-values were obtained for the tension tests done in both the RD and TD, and the results were predicted for a range of temperatures for Mg alloys, and were compared with the experimental data available in the literature. It was shown that employing the proposed relations for the evolution of slip resistance values and strain-rate sensitivity factor results in qualitatively correct predictions of the trends for the change in the stress-strain curves, and r-values with temperature. The simulations confirm the important role of slip systems at warm temperatures, particularly in the range of 100-200°C; therefore, the proposed relations can be used for simulating Mg alloy behavior over this range of temperatures. Also using these relations for predicting the effects of strain-rate change resulted in a decrease in the stress-level and an increase in the localization-strain with the decrease in the strain-rate, which is in agreement with available experimental results. In addition, the results provide the essential basis regarding the role of slip systems and their range of activity which can be used in a comprehensive model that takes into account all the deformation mechanisms (as proposed for future work in Section 7.4.2).

In the final stage of the work, in Chapter 6, a thorough study was done on the localization phenomenon in Mg alloys, seen both in the experiments reported in the literature and the simulations done in this study. A 3D rate-dependent crystal plasticity finite element model was used to investigate the localization and post-localization behavior of Mg alloys. The link between local textures, the assumed slip resistance values, the hardening parameters, and the localization phenomenon were studied.

Simulations were done for Mg alloys specimens with texture of a hot-rolled plate loaded under tension in the RD. To determine the effects of local texture, simulations were repeated with random redistribution of crystal orientation over the finite elements, while keeping the overall initial texture constant. It was observed that some random redistribution of the Euler angles can lead to local textures that accommodate localization easier and at a lower strain compared to other random redistributions. In addition, for the

realistic hardening values incorporated in the model, the difference between the stress-strain curves is significant only in the post-localization region. The localized region was studied closely by examining the texture evolution and slip system activity inside the localized region. Then the texture evolution and slip system activity of the entire specimen were compared to those of the localized region. It was observed that localization is a direct result of the higher intensity of certain textures in the localized area and, therefore, the location of the neck changes with the change in the distribution of orientations. Moreover, it is the assumed set of active slip systems and their slip resistance values that determines the expected form of texture in the localized area; i.e. the change in the slip resistances changes the expected texture in the necked area. For the in-plane tension of Mg alloy specimens cut from hot-rolled plates, this local texture was concluded to be the ones with higher intensity of basal texture. This knowledge would be of great help in identifying critical points, which can trigger the localization, in the forming processes.

7.3 ORIGINAL CONTRIBUTIONS

Precise modeling of Mg alloys response and the activity of various deformation mechanisms in these metals is still in its early stages. This work provides some of the critical background required for the correct modeling of Mg alloys, and forms a basis for predicting behavior of Mg sheets during and after forming processes. Modifying the available framework of the CPFE modeling and utilizing it, this project sought to determine the aspects of Mg alloy behavior that are caused and/or affected by the activity of slip systems. The in-depth study on the role of slip systems and the obtained results advance our knowledge of the micro-scale deformation in Mg alloys. This knowledge is used for improving the modeling of these materials at the macro-level.

The work clarifies the optimum size of the RVE and the required number of elements per grain in the CPFE modeling of HCP metals. The conclusions are critical to correctly model the mechanical response of these materials using the CPFE model and must be considered. The work also explains the role of strain-rate sensitivity in the micro- and macro-level response of Mg alloys. The conclusions regarding the effect of strain-rate

sensitivity on the slip system activity are used in the modeling of these materials. The result linking the micro- and macro-scale values of strain-rate sensitivity is critically used for assigning the m-values at the micro-scale from the experimental measurements.

This thesis improves upon existing magnesium models by establishing new relationships for the evolution of slip resistances and strain rate sensitivity with changes in temperature and strain rate. The proposed relations can be used for predicting Mg alloys behavior over a range of warm temperatures. In addition, they provide the basis for a comprehensive model which correctly predicts Mg alloy behavior at various temperatures and strain-rates.

The thesis provides great insight into the localization phenomenon, the results of which can be used for preventing unexpected early localized necking and extending the forming limits of the material. In a systematic, novel approach, the strain-localization in Mg alloys was investigated, and post-localization behavior of the material was explained. By tracking slip system activity and texture evolution in the necked area, a hypothesis linking the localization phenomenon with the activity of different slip systems, the orientation of crystals in the necked area, and other determining parameters was proposed. The findings explain some phenomena observed in Mg alloys, such as different post-localization softening behaviors, in terms of slip system activity. Previously, most of these phenomena have been exclusively attributed to the activity of other deformation mechanisms such as dynamic recrystallization (DRX). The results are of significant practical importance in improving the forming limits of Mg sheets; for example, by postponing the onset of localization by employing more uniform textures, or by extending the forming to the post-localization zone under controlled conditions.

Results of this work have been disseminated in the form of papers that have been or will be published. A list of publications is given in Appendix B.

7.4 RECOMMENDATIONS FOR FUTURE WORK

Considering the work done during the period of this project and the findings, some tasks are proposed for the continuation of the work as follow,

7.4.1 EXPERIMENTAL INVESTIGATION OF LOCALIZATION

Experiments are recommended for more extensive verification of the conclusions made on localization. In particular, tension tests can be done for multiple specimens cut from a hot-rolled plate–which theoretically have the same initial textures but different distributions of local textures. In these tests, an in-situ tracking of texture development in and outside the localized area should be done, which is feasible using the neutron diffraction technique (e.g. Hartig *et al*., 2006). Since the location of the localized area is not known before the start of the experiment, texture measurement should be done at different points of the undeformed samples. As proposed in this thesis, the section with the highest intensity of the basal texture should be tracked. Also, different post-localization behaviors of samples with the same overall initial texture but different spatial distribution of orientations can be verified by these experiments.

Further experimental work can be done on the effects of temperature and strain-rate on the localization phenomenon. By comparing the simulation results for pre- and post-localization zones with the experimental ones, stronger conclusions can be made regarding the dominant deformation mechanisms in each zone.

7.4.2 MULTIPLE DEFORMATION MECHANISMS

As was mentioned in Chapter 1, different deformation mechanisms are shown to be active during the deformation of Mg alloys at warm temperatures. The exact range in which each of these deformation mechanisms are active and the degree to which they affect the mechanical behavior of Mg alloys is still a controversial issue and the subject of several studies. Different groups have tried to model these deformation mechanisms; however, there does not exist any single model which takes into account all the main four deformation mechanisms that are active in Mg alloys, namely, slip, twinning, GBS, and DRX. The models that are proposed for different deformation mechanisms can be used to determine when each of these systems is significantly active by comparing predictions with experimental results. Temperatures at which significant deviation from the actual result is observed should indicate that other mechanisms are dominant.

It is recommended that, ultimately, a project be defined with the goal of gathering the proposed models for different deformation mechanisms in one single model. The CPFE model used in this work, with its unique features mentioned before, seems to be an ideal choice for this task. However, considerable amount of research and time are needed for accomplishing this goal. The obtained model not only can be used to predict the behavior of Mg alloys at different temperatures, but also can be utilized in parallel with the experimental tests to determine the range of temperatures and/or strain rates in which each deformation mechanism is active and the extent of its effect.

7.4.3 TEMPERATURE GRADIENT AND FORMING PROCESSES

As the main goal of many works on Mg alloys is improving is formability, especially at lower temperatures, a precise modeling of different forming processes can be of particular importance. The CPFE provides the required tools to model complex geometries, loading cases and temperature gradients. The relations proposed for the change in the activity of slip systems at different temperatures and strain rates can be developed further. These relations can, then, be implemented into a model which accounts for temperature gradient. Using such a model, a forming process such as hot-rolling can be modeled more precisely, providing valuable information regarding the parameters affecting the forming process. This information, in turn, can help improve the forming process itself and, consequently, increase the formability of the material.

7.4.4 EXPERIMENTAL INVESTIGATION

The results obtained in Chapter 5 were compared with some results reported in the literature; however, more experimental investigation is needed to further study the role of different deformation mechanisms in Mg alloys. Therefore, as a recommendation for the continuation of this work, in a systematic approach, a series of experiments is proposed for the specimens cut from a hot-rolled plate and loaded in the RD and TD; the detailed plan for these experiments is presented in Appendix C.

7.4.5 GRAIN SIZE (SCALE EFFECTS) AND GRAIN SHAPE

The current modeling method does not take into account the grain size effect, and, thus, the obtained results are independent of the scale. Therefore, one proposed task is introducing scale effects in the current model to yields more realistic predictions. In particular, in the constitutive description utilized in this thesis, the influence of inter- and intra-granular inhomogeneities, which is the origin of scale dependent behavior, is not explicitly incorporated (Evers *et al*., 2004). In general, such inhomogeneities at the micro-scale can be caused by externally applied macroscopic gradients of plastic deformation, by the presence of grain boundaries locally obstructing the plastic deformation (Becker and Panchanadeeswaran, 1995), or by a combination of both. Some methods have been proposed in the literature for incorporating the scale-effect in the crystal plasticity models (e.g. Evers *et al*., 2004) which can be implemented in the current CPFE model. The modified model would then account for the effects of grain-size.

Another issue which can be accounted for is the grain shape. This subject was briefly addressed in Chapter 4, but for purpose of the current work it was shown that simple cubic form for the grains would be sufficient to observe the trends of interest. However, the shape of the assumed grains, and the orientation gradient between the adjacent grains can be of great importance in a number of studies, such as investigating the effect of very coarse grains on the mechanical behavior of materials. Ideally a 3D grain-generating code can be used for producing the grains needed in the simulations. This would introduce the grain-shape effect in the modeling, which should yield more realistic results.

References

Agnew, S. R., Yoo, M. H. and Tome, C. N., 2001, Application of texture simulation to understanding mechanical behavior of Mg and solid solution alloys containing Li or Y, Acta Materialia, 49(20), 4277-89.

Agnew, S. R. and Duygulu, O., 2005, Plastic anisotropy and the role of non-basal slip in magnesium alloy AZ31B, International Journal of Plasticity, 21(6), 1161-1193.

Anand, L., 1982, Constitutive equations for the rate-dependent deformation of metals at elevated temperatures, Journal of Engineering Materials and Technology, Transactions of the ASME, 104(1), 12-17.

Anand, L., 1992, Rate dependent crystal plasticity: user material subroutine to be used with ABAQUS v5.8.

Anand, L. and Kalidindi, S. R., 1994, Process of shear band formation in plane strain compression of FCC metals: effects of crystallographic texture, Mechanics of Materials, 17(2-3), 223-243.

Anand, L. and Kothari, M., 1996, Computational procedure for rate-independent crystal plasticity, Journal of the Mechanics and Physics of Solids, 44(4), 525-558.

Anand, L., Balasubramanian, S. and Kothari, M., 1997, Constitutive modeling of polycrystalline metals at large strains, C. Teodosiu, Large deformation of crystalline aggregates, Springer, 376: 109-172.

Anand, L., 2004, Single-crystal elasto-viscoplasticity: Application to texture evolution in polycrystalline metals at large strains, Computer Methods in Applied Mechanics and Engineering, 193(48-51), 5359-5383.

Asaro, R. J., 1983, Micromechanics of crystals and polycrystals, Advances in Applied Mechanics, 23, 1-115.

Asaro, R. J. and Needleman, A., 1985, Texture development and strain hardening in rate dependent polycrystals, Acta Metallurgica, 33(6), 923-953.

Avedesian, M. M. and Baker, H., 1999, Magnesium and magnesium alloys, ASM International.

Balasubramanian, S. and Anand, L., 1996, Single crystal and polycrystal elasto-viscoplasticity: application to earing in cup drawing of FCC materials, Computational Mechanics, 17(4), 209-225.

Balasubramanian, S. and Anand, L., 2002a, Elasto-viscoplastic constitutive equations for polycrystalline FCC materials at low homologous temperatures, Journal of the Mechanics and Physics of Solids, 50(1), 101-126.

Balasubramanian, S. and Anand, L., 2002b, Plasticity of initially textured hexagonal polycrystals at high homologous temperatures: Application to titanium, Acta Materialia, 50(1), 133-148.

Barbe, F., Forest, S. and Cailletaud, G., 2001, Polycrystalline plasticity under small strains: Toward finer descriptions of microstructures, Cargese, France, Kluwer Academic Publishers, 191-206

Barnett, M. R., 2001, Influence of deformation conditions and texture on the high temperature flow stress of magnesium AZ31, Journal of Light Metals, 1(3), 167-177.

Barnett, M. R., 2003, A Taylor model based description of the proof stress of magnesium AZ31 during hot working, Metallurgical and Materials Transactions A: Physical Metallurgy and Materials Science, 34 A(9), 1799-1806.

Barnett, M. R., Davies, C. H. J. and Ma, X., 2005, An analytical constitutive law for twinning dominated flow in magnesium, Scripta Materialia, 52(7), 627-632.

Bassani, J. L. and Wu, T. Y., 1991, Latent hardening in single crystals II. Analytical characterization and predictions, Proceedings of the Royal Society of London, Series A (Mathematical and Physical Sciences), 435(1893), 21-41.

Bassani, J. L., 1994, Plastic flow of crystals, Advances in applied mechanics, 30, 191-258.

Becker, R. and Panchanadeeswaran, S., 1995, Effects of grain interactions on deformation and local texture in polycrystals, Acta Metallurgica et Materialia, 43(7), 2701-2719.

Becker, R., 1998, Effects of strain localization on surface roughening during sheet forming, Acta Materialia, 46(4), 1385-401.

Belytschko, T., Bazant, Z. P., Hyun, Y. W. and Chang, T. P., 1986, Strain-softening materials and finite-element solutions, Computers and Structures, 23(2), 163-180.

Bishop, J. F. W. and Hill, R., 1951, A theory of the plastic distortion of a polycrystalline aggregate under combined stresses, Philosophical Magazine, 42, 414-427.

Boyle, K. P. and Curtin, W. A., 2005, Grain interactions in crystal plasticity, Detroit, MI, USA, AIP, 433-8

Bronkhorst, C. A., Kalidindi, S. R. and Anand, L., 1992, Polycrystalline plasticity and the evolution of crystallographic texture in FCC metals, Philosophical Transactions of the Royal Society, Series A (Physical Sciences and Engineering), 341(1662), 443-77.

Brown, D. W., Agnew, S. R., Bourke, M. A. M., Holden, T. M., Vogel, S. C. and Tome, C. N., 2005, Internal strain and texture evolution during deformation twinning in magnesium, Materials Science and Engineering A, 399(1-2), 1-12.

Brown, S. B., Kim, K. H. and Anand, L., 1989, An internal variable constitutive model for hot working of metals, International Journal of Plasticity, 5(2), 95-130.

Buchheit, T. E., Wellman, G. W. and Battaile, C. C., 2005, Investigating the limits of polycrystal plasticity modeling, International Journal of Plasticity, 21(2), 221-49.

Budiansky, B. and Wu, T. T., 1962, Theoretical prediction of plastic strains of polycrystals, Fourth Congress Applied Mechanics, New York, ASME, 1175-85

Burke, E. C. and Hibbard, J. W. R., 1952, Plastic deformation of magnesium single crystals, American Institute of Mining and Metallurgical Engineers -- Journal of Metals, 4(3), 295-303.

Burke, M. A. and Nix, W. D., 1979, Numerical study of necking in the plane tension test, International Journal of Solids and Structures, 15(5), 379-393.

Canova, G. R., Fressengeas, C., Molinari, A. and Kocks, U. F., 1988, Effect of rate sensitivity on slip system activity and lattice rotation, Acta Metallurgica, 36(8), 1961-1970.

Chang, Y. W. and Asaro, R. J., 1981, An experimental study of shear localization in aluminium-copper single crystals, Acta Metallurgica, 29(1), 241-57.

Chen, W. H., 1971, Necking of a bar, International Journal of Solids and Structures, 7(7), 685-717.

Cheng, Y. Q., Chen, Z. H. and Xia, W. J., 2007, Drawability of AZ31 magnesium alloy sheet produced by equal channel angular rolling at room temperature, Materials Characterization, 58(7), 617-622.

Cole, G. and Quinn, J. F., 2007, Expanding the Application of Magnesium Components in the Automotive Industry: A Strategic Vision, SAE2007 World Congress, Detroit, Michigan, SAE,

Considere, M., 1885, Memoirs on the use of iron and steel in construction, Annales des Ponts et Chaussees, 574-775.

Daly, D., Duroux, P., Rachik, M., Roelandt, J. M. and Wilsius, J., 2007, Modelling of the post-localization behaviour in tube hydroforming of low carbon steels, Journal of Materials Processing Technology, 182(1-3), 248-256.

Davidenkov, N. N. and Spiridonova, N. I., 1946, Mechanical methods of testing, American Society for Testing Materials (ASTM), Philadelphia, PA, United States, 12

Dawson, P. R., Beaudoin, A. J., Jr. and Mathur, K. K., 1994, Finite element simulations of polycrystals, Chicago, IL, USA, ASME, 37-51

Dawson, P. R., 2000, Computational crystal plasticity, International Journal of Solids and Structures, 37(1-2), 115-130.

Dawson, P. R., Mika, D. P. and Barton, N. R., 2002, Finite element modeling of lattice misorientations in aluminum polycrystals, Scripta Materialia, 47(10), 713-717.

Dawson, P. R. and Tong-Seok, H., 2007, A two-scale deformation model for polycrystalline solids using a strongly-coupled finite element methodology, Computer Methods in Applied Mechanics and Engineering, 196(13-16), 2029-43.

Diard, O., Leclercq, S., Rousselier, G. and Cailletaud, G., 2005, Evaluation of finite element based analysis of 3D multicrystalline aggregates plasticity. Application to crystal plasticity model identification and the study of stress and strain fields near grain boundaries, International Journal of Plasticity, 21(4), 691-722.

Duygulu, O. and Agnew, S. R., 2003, The effect of temperature and strain rate on the tensile properties of textured magnesium alloy AZ31B sheet, H. Kaplan, Magnesium Technology 2003, TMS, San Diego, CA, United States: 237-242.

Engler, O., Huh, M. Y. and Tome, C. N., 2000, A study of through-thickness texture gradients in rolled sheets, Metallurgical and Materials Transactions A (Physical Metallurgy and Materials Science), 31A(9), 2299-315.

Eshelby, J. D., 1958, Twist in crystal whisker containing dislocation, Philosophical Magazine, 3(29), 440-447.

Evers, L. P., Brekelmans, W. A. M. and Geers, M. G. D., 2004, Scale dependent crystal plasticity framework with dislocation density and grain boundary effects, International Journal of Solids and Structures, 41(18-19), 5209-5230.

Gall, K., Lim, T. J., Mcdowell, D. L., Sehitoglu, H. and Chumlyakov, Y. I., 2000, The role of intergranular constraint on the stress-induced martensitic transformation in

textured polycrystalline NiTi, International Journal of Plasticity, 16(10-11), 1189-214.

Giessen, E. V. D., Wu, P. D. and Neale, K. W., 1992, On the effect of plastic spin on large strain elastic-plastic torsion of solid bars, International Journal of Plasticity, 8(7), 773-801.

Harren, S., Lowe, T. C., Asaro, R. J. and Needleman, A., 1989, Analysis of large-strain shear in rate-dependent face-centred cubic polycrystals: correlation of micro- and macromechanics, Philosophical Transactions of the Royal Society of London A (Mathematical and Physical Sciences), 328(1600), 443-500.

Hartig, C., Vogel, S. C. and Mecking, H., 2006, In-situ measurement of texture and elastic strains with HIPPO-CRATES, Materials Science and Engineering A (Structural Materials: Properties, Microstructure and Processing), 437(1), 145-50.

Hauser, F. E., Landon, P. R. and Dorn, J. E., 1955, Deformation and fracture mechanisms of polycrystalline magnesium at low temperatures, American Society for Metals -- Preprints19

Hecker, S. S., 1975, Formability of Aluminum alloys sheets, Journal of Engineering Materials and Technology, Transactions of the ASME, 97 Ser H(1), 66-73.

Hill, R., 1958, General theory of uniqueness and stability in elastic-plastic solids, Journal of the Mechanics and Physics of Solids, 6(3), 236-249.

Hill, R., 1965, Continuum micro-mechanics of elastoplastic polycrystals, Journal of Mechanics and Physics of Solids, 13(2), 89-101.

Hosford, W. F. and Caddell, R. M., 1993, Metal forming: mechanics and metallurgy, Prentice Hall.

Hutchinson, J. W., 1964, Plastic stress-strain relations of FCC polycrystalline metals hardening according to Taylor's rule, Journal of the Mechanics and Physics of Solids, 12(1), 11-24.

Hutchinson, J. W., 1976, Bounds and self-consistent estimates for creep of polycrystalline materials, Proceedings of the Royal Society of London. Series A, Mathematical and Physical Sciences, 348: 101-127.

Hutchinson, J. W. and Neale, K. W., 1977, Influence of strain-rate sensitivity on necking under uniaxial tension, Acta Metallurgica, 25(8), 839-46.

Inal, K., Wu, P. D. and Neale, K. W., 2000, Simulation of earing in textured aluminum sheets, International Journal of Plasticity, 16(6), 635-648.

Inal, K., Wu, P. D. and Neale, K. W., 2002a, Large strain behaviour of aluminium sheets subjected to in-plane simple shear, Modelling and Simulation in Materials Science and Engineering, 10(2), 237-252.

Inal, K., Wu, P. D. and Neale, K. W., 2002b, Instability and localized deformation in polycrystalline solids under plane-strain tension, International Journal of Solids and Structures, 39(4), 983-1002.

Inal, K., Wu, P. D. and Neale, K. W., 2002c, Finite element analysis of localization in FCC polycrystalline sheets under plane stress tension, International Journal of Solids and Structures, 39(13-14), 3469-3486.

Iwakuma, T. and Nemat-Nasser, S., 1984, Finite elastic-plastic deformation of polycrystalline metals, Proceedings of the Royal Society of London, Series A (Mathematical and Physical Sciences), 394(1806), 87-120.

Kalidindi, S. R., Bronkhorst, C. A. and Anand, L., 1991, On the accuracy of the Taylor assumption in polycrystalline plasticity, J. P. Boehler and A. S. Khan, Anisotropy and Localization of Plastic Deformation, Proceedings of Plasticity '91: The Third International Symposium on Plasticity and its Current Applications, London, Elsevier: 139-142.

Kalidindi, S. R., Bronkhorst, C. A. and Anand, L., 1992, Crystallographic texture evolution in bulk deformation processing of FCC metals, Journal of the Mechanics and Physics of Solids, 40(3), 537-69.

Kalidindi, S. R. and Anand, L., 1994, Macroscopic shape change and evolution of crystallographic texture in pre-textured FCC metals, Journal of the Mechanics and Physics of Solids, 42(3), 459-490.

Kalidindi, S. R., Salem, A. A. and Doherty, R. D., 2003, Role of deformation twinning on strain hardening in cubic and hexagonal polycrystalline metals, Advanced Engineering Materials, 5(4), 229-232.

Kaschner, G. C., Bingert, J. F., Liu, C., Lovato, M. L., Maudlin, P. J., Stout, M. G. and Tome, C. N., 2001, Mechanical response of zirconium - II. Experimental and finite element analysis of bent beams, Acta Materialia, 49(15), 3097-3108.

Keeler, S. P., 1968, Understanding sheet metal formability, Machinery (NY), 74(6-11).

Kelley, E. W. and Hosford, W. F., 1968, Plane-strain compression of magnesium and magnesium alloy crystals, Transactions of the Metallurgical Society of AIME, 242(1), 5-13.

Kim, S.-H., You, B.-S., Dong Yim, C. and Seo, Y.-M., 2005, Texture and microstructure changes in asymmetrically hot rolled AZ31 magnesium alloy sheets, Materials Letters, 59(29-30), 3876-3880.

Kleiner, S. and Uggowitzer, P. J., 2004, Mechanical anisotropy of extruded Mg-6% Al-1% Zn alloy, Materials Science and Engineering A, 379(1-2), 258-263.

Knockaert, R., Chastel, Y. and Massoni, E., 2002, Forming limits prediction using rate-independent polycrystalline plasticity, International Journal of Plasticity, 18(2), 231-47.

Kocks, U. F., Argon, A. S. and Ashby, M. F., 1975, Thermodynamics and kinetics of slip, B. Chalmers, J. W. Christian and T. B. Massalski, Progress in Materials Science, Oxford, Pergamon Press, 19: 231-234.

Kocks, U. F., 1976, Laws for work-hardening for work-hardening and low-temperature creep, Journal of Engineering Materials and Technology, Transactions of the ASME, 98(H1), 76-85.

Kothari, M. and Anand, L., 1998, Elasto-viscoplastic constitutive equations for polycrystalline metals: application to tantalum, Journal of the Mechanics and Physics of Solids, 46(1), 51-83.

Kroner, E., 1961, The new conceptions of the continuum mechanics of solid bodies, Physica Status Solidi, l(1), 3-16.

Lebensohn, R. A. and Tome, C. N., 1993, Self-consistent anisotropic approach for the simulation of plastic deformation and texture development of polycrystals: application to zirconium alloys, Acta Metallurgica et Materialia, 41(9), 2611-2624.

Lebensohn, R. A., Turner, P. A., Signorelli, J. W., Canova, G. R. and Tome, C. M., 1998, Individual and collective behavior of dislocations, Modelling and Simulation in Materials Science and Engineering, 6, 447-465.

Lee, D. and Zaverl, R., Jr., 1978, A generalized strain rate dependent constitutive equation for anisotropic metals, Acta Metallurgica, 26(11), 1771-80.

Lee, E. H., 1969, Elastic-plastic deformation at finite strains, Journal of Applied Mechanics, 36(1), 1-6.

Levesque, J., Inal, K., Neale, K. W., Mishra, R. K. and Luo, A. A., 2006, Numerical modelling of large strain deformation in magnesium, A. A. Luo, N. R. Neelameggham and R. S. Beals, Magnesium Technology 2006, TMS, San Antonio, TX, United States: 239-244.

Li, S., Van Houtte, P. and Kalidindi, S. R., 2004, A quantitative evaluation of the deformation texture predictions for aluminium alloys from crystal plasticity finite element method, Modelling and Simulation in Materials Science and Engineering, 12(5), 845-870.

Long, T. R. and Smith, C. S., 1957, Single-crystal elastic constants of magnesium and magnesium alloys, Acta Metallurgica, 5(4), 200-207.

Lou, X. Y., Li, M., Boger, R. K., Agnew, S. R. and Wagoner, R. H., 2007, Hardening evolution of AZ31B Mg sheet, International Journal of Plasticity, 23(1), 44-86.

Mandel, J., 1965, Generalization de theorie de la plasticite de W.T. Koiter, International Journal of Solids and Structures, 1, 273–295.

Mandel, J., 1972, Plasticite Classique et Viscoplasticite, CISM Courses and Lectures, No. 97, Berlin, Springer-Verlag.

Marciniak, Z. and Kuczynski, K., 1967, Limit strains in processes of stretch-forming sheet metal, International Journal of Mechanical Sciences, 9(9), 609-620.

Marin, E. B., Dawson, P. R. and Jenkins, J. T., 1995, Aggregate size effect on the predicted plastic response of hexagonal close-packed polycrystals, Modelling and Simulation in Materials Science and Engineering, 3(6), 845-64.

Marin, E. B. and Dawson, P. R., 1998a, On modelling the elasto-viscoplastic response of metals using polycrystal plasticity, Computer Methods in Applied Mechanics and Engineering, 165(1-4), 1-21.

Marin, E. B. and Dawson, P. R., 1998b, Elastoplastic finite element analyses of metal deformations using polycrystal constitutive models, Computer Methods in Applied Mechanics and Engineering, 165(1-4), 23-41.

Mathur, K. K. and Dawson, P. R., 1989, On modeling the development of crystallographic texture in bulk forming processes, International Journal of Plasticity, 5(1), 67-94.

Matin, P. H. and Smith, L. M., 2005, Practical limitations to the influence of through-thickness normal stress on sheet metal formability, International Journal of Plasticity, 21(4), 671-90.

Mika, D. P. and Dawson, P. R., 1998, Effects of grain interaction on deformation in polycrystals, Materials Science & Engineering A: Structural Materials: Properties, Microstructure and Processing, A257(1), 62-76.

Mikkelsen, L. P., 1997, Post-necking behaviour modelled by a gradient dependent plasticity theory, International Journal of Solids and Structures, 34(35-36), 4531-4546.

Myagchilov, S. and Dawson, P. R., 1999, Evolution of texture in aggregates of crystals exhibiting both slip and twinning, Modelling and Simulation in Materials Science and Engineering, 7(6), 975-1004.

Neale, K. W. and Chater, E., 1980, Limit strain predictions for strain-rate sensitive anisotropic sheets, International Journal of Mechanical Sciences, 22(9), 563-74.

Neale, K. W., Toth, L. S. and Jonas, J. J., 1990, Large strain shear and torsion of rate-sensitive FCC polycrystals, International Journal of Plasticity, 6(1), 45-61.

Neale, K. W., 1993, Use of crystal plasticity in metal forming simulations, International Journal of Mechanical Sciences, 35(12), 1053-1063.

Neale, K. W., Inal, K. and Wu, P. D., 2002, Numerical modelling of large-strain phenomena in polycrystalline solids, Key Engineering Materials, 233-236, 35-46.

Neale, K. W., Inal, K. and Wu, P. D., 2003, Effects of texture gradients and strain paths on localization phenomena in polycrystals, International Journal of Mechanical Sciences, 45(10), 1671-1686.

Needleman, A., 1972, A numerical study of necking in circular cylindrical bars, Journal of the Mechanics and Physics of Solids, 20(2), 111-27.

Needleman, A., 1988, Material rate dependence and mesh sensitivity in localization problems, Computer Methods in Applied Mechanics and Engineering, 67(1), 69-85.

Norris, D. M., Jr., Moran, B., Scudder, J. K. and Quinones, D. F., 1978, A computer simulation of the tension test, Journal of the Mechanics and Physics of Solids, 26(1), 1-19.

Parks, D. M. and Ahzi, S., 1990, Polycrystalline plastic deformation and texture evolution for crystals lacking five independent slip systems, Journal of the Mechanics and Physics of Solids, 38(5), 701.

Payne, H., Czyzak, S. J., Greiner, J. H. and Lin, T. H., 1958, A modification of Taylor's method for calculating the plastic stress-strain relation in face-centred cubic crystals, Journal of the Mechanics and Physics of Solids, 6(4), 314-320.

Peirce, D., Asaro, R. J. and Needleman, A., 1983, Material rate dependence and localized deformation in crytalline solids, Acta Metallurgica, 31(12), 1951-1976.

Pérez-Prado, M. T. and Ruano, O. A., 2002, Texture evolution during annealing of magnesium AZ31 alloy, Scripta Materialia, 46(2), 149-155.

Pi, H., Han, J., Tieu, A. K. and Jiang, Z., 2004, Current condition and development of crystal plasticity simulation in metal forming, Key Engineering Materials, 274-276(I), 637-642.

Pietruszczak, S. and Mroz, Z., 1981, Finite element analysis of deformation of strain-softening materials, International Journal for Numerical Methods in Engineering, 17(3), 327-34.

Prantil, V. C., Jenkins, T. J. and Dawson, P. R., 1995, Modeling deformation induced textures in titanium using analytical solutions for constrained single crystal response, Journal of the Mechanics and Physics of Solids, 43(8), 1283-302.

Prasad, Y. V. R. K. and Sasidhara, S., Eds, 1997, Hot working guide, a compendium of proceeding maps, ASM International

Raabe, D. and Roters, F., 2004, Using texture components in crystal plasticity finite element simulations, International Journal of Plasticity, 20(3), 339-361.

Raynor, G. V., 1959, The Physical Metallurgy of Magnesium and its Alloys, Pergamon Press.

Reed-Hill, R. E. and Robertson, W. D., 1957, Additional modes of deformation twinning in magnesium, Acta Metallurgica, 5(12), 717-727.

Reed-Hill, R. E. and Abbaschian, R., 1994, Physical Mettalurgy Principles, Boston, PWS Publ. Company.

Rice, J. R., 1971, Inelastic constitutive relations for solids: an internal-variable theory and its application to metal plasticity, Journal of the Mechanics and Physics of Solids, 19(6), 433-55.

Rice, J. R., 1977, The localization of plastic deformation, Proceedings of the 14th IUTAM Congress on Theoretical and Applied Mechanics, Delft, Netherlands, North-Holland: 207-20.

Roberts, C. S., 1960, Magnesium and its alloys, New York/London, Wiley.

Sachs, G., 1928, Condition of flow for the polycrystal derived from the shear stress law, Zeitschrift Verein Deutsche Ingenieure, 72, 734-736.

Saje, M., 1979, Necking of a cylindrical bar in tension, International Journal of Solids and Structures, 15(9), 731-742.

Sarma, G. B. and Dawson, P. R., 1996, Effects of interactions among crystals on the inhomogeneous deformations of polycrystals, Acta Materialia, 44(5), 1937-1953.

Savoie, J., Jain, M., Carr, A. R., Wu, P. D., Neale, K. W., Zhou, Y. and Jonas, J. J., 1998, Predictions of forming limit diagrams using crystal plasticity models, Materials Science and Engineering A: Structural Materials: Properties, Microstructure and Processing, A257(1), 128-133.

Schoenfeld, S. E., Ahzi, S. and Asaro, R. J., 1995, Elastic-plastic crystal mechanics for low symmetry crystals, Journal of the Mechanics and Physics of Solids, 43(3), 415-446.

Shahi, M. and Nemes, J. A., 2007, Crystal plasticity modeling of the slip systems activity in Mg alloys at higher temperatures, SAE SP, NUMB 2108, 49-56.

Simmons, G. and Wang, H., 1971, Single crystal elastic constants and calculated aggregate properties, Cambridge Mass, MIT Press.

Smith, W. F. and Hashemi, J., 2004, Foundations of Materials Science and Engineering, McGraw-Hill Professional.

Staroselsky, A. and Anand, L., 1998, Inelastic deformation of polycrystalline face centered cubic materials by slip and twinning, Journal of the Mechanics and Physics of Solids, 46(4), 671-696.

Staroselsky, A. and Anand, L., 1999, Modeling of inelastic deformation of FCC single- and polycrystalline materials with low stacking fault energies, Materials Research Society Symposium - Proceedings, 538, 515-521.

Staroselsky, A. and Anand, L., 2003, A constitutive model for HCP materials deforming by slip and twinning: application to magnesium alloy AZ31B, International Journal of Plasticity, 19(10), 1843-1864.

Staroselsky, A. V., 1998, Crystal plasticity due to slip and twinning, Mechanical Engineering Department, Massachusetts Institute of Technology, Doctoral dissertation.

Stoughton, T. B. and Xinhai, Z., 2004, Review of theoretical models of the strain-based FLD and their relevance to the stress-based FLD, International Journal of Plasticity, 20(8-9), 1436-86.

Stoughton, T. B. and Yoon, J. W., 2006, Review of Drucker's postulate and the issue of plastic stability in metal forming, International Journal of Plasticity, 22(3), 391-433.

Styczynski, A., Hartig, C., Bohlen, J. and Letzig, D., 2004, Cold rolling textures in AZ31 wrought magnesium alloy, Scripta Materialia, 50(7), 943-7.

Swift, H. W., 1952, Plastic instability under plane stress, Journal of Mechanics and Physics of Solids, 1(1), 1-18.

Taylor, G. I., 1938, Plastic strain in metals, Institute of Metals Journal, 62(1), 307-324.

Teodosiu, C., 1970, A dynamic theory of dislocations and its applications to the theory of the elastic-plastic continuum, Proceedings of the conference on fundamental

aspects of dislocation theory, Washington, DC, USA, National Bureau of Standards, II: 837-76.

Teodosiu, C. and Sidoroff, F., 1976, Theory of finite elastoviscoplasticity of single crystals, International Journal of Engineering Science, 14(2), 165-176.

Textools, 2002, Texture analysis software, Resmat Corp.

Thomason, P. F., 1969, An analysis of necking in axi-symmetric tension specimens, International Journal of Mechanical Sciences, 11(5), 481-90.

Tome, C. N., Lebensohn, R. A. and Kocks, U. F., 1991, Model for texture development dominated by deformation twinning: application to zirconium alloys, Acta Metallurgica et Materialia, 39(11), 2667-2680.

Tome, C. N., Maudlin, P. J., Lebensohn, R. A. and Kaschner, G. C., 2001, Mechanical response of zirconium - I. Derivation of a polycrystal constitutive law and finite element analysis, Acta Materialia, 49(15), 3085-3096.

Toth, L. S., Gilormini, P. and Jonas, J. J., 1988, Effect of rate sensitivity on the stability of torsion textures, Acta Metallurgica, 36(12), 3077-91.

Tugcu, P., Neale, K. W., Wu, P. D. and Inal, K., 2004, Crystal plasticity simulation of the hydrostatic bulge test, International Journal of Plasticity, 20(8-9), 1603-1653.

Tvergaard, V., 1978, Effect of Kinematic hardening on localized necking in biaxially stretched sheets, International Journal of Mechanical Sciences, 20(9), 651-658.

Tvergaard, V., Needleman, A. and Lo, K. K., 1981, Flow localization in the plane strain tensile test, Journal of the Mechanics and Physics of Solids, 29(2), 115-42.

Tvergaard, V., 1982, Influence of void nucleation on ductile shear fracture at a free surface, Journal of the Mechanics and Physics of Solids, 30(6), 399-425.

Tvergaard, V., 1993, Necking in tensile bars with rectangular cross-section, Computer Methods in Applied Mechanics and Engineering, 103(1-2), 273-290.

Van Der Giessen, E., Wu, P. D. and Neale, K. W., 1992, On the effect of plastic spin on large strain elastic-plastic torsion of solid bars, International Journal of Plasticity, 8(7), 773-801.

Van Der Giessen, E. and Neale, K. W., 1993, Analysis of the inverse Swift effect using a rate-sensitive polycrystal model, Computer Methods in Applied Mechanics and Engineering, 103(1-2), 291-313.

Van Houtte, P., 1978, Simulation of the rolling and shear texture of brass by the Taylor theory adapted for mechanical twinning, Acta Metallurgica, 26(4), 591-604.

Van Houtte, P., Delannay, L. and Kalidindi, S. R., 2002, Comparison of two grain interaction models for polycrystal plasticity and deformation texture prediction, International Journal of Plasticity, 18(3), 359-377.

Van Houtte, P., Li, S., Seefeldt, M. and Delannay, L., 2005, Deformation texture prediction: From the Taylor model to the advanced Lamel model, International Journal of Plasticity, 21(3), 589-624.

Vegter, H. and Van Den Boogaard, A. H., 2006, A plane stress yield function for anisotropic sheet material by interpolation of biaxial stress states, International Journal of Plasticity, 22(3), 557-580.

Wei, Y. J. and Anand, L., 2004, Grain-boundary sliding and separation in polycrystalline metals: Application to nanocrystalline fcc metals, Journal of the Mechanics and Physics of Solids, 52(11), 2587-2616.

Wonsiewicz, B. C. and Backofen, W. A., 1967, Plasticity of magnesium crystals, Metallurgical Society of American Institute of Mining, Metallurgical and Petroleum Engineers -- Transactions, 239(9), 1422-1431.

Wu, P. D. and Van Der Giessen, E., 1991, Analysis of elastic-plastic torsion of circular bars at large strains, Archive of Applied Mechanics, 61(2), 80-103.

Wu, P. D., Neale, K. W. and Van Der Giessen, E., 1996, Simulation of the behaviour of FCC polycrystals during reversed torsion, International Journal of Plasticity, 12(9), 1199-1219.

Wu, P. D., Neale, K. W., Van Der Giessen, E., Jain, M., Makinde, A. and Macewen, S. R., 1998, Crystal plasticity forming limit diagram analysis of rolled aluminum sheets, Metallurgical and Materials Transactions A (Physical Metallurgy and Materials Science), 29A(2), 527-35.

Wu, P. D., Inal, K., Neale, K. W., Kenny, L. D., Jain, M. and Macewen, S. R., 2001, Large strain behaviour of very thin aluminium sheets under planar simple shear, Delft, EDP Sciences, 5229-5236

Wu, P. D., Jain, M., Savoie, J., Macewen, S. R., Tugcu, P. and Neale, K. W., 2003, Evaluation of anisotropic yield functions for aluminum sheets, International Journal of Plasticity, 19(1), 121-38.

Wu, P. D., Macewen, S. R., Lloyd, D. J. and Neale, K. W., 2004, Effect of cube texture on sheet metal formability, Materials Science and Engineering A, 364(1-2), 182-187.

Wu, P. D., Macewen, S. R., Lloyd, D. J., Jain, M., Tugcu, P. and Neale, K. W., 2005a, On pre-straining and the evolution of material anisotropy in sheet metals, International Journal of Plasticity, 21(4), 723-739.

Wu, P. D., Graf, A., Macewen, S. R., Lloyd, D. J., Jain, M. and Neale, K. W., 2005b, On forming limit stress diagram analysis, International Journal of Solids and Structures, 42(8), 2225-2241.

Wu, P. D., Lloyd, D. J., Jain, M., Neale, K. W. and Huang, Y., 2007, Effects of spatial grain orientation distribution and initial surface topography on sheet metal necking, International Journal of Plasticity, 23(6), 1084-1104.

Yoo, M. H., 1980, Dislocation model for twinning and fracture and its application to hcp metals, Energy Technology Review, 825-830.

Yukutake, E., Kaneko, J. and Sugamata, M., 2003, Anisotropy and non-uniformity in plastic behavior of AZ31 magnesium alloy plates, Materials Transactions, 44(4), 452-457.

Zarandi, F., Seale, G., Mackenzie, L., Verma, R., Essadiqi, E. and Yue, S., 2007, Effect of Al and Mn additions on rolling and deformation behavior of AZ series magnesium alloys, To be published.

Zhou, Y., Neale, K. W. and Toth, L. S., 1991, Analytical solutions for the ideal orientations of FCC rolling textures, Acta Metallurgica et Materialia, 39(11), 2921-2930.

Zhou, Y. and Neale, K. W., 1995, Predictions of forming limit diagrams using a rate-sensitive crystal plasticity model, International Journal of Mechanical Sciences, 37(1), 1.

APPENDIX A TEXTURE GRADIENT IN HOT-ROLLED MG ALLOY

A.1 Introduction

In most forming processes, the as-formed materials do not show a uniform distribution of texture. In fact, significant texture gradients have been observed in various materials, e.g. the surface to mid-plane texture gradients in rolled sheets of metals (Engler *et al*., 2000) and surface to core texture gradients in extruded wires. These texture gradients not only can affect the mechanical behavior of material but also can be of great importance in enhancing our understanding of the deformation history for each point in the formed material.

Through-thickness texture gradient of different Mg alloy sheets has also been subject of a number of studies (e.g. Perez-prado and Ruano, 2002; Kim *et al*., 2005). In this appendix, the through-thickness texture gradient of *hot-rolled* and *hot-rolled and annealed* samples of Mg alloy (AZ31) sheets are studied.

A.2 Sample Preparation and Texture Measurement

The study was done on the samples cut from two specimens, formed through two different processes. The first specimen was a sheet of 2 mm thickness, obtained by hot-rolling with a 3 pass schedule with 30% reduction per pass at 50 rpm. The second sample had undergone the same rolling schedule with the same conditions. But, after being hot-rolled, it was annealed for 7 min at 450°C and then air-cooled. The initial thickness of both specimenswas 5mm, and both of them were annealed at 350°C for one hour before being rolled.

After mechanical polishing, the samples were etched by being rinsed in a chemical solution (10 ml Methanol, 90 ml Ethanol and 6 g Acid Citric) for about one minute. The samples were rinsed with ethanol and dried with a drier quickly after etching.

The texture measurement was done by x-ray diffraction using a Siemens D-500 texture Goniometer. As a measure of the texture gradient in the different layers of magnesium was desired, a low penetration x-ray beam was favored, thus the Copper tube was used, which produces x-ray beam with higher absorption and lower penetration. The texture

was measured at 4 different points through the thickness, namely, at surface, at mid-plane and at two points between.

In the first step, the three pole figures $\{0002\}$, $\{1000\}$ and $\{10\bar{1}1\}$ were measured for all four samples at the surface. In fact, for comparison the measurement was done for two different samples of each specimen. However, due to similar results for two different *hot-rolled* samples and two different *hot-rolled and annealed* samples, only one *hot-rolled* sample (MS1) and one *hot-rolled and annealed* sample (MS4) were chosen for further measurements.

As mentioned before, after measurements were done at the surface (MS1N1 and MS4N1), the samples were polished and a layer of the material was removed. We define "t" to be half the thickness of the samples. The second and third measurements (MS1N2, MS1N3, MS4N2 and MS4N3) were done for both samples at distances $0.3t$ and $0.6t$ from the surface. The last measurements (MS1N4 and MS4N4) were done at the mid-plane.

A.3 Results

Fig. 7.1 shows the $\{0002\}$ pole figure at different layers for both samples. As can be seen, the maximum intensity decreases from 6.8 at surface to 5.2 at mid-plane for the *hot-rolled* sample and from 5.9 to 4.0 for *hot-rolled and annealed* sample. This decrease was observed in other pole figures and the ODF as well. A noticeable phenomenon in the case of the hot-rolled sample is the change in the pole figure pattern from the basal texture at the surface to a split from the normal direction toward the rolling direction that happens near the mid-plane. This was seen only in the hot-rolled sample.

One cause of this split could be the temperature gradient from the surface to mid-plane during the rolling process. The higher temperature leads to the activity of different slip systems, which in turn can cause the split.

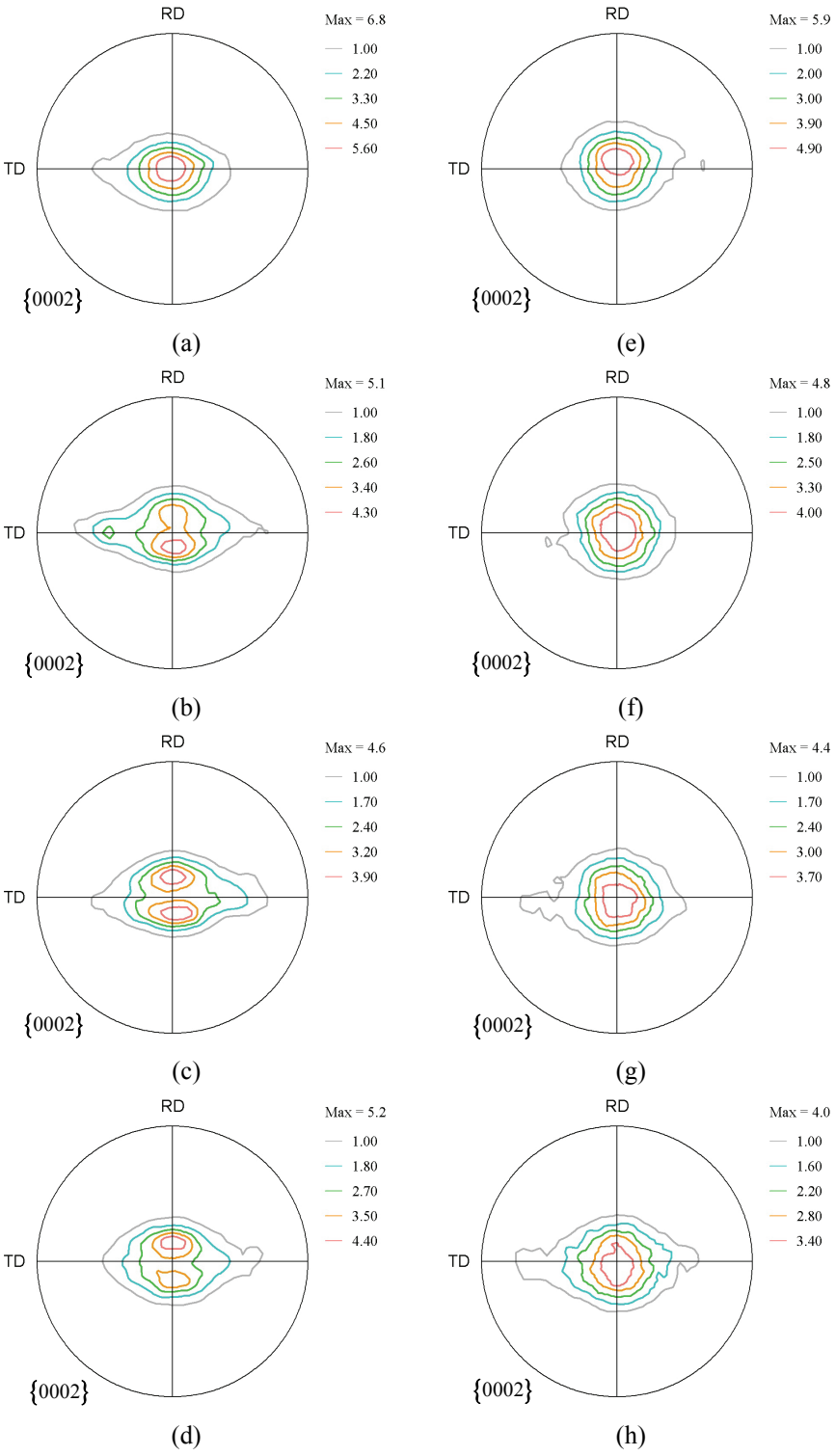

7.1 Change in $\{0002\}$ pole figure for *hot-rolled* (MS1, a-d) and *hot-rolled and annealed* (MS4, e-h) samples from surface to mid-plane

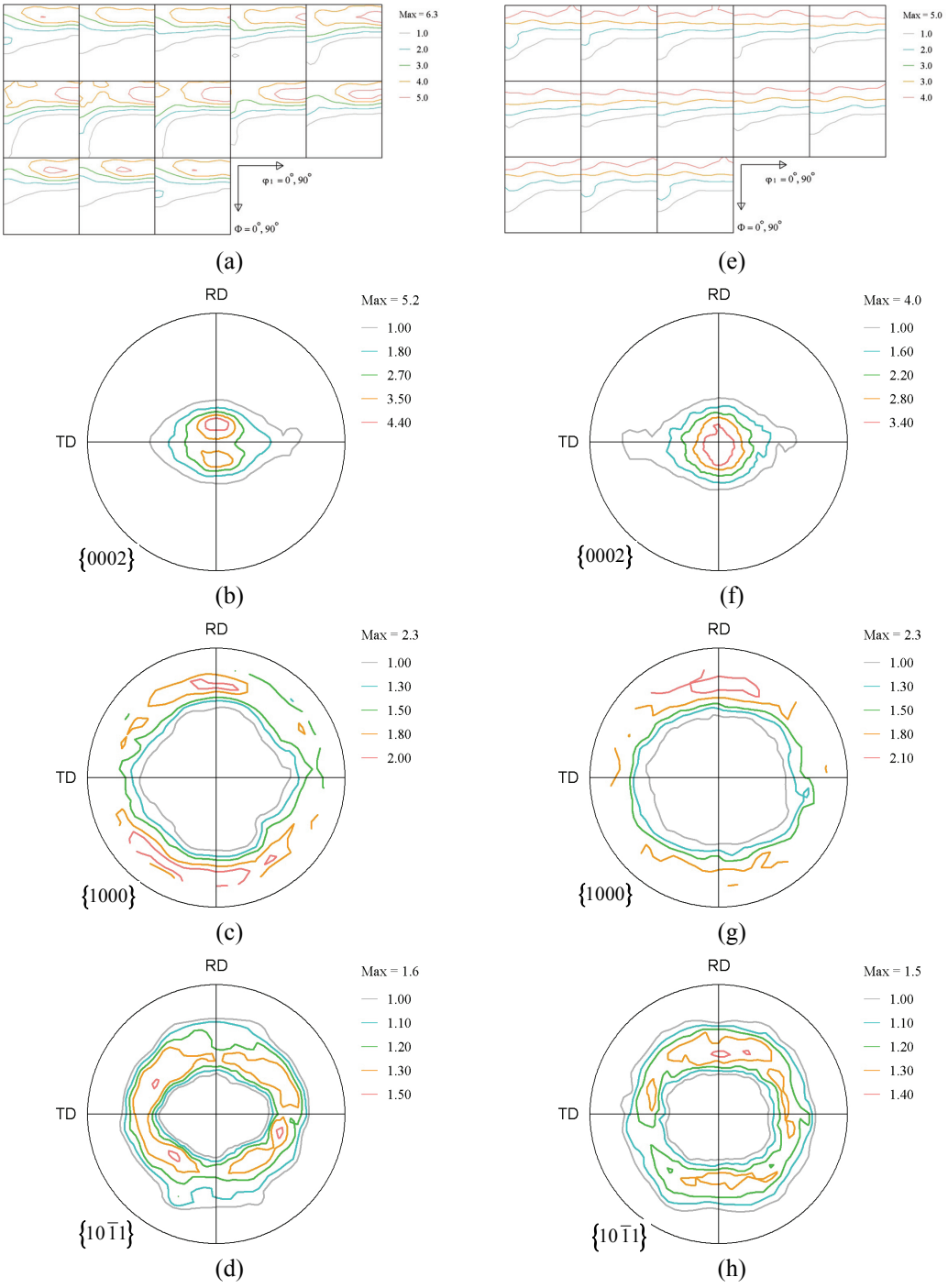

7.2 Texture Comparison between *hot-rolled* (MS1, a-d) and h*ot-rolled and annealed* (MS4, e-h) specimens at mid-plane

To better see the texture difference between the *hot-rolled* and *hot-rolled and annealed* samples, a direct comparison of the pole figures for these samples at mid-plane is shown in Fig. 7.2. The general difference in the ODF and pole figures of the two samples is the lower maximum intensity, 0-20%, for the annealed sample. Although there are some

partial differences between the ODFs of the two samples, the basic patterns are the same, and both of them show the same main features. The main difference observed in the pole figures, is the split present in the $\{0002\}$ pole figure of the hot-rolled sample around the normal direction toward the rolling direction.

A.4 Summary

The through-thickness texture gradient of *hot-rolled* and *hot-rolled and annealed* samples of Mg alloy (AZ31B) sheets was studied experimentally.

In general, the intensities of the annealed sample tended to be lower than the ones for only hot-rolled samples, and the maximum intensity was decreasing from the surface to mid-plane.

The inhomogeneity in the stress state and deformation can be the main cause of producing inhomogeneous texture in the final deformed samples. Also the temperature gradient from the surface to the mid-plane can be a major parameter. The reason for some of the differences is still unclear and demands further study. Also the effects of initial and final plate thicknesses, the reduction ratio, rolling temperature, and the roll speed on the texture-gradient should be studied more thoroughly.

APPENDIX B LIST OF PUBLICATIONS

1. Shahi, M., Nemes, J. A., Yue., S., The Effect of Local Texture on the Post-localization Behavior of Mg Alloys – Crystal Plasticity Modeling, To be submitted to International Journal of Solids and Structures.

2. Shahi, M., Nemes, J. A., Zarandi, F., Yue., S., Strain-rate Sensitivity in Mg Alloys and its Effect in the Crystal Plasticity Modeling, To be submitted.

3. Shahi, M., Nemes, J. A., Yue, S., 2007, Role of Individual Slip Systems and Strain Rate Sensitivity in the Mechanical Response of Mg Alloys at Warm Temperatures: CPFE Modeling, Submitted to International Journal of Computational Materials Science

4. Shahi, M., Nemes, J. A., 2007, Crystal Plasticity Modeling of the Slip Systems Activity in Mg Alloys at Higher Temperatures, SAE SP, NUMB 2108, 49-56.

5. Shahi, M., Nemes, J. A., 2007, Mg alloys at warm temperatures: Crystal Plasticity modeling, CMSC2007, Hamilton, Canada (abstract and presentation only)

APPENDIX C DESIGN OF THE PROPOSED EXPERIMENTS

C.1 Design of the Experiment Tables

To obtain a better understanding of the effect of different deformation mechanisms on Mg alloy behavior, a series of experiments are proposed over a range of temperatures and strain-rates for Mg alloy AZ31. The considered range of temperature is the so-called warm temperatures from approximately 75°C to 275°C. A range of strain rates that occur quite frequently in forming processes, between 0.001 s^{-1} and 1 s^{-1}, is considered.

To calibrate the computational models and to validate them, a set of well-documented experimental data is needed, which can be summarized as follows:

- Simple tension and compression test results at
  - temperatures from 75°C to 275°C
  - strain-rates from $0.001\,s^{-1}$ to $1\,s^{-1}$
- The following data is needed from the experiments
  - Initial and final texture of the material (preferably results for different initial textures: results from the tests on the samples cut in the RD and the TD from a hot-rolled plate is an example).
  - Stress-strain curves
  - Other data such as r-values
  - Experiment set-up (especially the temperature and strain-rate)

Regarding the characterization data, if such data are available and validated, it can be of great help in calibrating the model faster and more realistically. However, having these data is not crucial for running the crystal plasticity simulations; as such data can be approximated using inverse methods and the macro level experimental results.

Due to the large number of experiments needed with different combinations of strain-rate and temperature, a methodical selection procedure has been used for the design of experiments. In choosing this method, it is considered that most of “fractional factorial designs” (including Taguchi’s orthogonal arrays) are meaningful when the number of factors is 4 or higher; here, we have only two factors: strain rate and temperature.

Therefore, the Central Composite-Inscribed (CCI) method is used in designing the experiments matrix. Using this method, the number of all the possible combinations, which in this case is 20, is reduced to 9. These nine points are shown in Table C.1.

Table C.2 shows a combined CCI method, in which the number of selected points increases to 16, which is used to add to the accuracy of this approach. This will fill more design points in space, especially in the inner area which is the main area of interest.

Table C.1 Central Composite Design - Inscribed (CCI)

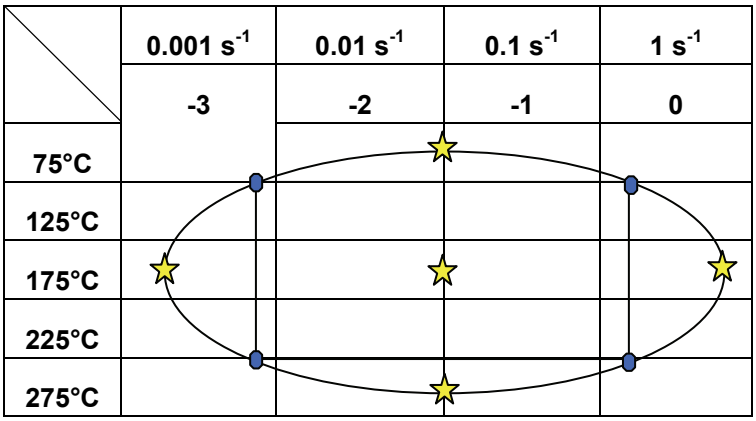

Table C.2 Combined Central Composite Designs - Inscribed (CCI)

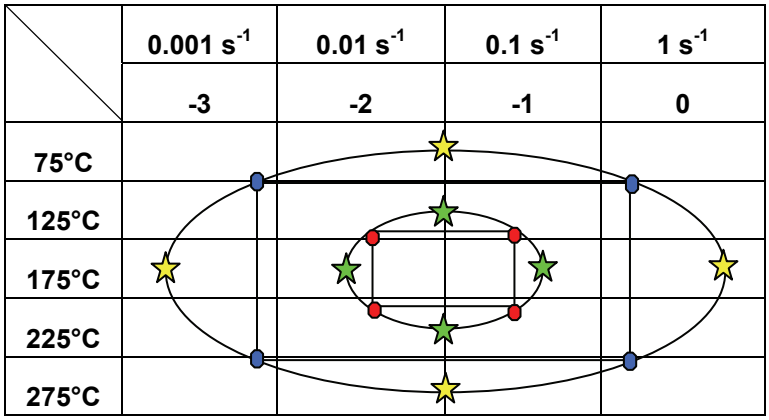

In order to obtain a consistent set of data, the points obtained using the combined method (Table C.2) will be proposed for doing the experiments (stress-strain curves). However, only the experiments shown by the data points in Table C.1 will be used for measurement of texture and r-value. It should be noted that although some of the selected temperatures appear to be quite close to each other (such as 75°C and 104°C) and we expect similar behaviors, the experiments at these temperatures are done at different strain-rates. In

other words, using this method, instead of doing the experiments at, for example, 90°C and several different strain rates, a limited number of tests are done at 75°C and 104°C and the strain rates obtained. With the current design, it is essential that the specimens for compression and tension be machined from the same rolled-plate, with known metallurgical characteristics such as composition, grain size, texture, and history.

C.2 Proposed Experiments

The recommended experiments are shown in Tables C.3 through C.6. It should be noted that for each combination, different specimens should be used for stress-strain curve, texture (and r-value) measurement and the strain-rate change. The experiments for obtaining the stress-strain curve should be done until fracture, while for the texture (and r-value) measurements, the experiments should be terminated at a strain of 0.15, which is usually before the instability region. For the strain-rate change, the experiments start with the strain-rate indicated in Table C.3, and the change strain-rates will be determined according to the flow behavior observed in the material. Some data on the effect of strain rate on flow behavior can also be obtained from the experiments in Table C.3 through C.6, i.e. same temperatures, different strain rates.

The total number of specimens needed is listed in Table C.7.

Table C.3 Combination of strain-rate and temerature; experiments to be done (**Tension - RD**)

Exp No	Temp (°C)	strain-rate (s^{-1})	Stress-Strain Curve	R-value	Texture*	Strain-rate Change Test
1	75	0.03	X			
2	75	0.03		X	√	
3	75	0.03				X
4	104	0.003	X			
5	104	0.003		X	√	
6	104	0.003				X
7	104	0.36	X			
8	104	0.36		X	√	
9	104	0.36				X
10	125	0.03	X			
11	125	0.03		X		
12	140	0.015	X			
13	140	0.07	X			
14	175	0.001	X			
15	175	0.001		X	√	
16	175	0.001				X
17	175	0.01	X			
18	175	0.03		X	√	
19	175	0.03				X
20	175	0.1	X			
21	175	1	X			
22	175	1		X	√	
23	175	1				X
24	210	0.015	X			
25	210	0.07	X			
26	225	0.03	X			
27	225	0.03		X		
28	246	0.003	X			
29	246	0.003		X	√	
30	246	0.003				X
31	246	0.36	X			
32	246	0.36		X	√	
33	246	0.36				X
34	275	0.03	X			
35	275	0.03		X	√	
36	275	0.03				X

* No need for separate samples (shown by √)

Table C.4 Combination of strain-rate and temperature at which the experiments need to be done (**Compression - RD**)

Exp No	Temp (°C)	strain-rate (s^{-1})	Stress-Strain Curve
1	75	0.03	X
2	104	0.003	X
3	104	0.36	X
4	125	0.03	X
5	140	0.015	X
6	140	0.07	X
7	175	0.001	X
8	175	0.01	X
9	175	0.1	X
10	175	1	X
11	210	0.015	X
12	210	0.07	X
13	225	0.03	X
14	246	0.003	X
15	246	0.36	X
16	275	0.03	X

Table C.5 Combination of strain-rate and temperature at which the experiments need to be done (**Tension - TD**)

Exp No	Temp (°C)	strain-rate (s^{-1})	Stress-Strain Curve	R-value
1	75	0.03	X	
2	75	0.03		X
3	104	0.003	X	
4	104	0.003		X
5	104	0.36	X	
6	104	0.36		X
7	125	0.03		X
8	175	0.001	X	
9	175	0.001		X
10	175	0.01	X	
11	175	0.03		X
12	175	1	X	
13	175	1		X
14	225	0.03		X
15	246	0.003	X	
16	246	0.003		X
17	246	0.36	X	
18	246	0.36		X
19	275	0.03	X	
20	275	0.03		X

Table C.6 Combination of strain-rate and temperature at which the experiments need to be done (**Compression - ND**)

Exp No	Temp (°C)	real strain-rate (s^{-1})	Stress-Strain Curve	R-value	Texture*
1	75	0.03	X		
2	75	0.03		X	√
3	104	0.003	X		
4	104	0.003		X	√
5	104	0.36	X		
6	104	0.36		X	√
7	125	0.03	X		
8	140	0.015	X		
9	140	0.07	X		
10	175	0.001	X		
11	175	0.001		X	√
12	175	0.01	X		
13	175	0.03		X	√
14	175	0.1	X		
15	175	1	X		
16	175	1		X	√
17	210	0.015	X		
18	210	0.07	X		
19	225	0.03	X		
20	246	0.003	X		
21	246	0.003		X	√
22	246	0.36	X		
23	246	0.36		X	√
24	275	0.03	X		
25	275	0.03		X	√

* No need for separate samples (shown by √)

Table C.7 Total number of specimens needed

Type of Specimen	Number of Samples (stress-strain)	Number ofSamples (R-value)	Number of Samples (Rate-jump)	No of Texture Measurements	Total No Samples needed
RD / Tens	16	11	9	(9)	36
RD / Comp	16	-	-	-	16
TD / Tens	9	11	-	-	20
ND / Comp	16	9	-	(9)	25
TOTAL	57	31	9	(18)	**97**